Technische Universität München

Department of Chemistry and Catalysis Research Center
Chair of Technical Electrochemistry

Performance and Durability of Ion Exchange Membrane Fuel Cells – From Electrocatalysis to Single Cells

Jan Nicolas Schwämmlein

Vollständiger Abdruck der von der Fakultät für Chemie der
Technischen Universität München zur Erlangung des akademischen Grades eines

Doktors der Naturwissenschaften (Dr. rer. nat.)

genehmigten Dissertation.

Vorsitzende:	Prof. Dr. Kathrin Lang
Prüfer der Dissertation:	1. Prof. Dr. Hubert A. Gasteiger
	2. Prof. Dr.-Ing. Kai-Olaf M. Hinrichsen
	3. Prof. Dr. Matthias Arenz

Diese Dissertation wurde am 20.04.2020 bei der Technischen Universität München eingereicht und durch die Fakultät für Chemie am 17.08.2020 angenommen.

“Nanos gigantum humeris insidentes.”
*“*D*warves perched on the shoulders of giants.“*

Bernhard von Chartres
ca. 1120

Abstract

The major challenge for a widespread implementation of hydrogen fuel cells in the automotive market is their high cost and short lifetime. These topics are addressed in this thesis for two distinct fuel cell systems, namely anion exchange membrane fuel cells (AEMFCs) and proton exchange membrane fuel cells (PEMFCs). First of all, the origin of the high hydrogen oxidation and evolution reaction (HOR/HER) exchange current density of bimetallic Pt-Ru alloys in alkaline media is investigated, providing a path for future catalyst development to reduce the cost of AEMFCs. Thereafter, the conductivity of a state-of-the-art anion exchange membrane is assessed at temperatures below the freezing point of water and compared to a commercial Nafion and an experimental hydrocarbon based membrane. Moving on to the durability of PEMFCs, an insight into the degradation of the anode catalyst layer during start-up and shut-down (SUSD) of the fuel cell is provided, which is scarcely investigated in the literature due to the prominent cathode degradation in SUSD events. Thereafter, different accelerated stress tests (ASTs) are used to degrade high and low loaded cathodes and to identify the evolution of the O_2 mass-transport resistances alongside other key performance indicators of the fuel cell. One of the thus developed ASTs is subsequently applied to a home-made Pt_xY/C catalyst, thoroughly characterized using physical-chemical and electrochemical methods. Finally, a supplementary study is conducted that employs electrochemical deposition of Pt on Sn as a model system for the development of future catalysts. Here, it is shown that surface oxide species can fully inhibit the Pt deposition process, as well as the direct formation of a Pt-Sn alloy via deposition of Pt on Sn.

Kurzfassung

Die größten Hürden für die Einführung von Wasserstoff-Brennstoffzellen im Automobilbereich sind deren hohe Kosten sowie deren Haltbarkeit. In dieser Arbeit werden diese Themen anhand von zwei verschiedenen Brennstoffzellensystemen, basierend auf Anionen- und Kationen-Austauschmembranen (AEMFCs und PEMFCs), untersucht. Zuerst wird der Ursprung der hohen Wasserstoffoxidations- und -reduktionskinetik bimetallischer Pt-Ru Legierungen im alkalischen Milieu untersucht, um einen Grundstein für die zukünftige Katalysatorentwicklung zu legen und somit die Kosten von AEMFCs zu mindern. Im Anschluss wird die Leitfähigkeit einer, dem heutigen Stand der Technik entsprechenden, Anionen-Austauschmembran bei Frostbedingungen bestimmt und mit einer kommerziell erhältlichen Nafion sowie einer experimentellen Kohlenwasserstoff-basierten Membran verglichen. Bezüglich der Haltbarkeit von PEMFCs wird zuerst ein Einblick in die Alterung der Katalysatorschicht auf der Anode bei Start-Stopp Vorgängen (SUSD) der Brennstoffzelle gegeben, welche aufgrund der dominierenden Kathodenalterung nur selten in der Literatur untersucht wird. Im Anschluss werden Kathoden mit hoher und niedriger Pt Beladung unterschiedlichen Alterungstests (ASTs) ausgesetzt, um aufkommende O_2 Massentransportwiderstände zusammen mit anderen wichtigen Brennstoffzellenparametern zu evaluieren. Im Folgenden wird einer der dabei entwickelten ASTs auf einen selbst hergestellten Pt_xY/C Katalysator angewendet, welcher zusätzlich mittels physikalisch-chemischen Analysemethoden untersucht wird. Abschließend wird eine ergänzende Studie präsentiert, in welcher die elektrochemische Abscheidung von Pt auf Sn als Modellsystem für die zukünftige Katalysatorentwicklung untersucht wird. Dabei konnte insbesondere gezeigt werden, dass Oxide auf der Zinnoberfläche die Pt Abscheidung vollständig verhindern können und dass sich Pt-Sn Legierungen direkt durch Abscheidung von Pt auf Sn bilden.

Content

List of Acronyms

AEMFC	Anion exchange membrane fuel cell
AST	Accelerated stress test
BE	Binding energy
COR	Carbon oxidation reaction
CV	Cyclic voltammogram
DSC	Differential scanning calometry
ECSA	Electrochemical surface area
EDX	Energy dispersive X-ray
EIS	Electrochemical impedance spectroscopy
EW	Equivalent weight
FEP	Fluorinated ethylene propylene
GDL	Gas diffusion layer
GEIS	Galvanostatic electrochemical impedance
HDPE	High density polyethylene
HER	Hydrogen evolution reaction
HOR	Hydrogen oxidation reaction
H_{upd}	Hydrogen under potential deposition
IR	Infrared
MEA	Membrane electrode assembly
MLE	Monolayer equivalent
MPL	Microporous layer
nccm	Normal cubic centimeters per minute
OER	Oxygen evolution reaction
ORR	Oxygen reduction reaction
PE	Polyethylene
PEEK	Polyetheretherketone
PEIS	Potentiostatic electrochemical impedance
PEMFC	Proton exchange membrane fuel cell
PFSA	Perfluorosulfonic acid
PTFE	Polytetrafluoroethylene
rf	Roughness factor
RH	Relative humidity
RHE	Reversible hydrogen electrode
SEM	Scanning electron microscope
SUSD	Start-up and shut-down
TEM	Transmission electron microscope
TGA	Thermogravimetric analysis
TS	Tafel slope
XRD	X-ray diffraction

1. Introduction

1.1. The Role of Fuel Cells in a Battery World

At least since the Paris agreement was signed by 195 members of the United Nations Framework Convention on Climate Change in 2015, a reduction of the global CO_2 emissions has become a common goal throughout the world.[1] The emission of CO_2 from the mobility sector accounts for 14% of the greenhouse gas emissions worldwide, governed by the widespread use of the internal combustion engine (ICE) fueled by diesel or gasoline (status 2014).[2] In Europe, 72% of the land-based transport emissions are caused by passenger vehicles and small vans, while 25% originate from heavy duty trucks and busses (status 2015).[3] The most promising two candidates to replace conventional ICEs in those applications are battery electric vehicles (BEVs) and fuel cell electric vehicles (FCEVs). Both technologies generally offer the opportunity to operate CO_2 neutral as long as the electricity is produced by renewable energy sources. This thesis deals with the development of fuel cells and the first section of the introduction compares fuel cell and battery technology to draw a conclusion for the most likely use of fuel cells.

System Cost Comparison.—In contrast to combustion engines, BEVs and FCEVs use electric energy to power a motor. Since electric motors are comparably simple and well-developed, they are not considered as a hurdle for the widespread commercialization of BEVs and FCEVs. Furthermore, in contrast to ICEs, consisting of many moveable parts, electric motors are durable and require little maintenance (e.g., no oil changes).

The required power for the motor in BEVs originates from a battery pack which has a certain amount of stored energy, depending on the desired driving range. The battery type that currently receives most attention for automotive applications is the Li ion battery which stores electricity by shifting Li ions between anode and cathode in an electrochemical intercalation reaction (other battery types are not considered here). While the power output of the battery (e.g., 125 – 135 kW for the BMW i3)[4] is typically sufficient compared to ICEs (e.g., 135 kW for the BMW 120i),[5] the energy of most commercially available BEVs is small (e.g., 38 kW h for the BMW i3), significantly limiting the

driving range of current systems (BMW specifies a theoretical range of 359 km for a consumption of 0.13 kW h km^{-1}, simultaneously giving an optimistic practical range of 260 km).[4] The reason for this shortcoming of BEVs is the overall price of the battery pack which amounts to ≈$5200 for a driving range of 200 km and to more than $15000 for a car with a range of 600 km, considering $200 kW^{-1} h^{-1} (for the very optimistic consumption of 0.13 kW h km^{-1}).[6,7] Even if a tremendous reduction of today's battery pack production costs is taken into account, potentially reaching values as low as $125 kW^{-1} h^{-1}, batteries that provide a range of 600 km would still cost ≈$10000. On the other hand, today's car owners are accustomed to very long driving ranges (e.g., 1000 km, calculated for a consumption of 6 L per 100 km at 60 L tank volume) in ICEs due to the simple implementation of large fuel tanks.

The second technology under consideration for automotive applications, H_2 powered proton exchange membrane fuel cells (PEMFCs) use the chemical energy liberated in the reaction of H_2 and O_2 (from air) to produce water in an electrochemical process (a more detailed overview on the working principle of PEMFCs is given in the next section). One of the main advantages of FCEVs is the decoupling of power generation by the fuel cell and energy storage in a H_2 tank. This enables the production of long range vehicles (e.g., approximately 500 km for the Toyota Mirai)[8] by adjusting the size of the H_2 storage tank to the desired range. Even though H_2 storage is more expensive compared to gasoline / diesel, it is still more than one order of magnitude more affordable than energy stored in a battery ($10.8 kW^{-1} h^{-1}, estimated for a 700 bar dual-tank configuration at a production volume of 500000 units annually), resulting in ≈$1800 for a 5 kg H_2 tank system (calculated by the lower heating value of 33.6 kW h $kg_{H_2}^{-1}$).[9] One major hurdle preventing widespread implementation of FCEVs is the price of fuel cell stacks, which is due to the high cost of certain cell components (e.g., bipolar plates) and the use of scarce Pt as a catalyst for the hydrogen oxidation reaction (HOR) on the anode and the oxygen reduction reaction (ORR) on the cathode. A reliable estimation of the total system cost for PEMFCs as a widespread system for transportation applications is not trivial to date, given that mass production of fuel cells has not yet started and current manufacturing costs of small scale FCEVs are not representative for the future. Nevertheless, system costs on the order of $45 kW^{-1} are achievable for mass market

production (assuming an annual production of 500000 systems) with current technology,[10] resulting in a total cost of $4500 for a 100 kW system (excluding the cost of the H_2 tank). While the individual component cost share for bipolar plates (30%) and the membrane electrode assembly (MEA, 60%) in mass produced stacks is predicted to remain reasonably constant in the future, the overall costs are expected to drop significantly upon commercialization. Even though future forecasts inherently contain large uncertainties, a significant price reduction of fuel cell stacks is expected after widespread commercialization (similar development as observed for batteries), and a cost of only $11.5 kW^{-1} for mass produced fuel cell stacks might be achievable in the coming years, leading to lowered system costs of $32.8 kW^{-1}, hence an affordable price around $3500 for a 100 kW PEMFC system (excluding the cost of the H_2 tank).[10]

Refueling and Infrastructure.—A great advantage of BEVs is that they can simply be charged at every regular household plug. However, this method results in very long recharging times (e.g., 15 h for 80% capacity of the BMW i3) due to the low power output. Even though long charging times may not be a big issue for applications with a plannable drive cycle, many customers might consider it a large disadvantage. Furthermore, low power charging is not readily available in cities, where a large fraction of the car owners does not have access to a plug close to the parking position. Therefore, great efforts are currently carried out to establish a sufficiently large charging infrastructure with a higher power output. Even though the charging time at such stations can be reduced to less than 1 h (e.g., ≈45 minutes with a 50 kW DC charger for 80% capacity of the BMW i3),[4] the charging takes significantly longer compared to refueling a gasoline tank in conventional ICEs. Additionally, large investments are necessary to build the charging points, modernize the metropolitan electricity grid and to provide the power necessary for simultaneous charging of several vehicles, as the following example shows. In a hypothetical scenario where solely 10% of the cars in the city of Munich are BEVs (≈80000)[11] and where only 50% of these vehicles were charged simultaneously with a 50 kW DC charger (e.g., after common working hours), a power output of more than 2 GW would be required. Comparing this to the average power production in Munich of < 1 GW (calculated from the annual electricity consumption of 7.5 TW h),[12] one receives a clear impression of the extraordinary investments into electricity generation

within / close to the city and the tremendous modernization costs for the electric grid to transport this power. In addition, the investment cost to provide electric charging stations for such a (small) fleet are on the order of ≈$1.5 billion (DC charging station prices vary significantly between ≈$10000 and ≈$40000).[13] Finally, the required charging time at such stations is insufficient for intermediate charging during long distance travel (e.g., intercity), a problem that Tesla has seemingly solved by the introduction of 120 kW super chargers next to the highway. While this clearly is a step forward for the applicability of BEVs, the high investment cost (≈$270000 per station)[14] and the still considerable waiting times (≈30 minutes to charge a Tesla vehicle, not accounting for time spent waiting on other users) are rather unfavorable.[15]

In contrast to BEVs, FCEVs can refuel much faster and have already practically achieved refueling times of < 5 min for passenger vehicles (e.g., 3 – 5 min for the Toyota Mirai),[8] comparable with gasoline. A further advantage over the infrastructure constraints of BEVs is that the refueling system would not be significantly different compared to gas stations, with a small amount of required H_2 filling stations and no need for the customer to change the current consumption scheme. Considering that only ≈10% of all currently available fueling stations would be mandatory to yield an acceptable, early stage network, a total of 1500 fueling stations would need to be set up in Germany. Depending on the specific type, the estimated cost of a H_2 fueling station is on the order of $2 – 3 million (anticipated costs in 2015),[16] whereas concepts for a low cost, early market alternative at a price of less than $500000 were already proposed.[17] Taking a rough estimate with an average cost of $1 million per fueling station and 1500 stations, full H_2 infrastructure coverage in Germany could be achieved with an investment of $1.5 billion. Even though this seemingly is a large number, setting up H_2 fueling stations throughout an entire country costs the same as the charging infrastructure for 10% of the vehicles in a single city. Furthermore, the dimension of this investment should be compared to the available capital in the automotive market, where a single company involved in the Diesel scandal recently had to pay a fine of more than $15 billion.[18]

Energy Generation and Storage.—The following provides a rough analysis of the greenhouse gas emissions produced by BEVs and FCEVs and the constraints of these

technologies regarding the electricity production from renewable sources. A more detailed analysis of the greenhouse gas emissions of different transportation technologies was carried out by the Joint Research Center of the European Commision.[19]

In Germany (status 2017), electricity is partially produced by combustion of fossil resources emitting CO_2 (37% coal, 13% natural gas, 1% oil), from renewable energy sources (33%) and by other means (12% nuclear, 4% other).[20] Accordingly, every kW h of electricity, produced in Germany, generates 489 g_{CO_2},[21] which in turn is responsible for 63.6 g_{CO_2} km^{-1} if used to power a BEV (assuming 0.13 kW h km^{-1},[4] and 100% charge efficiency). Even though these emissions are not negligible with respect to their global warming potential, they are significantly lower than those emitted by ICEs, which typically exceed 100 g_{CO_2} km^{-1} (e.g., 140 g_{CO_2} km^{-1} for the BMW 120i).[5] FCEVs use H_2 as a fuel, which is currently produced by steam reforming of natural gas (48%, Equation [1]), by petroleum refining (30%), or from coal gasification (18%), while only 4% are produced by water electrolysis (Equation [2]).[22]

$$CH_4 + 2H_2O \longrightarrow CO_2 + 4H_2 \qquad [1]$$

$$2H_2O \longrightarrow 2H_2 + O_2 \qquad [2]$$

According to Equation [1], 5.5 g_{CO_2} are produced chemically per gram of H_2 (4 mol H_2 per 1 mol CO_2; $M(H_2)$ = 2 g mol^{-1}, $M(CO_2)$ = 44 g mol^{-1}). Taking into account that the aforementioned reaction is endothermic, hence combustion of additional methane is required for heating, ≈9 g_{CO_2} $g_{H_2}^{-1}$ are produced,[23] which therefore amounts to 68.4 g_{CO_2} km^{-1} for FCEVs that use H_2 from methane steam reforming (calculated for a consumption of 7.6 g_{H_2} km^{-1} for the Toyota Mirai).[24] In contrast to steam reforming, a FCEV fueled by H_2 from electrolysis with the current electricity mix would emit a significantly larger amount of 176 g_{CO_2} km^{-1} (calculated using the lower heating value of 33.6 kW h $kg_{H_2}^{-1}$ and 70% efficiency for electrolysis in combination with the German CO_2 foot print for electricity of 489 g_{CO_2} kW^{-1} h^{-1}, amounting to 23.5 g_{CO_2} $g_{H_2}^{-1}$), comparable to current ICEs. While both, FCEVs fueled by H_2 from steam reforming and BEVs powered by the current electricity mix are capable to reduce CO_2 emissions in the

transportation sector, the long-term goal is the sole utilization of renewable energy sources, where both technologies operate CO_2 neutral.

Similar to other gases, H_2 can be transported relatively simple over large distances (e.g., by shipping), enabling large scale H_2 production in favorable locations (e.g., with high solar irradiation or large hydropower capabilities), where electricity is affordable and grid control is simple.[25] While transport of electricity for BEV charging is generally also possible and is a good option over short distances (small efficiency losses, simple infrastructure), its range is limited since long distance grids are very costly (e.g., over-seas).[26] A general issue associated with renewable energy sources are fluctuations in the produced amount of electricity due to a lack of control over, e.g., solar irradiation or the current wind situation. Nevertheless, the supply to the grid and the consumed electricity must be reasonably balanced to obtain a sufficient stability and uninterrupted power supply. In a transitioning phase towards full renewable energy production (e.g., 50% renewable energy share), fluctuations could be smoothed by adjusting the power consumption of certain applications. This is generally possible for water electrolysis where the production capacity can at least partially be increased or decreased to improve production-demand harmonization, while producing H_2 to fuel the FCEV fleet. Nevertheless, the extent to which the electrolyzer output can be reduced during low electricity production phases of renewable energies might be limited, since extended interrupts have a negative impact on the investment economics and very low H_2 production rates are technically difficult to achieve (formation of explosive H_2/O_2 mixtures due to gas crossover in PEM electrolyzers). Furthermore, producing a large H_2 stock for FCEVs with excess electricity requires a H_2 storage network that increases the production cost compared to on-demand H_2 production. In contrast to electrolyzers, charging of BEVs will most likely be mainly controlled by the customer needs (i.e., charging after work) and therefore, in addition to not contributing to the electricity leveling, actually requires additional efforts for on-demand energy supply. A concept to solve this is the so-called vehicle-to-grid approach, where BEVs supply their stored energy back to the grid if the current energy production by renewables is low.[27] While this might be a generally useful concept to balance the overall electricity situation, it is not yet clear if drawing the power from a private BEV is a very appealing approach for car owners who expect their

car to be charged at a specific time and to be operational at any time. Financial incentives for this service may, however, help convince the customer.

Especially, when producing electricity entirely from renewable sources, a large discrepancy between produced power and the actual demand is imminent and a real storage option (not only demand leveling) is necessary.[28] Storage solutions are categorized with respect to the storage time, where short storage times are used to guarantee a high power quality, daily storage enables primary regulation of different sources and supply reserves cover seasonal and long-term energy supply. Besides other solutions, H_2 can be produced on a large scale and stored for later use (not feasible for short-term storage) or the excess electricity can be used to charge stationary batteries that supply their energy back to the grid if needed. While producing new stationary Li ion batteries for energy storage is most likely not a cost competitive approach due to their high price per kW h (see above), second life batteries might be a useful option for an existing BEV mass market.[29] However, especially batteries which have been used for a long time in the demanding environment of a BEV (fast charges / discharges, low / high temperatures) are likely to exhibit a relatively high failure rate, compromising cost efficiency of this approach. Furthermore, Li ion battery technology may present safety concerns on a large scale due to the high amount of stored energy in a system that is susceptible to thermal runaways (especially for second life batteries). In principle, H_2 is an attractive option (low storage cost, see above) for medium to long-term energy storage and has been discussed in this context for several decades. This is especially true if FCEVs already have a high market share, since this implies that H_2 infrastructure is already present and integration of new devices is comparably simple. Nevertheless, electricity storage via H_2 suffers from a low round-trip efficiency, originating from efficiency losses during electrolysis and in the fuel cell.

Finally, whether H_2 is used in FCEVs or for electricity storage, it has to be considered that electrolysis is costlier than the direct use of electricity in a battery. Assuming an efficiency of 70% for the electrolysis, 48 kW h of electrical energy are needed to produce 1 kg_{H_2} (based on the lower heating value of H_2). For a FCEV with a consumption of 7.6 $g_{H_2}^{-1}$ km^{-1}, this results in an equivalent of 0.36 kW h km^{-1}, which is nearly three times more compared to a BEV. This simple energy comparison for the two technolo-

gies poses a clear advantage of BEVs and significant improvements are necessary with regards to H_2 production and fuel consumption in FCEVs. Nevertheless, the low price of electricity will most likely only apply to slow charging via a regular household plug, while using a public charging station (especially fast chargers) might induce significantly higher costs, limiting the fuel economy advantage of BEVs.

Current Status and Future Scenario.—It has to be mentioned at this point that the interpretation of fuel cell vs. battery powered mobility and the projection into the future represents the personal opinion of the author of this thesis. While short term solutions to reducing the CO_2 emissions from the transportation sector might exist without drastically changing the current mobility system (e.g., more efficient ICEs), the only feasible way that incorporates a medium- to long-term view is to fully avoid the combustion of fossil fuels and hence implement new technologies in the automotive sector. Currently, BEVs are more affordable than FCEVs, since batteries are already produced on a large scale and experienced tremendous production cost decreases in the last decades. Therefore, world-wide, more than 3 million BEVs are already in circulation (status 2017)[30] and car manufacturers have announced large investments for fleet electrification in the near future. Compared to the widespread series production of BEVs, the commercialization of FCEVs is a recent development and was only initiated by the release of the Hyundai ix35 (2014),[31] the Toyota Mirai (2015),[32] the Honda Clarity (2016),[33] and more recently by the Mercedes-Benz GLC F-Cell (2018).[34] While this shows the early commercialization of fuel cell technology in the automotive sector, mass production has not yet been realized, causing high expenses for the production of FCEVs. Nevertheless, current estimates predict that FCEV systems are likely to be significantly cheaper than BEVs over long distances (see calculations above) or for heavy duty activities (e.g., trucks). Therefore, many car manufacturers have intensified their fuel cell research efforts and announced small series FCEVs in the near future, e.g., Audi in 2020,[35] BMW in 2021[36] and GM in the early 2020s.[37]

Figure 1 provides an overview of the plausible markets for BEVs (red), FCEVs (green), a coexistence of both (brown shaded), as well as the future potential for fuel cells in the transportation sector (purple). Accordingly, BEVs are likely to dominate the light duty or short-range car market due to their lower production cost for low energy systems, as well as the lower price per traveled km. Nevertheless, many car owners might not be willing to purchase vehicles with a short range combined with long charging times or would like to own heavier vehicles (e.g., SUVs) which can currently (and in the near future) hardly be achieved economically with batteries. In the future, however, assuming further improvements of battery and charging technology, a higher penetration of BEVs into this segment might become plausible. Despite their high cost, unfavorable charging times and limited range, batteries have a clear advantage over FCEVs in that they have a lower cost per driven km due to the costly production of H_2 from electricity. This might be an even more important concern when energy production prices rise due

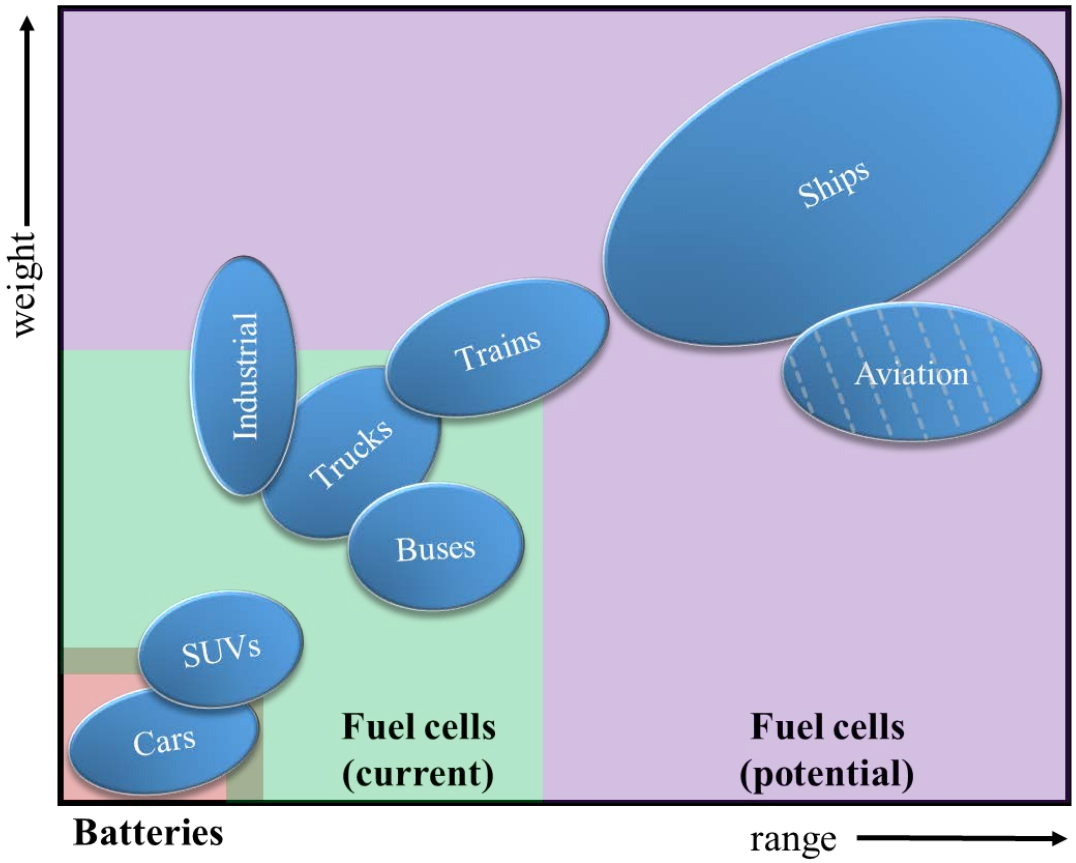

Figure 1. Schematic representation of the likely markets for batteries (red) and fuel cells (green) with respect to range and duty of the operation. The potential fuel cell market that has not yet been commercially established is shown in purple.

to the integration of renewable energies and when car owners are not willing to accept additional fuel expenses in favor of more convenient refueling times and long ranges. On the other hand, for long distance or heavy duty operations, implementation of batteries (e.g., in a truck presented by Tesla)[38] seems to make little sense due to excessive battery cost ($125000, 2 kW h mile^{-1}, 500 miles, $125 kW^{-1} h^{-1}). In this sector, FCEVs are clearly the more affordable choice if produced on a large scale (see calculation above). Hence, a great potential of fuel cells lies in applications where battery storage capacities are not affordable, e.g., for trucks,[39–41] trains,[42] or ships (not yet commercialized).[43] Fuel cell powered trains are, of course, only an option for routes that are not completely electrified and would otherwise require the use of diesel engines. Electrifying the shipping industry with fuel cells offers an enormous CO_2 reduction potential and might actually be the only reasonable alternative for clean transportation of goods in a globalized world. Even though research on fuel cell powered aviation exists and fuel cells are a far more likely power source for planes than batteries, the replacement of the conventional turbines can (if at all) only be a far future goal. In conclusion, future fuel cell development might enable fuel cell use in new markets that cannot be powered by a battery, but might also enable a penetration into the somewhat lighter car segment to establish a coexistence with BEVs.

With regards to the development of an early market, the implementation of FCEVs is stalled by the low amount of H_2 fueling stations in most regions of the world, where as little as 91 (Japan), 45 (Germany) or 40 (USA) fueling stations (status 2018) exist in world leading countries.[44] Compared to ≈15000 gasoline fueling stations in Germany (status 2017),[45] The H_2 infrastructure is seemingly very little developed and potential FCEV customers will most likely have this in mind before purchasing a new vehicle. In turn, fuel cell powered busses could be a great option to remove this initial barrier for FCEVs, since they operate on regular routes, where H_2 fueling stations can be easily set up. Similar to this concept, a fuel cell truck network can be pursued for long distance travel, e.g., with the help of subsidies (e.g., free highway fare). This would especially improve city-to-city fueling infrastructure, since trucks can refuel close to the highway. However, transportation of goods is commonly a long range process, demanding full H_2 coverage over a large area (e.g., along the main highways throughout Europe). Even

though full infrastructure for FCEVs is much more affordable compared to the enormous investments necessary for BEVs, small amounts of BEVs can be easily integrated into the current electricity system, especially for customers with access to private parking and plannable, short daily commutes (mainly countryside). The simple market entry of BEVs is another clear advantage over FCEVs that suffer from the chicken and egg problem where car manufacturers are not willing to produce cars that cannot be refueled while the infrastructure is not set up as long as it is not needed.

Assuming that the H_2 infrastructure can be developed, the preceding analysis shows that FCEVs and BEVs are likely to share the automotive market depending on the desired driving range, the refueling time constraints, the car price and the fuel economy considerations. Finally, the system choice might be influenced significantly if todays' mobility concept changes, as it is, e.g., possible for autonomously operating vehicles. In this case, non-customer owned cars could achieve a large fraction of the inner city and near city transport, where the drive cycle is plannable and cars could autonomously charge themselves. This might actually be the big breakthrough of BEVs, whereas it is not yet clear if autonomous driving results in such a drastic change of the mobility concept and early stage autonomous driving with user owned cars does not alter the current situation significantly. At last, the technological potential is only one of the influencing factors, while political decisions could be the actual steering wheel to govern the direction in the mobility sector. One example is the recent boost of fuel cell technology due to the claim of certain countries to support FCEVs (e.g., by 2030, one million FCEVs shall be deployed in China[46] and 800000 in Japan)[47] in order to accomplish a transition towards an environmentally friendly society.

1.2. Fuel Cell Working Principle

The following section shall provide a general overview of the working principle of low temperature PEMFCs, describing the used materials from the MEA to the stack level. The principle of anion exchange membrane fuel cells (AEMFCs), which are also part of this thesis, is similar to that of PEMFCs and the differences are described in section 1.4.

The Membrane Electrode Assembly.—In a fuel cell, the chemical energy stored in H_2 and O_2 (usually from air) is converted to electrical energy, while water and heat are produced according to Equation [3].

$$2H_2 + O_2 \longrightarrow 2H_2O \qquad [3]$$

In contrast to the oxyhydrogen reaction, where the chemical energy is liberated at once in an explosion, the overall reaction in a fuel cell is locally separated into the anodic HOR (Equation [4]) and the cathodic ORR (Equation [5]).

$$2H_2 \longrightarrow 4H^+ + 4e^- \qquad [4]$$

$$O_2 + 4H^+ + 4e^- \longrightarrow 2H_2O \qquad [5]$$

Since the two reactions occur in separate compartments, the electron has to travel through an external path, where the resulting current can be used as electrical power. To maintain charge neutrality, protons migrate from the anode to the cathode where water is formed as the only reaction product. To separate the HOR and the ORR, PEMFCs employ a polymeric membrane (shown in Figure 2) onto which the anode and cathode electrode are laminated to opposing sides, called MEA. Ideally, the membrane is able to conduct protons from one to the other side, while it is impermeable to gases, especially H_2 and O_2, and is completely electrically insulating. The most common type of membrane employed in state-of-the-art PEMFCs consists of perfluorosulfonic acid groups carried by a perfluorinated polymer backbone.[48] The strongly hydrophobic nature of the backbone, together with the hydrophilic sulfonic acid groups causes a phase separation, where water (produced by the reaction and introduced to the MEA with the reactant gases) forms a connected network within the hydrophilic phase. The sulfonic acid

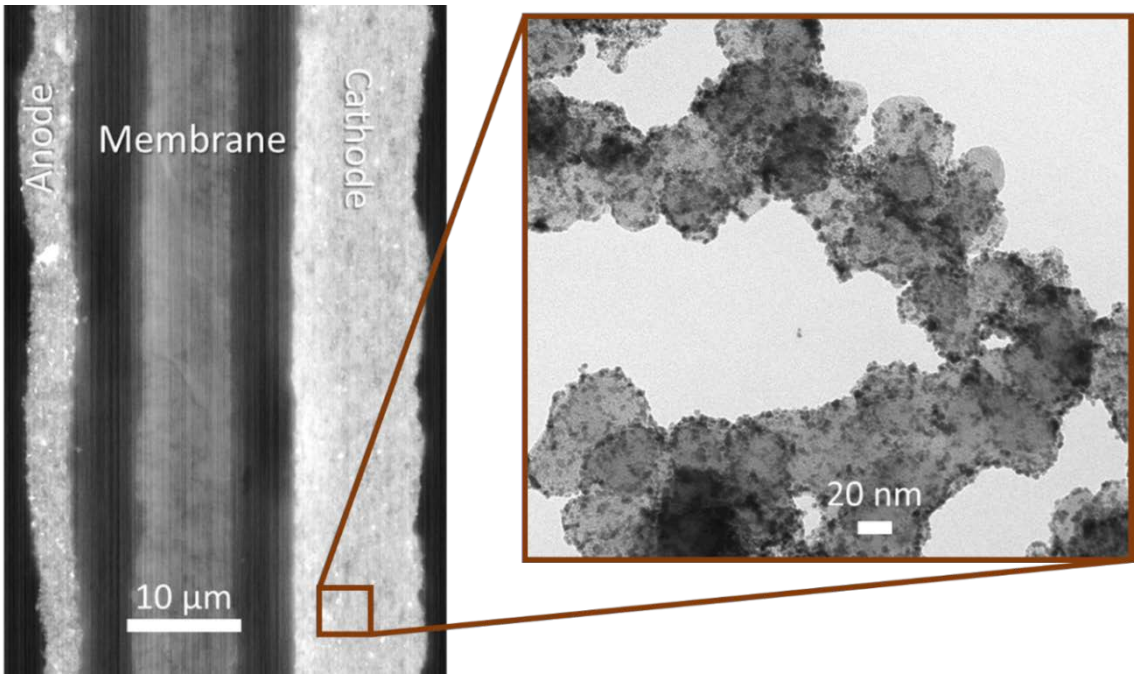

Figure 2. Cross-sectional image of a Gore Primea Mesga (A510.1/M715.18/C580.4, *W. L. Gore & Associates, Inc.*, USA) MEA (left side) taken with a SEM at 25 kV and a magnification of 1500x. The brown box (right side) shows a Pt/C catalyst (TEC10V50E, 50%$_{wt.}$, *Tanaka Kikinzoku Kogyo K.K.*, Japan), imaged by TEM at 100 kV and a magnification of 8900x. The Pt/C catalyst does not represent the actual catalyst in the Gore MEA, but is shown as a representative example.

groups dissociate in the presence of water, creating a highly acidic medium that enables facile proton transport through the well-known Grotthuss mechanism. In contrast to the protons, the anions are immobilized on the perfluorinated backbone and no transport of free anions occurs through the membrane. To achieve low ohmic losses associated with the transport of protons through the membrane, it needs to be as thin as possible, providing a low ionic resistance. Hence, state-of-the-art membranes are approximately 15 µm thick, using polytetrafluoroethylene (PTFE) as a reinforcement to maintain the structural integrity (bright band in the middle of Figure 2). The main influencing factor of the membrane conductivity during fuel cell operation (besides the temperature) is its water content, λ, expressed in $mol_{H_2O}\ mol_{SO_3^-}^{-1}$. In addition to reaction water produced on the cathode, the λ value is controlled by the degree of humidification of the gas supply. One strategy to achieve a high membrane conductivity is therefore to humidify the gas supply on the anode (water equilibrates quickly through the membrane), or on both sides of the MEA. Another class of membranes consists of a hydrocarbon backbone that carries the acidic side group.[49] These membranes are typically less costly due to the lack of the

perfluorination process and provide a lower gas permeability compared to perfluorosulfonic acid (PFSA) based membranes. Nonetheless, they commonly suffer from a lower degree of phase separation due to the less hydrophobic backbone, limiting their applicability for the more practical case of low humidity operation (further information in section 3.1.2).

Since the ORR and the HOR take place on the surface of the catalyst, Pt (or Pt alloys) is commonly prepared in the form of nanoparticles and deposited onto a support material to achieve a high surface area to mass ratio, i.e., a high electrochemical surface area (*ECSA*), shown in the transmission electron microscopy (TEM) image in Figure 2 for a commercially available $50\%_{wt.}$ Pt/C catalyst. For the electrochemical reactions in a fuel cell, electrons, protons and the respective gas (O_2 or H_2) have to be simultaneously present at the catalyst (so-called triple-phase interface). Considering the most common support material (carbon black), electrons are easily transported through the catalyst layer due to the high electrical conductivity of carbon blacks. Furthermore, the high porosity of carbon black enables gas transport through the void volume towards the catalyst. Simultaneously, product water can be removed from the structure through these pores and flooding of the catalyst layer is avoided. Nevertheless, the transport of protons over the carbon structure to the Pt particles is not possible, requiring the use of an additional proton transport medium, the so-called ionomer. The ionomer typically consists of the same material as the membrane and is deposited as a thin layer on the carbon surface. While this thin layer conducts protons through the electrode sheet to the surface of the catalyst particles, it needs to be permeable for O_2 (or H_2), as it also often covers the Pt particles. Even though the ionomer structure is similar to the membrane, where gas transport from one to the other side is limited (> 10 µm), O_2 (or H_2) supply to Pt is possible through the thin ionomer film (< 10 nm) which is believed to cover the Pt nanoparticles. To obtain a well-connected ionomer network throughout the entire electrode which accesses all Pt particles, a sufficient amount of ionomer needs to be incorporated into the electrode, whereby an excess of ionomer can lead to pore clogging and a limited gas transport, hence low fuel cell performance. While the ionomer content in the electrode can easily be varied by choosing the appropriate ionomer to carbon (I/C) ratio during MEA fabrication, the homogeneity of its distribution within the layer is affected by various factors and needs to be optimized for high performance MEAs.[50] As

a substitute for carbon, conductive oxides, such as antimony doped tin oxide (ATO, see section 3.3.1), were proposed in the literature due to their superior stability at elevated potentials (see below for degradation issues).[51] However, these supports suffer from a low conductivity, dopant leaching, and a low stability in reductive atmosphere, hence are not yet commercialized.

Gas Diffusion Layers and Microporous Layers.—The reactant gases need to be distributed over the electrodes to allow the participation of the entire catalyst layer in the electrochemical reaction, hence optimize the utilization of Pt. Especially below the contacting area to the flow field (so-called land, more details below), gas needs to be transported in-plane and direct contacting of the electrode from the outside is not feasible. Therefore, PEMFCs employ a so-called gas diffusion layer (GDL) where no reaction takes place, but gas is distributed homogeneously over the entire area. The most common type of GDL is based on carbon fibers (Figure 3a), offering a high pore volume that enables efficient gas phase transport. Simultaneously, the high electrical conductivity of carbon minimizes ohmic losses associated with the conduction of electrons between the electrodes and the flow fields. The structure of the fibers also guarantees high mechanical stability and allows a certain degree of compressive strain that distributes the mechanical pressure applied from the outside. Hence, the GDL acts similar to a spring, where the pressure on the MEA is balanced, which is especially relevant for

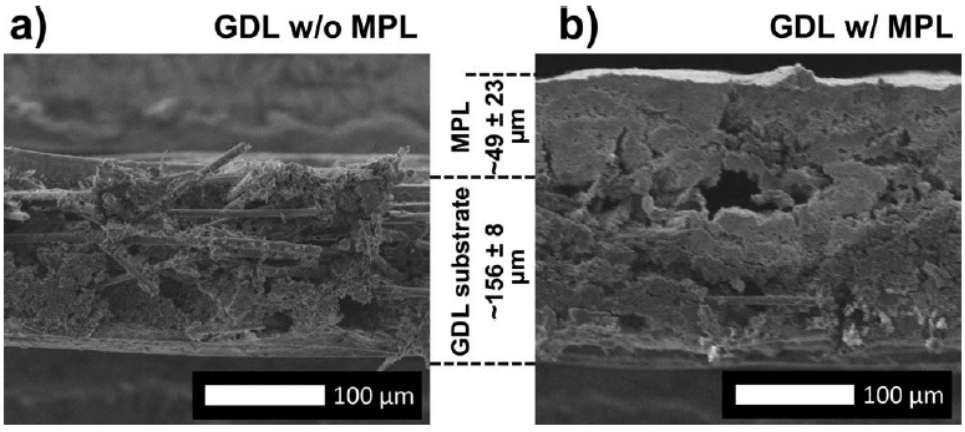

Figure 3. SEM image of a commercially available a) GDL (25 BA, *SGL Carbon SE*) and b) the same GDL with an MPL (25 BC, *SGL Carbon SE*). Images are taken with an acceleration voltage of 5 kV, using a secondary electron detector. Reproduced from Simon et al. under the terms of the Creative Comments Attribution 4.0.[52]

differential gas pressure (between anode and cathode) operation. Nevertheless, if the applied pressure is too high, the GDL can be over-compressed, resulting in a loss of void volume, hence a hindered gas transport. In addition to supplying reactants towards the electrode, water needs to be released from the MEA to avoid catalyst layer flooding, which is again associated with severely limited gas transport. To ensure the efficient removal of water through the GDL, the carbon fibers are hydrophobized by a PTFE treatment during the production process. The polymer is also used as a binder to glue the fibers together and ensure high mechanical stability. Even though water is repelled by the hydrophobic fibers, most layers flood at high humidity operating conditions, where water accumulates in the large pores of the structure. Therefore, a microporous layer (MPL) can be coated onto the GDL to enhance the removal of water at the GDL / electrode interface. Common MPLs consist of carbon black in combination with a PTFE binder for hydrophobization and have a significantly smaller pore size network (on the order of hundreds of nm) compared to the GDL (on the order of tens of µm). The small pores of the MPL prevent the accumulation of water due to a high capillary pressure. Nevertheless, incorporation of a certain degree of larger pores (on the order of tens of µm) aids the removal of water through liquid pathways.[53] Additionally, the high surface area of the MPL can improve the electric contact between the electrode and the GDL. Finally, the GDL allows the transport of reaction heat from the electrode to the outside, whereby the thermal conductivity can vary significantly for different materials.

The Fuel Cell Stack and System.—In order to achieve a sufficient power output for the use of fuel cells in automotive applications, several cells are connected to each other in series, where the current flows through every cell and the voltage adds up along the stack (e.g., 244.8 V through 34 modules with 7.4 V for the Toyota Mirai during operation).[8] The electrical connection between the individual cells is achieved by bipolar plates, where the anode and cathode flow fields of two different cells are located at opposing sides of the plate, exemplarily shown in Figure 4. The coolant is commonly located between anode and cathode, so that every cell is cooled individually, mitigating thermal gradients within the PEMFC stack. To avoid high voltage safety concerns, the coolant has to have a relatively low conductivity, hence the coolant water is usually purified from ionic contaminants. The first and the last plate are called endplates which

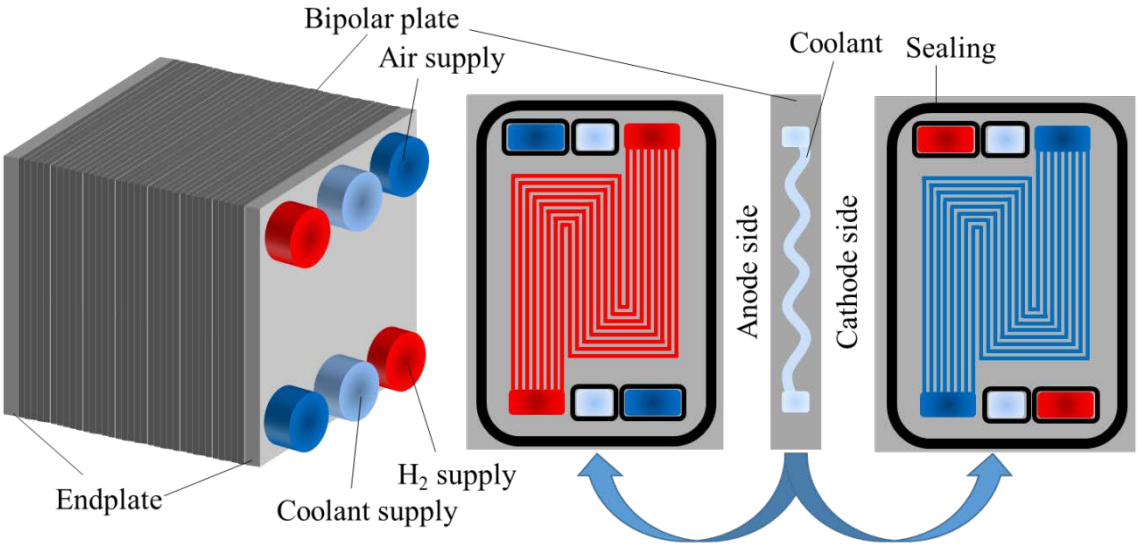

Figure 4. Schematic representation of a fuel cell stack, showing multiple bipolar plates connected in series, including H_2, air and coolant supply and exhaust lines. Each bipolar plate has an anode and a cathode side, including the coolant flow in the middle (shown on the right). The flow field including gas in- and outlets are shown for each side, while all additional components (e.g., MEA, cell voltage monitor, load cables, etc) are not included here. Since many different designs for the stack exist, this drawing represents only an example.

have only one flow field facing the stack and are used to mechanically hold the stack assembly together. H_2 and air are transported through a supply line to the individual cell inlets, where the gas is distributed over the GDL area, leaving the cell at the respective outlet. The gas entering the flow fields is commonly divided into several channels (shown in red for the anode and in blue for the cathode in Figure 4, right side), separated by the so-called land area. The land compresses the GDL and ensures electrical connection between the bipolar plate and the GDL / MEA. The channel geometry and the applied operating conditions (gas flow rate, humidity) result in a pressure drop between flow field in- and outlet that forces the gas through the channel. While a low pressure drop is desirable during low humidity operation to enhance the performance, a high pressure drop is advantageous at high humidity (e.g., at high current density) to remove liquid water droplets when oversaturation occurs. In general, the gas flow rate, $\dot{n}$, is adjusted to the applied current density, defined as gas stoichiometry, s, and calculated according to Equation [6].

$$s = \frac{\dot{n}_{\text{feed}}}{\dot{n}_{\text{consumed}}} > 1 \qquad [6]$$

To maximize the utilization, the stoichiometry for H_2 is typically close to 1 (e.g., 1.02) and to minimize the power consumption of the air compressor, the cathode stoichiometry is usually below 2 (e.g., 1.5).

For automotive applications, the flow field design needs to enable gas transport at both, low (little gas flow, low pressure drop) and high current density (high gas flow, high pressure drop). Furthermore, operation within a broad range of gas humidity values needs to be possible, where the membrane remains well-humidified and product water is easily removed from the flow field channels. The blocking of channels, or of an entire flow field can result in severe degradation of the fuel cell system (H_2 starvation, see below), or at least cause a loss of performance. Straight or serpentine type flow fields are among the most common designs, but also porous foams or meshes are used in certain applications (an introduction to the basics of droplet formation can be found in the Handbook of Fuel Cells).[54] Bipolar plates for automotive PEMFC stacks are commonly made of titania or stainless steel, whereby steel is less costly but more prone to degradation in the acidic environment of the fuel cell (release of HF due to membrane decomposition, see below).[55] The corrosion resistance can be enhanced by a coating layer on top of the plate. Carbon-based bipolar plate materials are another alternative that do commonly not require a coating, but are usually thicker compared to their metal equivalents. To retain the gas within the cell compartment and avoid the intrusion of air from the outside, every bipolar plate employs a certain type of sealing technology to the outside. Additionally, sealing of the cell compartment to foreign supply channels (e.g., sealing the anode to air and coolant) is very important to avoid gas mixing and ensure safe operation.

The PEMFC stack is embedded into a fuel cell system, illustrated by a simplified overview in Figure 5. The O_2 for the cathode is supplied by a compressor (ideally coupled with an expander) that takes air from the surrounding environment and compresses it to the desired operating pressure. While a higher gas pressure commonly results in enhanced fuel cell performance, it also requires a more expensive compressor module, more energy consumption for the air supply and a better sealing technology. Hence, fuel cell systems are often operated at gas pressures around 200 kPa_{abs}, whereas also ambient

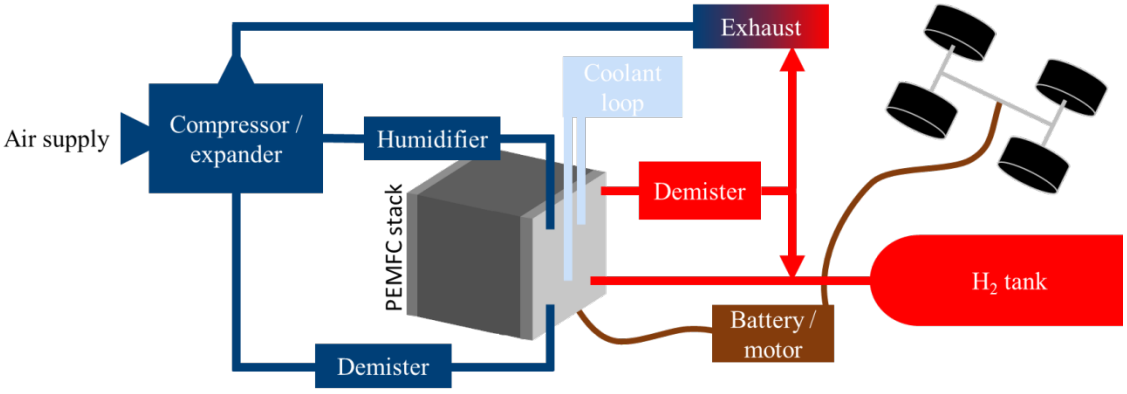

Figure 5. Schematic setup of an automotive fuel cell system. For simplicity, many elements, such as pumps, valves, a low temperature coolant loop, and other devices are not shown. Depending on the manufacturer, significantly different designs are possible and this scheme represents only a rough overview.

or high pressure systems (e.g., 300 kPa_{abs}) can be employed. To ensure a high membrane water content, the air supply is often humidified prior to entering the stack, whereby the water required for humidification is recovered from the exhaust gas before entering the expander. Since the water handling system increases the cost of the PEMFC, certain automotive systems employ other methods of water management to eliminate the humidifier (e.g., the Toyota Mirai).[56] In contrast to the air which is supplied from the environment, H_2 originates from an onboard pressure tank (often 700 bar) and is humidified by H_2 recovered from the fuel cell outlet. Since common membranes allow a limited crossover of N_2 and O_2 from the air side into the anode compartment, N_2 accumulates in the H_2 feed over time (permeating O_2 is consumed by reaction with H_2). This can significantly decrease the fuel cell performance (see section 3.2.1) and when the N_2 content in the anode reaches a certain threshold, the H_2/N_2 mixture is combined with air and exhausted from the system (usually catalytically combusted). In addition to the gas handling, fuel cell systems consist of a coolant loop to avoid strong heating of the stack under operation. In addition to this “high temperature” loop, another “low temperature” coolant loop may be implemented for all other devices. Finally, the power of the fuel cell is supplied either to the battery of the vehicle or directly to the electric motor that drives the propulsion system of the FCEV.

1.3. PEMFC Performance and Durability

The following section provides an overview on the losses occurring in PEMFC systems at the example of a H_2/air polarization curve measured on a 5 cm^2 single cell at differential-flow conditions. The performance of automotive MEAs under practical conditions is different, but the same general concepts apply. A complete description on how to measure the individual loss terms is given in the experimental section. In addition to the voltage loss analysis, this section covers an overview on the degradation phenomena in PEMFCs.

H_2/air performance.—The thermodynamic equilibrium potential of the fuel cell reaction (Equation [3]) can be calculated according to the Nernst equation for the two individual reactions (Equation [4] and [5]). Here, E_{rev} is the cell potential at the operating conditions, E_0 is the equilibrium potential of the individual reactions at standard conditions (1.23 V_{SHE} for the ORR/OER and 0 V_{SHE} for the HOR/HER), R is the ideal gas constant (8.3 V A s K^{-1} mol^{-1}), T is the temperature, n is the number of transferred electrons (4 for the reaction shown in Equation [3]), F is the Faraday constant (96485.3 A s mol^{-1}), and p is the partial pressure of the gas divided by the reference gas pressure at standard conditions (101.3 kPa).

$$E_{\mathrm{rev}} = E_0^{\mathrm{OER/ORR}} - E_0^{\mathrm{HOR/HER}} + \frac{R \cdot T}{n \cdot F} \cdot \ln\left(p_{\mathrm{O_2}} \cdot p_{\mathrm{H_2}}^2\right) \quad [7]$$

When a current is drawn from the fuel cell, the thermodynamic potential is lowered by so-called overpotentials. Overpotentials caused by the electrochemical kinetics are generally described by the Butler-Volmer equation. In this, i is the current density, i_0 is the exchange current density, rf is the roughness factor (active surface area of the catalyst, e.g., Pt, with respect to the electrode area, typically given in cm_{Pt}^2 cm^{-2}), α_a and α_c are the anodic and cathodic transfer coefficients, and η is the overpotential.

$$i = i_0 \cdot rf \cdot \left(e^{\frac{\alpha_a \cdot F}{R \cdot T} \cdot \eta} - e^{-\frac{\alpha_c \cdot F}{R \cdot T} \cdot \eta}\right) \quad [8]$$

The Butler-Volmer equation considers the reaction in the cathodic (e.g., ORR), as well as the backwards reaction in the anodic direction (e.g., OER), weighing their contribution to the overall current by the applied overpotential in combination with the transfer

coefficient. Fast reaction kinetics, i.e., a high exchange current density, result in small kinetic overpotentials, and the same can be achieved by a high roughness factor, i.e., more catalytically active surface area. If the overpotential for the reaction is large, i.e., far away from the equilibrium potential, where one reaction direction dominates, the backwards reaction can be neglected and the Butler-Volmer equation can be simplified to the so-called Tafel equation, where *TS* is the Tafel slope (where $TS = 2.303 \cdot \frac{R \cdot T}{\alpha_{a/c} \cdot F}$).

$$\eta = \frac{R \cdot T}{\alpha_{a/c} \cdot F} \cdot \ln\left(\frac{i}{i_0 \cdot rf}\right) = TS \cdot \lg\left(\frac{i}{i_0 \cdot rf}\right) \quad [9]$$

For very small overpotentials, the mathematic approximation, $e^x \approx 1 + x$ is used to yield the micro-polarization approximation.

$$i = i_0 \cdot rf \cdot \frac{(\alpha_a + \alpha_c) \cdot F}{R \cdot T} \cdot \eta \quad [10]$$

For both reactions of interest in a PEMFC, Pt is the best monometallic catalyst known to date, where the HOR proceeds very fast with an exchange current density on the order of 240 mA cm_{Pt}^{-2} (determined by H_2 pump measurements at 80°C, 100 kPa H_2, 100% relative humidity (*RH*) at 2 mV s^{-1}),[57] whereas the ORR is sluggish and the activity is commonly reported at a potential of 0.9 V_{RHE} (200 µA cm_{Pt}^{-2}, measured at a differential-flow of H_2/O_2 at 80°C, 120 kPa O_2, 100% *RH*).[58] The Tafel equation can usually be used to describe the sluggish ORR kinetics, while the micro-polarization approach often suffices to correctly represent the fast HOR kinetics. On the one hand, the high HOR/HER exchange current density enables very low Pt loadings on the anode of PEMFCs (≤ 50 μg_{Pt} cm^{-2}) and a quasi-negligible overpotential under most operating conditions. On the other hand, the low ORR kinetics contribute significantly to the overall overpotential (shown in red in Figure 6) and advanced catalysts (e.g., bimetallic alloys, see section 3.2.3) are used to achieve loadings on the order of 0.1 – 0.2 mg_{Pt} cm^{-2} for state-of-the-art cathodes.[59] Clearly, reducing the cathode loading of a catalyst induces higher kinetic losses according to the Tafel equation, as shown in Figure 6a for a Pt loading of 0.1 mg_{Pt} cm^{-2} compared to 0.4 mg_{Pt} cm^{-2} in Figure 6b. In addition to the kinetic ORR overpotential, the conduction of protons through the membrane ($R_{membrane}$) and of electrons through the catalyst layer/MPL/GDL to the flow fields (so-called

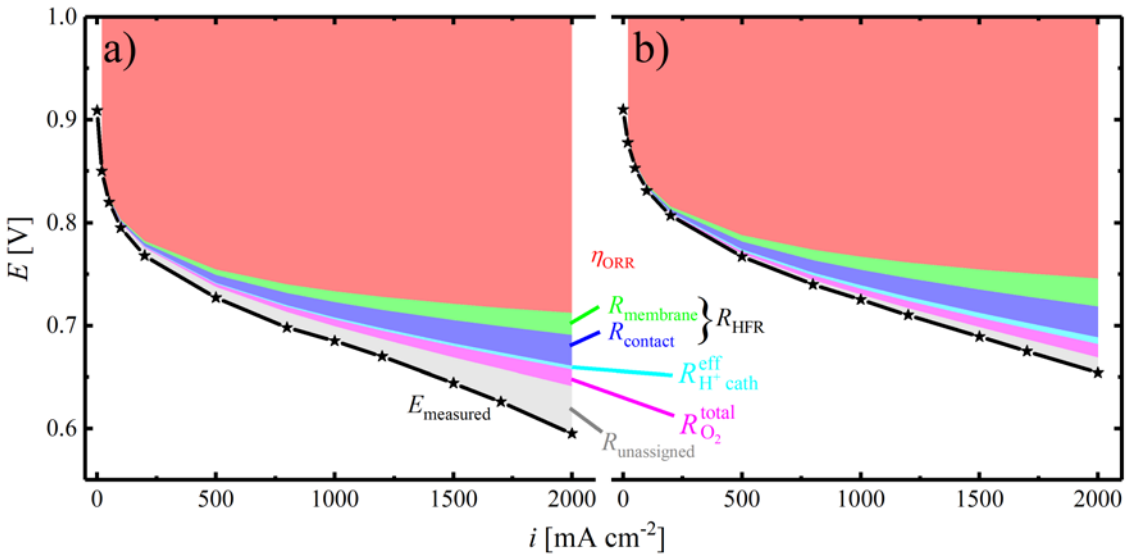

Figure 6. Voltage loss analysis for differential-flow polarization curves (black lines) using 2000 nccm / 5000 nccm of H_2/air on anode / cathode at 170 kPa_{abs}, 100% *RH* and 80°C for a cathode loading of the Pt/C catalyst of a) 0.1 mg_{Pt} cm^{-2} (TEC10V20E, *Tanaka Kikinzoku Kogyo K.K.*, Japan) and b) 0.4 mg_{Pt} cm^{-2} (TEC10V50E, *Tanaka Kikinzoku Kogyo K.K.*, Japan). The anode loading is 0.1 mg_{Pt} cm^{-2} in both cases and the ionomer to carbon (I/C) ratio is 0.65 g_I g_C^{-1} on anode and cathode, using a PFSA-based ionomer and membrane (15 µm). The GDL and MPL (H14C7, *Freudenberg KG*, Germany) are the same on both sides, assembled at a compression of 20%. The MEA size is 5 cm^2 and the flow fields have 7 channels with 0.5 mm lands and channels in serpentine arrangement (c.f., Figure 22a).

contact resistance, $R_{contact}$) induces ohmic losses, typically summarized in the high frequency resistance, R_{HFR}. The contact resistance is a function of the pressure applied on the flow fields to compress the GDL, and the membrane resistance depends on its thickness and the water content. For state-of-the-art membranes with a thickness on the order of 15 µm under well-humidified conditions, the two resistances have a similarly small contribution to the overall losses. However, the impact of these ohmic losses increases at high current density and can be very significant if the water content of the membrane is low (e.g., due to an insufficient heat conduction through the GDL) or if the bipolar plate coating is corroded. Furthermore, the transport of protons through the cathode catalyst layer results in an additional loss term, $R^{eff}_{H^+\,cath}$ (turquoise area in Figure 6), which contributes insignificantly to the overall losses for optimized catalyst layers at high *RH*. Similar to the membrane resistance, the proton sheet resistance increases significantly as the humidity decreases. The proton sheet resistance on the anode is a minor voltage loss due to the fast HOR kinetics on Pt in acidic media, enabling a reaction in the close vicinity of the membrane, hence a short proton transport pathway. Another contributor to the overall voltage losses in a fuel cell system is the so-called O_2 mass-transport re-

sistance, $R_{O_2}^{total}$ (pink area in Figure 6) that results from a decrease of the O_2 concentration (21% in air) within the electrode due to its consumption in the electrochemical reaction. The O_2 mass-transport is strongly dependent on the employed GDL / MPL system and can severely limit the fuel cell performance if liquid water accumulates in the pores of the GDL, at the MPL / electrode interface or within the electrode.[53]

Since the reduction of the total amount of Pt is crucial for the commercialization of fuel cell systems (see section 1.1), novel catalysts with a higher ORR activity are often investigated (e.g., core-shell structures, shape-controlled particles) to reduce the noble metal loading while maintaining a small kinetic ORR overpotential. However, these catalysts often provide a low *ECSA* compared to commercial Pt/C and several studies have shown that decreasing the cathode *rf* induces a high O_2 mass-transport resistance. While the origin of this phenomenon is not yet completely understood, the resistance is frequently referred to as local O_2 mass-transport resistance.[60–62] Furthermore, the O_2 mass-transport resistance is connected to the location of the Pt nanoparticles on the carbon. Using catalysts where Pt is located within the pores of the carbon seems to hinder the transport of O_2 to the particle, whereas depositing it on the outside makes it more accessible and reduces the O_2 mass-transport overpotential.[63] Nevertheless, Pt particles deposited on the outer surface of the carbon are in close contact with the ionomer, which is known to poison the ORR activity of Pt due to the adsorption of sulfate and the sulfonic acid groups, causing a higher kinetic ORR overpotential.[64,65] Therefore, a novel carbon structure where Pt is located within mesopores was recently proposed. These pores provide reasonable O_2 accessibility while simultaneously protecting the Pt particle from ionomer adsorption.[66]

Finally, the in-situ diagnostic toolset for the characterization of fuel cells cannot completely account for all phenomena occurring in the H_2/air polarization curve, leaving the unassigned voltage losses, $R_{unassigned}$. For cathodes with a high Pt loading, these losses are comparably small (Figure 6b), while lower loadings (Figure 6a), or more precisely low cathode *rf* values, result in large unassigned losses (see section 3.2.2 for more details).

Electrode Degradation.—In addition to the high cost of fuel cell stacks discussed earlier, their long-term durability is a major challenge to be addressed in the future.[67] Amongst others, significant degradation occurs in the electrodes, in the membrane and at the bipolar plates. This section describes the degradation on anode and cathode.

When the fuel cell supplies power (e.g., during acceleration of the FCEV), its voltage decreases due to increasing overpotentials with increasing applied current density, as shown in Figure 6. While the potential on the anode remains (η_{HOR} < 20 mV) reasonably close to the Nernstian equilibrium potential of the HOR/HER (0 V_{RHE}) at practical current densities up to 3 A cm^{-2} (fast HOR kinetics in pure H_2),[68] significant overpotentials are observed on the cathode, especially at lower Pt loadings (slow ORR kinetics in air).[69] Hence, the potential of the cathode shifts between the open circuit voltage (OCV) of ≈0.95 V_{RHE} and ≈0.65 V_{RHE} during load cycling in automotive applications.[70] Cell voltages below ≈0.65 V are commonly not allowed due to excessive heat production and the practical limits (radiator size) to remove it. Taking a look at the electrochemical processes on Pt in the applied potential range of a fuel cell (grey shaded area in Figure 7) reveals a reduction of the oxidized Pt surface at decreasing potential and an oxidation of metallic Pt at higher potentials. A common phenomenon during the process of repetitive oxidation and reduction is the dissolution of Pt from the surface of the nanoparticle into the electrolyte phase (i.e., the humidified ionomer and membrane), driven by the solubility of Pt ions in acidic media.[71] Since the Pt ions are mobile in the electrolyte phase, they can diffuse or migrate away from the nanoparticle to redeposit when a suitable potential is reached. This redeposition can, e.g., occur on another Pt nanoparticle, causing a growth of this particle. Since large nanoparticles are more stable compared to smaller ones, this process overall favors an increase of the average diameter of Pt in the electrode, as well as a loss of *ECSA*.[72,73] Furthermore, Pt ions are able to diffuse towards the membrane, where they can be reduced by H_2, crossed over from the anode compartment.[74] When these particles precipitate at a location that is not electrically connected to the electrode (the membrane is an electrical insulator), they cannot participate in the desired electrochemical process on the cathode. Hence the effective cathode *rf* available for ORR decreases and the overall fuel cell performance is lowered. In addition to these degradation processes on the Pt particles, carbon itself is

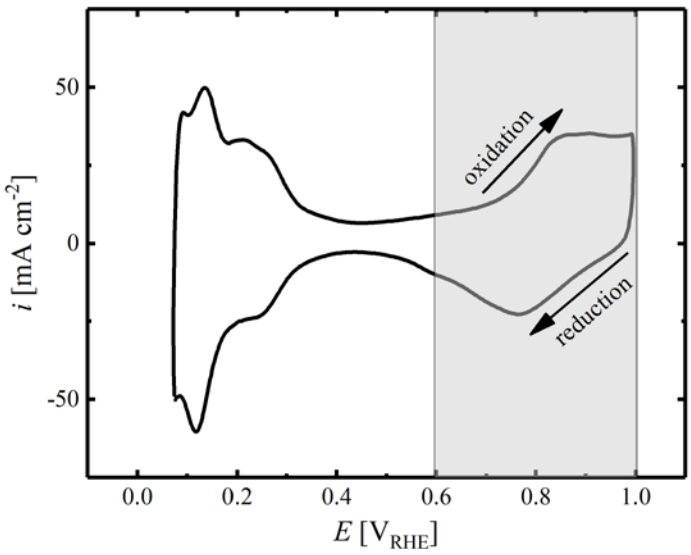

Figure 7. CV of a 5 cm^2 Pt/C (TEC10V50E, 50%$_{wt}$) electrode at a loading of 0.4 mg_{Pt} cm^{-2}, recorded at 40°C, ambient pressure, supplying 5% H_2 in N_2 (100% *RH*) / N_2 (dry) to anode / cathode at a flow of 200 / 50 nccm, interrupting the cathode gas flow during the CV. The scan rate is 150 mV s^{-1}, measured between 0.07 and 1.00 V_{RHE}. The data is taken from the study of Harzer et al.[58]

thermodynamically not stable at potentials > 0.2 V_{SHE}.[75] Fortunately, the kinetics of the carbon oxidation reaction (COR) are very sluggish and the exposure of carbon to potentials < 0.9 V_{RHE} does not noticeably corrode the support material.[76–78] However, under certain circumstances such as anode H_2 starvation or start-up / shut-down (SUSD) of the fuel cell, the electrode potential can rise to high anodic potentials (>1.2 V_{RHE}). After an idle time of the fuel cell stack (e.g., parking the car for several days / weeks), the H_2 in the anode compartment is consumed and the entire cell is filled with air due to the imperfect sealing of the stack. In such a case, H_2 needs to be sent through the anode to start regular operation, causing the coexistence of H_2 and air in the same electrode compartment for a limited amount of time. Conceptually, the two sections of the cell can be separated into a fuel cell compartment (Figure 8, below the dash dotted line) and an electrolytic cell (Figure 8, above the dash dotted line) due to the insufficient in-plane H^+ conductivity within the same electrode. In other words, the resistance for a proton to travel from the H_2-filled anode compartment (lower red section in Figure 8) to the air-filled anode compartment (upper blue section) is high, while the short distance between anode and cathode through the membrane (horizontally in Figure 8) can be easily accomplished. In accordance with this, the HOR proceeds in the H_2-filled compartment of

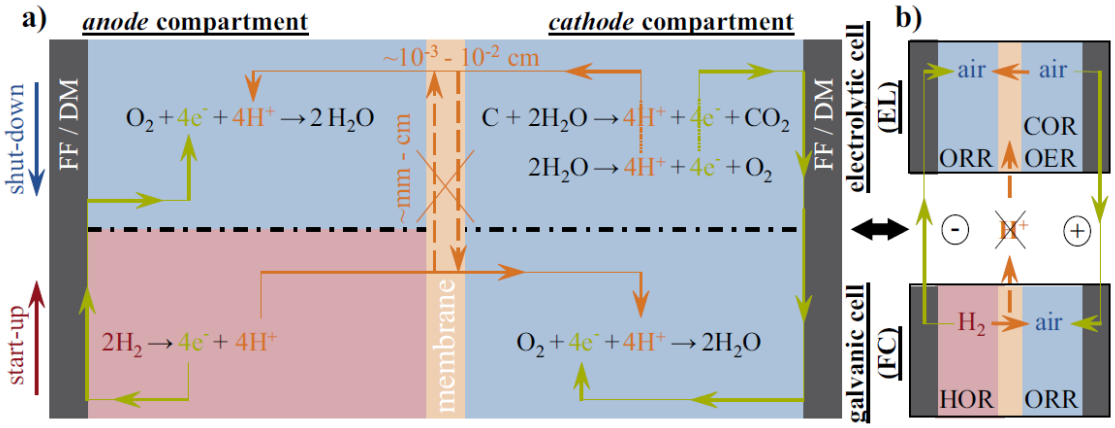

Figure 8. Schematic of a SUSD event in a PEMFC, sketching the passage of a H_2/air_{anode} front through the anode flow field (H_2-filled regions in red, air-filled regions in blue) while the cathode flow field is filled with air. a) Illustration of the reactions occurring during the SUSD event, with sketched pathways of electrons (in green) through the electrode, diffusion medium (DM) and flow field (FF) as well as of protons (in orange) across the membrane; b) Conceptual separation into a fuel cell (FC) segment and an electrolytic cell (EL) segment (H_2-filled and air-filled flow field segments are indicated in red and in blue, respectively). In-plane proton conduction is only possible within very short distances from the H_2/air_{anode} front (≈120 µm for a 20 µm thick membrane) and not over extended distances, which is indicated by the crossed-out arrows. The figure is reprinted from Mittermeier et al. under the terms of the Creative Comments Attribution 4.0.[79]

the anode and the ORR takes place in the cathode compartment opposite of it, with the proton traveling through the membrane. However, no external load is applied, but electric contact within each of the electrodes is given (high conductivity of carbon in the electrode and of the flow fields / bipolar plates). Therefore, the fuel cell reactions supply the power to the electrolytic cell (conceptually shown in Figure 8b), where ORR takes place in the air-filled anode compartment, countered by an oxidative current in the cathode compartment (so-called reverse-current mechanism). Depending on the reaction kinetics (type of catalyst and reaction conditions) and the stability of the carbon type (carbon black or graphitized carbon) employed as support, the current results from the oxygen evolution reaction (OER) and from the carbon oxidation reaction (COR). Since the OER kinetics on Pt are slow (Ir and Ru are the most active monometallic OER catalysts),[80–82] COR is often the main reaction during SUSD (the shut-down process is conceptually similar to the start-up). As mentioned earlier, carbon is the structure-giving element in the electrode and provides a large void volume for gas transport and water removal in the electrode layer (see section 1.2). However, little carbon mass loss (on the order of ≈5 – 7%$_{wt.}$) is needed until the structure collapses, associated with severe performance losses due to insufficient O_2 supply on the cathode.[83] Additionally, SUSD

leads to a significant loss of *ECSA* on the cathode due to the physical detachment of Pt nanoparticles from the support and due to the highly oxidative potential that leads to a dissolution of Pt. Compared to the ageing mechanisms during load cycling, Ostwald ripening is not the main *ECSA*-loss contributor in the SUSD process, since the potential of the cathode remains high throughout the entire time. On the other hand, the mechanism of Pt deposition in the membrane due to H_2 crossover is dominant and a clear Pt deposition band is the result of accelerated stress tests (ASTs) for SUSD. Due to the harsh degradation of the cathode during SUSD events, the anode side is commonly not in the focus of studies presented in the literature. However, Engl et al. reported recently that the change of potential on the anode (0 V_{RHE} in H_2 and ≈1 V_{RHE} in air), induced by the repetitive switching of the gas atmosphere, results in significant anode degradation.[84] In this sense, the degradation is similar to that during voltage cycling, where the surface of Pt is repetitively oxidized and reduced, leading to Ostwald ripening and a loss of *ECSA*. This becomes increasingly relevant as different mitigation strategies (e.g., lower temperature,[79,85] short residence time,[86] and low *RH*)[87,88] are employed to protect the cathode, enabling a larger amount of SUSD events to occur before the performance loss is too high. More information on anode degradation during SUSD events can be found in section 3.2.1. Finally, it has to be mentioned that PEMFC stack start-ups are likely to occur in automotive applications after the car had not been used for a certain amount of time, while the conceptual shut-down can most likely be avoided. The total number of start-up events can be limited by maintaining H_2 in the anode compartment for as long as possible (e.g., leaking a small amount of H_2 from an additional, low pressure tank into the stack). This strategy also ensures that start-up events do not occur at elevated temperature (e.g., restarting the car directly after operation), where cathode degradation is significantly accelerated due to faster COR kinetics.[79]

Even though H_2 starvation is not studied in the frame of this thesis, the concept is briefly explained for completeness. Similar to SUSD, local H_2 starvation can result in a reverse-current event, since O_2 and N_2 permeate through the membrane from the cathode to the anode. In anode regions where H_2 is present, O_2 is immediately consumed in a catalytic reaction. However, in starved regions (e.g., due to channel blockage by a water droplet) the crossover O_2 undergoes ORR on Pt, resulting in the same conceptual sepa-

ration of the cell into a fuel cell compartment and an electrolytic cell as for SUSD, hence in COR on the cathode opposing the starved anode side. In contrast to start-up events which usually take place at ambient temperature, local H_2 starvation occurs during operation, i.e., at high operating temperatures. Therefore, local H_2 starvation results in severe cathode degradation, highlighting the importance of an elaborate flow field structure to avoid water accumulation.

Severe degradation of PEMFC stacks is also the result of a H_2 supply interrupt for an entire cell during operation. Gross H_2 starvation causes the performance of the starved cell to decrease until no power can be drawn from the cell. However, in a PEMFC stack, the cells are connected in series, hence each of them needs to sustain the same current. All cells supplied with H_2 act as a power supply, while the starved cell uses the power to sustain the applied current, i.e., it acts as an electrolytic cell. In this case, the anode potential increases until a suitable oxidation reaction takes place. While generally, OER and COR are possible reactions, the slow kinetics of the OER on most anode catalysts result in severe COR. As this phenomenon occurs on a cell level during operation, it leads to rapid PEMFC failure and needs to be avoided at any cost.[89,90]

Membrane and Ionomer Stability.—Even though membrane and ionomer degradation are not tested in the experiments comprising this thesis, a short overview is given here. Further details on membrane ageing can be found in suitable text books.[55]

In general, membrane degradation is caused by mechanical stress or by chemical decomposition, whereas the operating temperature of PEMFC systems (< 110°C) on its own has no negative influence on membrane lifetime. Mechanical failure can already occur during the MEA preparation process, e.g., when dust particles settle on the membrane and pinch through it when compressive force is applied in the fabrication process (e.g., during hot pressing). Furthermore, the carbon fibers in the GDL can form pinholes in the membrane when the MEA and the GDLs are compressed in the cell assembly. This phenomenon can be partially avoided if the ridge of the GDL that originates from cutting it to the appropriate size, points towards the flow fields. Membrane failure can also be observed during operation when differential pressure spikes occur between anode and cathode. On a laboratory scale, this is often observed in the course of an emer-

gency shut-down of the test station where N_2 is purged through the cell at a high flow rate to remove the reactive gases. Due to the sudden pressure change, the membrane cracks in the inlet area of the flow fields and the subsequent mixing of H_2 and air/O_2, when testing proceeds, can induce uncontrolled heating, hence severe membrane decomposition. Furthermore, changing the water saturation level of the membrane between the dry and the wet state induces mechanical stress due to swelling and contracting of the polymer. Cycling of the *RH* is therefore often used as AST to probe the mechanical stability of novel membranes.[91] As previously mentioned, the mechanical stability of state-of-the-art membranes is commonly enhanced by a PTFE reinforcement that enables the use of thin membranes (< 20 µm).

Chemical degradation of the membrane and the ionomer in PEMFCs is mainly related to the in-situ formation of hydroxyl radicals due to the concurrent presence of O_2, H_2 and Pt (note, that the membrane allows for a certain amount of gas crossover between anode and cathode). In this case, H_2 is adsorbed on the Pt catalyst in the anode compartment (Equation [11]) to react with O_2 to form hydroperoxide radicals (Equation [12]). When combined with another adsorbed hydrogen, hydrogen peroxide is formed (Equation [13]), which can diffuse through the MEA.

$$H_2 \longrightarrow 2H\cdot \qquad [11]$$

$$H\cdot + O_2 \longrightarrow HO_2\cdot \qquad [12]$$

$$HO_2\cdot + H\cdot \longrightarrow H_2O_2 \qquad [13]$$

Hydroxyl radicals (·OH) form in the decomposition process of hydrogen peroxide, which is strongly accelerated by the presence of transition metal cations, such as Fe^{2+}. The hydroxyl radicals can attack hydrogen atoms generally present at the endgroups of the perfluorinated backbone (endgroup unzipping mechanism, Equation [14]) or at the sulfonic acid group (side chain unzipping mechanism, Equation [15]).

$$\text{-}(CF_2)_n\text{-}CF_2H + OH\cdot \longrightarrow \text{-}(CF_2)_n\text{-}CF_2\cdot + H_2O \qquad [14]$$

$$\text{-}(CF_2)_n\text{-}CF_2\text{-}CF_2SO_3H + OH\cdot \longrightarrow \text{-}(CF_2)_n\text{-}CF_2\text{-}CF_2\cdot + H_2O + SO_3 \qquad [15]$$

The remaining ionomer chain can then decompose by releasing HF, making the fluoride ion release rate a suitable indicator for membrane stability in chemical ASTs. The end-group unzipping mechanism can be inhibited by post-fluorination of the ionomer. In contrast, the sidechain unzipping mechanism cannot be generally prevented due to the necessity of the sulfonic acid group. Fortunately, this mechanism only occurs when the sulfonic acid group is protonated, i.e., at low *RH*, and can therefore be mitigated by the correct choice of PEMFC stack operating conditions. Additionally, radical scavengers, such as $Ce^{3+/4+}$, are used to significantly improve membrane stability. Ce^{3+} ions can be oxidized in the reaction with hydroxyl radicals to subsequently get reduced by H_2 in the anode electrode and regenerate the scavenger ion.[92]

Bipolar Plate Corrosion.—As mentioned previously, the introduction of Fe^{2+} ions to the MEA significantly accelerates membrane and ionomer degradation and therefore has to be avoided. Nevertheless, bipolar plates are often made of stainless steel due to the cost advantage over titanium or graphite. However, in the vicinity of the acidic medium of the PEMFC (e.g., due to the release of HF in the course of membrane degradation), pure stainless steel does not provide a sufficient stability and is therefore not suitable for fuel cell applications. Furthermore, the corrosion of the bipolar plate increases the contact resistance to the GDL, hence reduces fuel cell performance. As a solution, applying one or multiple protective coatings onto the bipolar plate prevents corrosion and reduces the contact resistance.

1.4. AEMFCs – a Far-Future Alternative

PEMFCs are the most common type of hydrogen fuel cells and are anticipated for the widespread use in automotive applications in the near future. However, the acidic medium in the PEM requires the use of noble metal electrocatalysts on both sides of the fuel cell, since many other metals are not sufficiently stable at pH ≈ 0 in the applied potential range (approximately between 0 and 1 V_{RHE}).[93] On the one hand, the employment of Pt in PEMFCs is only a minor issue on the anode, since the HOR/HER kinetics are so fast that small Pt quantities suffice on the anode (≤ 50 μg_{Pt} cm^{-2}).[57,94] On the other hand, as shown before, the sluggish ORR kinetics require a much larger amount of Pt on the cathode side (≥ 100 μg_{Pt} cm^{-2}).[69,95,96] A significantly larger fraction of the metals in the periodic table of elements is stable at high pH, enabling a much wider choice of materials for alkaline fuel cells.[93] During the last century, alkaline fuel cells (using liquid KOH as an electrolyte) have already proven to be the power source of choice for the Apollo space missions.[97] Furthermore, several researchers have shown that abundant, low cost materials (e.g., based on Ag[98,99] or completely noble metal free catalysts)[100] have the capability to efficiently catalyze the ORR in alkaline media. However, when transitioning from the acidic to the alkaline media, the most active monometallic anode catalyst, Pt, suffers from a reduction of the HOR/HER exchange current density by two orders of magnitude.[57,101,102] The origin of this significant activity difference between acid and alkaline media remains unknown, but several hypothesis have been postulated in the literature: i) a change of the reaction mechanism that requires hydroxide species to react with Pt-H_{ads} in alkaline media,[103] ii) an additional reaction barrier due to the reorganization of interfacial water (calculated for the HER),[104] iii) and a shift of the Pt-H_{ads} binding energy (BE) induced by the alkaline media.[105] As a consequence, AEMFCs require highly Pt loaded anodes (≥ 0.3 mg_{Pt} cm^{-2}).[106] Nevertheless, even in this case, the HOR overpotential constitutes a significant voltage loss contribution in an AEMFC, as shown (purple area) in Figure 9b for a loading of ≈0.4 mg_{Pt} cm^{-2}. Since no sufficiently active substitute for Pt as HOR catalyst exists at the moment, the issue of too high noble metal requirements discussed earlier for PEMFCs is shifted from the cathode to the anode in AEMFCs. At the same time, the ORR overpotential (red area in Figure 9b) on the cathode is still responsible for a large voltage drop in AEMFCs, since Pt provides a

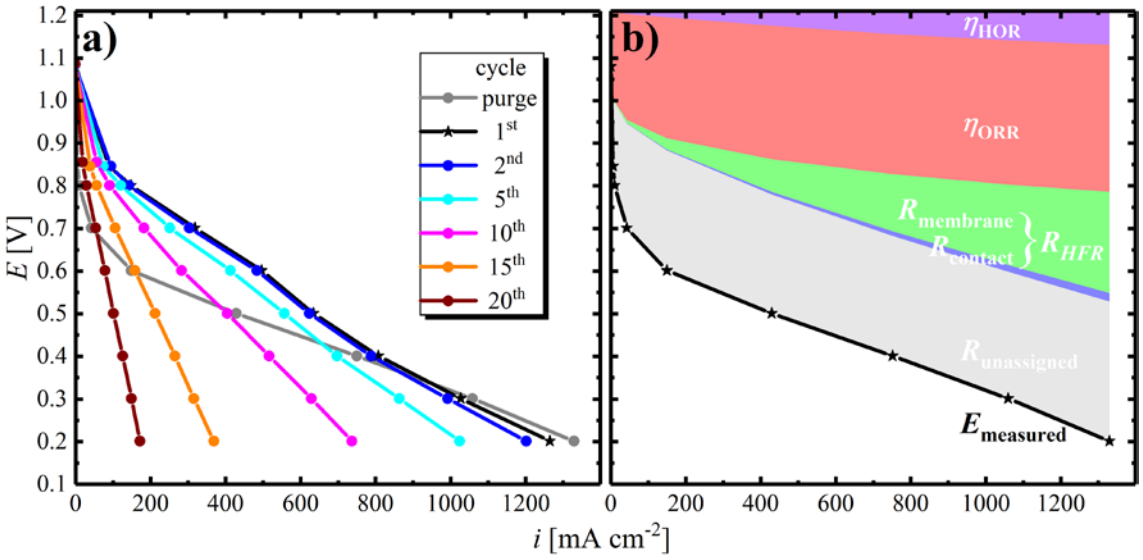

Figure 9. a) H_2/O_2 polarization curves using 1000 nccm / 500 nccm of H_2/O_2 on anode / cathode at 110 kPa_{abs}, 80% *RH* and 50°C, where the anode / cathode loading of the Pt/C catalyst is 0.39 / 0.40 mg_{Pt} cm^{-2} (TEC10V50E, *Tanaka Kikinzoku Kogyo K.K.*, Japan, black curve) at an I/C ratio of 0.8 g_I g_C^{-1}, using the FAA-3 ionomer (*Fumatech GmbH*, Germany) and a Tokuyama A201 membrane (28 µm, *Tokuyama Corp.*, Japan). The GDL and MPL (Sigacret 25BC, *SGL Carbon GmbH*, Germany) are the same on both sides, assembled at a compression of 20%. The MEA size is 5 cm^2 and the flow fields have 7 channels with 0.5 mm lands and channels in serpentine arrangement (c.f., Figure 22a). b) Voltage loss analysis for the 1st cycle of the polarization curve, including the HOR overpotential, η_{HOR} (calculated from the Butler-Volmer Equation [8] with i_0 = 1.68 mA cm_{Pt}^{-2} at 50°C, derived from i_0 = 0.57 mA cm_{Pt}^{-2} for an activation energy, E_a = 29.5 kJ mol^{-1} at 21°C according to $i_0^{50°C} = i_0^{21°C} \cdot e^{\frac{E_a}{R}\cdot\left(\frac{1}{294K}-\frac{1}{333K}\right)}$)[101], the ORR overpotential, η_{ORR} (calculated according to the Tafel Equation [9], using the theoretical *TS* = 64 mV dec^{-1} at 50°C, with $i_0 = 2.6 \cdot 10^{-8}$ A cm_{Pt}^{-2}, derived from $i_0 = 3.1 \cdot 10^{-9}$ A cm_{Pt}^{-2} for E_a = 67 kJ mol^{-1} at 25°C, corrected for the partial pressure of O_2 at the measurement conditions),[107] the membrane and contact resistance (estimated from the *HFR* of 193 mΩ cm^{-2}, measured at OCV via PEIS between 500 kHz and 10 Hz with an amplitude of 2 mV, assuming a contact resistance of 15 mΩ cm^{-2}) and the residual voltage losses, $R_{unassigned}$. All calculations assume an *ECSA* of 54 m_{Pt}^2 g_{Pt}^{-1}, obtained by CO stripping measurements in a PEMFC for the same catalyst.

similar activity in alkaline compared to acidic medium.[107] Even though the use of Pt as ORR catalyst can be avoided in AEMFCs which reduces the cathode electrode cost, there is so far no alternative ORR catalyst that would significantly reduce the overpotential from that shown in Figure 9b.

In addition, one of the biggest challenges of AEMFCs is the membrane that has a roughly 3-fold lower conductivity compared to PEMs (see section 3.1.2 for more information), originating partially from their early development status, as well as from the low ionic mobility of the hydroxide ion compared to the proton.[108,109] A low membrane conductivity directly results in a high voltage drop, shown (green area) in Figure 9b as

the main fraction of the *HFR* (in addition to the contact resistance, blue area). Considering the approximately 3x lower conductivity of the AEM compared to a standard PEM and the fact that it is roughly twice as thick as the membrane used in the measurement shown in Figure 6, one may expect a high voltage drop for the AEMFC. Nevertheless, the excessive ohmic losses of 180 mV at 1 A cm^{-2} in the AEMFC caused by $R_{membrane}$ compared to 15 mV for the PEM cannot be explained solely by the low membrane conductivity. Furthermore, it is not expected that this discrepancy is solely a result of the different *RH* (80% for the AEMFC vs. 100% for the PEMFC) and temperature (50°C vs. 80°C) in the two measurements. Hence, further improvements of the MEA fabrication process are required to achieve the *HFR* expected for the AEMFC system. Even though the OH^- conduction resistance in anode and cathode are not considered in the analysis due to a lack of an experimental quantification, the origin of the large unassigned voltage losses in the performance curve of the AEMFC remains unclear. This suggests that in addition to improvements of the membrane, the ionomer and the catalyst in AEMFCs, the MEA fabrication process (described in detail in the experimental section) might also be responsible for unaccounted losses.

Another drawback of AEMFCs is the fast exchange of the hydroxide ions by carbonate / bicarbonate due to the acidity of CO_2 in ambient air, causing a severe loss of ionic conductivity and a significantly lower performance for H_2/air operation.[110] The effect of carbonate poisoning can be observed (grey curve) in the initial polarization curve in Figure 6a, where the operation in H_2/O_2 causes a migration of the carbonate ions (due to previous air exposure) to the anode, where they are released into the exhaust in the form of CO_2. Associated with the higher conductivity of the OH^- ion, the performance in the subsequent polarization curve increases significantly (black curve in Figure 6a). Clearly, when air is used as a supply gas on the cathode, the introduction of CO_2 would lower the fuel cell performance dramatically.

Finally, the stability of the MEA prepared with the AEM and the alkaline ionomer is insufficient, since already subsequent polarization curves cannot maintain the original performance and a quasi-complete performance loss is observed after 20 polarization curves. Since the *HFR* increase in the course of the measurement does not cover the observed losses, the low stability of the AEMFC is most likely associated with the ion-

omer, and further research is required to understand this phenomenon and achieve a more stable MEA. According to this analysis, AEMFCs can only be considered as a far-future alternative for PEMFCs, with significant research efforts being required on a material and an MEA design level to obtain a decent fuel cell performance.

2. Experimental Methods

This chapter serves as a guide for the execution of experiments and the evaluation of the recorded data to introduce researchers to the techniques used in the group of Technical Electrochemistry at the Technical University of Munich in the field of fuel cells. For an overview on the specific experimental details (e.g., operating conditions), the reader is referred to the individual publications that are presented in chapter 3.

2.1. Catalyst Synthesis

2.1.1. Ru@Pt/C Core-Shell Nanoparticle Preparation via Polyol Reduction

The synthesis of Ru@Pt core-shell nanoparticles is based on the so-called polyol reduction process, where ethylene glycol is used as both solvent and reducing agent for the precursor. A two-step reduction is carried out to obtain the core-shell structure, starting with the preparation of Ru nanoparticles and subsequently coating them with a Pt shell. The schematic overview of the individual synthesis steps is shown in Figure 10 and the detailed process is described in the following section, as well as in the corresponding publication.[111]

For the core, 4.2 mg $RuCl_3$ (45–55% Ru content, *Sigma Aldrich Corp.*, Germany), together with 2.1 mg polyvinylpyrrolidone (PVP) (average $M_w \approx 55000$ g mol^{-1}, *Sigma Aldrich Corp.*, Germany) as a capping agent are weighed into a three-neck round bottom flask and 40 mL ethylene glycol (99.8%, anhydrous, *Sigma Aldrich Corp.*, Germany) is added. While the ethylene glycol is delivered as water-free solvent and deaerated by Ar purging (6.0-grade, *Westfalen AG*, Germany) directly after the transfer into the reaction vial, no Schlenk techniques are used in the synthesis process, nor is it carried out in a glovebox. The short exposure of ethylene glycol to ambient air upon filling the reaction vessel does not alter the reproducibility of the synthesis, whereas a pre-contamination of the ethylene glycol by water was identified to negatively influence the structure of the final catalyst. Full dissolution of the Ru precursor is typically achieved within ≈60 min, after which the reaction is initiated by increasing the temperature to 155°C at a constant rate of 4°C min^{-1}, regulated by an automated temperature control device (Model 310, *J-KEM, Inc.*, USA). To ensure the complete reduction of $RuCl_3$ to

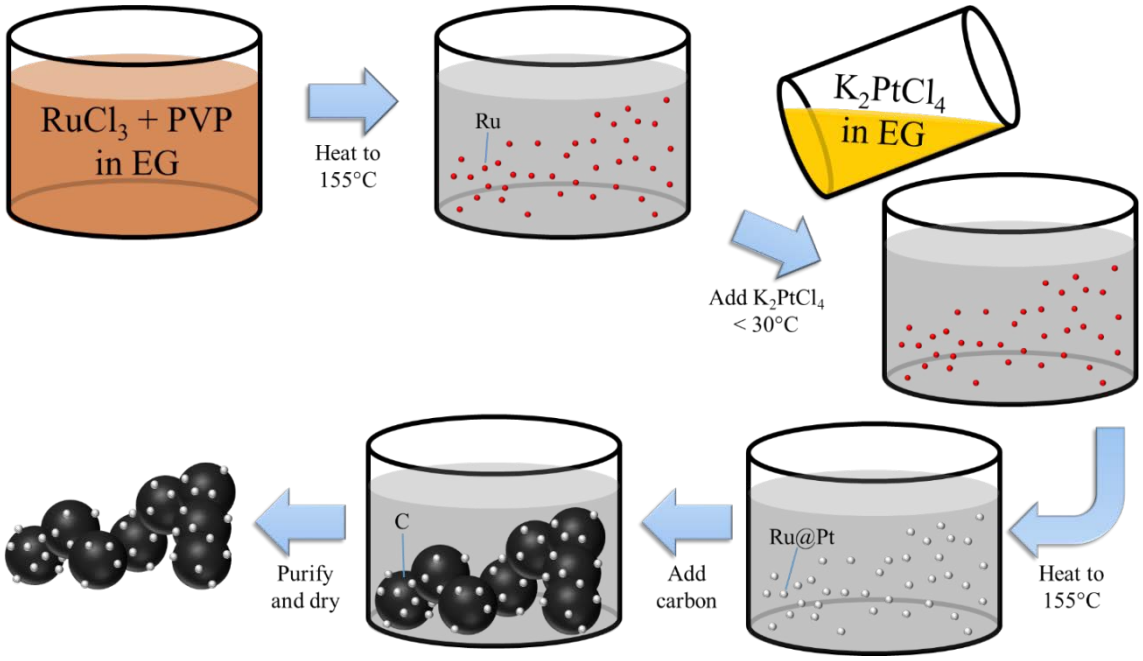

Figure 10. Schematic synthesis overview for Ru@Pt/C catalysts by subsequent heating of $RuCl_3$ and K_2PtCl_4 in ethylene glycol (EG), using polyvinylpyrrolidone (PVP) as a capping agent and finally supporting the core-shell nanoparticles on Vulcan carbon (C). The solution is continuously purged with Ar during the synthesis process which is carried out in a round-bottom flask (for simplicity represented by a beaker).

Ru, the temperature is maintained at 155°C for 90 min, subsequently switching the heating off, allowing the mixture to slowly approach room temperature (25°C). The cooling is enhanced by removing the heating device around the flask, allowing for a shortened overall synthesis time.

During the cooling process, the K_2PtCl_4 salt (99.99% [metals basis], *Sigma Aldrich Corp.*, Germany) is weighed into another flask (the amount depends on the desired thickness of the shell and can be calculated according to Equation [4] in Schwämmlein et al.),[111] subsequently adding 40 mL ethylene glycol and initiating Ar purging. The majority of the purchased K_2PtCl_4 precursor batches has the form of large crystalline needles, so that grinding in a mortar is advisable in order to allow for fast dissolution (commonly ≈30 min for a fine powder). At less than 30°C, the Pt precursor solution is added at once (low reproducibility was found for droplet addition) to the dispersion of Ru and stirred for 10 min. Afterwards, the temperature is increased to 155°C at the same heating rate as before and maintained at this temperature for 90 min. Finally, heating is stopped and the heating jacket is removed to cool down the reaction vessel. Meanwhile, Vulcan carbon (*Tanaka Kikinzoku International K.K.*, Japan) is dispersed in 80 mL eth-

ylene glycol, into this mixture, the dispersion containing the Ru@Pt particles is added and then the mixture is stirred for 14 h. The amount of the carbon support can be adjusted to obtain the desired catalyst loading.

For purification, acetone (technical grade, purified twice in a rotary evaporator) is added to the mixture (approximately 1:1 volume ratio) and the solvents are removed by centrifugation at 11500 rpm, 5°C and 10 min (ultra-centrifuge, 5810 R, *Eppendorf GmbH*, Germany). Finally, the catalyst is washed three times with acetone, once with 2-propanol (Chromasolv Plus, 99.9%, *Sigma Aldrich Corp.*, Germany), and then dried at 70°C in air for at least 24 h. To produce larger quantities of the catalyst (≈0.4 g), scale-up of the synthesis was already achieved by two students in the group (Björn Marcel Stühmeier and Nhat Long Tran Pham) by simply increasing the precursor and solvent amount while maintaining the same ratios.

2.1.2. Synthesis of Pt_xY/C by H_2 at Elevated Temperature

In contrast to most yttrium salts, such as yttrium oxide and hydroxide, yttrium halides can be reduced at practically achievable temperatures in H_2, as recently shown by Roy et al.[112] Hence, the synthesis method for bimetallic Pt-Y alloys supported on carbon, presented here, is based on the reduction of YCl_3 on a Pt/C catalyst at high temperature in H_2 environment. An overview of the reaction is provided in the scheme of Figure 11 and detailed information can be obtained in the corresponding publication.[113] To avoid the formation of yttrium oxides / hydroxides during the synthesis, the intrusion of O_2 or H_2O must be avoided, hence the entire preparation excludes ambient air exposure through working in inert atmosphere (*M. Braun Inertgas-Systeme GmbH*, Germany) and employing standard Schlenk techniques.

First of all, the precursor suspension containing YCl_3 and Pt/C is prepared in acetonitrile (≥99.9%, *Sigma Aldrich Corp.*, Germany), where a high solvent to precursor ratio is necessary (≈24 mL $g^{-1}_{YCl_3}$) to ensure complete dissolution of the yttrium salt. The solvent is purified beforehand by a molecular sieve to remove trace water, degassed by sonication (Elmasonic S 30 H, *Elma Schmidbauer GmbH*, Germany) and handled solely in Ar atmosphere. For the synthesis described in this thesis, the required amount of YCl_3 and Pt/C (molar Pt:Y ratio of 1:1) are mixed in an agate mortar and added to acetonitrile in a Schlenk tube inside the glovebox. Dissolution of the yttrium precursor and dispersion of Pt/C are simultaneously ensured by sonication of the mixture for 3 minutes. To remove the solvent and distribute YCl_3 on the Pt/C catalyst, the mixture is immersed into liquid N_2, subsequently carefully reducing the pressure inside the vessel to ≈10^{-1} mbar with a vacuum pump (Rotary-Vane RZ6, *Vacuubrand GmbH & Co.*, Germany). During the approximately 24 h long process, the mixture has to be continuously cooled by liquid N_2 to avoid the melting of the solvent and to ensure proper freeze drying. While the process is generally successful to prepare the precursor for the synthesis, the amount of solvent used for the dissolution of YCl_3 is rather high and needs to be improved in the future to control the local Pt:Y ratio on the carbon support. After complete drying, the precursor is homogenized by grinding in an agate mortar inside the glovebox, is then placed in an Al_2O_3 crucible (sapphire, 150 µL, *THEPRO GbR*, Germany) and finally transferred from the glovebox into a continuously Ar-purged

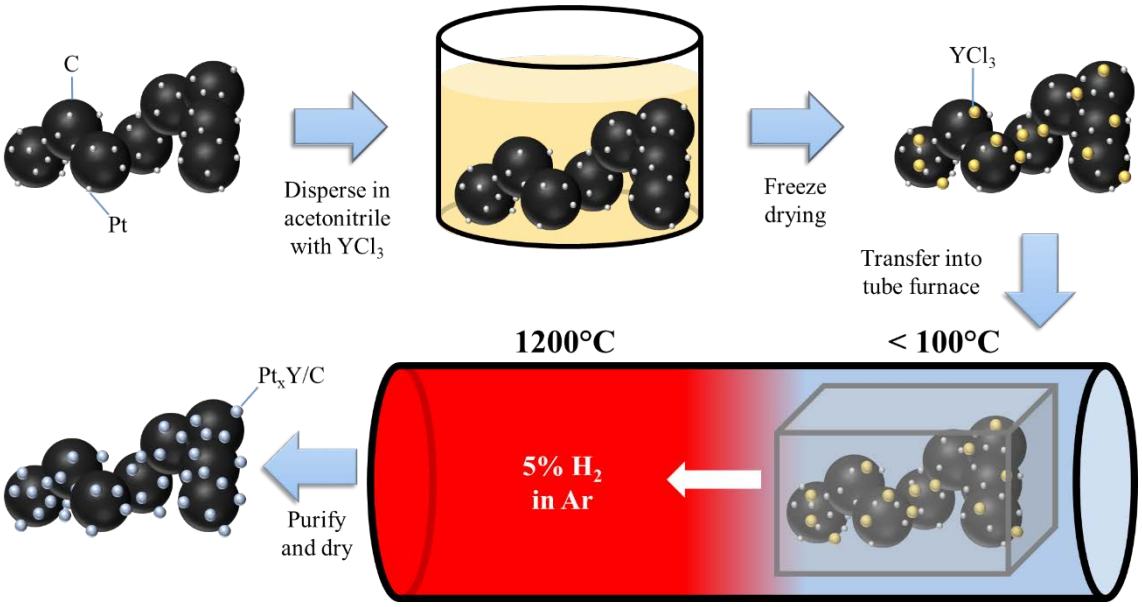

Figure 11. Schematic synthesis route for Pt_xY/C catalysts, starting with a commercially available Pt/C catalyst. The catalyst is impregnated with an YCl_3 precursor in acetonitrile, freeze dried, heated in a tube furnace and finally washed and dried to obtain the catalyst.

(500 mL min^{-1}) Al_2O_3 tube furnace (LK 1300-150-600-3, *HTM Reetz GmbH*, Germany). Even though the contact time with ambient air during the transfer into the tube furnace is very short (< 30 s), the side phases of YOCl and Y_2S_2O (presumably by reaction with Sulphur impurities in the carbon black) in the final product (see section 3.2.3) indicate that yttrium oxides / hydroxides are formed in this phase. Therefore, the synthesis method needs to be improved in the future to fully avoid air contact, e.g., using an inert gas chamber to transfer the sample from the glovebox into the tube furnace. To start the reduction process, the tube furnace is heated to 1200°C (c.f., Figure 12) while the crucible remains outside of the heated zone until the desired temperature is reached (the part of the tube carrying the crucible is cooled by air ventilation during this time). Subsequently, the gas atmosphere is changed to 5% H_2 in Ar (500 mL min^{-1}) and the crucible is pushed into the hot zone of the tube with an Al_2O_3 rod through a polysiloxane sealing. In the future, the temperature necessary for reduction of YCl_3 and alloying of Y and Pt has to be optimized to achieve a smaller average Pt_xY particle size. Furthermore, the effect of the heating ramp has to be evaluated and the possibility to use a slower rate should be considered. After the desired reaction time of 1 h, the heating is turned off, leaving the furnace to cool down to room temperature over ≈5 h, maintaining a constant Ar flow of 200 mL min^{-1}. To slightly oxidize the surface of the catalyst, a low amount

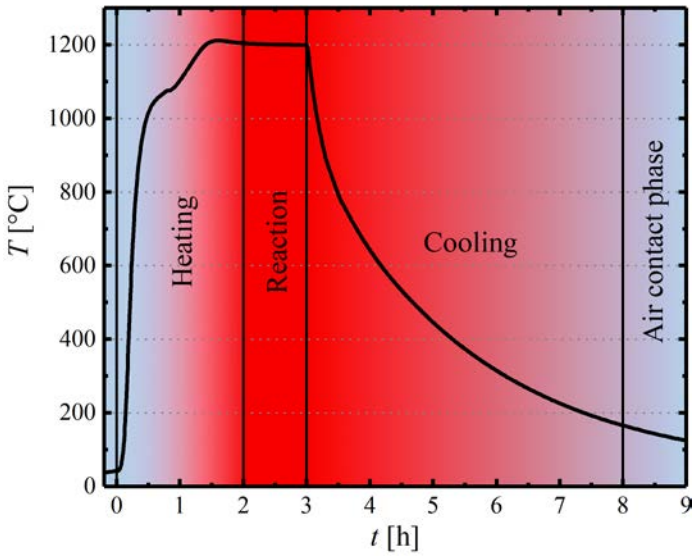

Figure 12. Heating profile for the tube furnace used to prepare Pt_xY/C catalysts. The different steps of catalyst insertion and cooling are depicted in the graph.

of air is mixed into the argon gas stream at low temperature, until the catalyst can be removed from the tube and handled in ambient atmosphere. To remove undesired side phases from the catalyst and surplus yttrium, the catalyst is leached under stirring in a 1 M H_2SO_4 solution (ACS reagent, *Sigma Aldrich Corp.*, Germany) at a solvent to catalyst ratio of ≈0.1 L g_{cat}^{-1}; during this time, the vessel is continuously purged with argon. After 3 h, the catalyst is recovered by centrifugation (5 min at 11500 rpm, 5810 R, ultracentrifuge, *Eppendorf GmbH*, Germany) and washed with ultrapure water (18.2 MΩ, MilliQ Ingegral, *Merck Millipore KGaA*, Germany) until a neutral pH is reached (≈5 times). To dry the catalyst, it is stored overnight at 60°C in air and finally at room temperature in a closed vial until used. A typical synthesis quantity is 1 g, whereas the catalyst amount can be adjusted by simple up- or downscaling of all quantities (e.g., using several sapphire crucibles at the same time).

2.2. Electrochemical Catalyst Screening in RDE

This section focusses on a detailed explanation of the rotating disk electrode (RDE) method to evaluate the electrochemical kinetics of catalysts for the HOR and ORR. One of the most prominent challenges of measurements in liquid medium is the contamination of the electrolyte, potentially affecting the kinetic analysis of electrocatalysts.[114] In comparison with the large ratio of Pt surface area to ink volume in PEMFCs of ≈0.5 m^2_{Pt} mL^{-1}_{ink} (calculated for a 20%$_{wt.}$ Pt/C catalyst with an *ECSA* of 70 m^2_{Pt} g^{-1}_{Pt} at 0.03 g_{carbon} mL^{-1}_{ink}), the Pt surface area to liquid volume ratio is significantly smaller in RDE experiments due to the large amount of electrolyte used during the measurement (on the order of $2 \cdot 10^{-6}$ m^2_{Pt} $mL^{-1}_{electrolyte}$, calculated from 9 μg_{Pt} cm^{-2} for a 1 µm thick film, using a 20%$_{wt.}$ Pt/C catalyst with an *ECSA* of 70 m^2_{Pt} g^{-1}_{Pt} on a disk with a surface area of 0.196 cm^2, assuming an electrolyte volume of 50 mL). Hence, RDE measurements require a very high level of purity for all used materials (the concentration of contaminants in the electrolyte needs to be ≈5 orders of magnitude lower than that in the solvent of the ink for MEA preparation) as well as a clean working style which is thoroughly described in the following sections.

2.2.1. Measurement Preparation

Cell Component Cleaning in Caro's Acid.—A common procedure to clean various materials (especially glass ware) is based on Caro's acid (also known as Piranha solution), which is a 3:1 mixture of concentrated H_2SO_4 (AnalaR Normapur, 95%, *VWR International GmbH*, Germany) and H_2O_2 (PanReac, 50%, *Applichem GmbH*, Germany). The highly oxidative environment in this solution originates from the in-situ formation of peroxysulfuric acid (H_2SO_5) from the two components. Due to the oxidation strength of Caro's acid, its preparation, handling and disposal must be carried out with extraordinary care (i.e., usage of a laboratory coat, a protective apron, a face shield, and acid handling gloves). Furthermore, the exposure of the solution to organic compounds such as ethers and ketones (e.g., leftovers in glass ware) has to be strictly avoided due to a highly exothermal reactivity. Caro's acid is prepared by slow addition of the components into a large beaker (heat resistant borosilicate glass), which is then left to cool to room temperature, and is subsequently transferred into a large container where it is

stored with a glass plate on top. The solution should be replaced every ≈6 month, transferring the acid into plastic containers, which are labeled with “concentrated acid” to avoid the mixing with dilute acids.

For RDE experiments, all cell components have to be cleaned before initial use, after extended measurement periods or after detection of a contamination issue. All materials that are to be exposed to Caro’s acid have to be properly pre-cleaned (no solvent or catalyst residues, no marker writing, no labels) prior to insertion into the bath to avoid the introduction of organic substances into Caro’s acid. Furthermore, it has to be verified that the material is fully stable in the acid (e.g., some polymers decompose in Caro’s acid), and that they do not decompose the cleaning solution (e.g., Pt). Glass ware is then slowly put into the acid basin using long pincers which are covered with PTFE to avoid corrosion. All components should be fully submerged in the solution, releasing all gas from the interior void volume and placing the openings to face upwards. The time required to fully clean glass ware or other components depends on the degree of contamination, but as a rule of thumb, 1-2 days submersion in Caro’s acid are sufficient in most cases. Thereafter, glass ware can be removed from the basin using long pincers, placing the components on a clean collection tray that is solely dedicated (and labeled) to this purpose. To remove the acidic residues from the glass ware, the components have to be thoroughly rinsed with purified water (Elix, 15 MΩ cm, *Merck Millipore KGaA*, Germany) and the waste water is disposed in an acid canister. Finally, the glass ware is transferred into a large (clean) beaker, which is filled with ultrapure water (18.2 MΩ · cm, MilliQ Ingegral, *Merck Millipore KGaA*, Germany) and heated to the boiling point for at least 20 min. To fully remove sulfate contamination, the water in the beaker is discarded and the procedure is repeated ≈6 times. The beaker can now be used to store the glass ware in ultrapure water and for cleaning after any experiment (boiling ≥ 3 times in ultrapure water).

Handling of Clean Components.—To avoid contamination of the clean cell components, special care needs to be taken during the preparation and measurement phase. As a general rule, everything in contact with the electrolyte solution or with anything that is stored / cleaned together with the cell components after the measurement has to remain clean. This can be ensured by handling those components only with special, clean

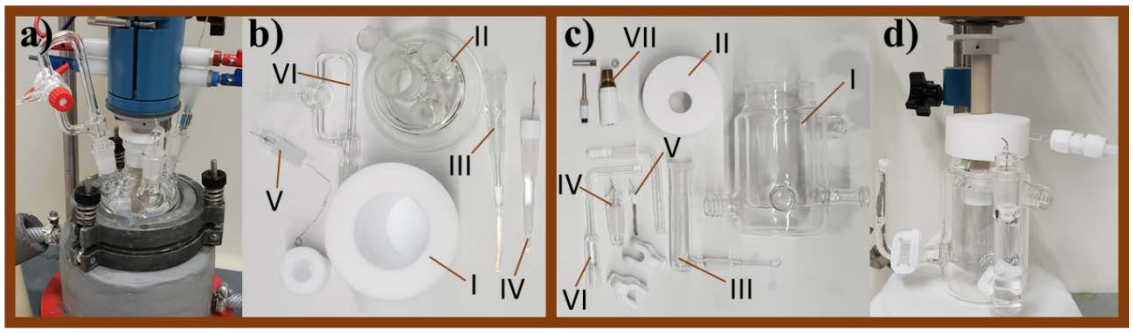

Figure 13. a) Cell setup and b) individual components for RDE measurements in alkaline solution. c) Components and d) cell setup for acid solution. The hardware consists of I) an electrolyte reservoir, II) a lid, III) an electrolyte bridge / Luggin capillary, IV) a reference electrode, V) a counter electrode, VI) a bubbler and VII) an electrode holder with electrode.

gloves (Kimtech Pure G3 Sterile Cleanroom Gloves, *Kimberly-Clark Corp.*, USA) and lint-free cloths (Cleanroom knit wipers, *VWR International GmbH*, Germany). Care needs to be taken when taking clean gloves or lint-free wipes out of the storage bag to avoid contamination of the entire package. To open a new bag of clean gloves (or lint-free cloths), the outer packaging bag is opened with scissors and the interior bag is taken out, turned around and put back into the covering bag. Since the gloves stick together when taken out of the bag, the entire bag should be massaged from the outside after opening in order to loosen the gloves from each other. To maintain the special gloves clean, touching any non-clean environment (e.g., touching the clean glove with a regular glove at the palms to put it on) requires the exchange of the glove for a clean glove. Therefore, the most practical way for advanced RDE users is to assemble the cell and prepare the measurement with a special, clean glove on the one hand and a regular glove on the other hand. All cell components are put on a large lint-free cloth which has not been in contact with any non-clean environments (shown in Figure 13).

The cell consists of a large vessel (PTFE for base, glass for acid) for the electrolyte (I), covered with a lid (II). Since glass is easily etched by base solutions it is not supposed to be in contact with alkaline electrolyte. The reference electrode (IV) is either Ag/AgCl, sat. KCl for experiments in base or a reversible H_2 electrode (RHE) composed of a Pt wire,extending in a tube filled with electrolyte and a H_2 gas bubble for experiments in aced. It is placed into a Luggin capillary (III) with a small opening at its end (acid), or with a Nafion membrane between two shrink tubes (base). The Pt counter electrode (V) and the gas bubbler (VI) are placed in the remaining holes and the elec-

trode holder (VII) is assembled on a glass plate by pushing the electrode into the U-cup from the back, and finally introduced to the electrolyte through the lid. The cell temperature is regulated by a heating / cooling jacket. During the measurement, the cell needs to be kept away from contamination sources and is therefore placed on a lint-free cloth under the rotator (*Pine Research Instrumentation*, USA) in the measurement area. The holder for the alkaline cell compartment, as well as the holding fixtures need to be maintained clean and are cleaned prior to measurements by wiping them off with a lint-free cloth, wetted with ultrapure water.

Mechanical Polishing of RDE Electrodes.—RDE is carried out on metallic electrodes or on thin catalyst films on a carrier electrode, e.g., glassy carbon (GC) or Au (5 mm diameter, *Pine Research Instrumentation*, USA). To assure reliable measurements with controlled hydrodynamics during rotation, the electrode should be reasonably flat without large deformations or scratches. The electrode surface roughness can be controlled by mechanical and / or electrochemical polishing, while mechanical polishing suffices in most cases and is significantly easier to execute. As a reference, high resolution SEM images of a mechanically polished Sn surface (99.999%, *MaTecK Material-Technologie & Kristalle GmbH*, Germany) are shown in Figure 14.

For mechanical polishing, the electrode is either put in a PTFE holder with an indentation to align the electrode surface with the top of the holder or it is embedded in epoxy resin. While embedding in a resin yields significantly better polishing results and might be needed in certain cases, it is a much more time consuming process and the simple placement in a holder is more practical. To embed the electrode, it is placed face down in a PTFE holder with the proper dimensions for the polishing machine holder. While pushing the electrode down (e.g., with a wooden stick), the resin is poured into the holder and left to harden overnight. It is very important to use a resin which can be removed after fulfillment of the polishing and the best candidate identified in the group of Technical Electrochemistry is methyl methacrylate (VariDur 200, *Bühler GmbH*, Germany). After the resin has fully hardened, the embedded electrode is polished with a polishing machine according to a procedure which needs to be optimized for each material. During the work for this thesis, a procedure to polish polycrystalline Pt and

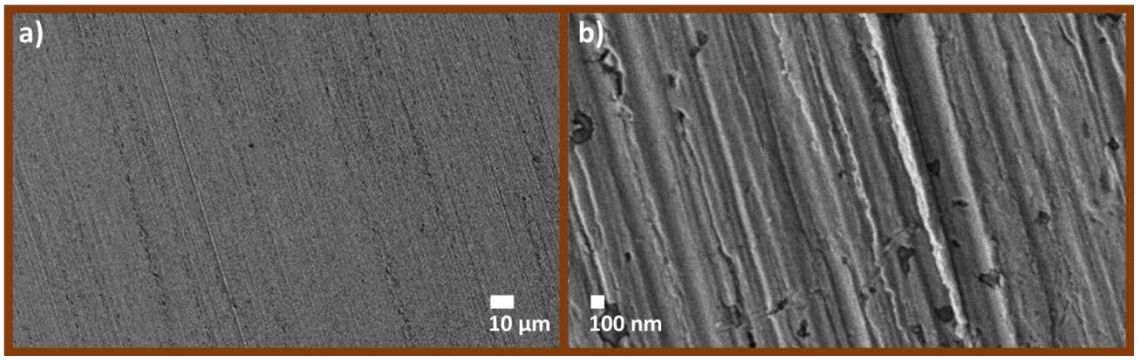

Figure 14. SEM images of a mechanically polished Sn electrode, taken with a field emission device (JSM-7500F, *JEOL GmbH*, Germany). The polishing procedure is shown in Table II.

polycrystalline Sn electrodes on a Bühler Polishing maschine (MetaServ 250 / vector head, *Bühler GmbH*, Germany) was developed and is shown in Table I and Table II. The given polishing times are merely a guideline and in the case that one of the steps is not capable of removing the scratches on the electrode surface from the previous sequence, it has to be repeated before moving on. The polishing pad should only be used for one type of polishing paste / material and therefore, has to be properly labeled to avoid confusion. All electrodes have to be cleaned well with deionized water and sonicated in ultrapure water (5 times for 1 minute with exchange of water) before moving on to the next step. The sonication of Sn is shortened (2 times for 1 minute) after execution of the polishing step with 0.3 µm alumina, since Sn metal is soft and a surface

Table I. Polishing procedure for polycristalline Pt electrodes. All polishing materials are provided by *Bühler GmbH* (Germany).

Pad	Paste	Pressure	Time	Direction	Information
TexMet C	Diamond (9 µm)	10 N	5 min	Co-rotation	Add Microfluid during
TexMet C	Diamond (3 µm)	10 N	5 min	Co-rotation	Polishing to maintain
TexMet C	Diamond (1 µm)	10 N	5 min	Co-rotation	the pad wet
MasterTex	Al_2O_3 paste (0.3 µm)	15 N	5 min	Counter	
MasterTex	Al_2O_3 (0.05 µm)	15 N	10 min	Counter	

Table II. Polishing procedure for polycristalline Sn electrodes. All polishing materials are provided by *Bühler GmbH* (Germany).

Pad	Paste	Pressure	Time	Direction	Information
Microcloth	Al_2O_3 (1 µm)	15 N	5 min	Counter	Add Microfluid during
Microcloth	Al_2O_3 paste (0.3 µm)	15 N	5 min	Counter	polishing to maintain
Microcloth	Al_2O_3 (0.05 µm)	10 N	10 min	Counter	the pad wet

roughening is observed after extended sonication. An optical microscope can be used to control the current status of the electrode surface after each polishing step, where the scratches should have similar dimensions as the average particle size of the polishing paste. After the polishing process is completed, the pad is cleaned with a strong flow of deionized water to remove old polishing residue (important especially for alumina paste), and is subsequently dried to avoid mold formation. The resin of embedded electrodes is removed by a combined mechanical and chemical procedure. First of all, holes are drilled in a circle around the electrode into the resin with a drilling machine. Thereafter, the resin block is submerged in acetone for at least 24 h, where the polymer swells and the electrode is slowly lifted out of the resin body. During this time, the container is closed with a lid to avoid evaporation of the solvent.

Electrode Cleaning.—While the purity in the bulk of the electrode is often high and of no concern regarding the contamination of the RDE experiment, a significant amount of impurities from the preparation process and material handling can adsorb on its surface (e.g., on new electrodes, after polishing, or due to extended usage). Therefore, the electrodes are cleaned prior to the measurement. Pt, as a noble metal, allows for a comparably harsh cleaning treatment in Caro's acid. Since Pt decomposes H_2O_2, it cannot simply be put into the Caro's acid bath used for general cleaning, but a small fraction of the acid can be separated for this purpose. After the cleaning, the electrode should be rinsed well with ultrapure water and boiled several times in ultrapure water using a small (clean) beaker. Other metals used for the experiments in this thesis, such as Sn, do not allow such a treatment due to instability in acid. Therefore, Sn electrodes are cleaned by sonication in 2-propanol / water mixtures and finally in water. Carrier electrodes (e.g., GC or Au) for thin-film RDE measurements have to be cleaned from residual catalysts by wiping the electrode off with a lint-free cloth wetted with 2-propanol and subsequent sonication (> 3 times) in a mixture of ultrapure water and 2-propanol.

After electrode cleaning, all materials have to be handled with great care and should not get in touch with any non-clean environment. To prepare the measurement, the electrode is placed on a lint-free cloth and the holder is disassembled next to it. A good way to insert the electrode into the holder is to push the electrode onto a clean, flat glass plate to ensure proper alignment (misalignment may alter the hydrodynamics and yield

erroneous results). The full electrode is thereafter cleaned by dipping it into 5 M KOH (99.99% purity, semiconductor grade, *Sigma Aldrich Corp.*, Germany) and 2 M $HClO_4$ (60%, Cica Reagent, *Kanto Chemical Co., INC.*, Japan), followed by ultrapure water (only for electrode materials that are stable in acid and base).

Catalyst Coating for Thin-Film RDE.—To ensure a good reproducibility in thin-film RDE measurements, the quality of the coating is very important. The same catalyst, coated from the same ink, on the same carrier electrode can yield significantly lower activity if the coating is inhomogeneous. An ink is composed of the catalyst (e.g., Pt/C), a mixture of solvents (e.g., 2-propanol and H_2O), and an ionomer. While the addition of Nafion leads to a lower measured activity,[115] it aids to achieve a good catalyst dispersion in the ink, a homogeneous film distribution on the electrode and a better adhesion of the coating to the carrier electrode (important during rotation). Furthermore, since a frequent goal of RDE measurements is to screen catalysts for PEMFCs or AEMFCs, the use of an ionomer guarantees a more realistic estimate of the kinetic parameters. A generally applicable ink formulation for Pt/C catalysts is shown in Table III as a guideline for the development of formulations for novel catalysts. To prepare the ink, the approximate amount of catalyst is weighed into a small vial. As it is challenging to adjust the catalyst weight to the exact value, the total amount of prepared ink is altered by choosing the appropriate solvent quantity depending on the actually used catalyst amount. The water is added with a pipette (Eppendorf Research plus, *Eppendorf AG*, Germany) on the basis of the volume, thereafter adding 2-propanol to the vial with a new tip while weighing the vial on a balance. The control of the mass during the addition guarantees a high accuracy. The thus prepared ink is sonicated for 20 min in a strong sonication bath (Elmasonic S 30 H, *Elma Schmidbauer GmbH*, Germany) filled with a water-ice mixture to avoid the rise of temperature in the closed vial (wrapped with Parafilm, *VWR*

Table III. Formulation to prepare ≈3 mL of an ink with a 20%$_{wt.}$ Pt/C catalyst, using a 5%$_{wt.}$ Nafion solution and a mixture of 70%$_{vol.}$ 2-propanol with 30%$_{vol.}$ H_2O, giving the relevant mass, *m*, and volume, *V*, values of the individual components.

***m*(Pt/C)**	***m*(2-propanol)**	***m*(H_2O)**	***V*(Nafion)**	**I/C**	***V*(coat)**	**Thickness**	***m*(Pt)**
mg	g	g	µL	$g_I\ g_C^{-1}$	µL	µm	$\mu g_{Pt}\ cm^{-2}$
4.0	1.8	1.0	7.0	0.1	7.0	1.0	8.7

International GmbH, Germany). Thereafter, the ionomer is added to the solution with a pipette, ensuring full transfer from the tip by repetitive soaking and dispensing of the ink into the vial. To disperse the ionomer in the ink, the vial is sonicated (> 5 min) in a low energy sonication bath (Elmasonic S 10, *Elma Schmidbauer GmbH*, Germany). Before taking the desired coating amount with a pipette, the ink is taken out of the bath, without letting it rest for more than 1 min. Even though the ink should be well dispersed, it is advantageous to pick up the ink volume for the coating from the center of the vial, as opposed to the bottom or top in order to avoid a variation of the coated catalyst mass.

In general, a large variety of coating methods can be applied to obtain a good film quality, such as spin coating, air stream drying, ambient drying, infrared (IR) lamp application or controlled atmosphere drying. In order to achieve a homogeneous catalyst film on the electrode, the coating procedure has to be optimized individually for every catalyst / solvent / ionomer system. Even though many catalysts are similar to each other, a small variation of an important property (e.g., carbon support surface properties) may require the optimization of the coating procedure. Spin coating, where the electrode is rotated around its axis while drying, is mainly used due to its ability to flatten the droplet on the surface of the electrode. In this case, tuning of the rotation rate and the solvent properties (good dispersability of the catalyst and appropriate drying rate) can lead to a reproducibly high coating quality.[116] Similarly, the air stream pushes the droplet down to flatten it, with the difference that the high air stream induces fast evaporation of the solvent, which might be beneficial in certain cases. The other class of drying methods is stationary without altering the form of the droplet, but changing evaporation rate. The droplet could be simply left to dry at ambient air, or the evaporation can be enhanced by the use of an IR lamp or slowed down by covering the electrode with a beaker to contain the solvent atmosphere. To achieve very slow drying, the covering beaker is rinsed inside with the solvent mixture of the ink (without catalyst and ionomer), creating an internal solvent atmosphere that hinders evaporation. Generally, stationary drying with a covering beaker is a simple way, can yield very good results if properly optimized and is therefore the method of choice in this thesis.

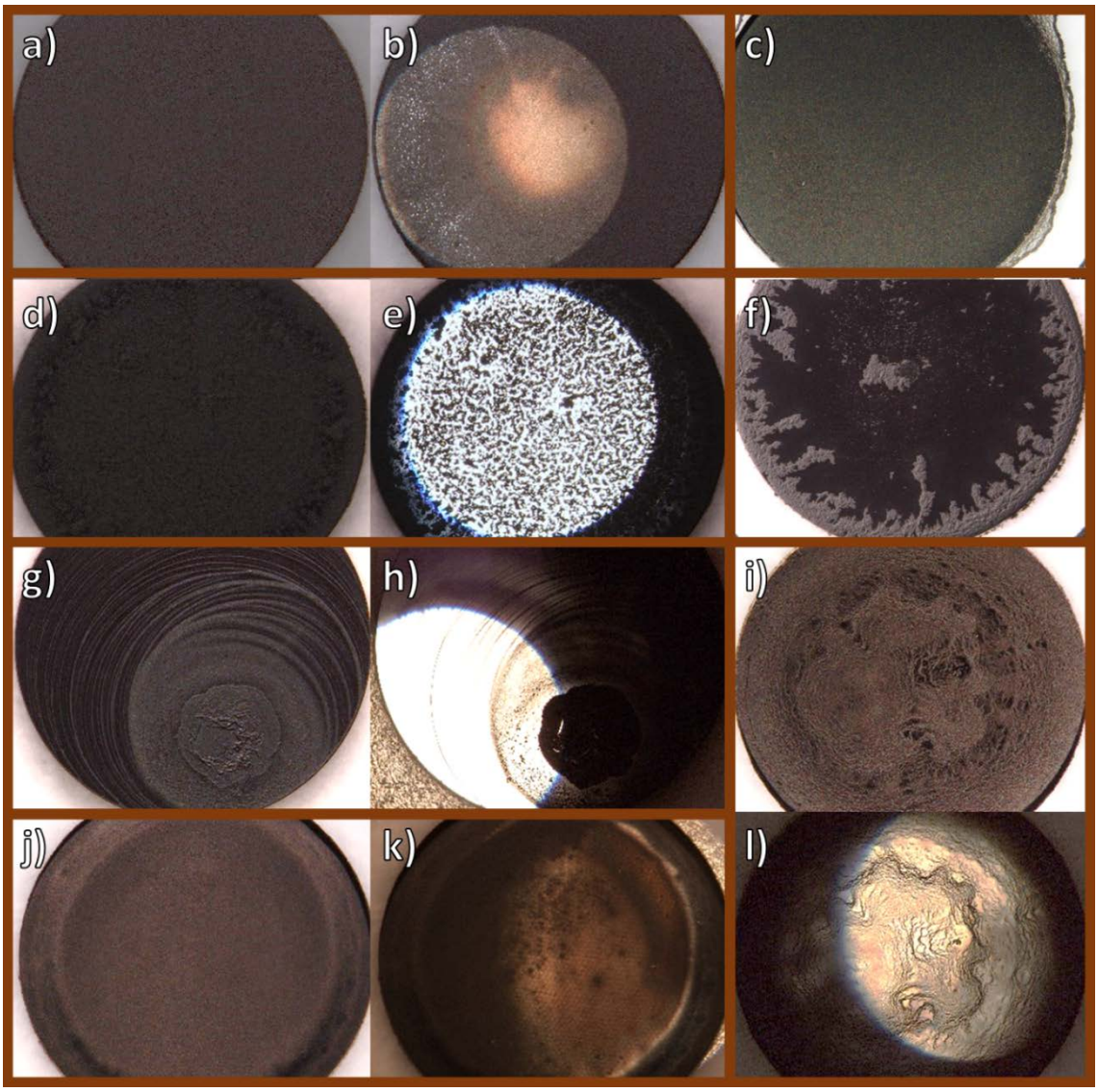

Figure 15. Images taken with an optical microscope (Stemi 2000-c, *Carl Zeiss AG*, Germany), showing a) + b) a homogeneous coating, c) a coating from a high droplet volume, d) + e) an inhomogeneous coating, f) a coating prepared from an "aged" ink, g) + h) a coating dried under a strong air stream, i) + l) a slowly dried coating in a controlled solvent atmosphere and j) + k) a coating with a coffee ring. The ink was prepared with a $9\%_{wt.}$ Ru@Pt/C catalyst using $70\%_{vol.}$ 2-propanol, $30\%_{vol.}$ H_2O and an I/C ratio of 0.15 $g_I\ g_C^{-1}$.

In the following, several examples of thin catalyst films are intended to show a representative good catalyst layer (Figure 15a + b), as well as different coating issues (Figure 15c- l). Figure 15a and b show images of a homogeneous catalyst film of Ru@Pt/C with a thickness on the order of 0.7 µm on an RDE electrode, taken with an optical microscope. The coating is prepared by dropping 7 µL of an ink on a GC disk, leaving it to dry steadily with a lid. While the regular microscopy mode (Figure 15a) can be used to obtain a good image of the electrode and to ensure that the catalyst is well-distributed

over the entire electrode area, shining light (KL 2500 LCD, *Schott AG*, Germany) through the ocular (Figure 15b) helps to identify inhomogeneous areas. Homogeneous coatings reflect the light with a similar intensity and no bright or dark spots are observed (colors are not taken into account). In contrast, the counter-light image of the coating in Figure 15e clearly reveals inhomogeneities, even though the regular imaging mode (Figure 15d) suggests an acceptable coating. Therefore, it is very important to image with both modes and to identify electrodes that are not suitable for the extraction of kinetic data prior to conducting any measurements. Another common mistake is the choice of a too large coating quantity, leading to a spillover of the catalyst to the electrically insulated PTFE holder (Figure 15c). In this case, the solid content in the ink is increased, so that a lower amount of ink can be used to achieve the same catalyst thickness. For inks based on a mixture of 2-propanol and H_2O as solvents, a suitable droplet size is 7 µL for a 0.2 cm^2 disk substrate, coated with an Eppendorf pipette (according to the recipe in Table III). Coating from an ink that has already rested for several days is generally not advisable, since this can lead to a settling of the solid particles in the ink and an insufficient re-dispersion by sonication, hence an inacceptable coating quality (Figure 15f). For air-stream drying of the coating, the distance of the electrode from the air outlet and the total air flow have to be carefully adjusted in order to avoid fast drying under a strong air flow, leading to the accumulation of the coating on a certain part of the electrode (Figure 15g + h). Furthermore, slowing the drying process down significantly by controlled atmosphere drying requires a stable dispersion to avoid inhomogeneous deposition during the drying process (Figure 15i + l). Another typical phenomenon is the formation of a coffee ring (Figure 15j + k) due to an outwards directed flow of the suspended material during drying of the droplet.[117] This can typically be avoided by an optimization of the solvent mixture in the ink or by employing a different drying technique.

In addition to the challenges mentioned here, a misalignment of the U-cup and the exchangeable electrode has to be circumvented, since this might negatively influence the coating quality. As a general strategy, several electrodes should be coated with the same ink after optimization of the formulation, discarding all inhomogeneous coatings.

Electrolyte Preparation.—As discussed earlier, the electrolyte is a major source of contamination in RDE measurements. Therefore, the electrolyte solution has to have a very high purity, needs to be treated with care and has to be prepared fresh before the measurement. For measurements in perchloric acid, different acid suppliers were tested by Timon Geppert, Dr. Hany A. El-Sayed, Dr. Thomas Mittermeier and Jan N. Schwämmlein. The concentrated acid supplied by Kantochem (60%, Cica Reagent, *Kanto Chemical Co., INC.*, Japan), was identified to be suitable for RDE measurements, since the typical H_{upd} features on Pt and the Pt-oxide peaks are well-visible and reliable ORR activity values are obtained when all other sources of contamination are controlled.[50] The concentrated acid is stored at ≈7°C in the refrigerator to avoid decomposition over time. To prepare the dilute electrolyte solution (typically 0.1 M), Erlenmayer flasks with an indent on the top (designed by Benedikt A. Brandes) have proven to be the best vessel due to their easy handling and little acid spill during decantation. The glass lid with a fixed glass cover (also designed by Benedikt A. Brandes) as well as the top part of the flask (indicated by a line) are only allowed to be touched with special, clean gloves to avoid contamination of the electrolyte. To prepare the solution, the flask is filled halfway with ultrapure water, the acid is weighed into an additional (clean) beaker and subsequently poured into the electrolyte flask. Afterwards, the flask can be filled with ultrapure water to the marker line in order to achieve the desired dilution.

For measurements in the alkaline medium, sodium hydroxide monohydrate (99.9995%, metals basis, TraceSELECT, *Sigma Aldrich Corp.*, Germany) flakes are dissolved in ultrapure water using a PTFE beaker. After opening the $NaOH \cdot H_2O$ container, it is stored in dry, inert (Ar) environment using a desiccator to avoid the intrusion of moisture and CO_2. After the desiccator has been opened to ambient air, the dry atmosphere is replenished by repetitive (3x) vacuum application and Ar flushing. To remove moisture from the container, the lid is not fully closed when stored in the desiccator. When care is taken to avoid the intrusion of moisture and other contaminants, the electrolyte precursor can be used for approximately 2-3 weeks after it has been opened (labeling the container with the date upon opening). While the electrolyte solution can also be prepared from KOH (99.99% purity, Emsure, *Merck KGaA*, Germany),[118] sodium hydrox-

ide monohydrate can be purchased at high purity, hence mitigates contamination issues.[102]

To prepare borate buffer solutions, the calculated quantity of boric acid (99.97%, trace metals basis, *Sigma Aldrich Corp.*, Germany) and sodium hydroxide solution (0.1 M, prepared from sodium hydroxide monohydrate) are mixed and ultrapure water is added to reach the desired dilution. A small fraction of the electrolyte is separated to measure the pH with a pH meter (PC 5000 L, *VWR International GmbH*, Germany) without contaminating the stock solution. The pH can thereafter be adjusted by further addition of the acid or base component.

Cell Assembly.—For RDE measurements, the acid (Figure 13d) or alkaline (Figure 13a) cell setup is assembled. To avoid contamination of the clean components, they are only handled with special gloves, are not allowed to be in contact with any non-clean environments and are placed on a clean, lint-free cloth.

After inserting the side compartments into the main vessel, the electrolyte is filled into the cell and the reference electrode (e.g., RHE or Ag/AgCl reference electrode) is inserted into the side compartment. The use of certain reference electrodes (e.g., Ag/AgCl in sat. KCl) requires their separation from the main compartment by an electrolyte bridge (see Figure 13a) to avoid contamination of the electrolyte with ionic species. Note, that the reference electrode potential has to be determined to convert the measured potential to the RHE scale. The calibration procedure is described at the end of the following section. The Pt counter electrode is immersed into the remaining compartment of the cell (separated by a Vycor frit in acid solution), the assembly is closed with the PTFE lid and purged with Ar (6.0 grade, *Westfalen AG*, Germany). The working electrode is screwed into the polyetheretherketone (PEEK) shaft by holding it with a lint-free cloth on the sides and taking care that the shaft is not in contact with the lid. After finishing the assembly process, the cell has to be inspected to identify gas bubbles that block electrolyte pathways, especially below the working electrode and in the side compartments of the cell. If the gas bubble cannot be removed from the coating, the electrode is taken out of the solution, turned upside down and a droplet of ultrapure water is

placed on the coating. After a waiting time (on the order of 30 minutes), the electrode can be re-inserted into the electrolyte.

2.2.2. Measurement Execution and Data Evaluation

In the following, the measurement procedure for the determination of the *ECSA*, the ORR activity and the HOR kinetics are described for a Pt/C catalyst.

Electrochemical Catalyst Cleaning.—Most measurement procedures include an electrochemical pre-treatment to clean the catalyst's surface by cycling the potential in a predefined window. The anodic and cathodic potential limits have to be chosen appropriately for each catalyst, so that the desired surface morphology remains unaltered while a sufficient cleaning effect is observed. During the potential cycling, the surface is repeatedly oxidized and reduced, which causes a reorganization of the surface, an oxidation of adsorbates (e.g., organic contaminations) and the removal of adsorbates due to the formation of the oxide layer. For Pt, the electrochemical cleaning can typically be observed by a lowering of the anodic current at $E > 0.8\ V_{RHE}$ until a current plateau is observed, as well as an increase of the hydrogen adsorption (H_{ads}) / desorption (H_{des}) features (the process is often referred to as hydrogen under potential desposition, H_{upd}) at $E < 0.4\ V_{RHE}$, as shown in Figure 16a.

The cleaning process is completed as soon as no significant change of the features in the

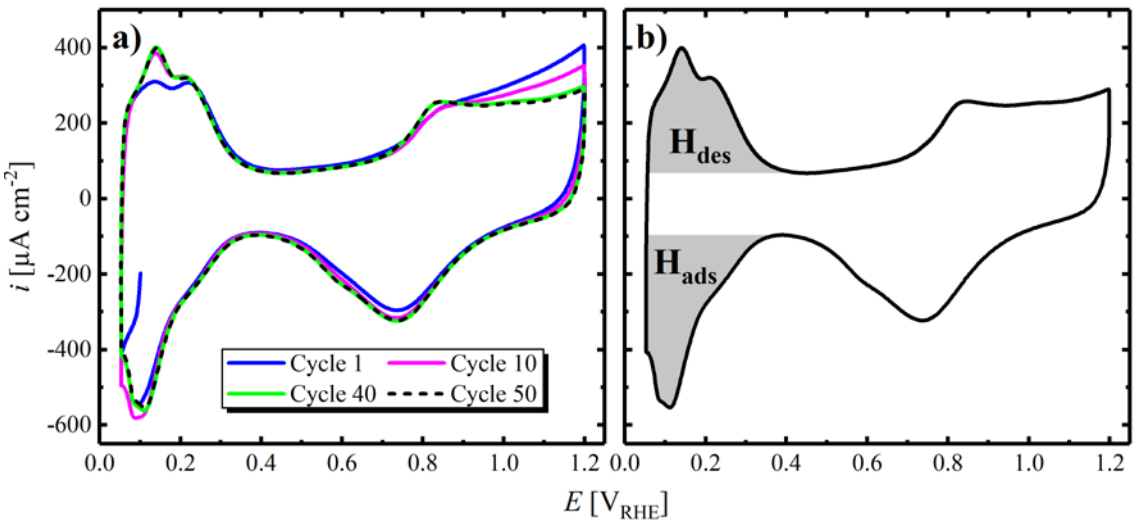

Figure 16. Cyclic voltammograms of a 20%$_{wt.}$ Pt/C catalyst (TEC10V20E, *Tanaka Kikinzoku Kogyo K.K.*, Japan) in Ar-saturated 0.1 M $HClO_4$ at a scan rate of 50 mV s^{-1} between 0.05 and 1.20 V_{RHE} at room temperature without rotation, showing a) subsequent potential cycles in the course of the electrochemical cleaning procedure and b) the integration of the H_{ads} and H_{des} features to evaluate the catalyst's *ECSA*. The loading on the GC disk is 9.3 $\mu g_{Pt}\ cm^{-2}$, resulting in a film thickness of 1 µm. The I/C ratio is 0.1 $g_I\ g_C^{-1}$.

voltammogram can be observed (assuming a suitable potential window), which is often achieved after approximately 10 – 20 cycles and shown in Figure 16a for cycle 40 and 50. Depending on the material stability, the potential window for different catalysts varies significantly, e.g., an anodic potential limit of 1.2 V_{RHE} is acceptable for Pt/C, whereas the stability of Ru@Pt core-shell particles requires to limit the potential to 0.8 V_{RHE} (see section 3.1.1) and completely different potentials between -0.35 and 0.15 V_{RHE} are used to clean a metallic Sn electrode (see section 3.3.1).

ECSA determination by H_{upd}.—Subsequently, the *ECSA* of the Pt/C catalyst is determined via integration of the H_{ads} and H_{des} charge. Since no significant contribution of the continuous HER is observed above ≈0.05 V_{RHE} at the measurement conditions for this catalyst, the charge of the pseudo-capacitive adsorption of hydrogen on Pt (Equation [16]) can be correlated directly to the *ECSA*.

$$Pt + H^+ + e^- \rightleftharpoons Pt\text{-}H_{ads} \qquad [16]$$

The maximum / minimum of the capacitive current (originating from charging of the electrochemical double layer) at potentials between ≈0.35 and ≈0.5 is used as a baseline for the integration, since it is independent of the potential and needs to be subtracted from the total charge to obtain the *ECSA*. Finally, the currents in the H_{des} and H_{ads} region are integrated, averaged and divided by the scan rate, υ (in units V s^{-1}), to yield the average charge of the H_{upd} process, C, according to the following equation.

$$C = \frac{H_{ads} + H_{des}}{2 \cdot \upsilon} \qquad [17]$$

To correlate this charge with the surface area of the catalyst, A_{Pt}, on the electrode (Equation [18]), the so-called specific charge, C_{spec}, of 210 µC cm^{-2} for a polycrystalline Pt surface is used.

$$A_{Pt} = \frac{C}{C_{spec}} \qquad [18]$$

Finally, the catalyst *ECSA* can be obtained (Equation [20]) by dividing the Pt surface area by the areal mass of Pt, m_{Pt}, (calculated according to Equation [19]; given in units of g_{Pt} cm^{-2}), which is linked to the electrode roughness factor by Equation [21].

$$m_{\mathrm{Pt}} = \frac{V_{\mathrm{coat}} \cdot m_{\mathrm{cat}} \cdot x_{\mathrm{Pt}}}{V_{\mathrm{ink}} \cdot A_{\mathrm{electrode}}} \quad [19]$$

Here, V_{coat} is the volume dropped on the disk with a pipette, m_{cat} is the total mass of catalyst in the ink, V_{ink} is the total ink volume, $A_{electrode}$ is the GC disk area and x_{Pt} is the Pt weight fraction in the catalyst.

$$ECSA = \frac{A_{\mathrm{Pt}}}{m_{\mathrm{Pt}}} \quad [20]$$

$$rf = ECSA \cdot m_{\mathrm{Pt}} \quad [21]$$

Exemplarily, all relevant values for the measurement shown in Figure 16b are provided in Table IV, resulting in an *ECSA* of 62.1 $m^2_{Pt}\ g^{-1}_{Pt}$ and a *rf* of 5.8 $cm^2_{Pt}\ cm^{-2}$.

Table IV. Experimental values needed to calculate the *ECSA* and *rf* for the measurement shown in Figure 16, including the integrated H_{ads} and H_{des} area, the scan rate, υ, the specific charge for the H_{upd} process on Pt, C_{spec}, the mass of catalyst in the ink, m_{cat}, the volume of the ink, V_{ink}, and the electrode area, $A_{electrode}$.

H_{ads}	H_{des}	υ	C_{spec}	V_{coat}	m_{cat}	x_{Pt}	V_{ink}	$A_{electrode}$
µA V cm^{-2}	µA V cm^{-2}	mV s^{-1}	µC cm^{-2}_{Pt}	µL	mg	$\%_{wt.}$	mL	cm^2
62.9	58.9	50	210	6.5	3.8	20	2.7	0.196

ECSA determination by CO stripping.—If the *ECSA* determination by the H_{upd} method is not sufficiently accurate (e.g. at a low Pt loading), not well defined (e.g., for certain Pt alloys) or not possible (e.g., due to the lack of the H_{ads} process on certain metals), the *ECSA* can alternatively be determined by the CO stripping procedure. To start the measurement, CO (4.8 grade, *Westfalen AG*, Germany) is purged through the electrolyte solution (typically for 3 min) to be adsorbed on the catalyst surface at a low applied potential (e.g., 60 mV_{RHE}). As shown in Equation [22], the adsorption process of CO on Pt does not involve the transfer of an electron, hence no adsorption current is observed during the potentiostatic phase (note that the current peak right after initiating the CO purging originates from the displacement of previously adsorbed species).

$$Pt + CO \rightarrow Pt\text{-}CO_{ads} \quad [22]$$

While maintaining the potential constant, CO is removed from the solution by Ar (6.0 grade, *Westfalen AG*, Germany) purging for approximately 30 min to avoid oxidative currents from continuous CO oxidation in the anodic scan.

Finally, a cyclic voltammogram (CV) is executed from the holding potential in anodic direction to oxidize the adsorbed CO according to Equation [23].

$$Pt\text{-}CO_{ads} + H_2O \rightarrow Pt + CO_2 + 2H^+ + 2e^- \qquad [23]$$

The oxidation of CO results in an anodic peak (see Figure 17, black line). The peak potential for different metals, alloys or crystal facets varies significantly and is often used to characterize the surface of newly developed catalysts (c.f., section 3.1.1). To discriminate the CO oxidation charge from other currents in this potential range (i.e., Pt oxidation and double layer charging), a second scan is recorded with the same upper potential limit (Figure 17, blue line) and used as a baseline for the integration. The resulting integral can be used to estimate the catalyst *ECSA* analogous to the calculations for the H_{upd} method provided above, using a specific charge of 420 µC cm^{-2} (transfer of 2 e^-) for CO stripping. The integral shown in Figure 17, is 24.3 µA V cm^{-2}, resulting in an *ECSA* of 62.0 m^2_{Pt} g^{-1}_{Pt} and an *rf* of 5.8 cm^2_{Pt} cm^{-2}, i.e., the same value as for the H_{upd} method.

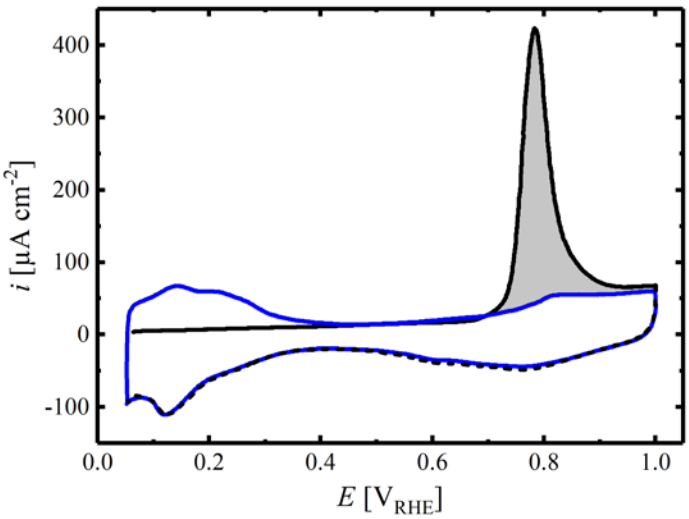

Figure 17. CV of a 20%$_{wt.}$ Pt/C catalyst (TEC10V20E, *Tanaka Kikinzoku Kogyo K.K.*, Japan), showing the CO oxidation in the anodic scan (solid, black line), the following cathodic scan (dashed, black line) and the subsequent cycle (blue line), used as a baseline for the integration. The CV employs a scan rate of 10 mV s^{-1} between 0.05 and 1.20 V_{RHE} in stagnant, Ar-saturated, 0.1 M $HClO_4$ at room temperature. The loading on the GC disk is 9.3 µg_{Pt} cm^{-2}, resulting in a film thickness of 1 µm. The I/C ratio is 0.1 g_I g^{-1}_C.

Evaluation of the ORR Activity.—In the following section, the determination of the ORR mass and specific activity is described for a Pt/C catalyst. Since contaminants are released into the electrolyte during the electrochemical cleaning procedure, the previously used electrolyte is exchanged with a fresh one beforehand. Then, the solution is saturated by purging O_2 for approximately 10 min, subsequently recording a CV at the desired scan rate and rotation rate.

In the course of the cathodic going scan (blue line in Figure 18a), the current increases due the higher applied ORR overpotential. This increase slows down at higher ORR currents (> 3 mA cm^{-2}) due to the arising O_2 mass-transport limitations from the bulk of the solution towards the surface of the disk. The maximum transport rate at the chosen conditions is expressed as a current plateau (so-called limiting current, i_{lim}), where the O_2 concentration at the surface of the disk approaches zero. As shown in Figure 18a, the current at the same potential (in the kinetic region) is higher in the anodic scan (black) compared to the cathodic scan. This hysteresis originates from the removal of hydroxide / oxide species on Pt at low potentials, hence a higher measured ORR activity on the metallic surface. Since most ORR activity values reported in the literature use the anodic scan for their analysis, this method is also employed here. Furthermore, adsorption

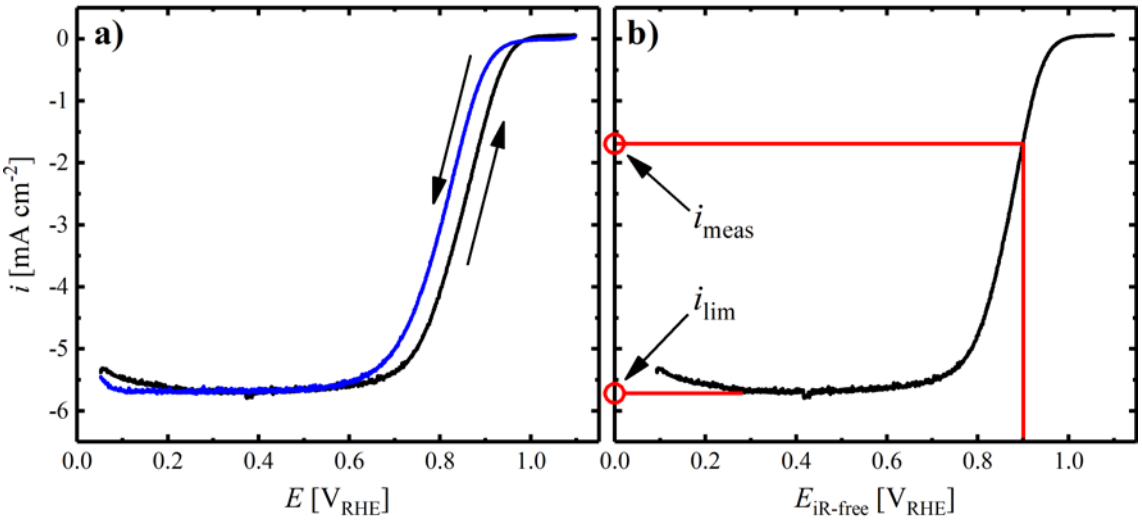

Figure 18. a) Anodic (black) and cathodic (blue) scan (direction indicated by an arrow) of a CV in O_2-saturated, 0.1 M $HClO_4$ at a scan rate of 10 mV s^{-1} between 0.05 and 1.10 V_{RHE}, applying a rotation rate of 1600 rpm at room temperature. The loading of the 20%$_{wt.}$ Pt/C catalyst (TEC10V20E, *Tanaka Kikinzoku Kogyo K.K.*, Japan) on the GC disk is 9.3 μg_{Pt} cm^{-2}, resulting in a film thickness of 1 µm. The I/C ratio is 0.1 g_I g_C^{-1}. b) Anodic scan corrected for the *iR*-drop (≈39 Ω for the 0.2 cm^2 disk in this measurement) in order to extract the measured current at 0.9 V_{RHE}, i_{meas}. The limiting current, i_{lim}, is indicated by an arrow.

phenomena have to be considered with respect to the choice of the scan rate, since the time dependent surface oxidation is more pronounced at low scan rates, leading to a lower measured ORR activity. Moreover, many contaminants are adsorbed in the low potential region, hence scanning slower provides more time for these species to negatively impact the measurement. However, slow scan rates provide the advantage that the ratio between the faradaic ORR current and the capacitive / pseudo-capacitive currents (double layer charging, oxide formation) is higher, enabling a more accurate estimation of the ORR activity. In general, fast rotation provides higher O_2 mass-transport towards the electrode, hence a lower influence of the O_2 mass-transport overpotential. Nevertheless, very high rotation rates can induce turbulent flow within the electrolyte or lead to partial detachment of the catalyst layer from the GC disk. A good tradeoff between all of these considerations is to rotate at 1600 rpm and apply a scan of 10 mV s^{-1}, as shown in Figure 18a.

For the evaluation, the measured potential, *E*, in the anodic scan is corrected for the *iR*-drop according to Equation [24] to obtain the *iR*-free potential, $E_{iR\text{-free}}$, and the current at 0.9 V_{RHE} is extracted (c.f., Figure 18b). The solution resistance can be determined by electrochemical impedance spectroscopy (EIS), as the high frequency x-axis intersect in a Nyquist plot (the determination of the high frequency resistance, R_{HFR}, in RDE is analogous to PEMFCs, described in section 2.3.3).

$$E_{iR-\text{free}} = E - i \cdot R_{HFR} \quad [24]$$

To compensate for capacitive charging, the current of the anodic scan of a CV at the same scan rate in inert atmosphere, i_{cap}, is subtracted from the extracted ORR current (see Equation [25]) and diffusion effects are taken into account by correction for the measured limiting current, i_{lim} according to Equation [26] to obtain the kinetic current, i_{kin}.

$$i_{\text{corr}} = i_{\text{meas}} - i_{\text{cap}} \quad [25]$$

$$i_{\text{kin}} = \frac{i_{\text{corr}} \cdot i_{\text{lim}}}{i_{\text{lim}} - i_{\text{corr}}} \quad [26]$$

Finally, the specific ORR activity, $i_{spec}^{0.9\,V}$, can be calculated by division of the transport- and *HFR* corrected geometric ORR current density, i_{kin}, by the roughness factor (Equa-

tion [27]), which is related to the ORR mass activity, $i_{mass}^{0.9\,V}$, through the *ECSA* (Equation [28]).

$$i_{spec}^{0.9\,V} = \frac{i_{\mathrm{kin}}}{rf} \quad [27]$$

$$i_{mass}^{0.9\,V} = i_{spec}^{0.9\,V} \cdot ECSA \quad [28]$$

As an example for the data treatment, the values necessary to calculate the ORR activity of the measurement provided in Figure 18 are given in Table V.

Table V. Values to calculate the ORR activity for the measurement in Figure 18, including the extracted current at 0.9 V_{RHE}, i, the capacitive current, i_{cap}, the limiting current, i_{lim}, as well as the *rf* and *ECSA* values.

i_{meas}	i_{cap}	i_{lim}	*rf*	*ECSA*	$i_{spec}^{0.9\,V}$	$i_{mass}^{0.9\,V}$
mA cm^{-2}	µA cm^{-2}	mA cm^{-2}	cm_{Pt}^{2} cm^{-2}	m_{Pt}^{2} g_{Pt}^{-1}	µA cm_{Pt}^{-2}	A g_{Pt}^{-1}
1.7	50.0	5.7	5.8	62.1	400	249

Determination of the HOR/HER Kinetics.—Similar to the evaluation of the ORR activity, this section presents the individual steps to obtain the HOR/HER exchange current density of Pt/C in alkaline media. Note that a determination of the HOR/HER kinetics on Pt in acid is not feasible via the RDE method for most catalysts due to very fast reaction kinetics and the quickly arising H_2 mass-transport overpotentials in liquid electrolyte. To determine the HOR/HER exchange current density in alkaline electrolyte, the electrolyte solution (after catalyst cleaning and electrolyte exchange as described in the previous section) is saturated with pure H_2 and a CV is executed (as for the ORR, a scan rate of 10 mV s^{-1} and a rotation rate of 1600 rpm is reasonable), shown in Figure 19a. In contrast to measurements of the ORR activity, the hysteresis between the anodic and cathodic scan of the CV is small for the determination of the HOR/HER kinetics (no change of the surface oxidation state). However, the cathodic going branch of the CV is commonly evaluated to limit the influence of adsorbed contaminants in the low potential region. The kinetic current can be obtained by correction for diffusion effects according to Equation [29], where *r* is the HOR/HER reaction order (assumed to be 0.5 for Pt).[102] While the here-described method, established by Rheinländer et al., only applies this correction to the HOR branch (positive currents),[102] Zheng et al. proposed to correct both the HOR and the HER branch (negative currents).[119]

$$i_{\mathrm{kin}} = i \cdot \left(1 - \frac{i}{i_{\mathrm{lim}}}\right)^{-r} \qquad [29]$$

The measured potential is corrected for the *iR*-drop (Equation [24]) and the potential shift due to the depletion of H_2 at the surface of the electrode is taken into account by the following equation to obtain the fully corrected potential, $E_{iR-\mathrm{free}}^{\eta_{\mathrm{diff}}-\mathrm{free}}$. In this, *R* is the ideal gas constant (8.3 V A s mol^{-1} K^{-1}), *F* is the Faraday constant (96485.3 A s mol^{-1}) and *T* is the temperature (298 K).

$$E_{iR-\mathrm{free}}^{\eta_{\mathrm{diff}}-\mathrm{free}} = E_{iR-\mathrm{free}} + \frac{R \cdot T}{2 \cdot F} \ln\left(1 - \frac{i}{i_{\mathrm{lim}}}\right) \qquad [30]$$

To obtain the HOR/HER exchange current density, i_0, the corrected data can be fitted to the Butler-Volmer equation (Equation [31]), as shown in Figure 20b). In this case, the overpotential, η, is the fully corrected potential and α_a / α_c are the anodic / cathodic transfer coefficients. Note that the fitting range should ideally cover at least one *TS* to be significant (partially fulfilled in Figure 20b), whereby owing to the inaccuracies of the transport corrections, only currents within ≈70% of i_{lim} should be considered for the analysis.

$$i_{\mathrm{kin}} = i_0 \cdot rf \cdot \left(e^{\frac{\alpha_a \cdot F}{R \cdot T} \cdot \eta} - e^{-\frac{\alpha_c \cdot F}{R \cdot T} \cdot \eta}\right) \qquad [31]$$

In the so-called micro-polarization region ($|\eta| \leq 5$ mV), Equation [31] can be linearized by assuming $e^x \approx 1 + x$, resulting in the following correlation (c.f., Figure 20a):

$$i_{\mathrm{kin}} \approx i_0 \cdot rf \cdot \frac{(\alpha_a + \alpha_c) \cdot F}{R \cdot T} \cdot \eta \qquad [32]$$

The fit of the fully corrected data according to the described procedure is shown for the micro-polarization region in Figure 20a and the Butler-Volmer fit is given in Figure 20b).

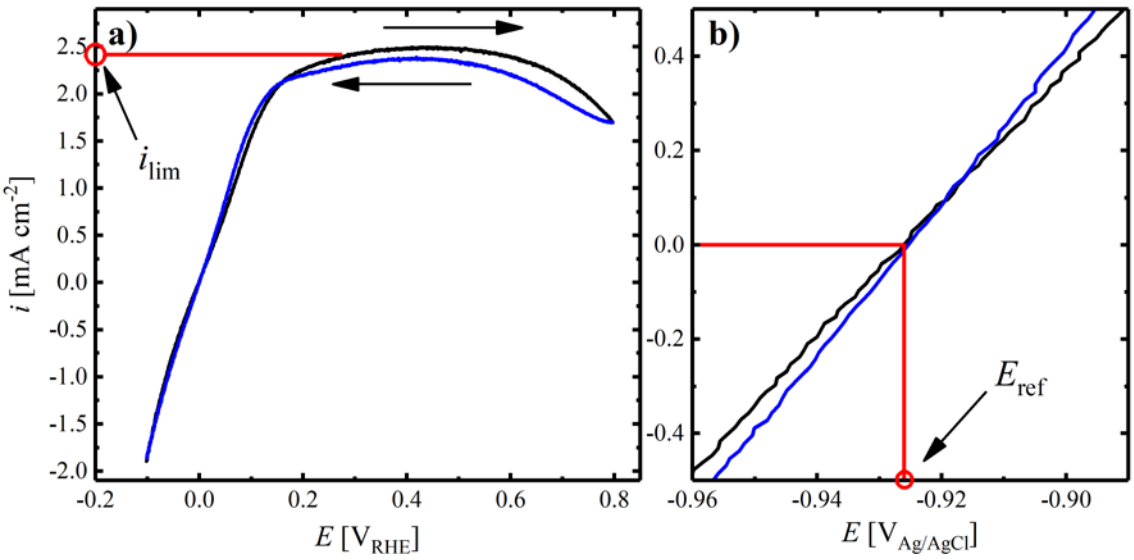

Figure 19. a) Anodic (black line) and cathodic (blue line) scan (direction indicated by an arrow) of a CV in H_2-saturated, 0.1 M NaOH at a scan rate of 10 mV s^{-1} between -0.1 and 0.8 V_{RHE}, applying a rotation rate of 1600 rpm at room temperature. The noble metal loading of the Ru@Pt core-shell catalyst (0.3 MLE, 8.5%$_{wt.}$ noble metal on Vulcan carbon, see Schwämmlein et al. for detailed information)[111] on the GC disk is 1.3 μg_{NM} cm^{-2}, with a corresponding Pt loading of 0.4 μg_{Pt} cm^{-2}, resulting in a film thickness of 0.4 µm. The I/C ratio is 0.15 g_I g_C^{-1}. The limiting current, i_{lim}, is indicated by an arrow. b) Zoom-in of the potential measured versus the reference electrode (Ag/AgCl, sat. KCl) to determine the reference electrode potential, E_{ref}, for the potential correction to the RHE scale.

As a result of the data evaluation, Table VI lists the HOR/HER exchange current density, including the individual transfer coefficients, derived from the Butler-Volmer fit in Figure 20b, as well as the slope of the linear fit in the micro-polarization region in Figure 20a. Even though the exchange current density values obtained by the micro-polarization approach and the Butler-Volmer fitting should ideally be identical, the two methods are suspected to different uncertainties originating from the applied corrections in the different current regimes. In addition, the *ECSA* and *rf* values for the measurement are given to calculate i_0 for the micro-polarization fit. Note, that the evaluation of the micro-polarization region according to Equation [32] can only yield the desired i_0 if the sum of alphas is known (e.g., by prior fitting of the data to the Butler-Volmer equation).

Table VI. Values to calculate i_0 for the measurement in Figure 20, including the *ECSA* and *rf* values, as well as the result of the Butler-Volmer fit and the linear fit in the micro-polarization region.

rf	***ECSA***	i_0 **(BV)**	α_a	α_c	**Slope (micro-pol)**	i_0 **(micropol)**
cm^2_{NM} cm^{-2}	m^2_{NM} g^{-1}_{NM}	mA cm^{-2}_{NM}	-	-	mA cm^{-2}_{NM} V^{-1}	mA cm^{-2}_{NM}
1.3	100.9	0.6	0.6	0.4	16.1	0.4

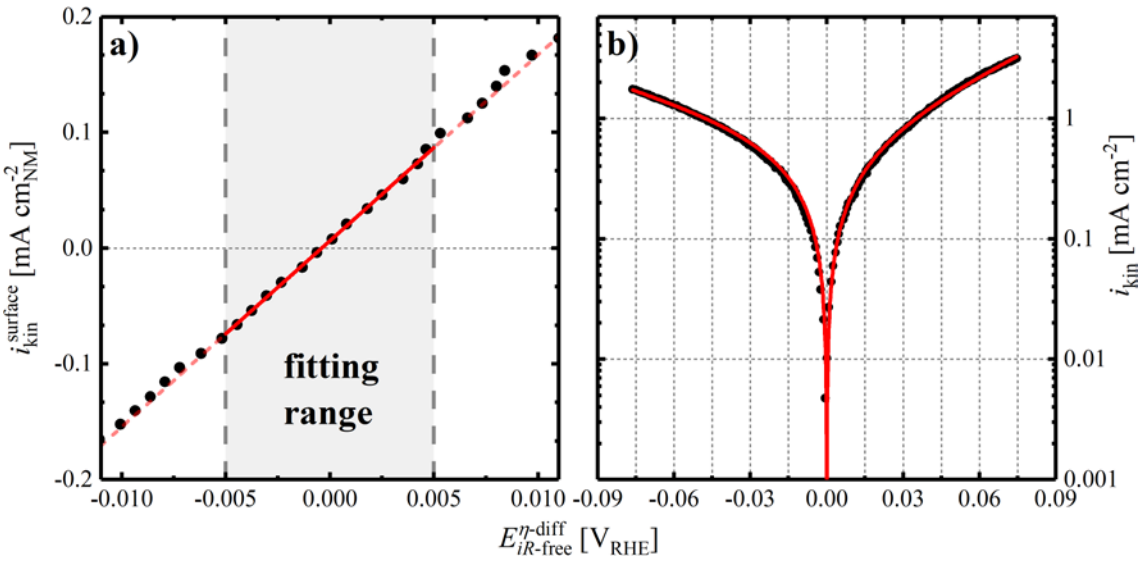

Figure 20. a) Micro-polarization region, including the linear fit (red line) showing the kinetic current versus the fully corrected potential of the cathodic scan of the CV shown in Figure 19 (black circles), recorded on a Ru@Pt core-shell catalyst (0.3 MLE, 8.5%$_{wt.}$ noble metal on Vulcan carbon, see Schwämmlein et al. for detailed information)[111] in H_2-saturated, 0.1 M NaOH between -0.1 and 0.8 V_{RHE} at 10 mV s^{-1}, 1600 rpm and room temperature. The noble metal loading on the GC disk is 1.3 μg_{NM} cm^{-2}, with a corresponding Pt loading of 0.4 μg_{Pt} cm^{-2}, resulting in a film thickness of 0.4 µm. The I/C ratio is 0.15 g_I g_C^{-1}. b) Butler-Volmer fit (red line) according to Equation [31] for the same data set (black circles). The figure is based on data recorded in the frame of the publication presented in section 3.1.1.[111]

Reference Electrode Calibration.—For RDE measurements, the actual reference electrode potential has to be determined at the end of the experiment to ensure a valid conversion of the measured potential to the desired scale (e.g., RHE). The calibration procedure should also be executed when an RHE reference electrode is used, since these electrodes often show a small potential shift (e.g., due to residual O_2 in the reference electrode compartment). The calibration can be accomplished by recording a CV of a Pt electrode (commonly polycrystalline Pt disk or Pt ring) in H_2-saturated electrolyte. For simplicity, the example provided in this thesis is a CV of the Ru@Pt catalyst (Figure 19b). In this CV, the potential at 0 A is extracted for the anodic and cathodic scan (essentially the same in Figure 19b) and the average is subtracted from the measured potential to convert the potential to the RHE scale. If the 0-crossing varies in subsequent cycles, the electrode has to be cleaned (e.g., electrochemically by CVs) and the procedure is repeated.

2.3. Single Cell Fuel Cell Testing

This section describes the preparation procedure for single cell PEMFC and AEMFC tests, including the preparation of the MEA, as well as the cell setup and assembly for various measurements. Furthermore, a detailed guide for a full voltage loss analysis of the H_2/air performance is given, consisting of ORR activity determination, current and potential corrections for the H_2 crossover, the ohmic short of the membrane and the *iR*-drop, measurement of the proton conduction resistance in the cathode and the O_2 mass-transport resistance. Information regarding the experimental details on fuel cell operating conditions and the measurement procedures used to obtain the data presented in chapter 3 can be retrieved from the individual publications.

2.3.1. MEA Fabrication Procedure

A detailed description of the MEA fabrication process for PEMFCs in our laboratory was recently published in the doctoral thesis of Gregor Harzer.[120] Therefore, the description of the MEA preparation process in this thesis is given for an AEMFC and differences compared to PEMFCs are detailed at the end of this section. All MEAs used in this thesis are fabricated by the decal transfer method in three general steps: ink preparation, coating, hot pressing. Typical formulations to produce 10 mL of an AEMFC and 5 mL of a PEMFC ink are shown in Table VII, where all values are adjustable to the desired quantity by simple scaling. First of all, the ionomer (FAA-3, solid ionomer sheet in the Br^- form, *Fumatech GmbH*, Germany) is dissolved in a mixture of 90%$_{wt.}$ 2-propanol (Chromasolv Plus, 99.9%, *Sigma Aldrich Corp.*, Germany) and 10%$_{wt.}$ H_2O (18.2 MΩ, MilliQ Ingegral, *Merck Millipore KGaA*, Germany) using a 15 mL capped

Table VII. Typical ink formulation to prepare MEAs with a loading of 0.4 mg_{Pt} cm^{-2}, using the FAA-3 ionomer (solid ionomer sheet in the Br^- form, *Fumatech GmbH*, Germany) for AEMFCs and a PFSA-based ionomer (20%$_{wt.}$ in 79%$_{wt.}$ H_2O and 1%$_{wt.}$ 1-propanol) for PEMFCs. Both inks employ a commercially available 47%$_{wt.}$ Pt/C catalyst (TEC10V50E, *Tanaka Kikinzoku Kogyo K.K.*, Japan). As a solvent, 2-propanol is used for AEMFCs, whereas 1-propanol is used for PEMFCs. All required masses, *m*, the desired ink volume, *V*(ink), as well as the resulting carbon content in the ink, x_C, and the I/C ratio in the final electrode are given below.

	***m*(Pt/C)**	***m*(solvent)**	***m*(H_2O)**	***V*(ink)**	x_C	***m*(ionomer)**	**I/C**
	mg	g	g	mL	mg mL^{-1}	g	g_I g_C^{-1}
AEMFC	940.0	6.7	0.7	10.0	50.0	0.4	0.8
PEMFC	280.0	3.6	0	5.0	30.0	0.5	0.65

HDPE bottle (quantities according to Table VII). A simple way to dissolve the solid ionomer is to wrap the vial with Parafilm (*Sigma Aldrich Corp.*, Germany) and place it onto a roller mill at a low mixing speed (60 rpm, Ratek BTR5-12V, *Ratek Instruments Pty. Ltd.*, Australia). This procedure results in an ionomer solution of ≈5%$_{wt.}$ before addition of the catalyst powder. In the meantime, the appropriate amount of catalyst (47%$_{wt.}$ Pt/C, TEC10V50E, *Tanaka Kikinzoku Kogyo K.K.*, Japan) is weighed into a separate high density polyethylene (HDPE) bottle, already containing 15 g of ZrO_2 beads (5 mm, *Glen Mills Inc.*, USA), using a disposable plastic spatula. After full dissolution of the ionomer in the solvent mixture, the two vials are transferred into inert atmosphere (e.g., using a N_2 purged glovebox), opening the lids to release the O_2 from the interior. Thereafter, the dissolved ionomer is poured at once into the Pt/C containing vial to wet the catalyst and avoid ignition. Weighing the vial before and after the transfer yields the total amount of ionomer and solvent to be used for the calculation of the I/C ratio in the final catalyst layer. After the transfer, the closed vial is wrapped with Parafilm and placed onto the roller mill for 24 h at 60 rpm and ambient temperature (25°C).

Before the mixing process is finished, several decal sheets are cut to the appropriate size and placed on clean glass plates. For AEMFC inks based on the FAA-3 ionomer, hydrophobic decals (e.g., virgin PTFE or PTFE-coated fiberglass, *Fiberflon GmbH & Co. KG*, Germany) do not yield acceptable coating results with the explored ink formulations, whereas homogeneous films are obtained on etched fluorinated ethylene propylene (FEP, extruded, *Angst+Pfister GmbH*, Switzerland). Since a flat surface is essential to obtain acceptable coatings, air bubbles and wrinkles are removed prior to fixing the decal sheet by repeated, outwards-directed wiping with a tissue, wetted with 2-propanol. After cleaning both sides of the decal sheet with 2-propanol, it is fixed to the glass plate by a single piece of tape on the top over the entire width. Subsequently, the Mayer rod coater (K Control Coater, *RK PrintCoat Instruments Ltd.*, England) is aligned to the appropriate height with the calibration bar and the desired coating bar is placed into the machine without additional weights on the sides of the bar. For the coating, the ink is dropped in a line next to the coating bar with a disposable plastic pipette and the automatic coating process is initiated immediately afterwards at a slow speed (machine set-

ting of one). After the coating process is finished, the glass plate can be removed from the machine and dried horizontally at ambient temperature in a rack, covered on top to avoid the settling of dust on the coating. As soon as all of the solvent has evaporated (typically overnight), decals with the appropriate size (5 or 50 cm^2) are cut out from the coating with a cutting tool (blades facing the coating) in a hydraulic press (*Collin Lab & Pilot Solutions GmbH*, Germany) at low pressure, using a PE block as counterpart for the blades (*Spahn GmbH & Co. KG*, Germany). Areas with a lower Pt/C loading (e.g., at the edges and at the end of the coating) can be identified by shining light through the glass plate to illuminate the bottom of the decal. Coatings that employ the FAA-3 ionomer are not dried in an oven after the room temperature drying step to avoid the formation of wrinkles and to keep the decal flat.

MEAs for AEMFC are prepared by hot pressing two decal sheets to a piece of membrane (Tokuyama A201, *Tokuyama Corp.*, Japan), using Kapton (*Du Pont Corp.*, USA) as a protecting layer on both sides and foamed PTFE (Gylon Style 3545 Soft, *Garlock GmbH*, Germany) as a pressure distribution medium. The membrane can be labeled with a regular ballpoint pen on the bottom, marking the anode and cathode side. The Kapton sheets are cleaned (e.g., on a glass plate) on both sides with 2-propanol and a tissue (Kimwipe, *Sigma Aldrich Corp.*, Germany) to ensure that they are free of dust particles and one of the sheets is placed on top of a piece of Gylon (e.g., 10 x 10 cm for 50 cm^2 and 7 x 5 cm for 5 cm^2 MEAs), already resting on the aluminum plate for hot pressing. A decal sheet is put face-up on the Kapton foil and covered with the membrane, placing a second decal face-down on top of the other one. The two decals should be reasonably aligned to each other and the entire assembly has to be flat in order to ensure a good decal transfer. The second Kapton layer can now be placed on top, contacting at one side to gently roll the sheet down without altering the position of the decals on the membrane. Finally, the second Gylon layer is put on top of the Kapton foil, finishing the assembly by placing the second hot pressing plate on top. In case of electrostatic interaction between the various layers, the electrostatic charge has to be removed from the Kapton foil beforehand. The stack is then put into the already preheated hot press at a temperature of 110°C, which is applied for 10 min at a pressure of 1 kN cm^{-2}. After the press has opened, the hot assembly is taken out and directly opened to peel the decal foil from the MEA. The electrode loading can be determined by sub-

tracting the weight of the empty decals from the value before the transfer, and the MEA can be stored in between the Kapton foils.

Before the use of the MEA in an AEMFC test, it is taken out of the protecting layers and placed into a plastic beaker, already containing a solution of 1 M Na_2CO_3 (anhydrous, for analysis, *Sigma Aldrich Corp.*, Germany). The MEA is fully submerged in the solution for 24 h and the ion exchange is repeated 3 times with a fresh solution. Since MEAs for AEMFCs are handled in ambient air, the exchange of all ionic groups in the ionomer phase to OH^- has no advantage compared to the exchange with CO_3^{2-} due to the rapid neutralization reaction with CO_2. After completion of the ion exchange, the MEA is thoroughly rinsed with ultrapure water and stored in water for at least 24 h. The ion exchange according to this procedure is necessary to convert all ionic groups of the FAA-3 ionomer from the Br^- form in which it is delivered to the (bi-)carbonate form (the Tokuyama A201 membrane is already delivered in (bi-)carbonate form).

In general, the MEA fabrication procedure for PEMFC tests is very similar to that described above and the differences are shortly described in the following. First of all, the ionomer is commonly not purchased as a solid, but as a solution of an alcohol (e.g., 1-propanol), H_2O and the PFSA ionomer. Hence, the ink components are mixed in a different order: The appropriate amount of H_2O is dropped onto the catalyst (weighed into a HDPE bottle, already containing 16.5 g ZrO_2 beads), the bottle is closed and transferred into inert atmosphere, together with a second bottle which contains solely the solvent (bottle and solvent weight known). After releasing the air from the bottles, the solvent is added to the catalyst at once and the empty bottle is weighed to determine the missing amount of solvent. Finally, the ionomer solution is added to the ink with a pipette. In contrast to AEMFC inks, the mixing time is 18 h and the ink is coated on virgin PTFE decals. Furthermore, the coatings are dried first at room temperature overnight, cut out and subsequently dried at 80°C for ≈1 h before hot pressing at 155°C for 3 min at 0.11 kN cm^{-2}. Since most PFSA membranes and ionomers are delivered in the H^+ form, no ion exchange is necessary for those MEAs.

2.3.2. Cell Hardware and Assembly

The cell setup for fuel cell testing consists of aluminum endplates with integrated rod heaters (6.5 mm diameter, 100 mm length, 250 W, *Horst GmbH*, Germany), Au-coated Cu current collector plates, graphite flow fields (*Poco Graphite, Entegris GmbH*, Germany), gas in- and outlets, as well as electrical connections for the voltage sense cables and the current lead cables, shown schematically in Figure 21 with an MEA, GDLs and gaskets. The voltage sense cables are inserted horizontally into the flow fields and the current lead cables are connected vertically to the current collector plate to minimize interference in impedance measurements. The temperature sensor is inserted into the top of the graphite flow field to measure the temperature in the center of the active area. Cell cooling is achieved by fans on both sides of the setup. The common gas operating mode is counter-flow with heated gas inlets (20°C above cell temperature).

Different types of single cell fuel cell test hardware are used for the experiments described in this thesis, with an active area of 5 or 50 cm^2. While 50 cm^2 cells are used for SUSD and conductivity measurements at low temperature, 5 cm^2 tests are utilized for accelerated stress test measurements. The advantages of a large active area are fewer edge effects and measurements closer to the actual application, where active areas on the order of hundreds of cm^2 are employed. However, the easily achievable differential-flow conditions and the low amount of catalyst needed for small scale tests offer great

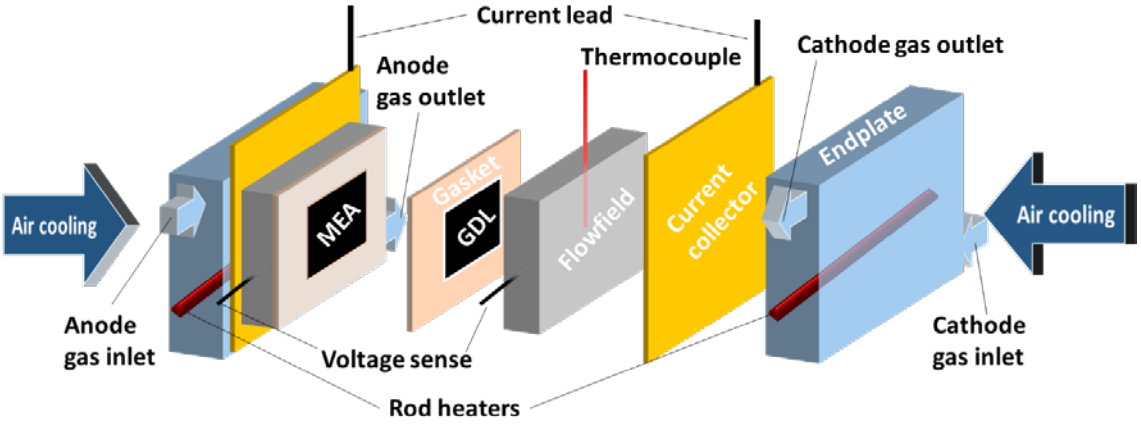

Figure 21. Schematic single cell fuel cell testing setup including aluminum endplates with rod heaters, Au-coated Cu current collectors, graphite flow fields, PTFE-coated fiberglass gaskets and the MEA with GDLs. To enhance electrical conductivity, GDLs were placed between the endplates and current collectors.

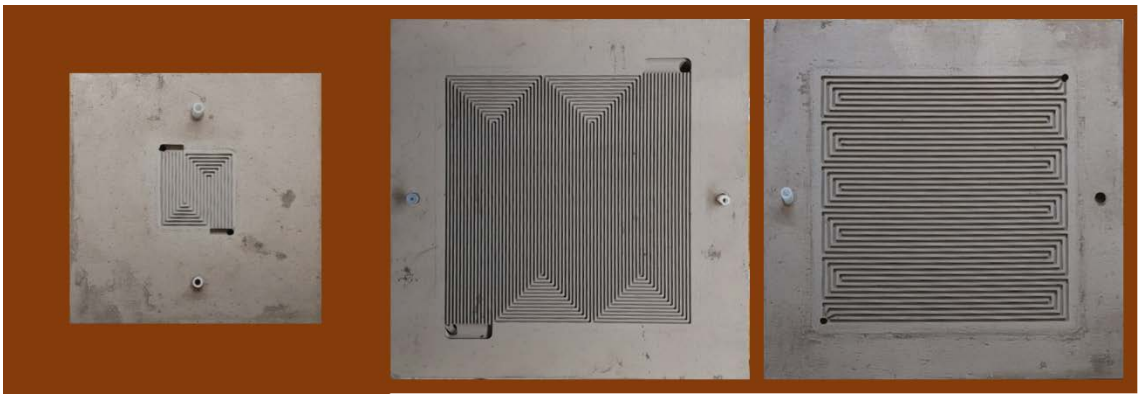

Figure 22. Graphite flow fields for single cell fuel cell testing with an active area of a) 5 cm^2 and 7 parallel channels b) 50 cm^2 and 14 parallel channels, and c) 50 cm^2 with 4 parallel channels.

possibilities for research purposes. Figure 22 shows the flow field types used in this study, including a) 5 cm^2 flow fields with 7 parallel channels in serpentine arrangement for differential-flowmeasurements (0.5 mm wide lands and channels), b) 50 cm^2 flow fields with a similar style, but 14 parallel channels at a width and depth of 0.5 and 0.8 mm, respectively, separated by 0.5 mm wide lands, and c) 50 cm^2 flow fields with 4 parallel channels (0.79 mm wide and 1.0 mm deep channels and 0.8 mm wide lands) in serpentine arrangement.

For assembly, the hardware is placed on a holder and the screws in the endplate are untightened to open the cell, leaving the flow field on top, as shown schematically in Figure 21 (left side without MEA and gasket). The anode gasket (Fiberflon, *Fiberflon GmbH & Co. KG*, Germany) is placed on the flow field, inserting the GDL facing the MEA with the MPL in the free area in the center of the gasket. To minimize the occurance of occasionally shortened membranes after assembly, the GDL and gasket burr should face the flow field instead of the membrane (when cutting the GDL, the blades have to face the MPL). In a reasonable alignment of the active area and the GDL, the MEA is placed on top of the stack, is covered with another GDL and a gasket from the top and the cell is closed with the remaining parts. The alignment pins (c.f., Figure 22), together with pre-punched holes in the gaskets and membrane ensure a well-aligned setup. In this assembly, the contacting pressure of the flow field and the GDL / MEA (typically on the order of 1.5 MPa) is achieved by the choice of the appropriate gasket thickness. A typical value for the GDL compression, *C*, is 20%, calculated for the

thickness values, *t*, of the individual components according to Equation [33]. For detail discussion, see Simon et al.[52]

$$C = \left(1 - \frac{\left(t_{gasket}^{anode} + t_{gasket}^{cathode}\right) \cdot 0.93 - t_{electrode}^{anode} - t_{electrode}^{cathode}}{t_{GDL}^{anode} + t_{GDL}^{cathode}}\right) \cdot 100\% \qquad [33]$$

However, a pressure distribution test (e.g., using Prescale Super Low, *Fujifilm Corp.*, Japan) should be carried out for every combination of flow fields and GDLs to ensure a good contact resistance and compression homogeneity of the final assembly. To identify shortened MEAs after assembly, the electrical resistance between the two current collectors is measured, where typical values on the order of 5 – 10 kΩ cm^2 are obtained with a lower threshold of ≈1 kΩ cm^2 for useable MEAs.

2.3.3. Voltage Loss Analysis for H_2/air Performance

In the following, the procedure to measure the voltage loss contributors of a H_2/air polarization curve is described (c.f., Figure 6, section 1.3). Note, that the conditions of the measurements in chapter 3 are not given here, but can be retrieved from the corresponding publications.

ORR activity determination in PEMFCs.—After the MEA ramp-in procedure and voltage recovery, the ORR activity of the cathode catalyst can be determined by differential-flow polarization curves at a high flow (e.g., 2000/5000 nccm) of H_2/O_2 on anode / cathode, respectively. The conditions (gas flows, inlet pressure, cell temperature, gas humidity) should be the same as in the H_2/air polarization curve of interest. Figure 23a shows a differential-flow polarization curve for a Pt/C loading of 0.4 (black) and 0.1 mg_{Pt} cm^{-2} (blue). To obtain the catalyst's ORR activity, the following corrections are applied to the measured data: the voltage is corrected for the i) *iR*-drop and ii) the

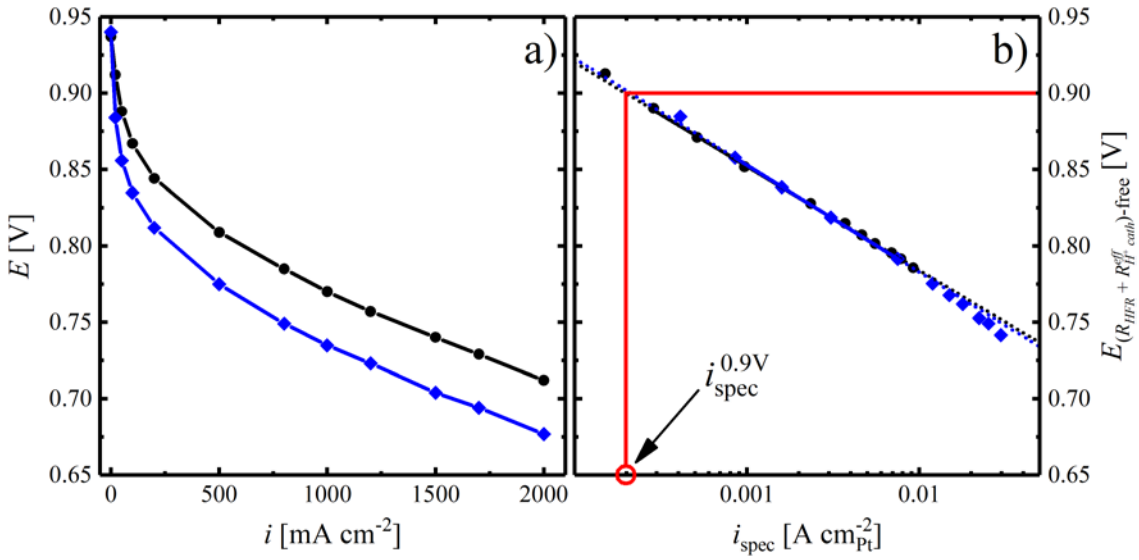

Figure 23. a) Differential-flow polarization curves using 2000 nccm / 5000 nccm of H_2/O_2 on anode / cathode at 170 kPa_{abs}, 100% *RH* and 80°C for a cathode loading of the Pt/C catalyst is 0.4 mg_{Pt} cm^{-2} (TEC10V50E, *Tanaka Kikinzoku Kogyo K.K.*, Japan, black curve) and 0.1 mg_{Pt} cm^{-2} (TEC10V20E, *Tanaka Kikinzoku Kogyo K.K.*, Japan, blue curve). The anode loading is 0.1 mg_{Pt} cm^{-2} in both cases and the I/C ratio is 0.65 g_I g_C^{-1} on anode and cathode, using a PFSA-based ionomer and membrane (15 µm). The GDL and MPL (H14C7, *Freudenberg KG*, Germany) are the same on both sides, assembled at a compression of 20%. The MEA size is 5 cm^2 and the flow fields have 7 channels with 0.5 mm lands and channels in serpentine arrangement (c.f., Figure 22a). b) Fully corrected polarization curve according to the procedure described below, normalizing the current to the surface area of Pt. The resulting Tafel slopes (dotted lines) are ≈70 mV dec^{-1} and ≈73 mV dec^{-1} for the 0.4 and 0.1 mg_{Pt} cm^{-2} loadings, respectively.

effective proton conduction resistance in the cathode. The current is adjusted by the iii) H_2 crossover and iv) the electrical short current. Finally, the potential is plotted vs. the surface area normalized current in a logarithmic scale to obtain the so-called Tafel plot, shown in Figure 23b). The Tafel slope is commonly evaluated between ≈50 and ≈500 mA cm^{-2}, where the H_2 crossover and electrical short currents are not significant fractions of the measured current. At the same time, high current densities are avoided, so that O_2 mass-transport related overpotentials do not play a role. However, very low cathode Pt loadings or deteriorated electrodes may require a shift of the fitting range to lower geometric current densities. The ORR activity of the cathode catalyst can be extracted from the fitted line in Figure 23b as the current at 0.9 V ($i_{spec}^{0.9V}$). The *ECSA* of the used catalyst can be derived from H_{upd} measurements or by the CO stripping procedure, analogous to the evaluation presented in section 2.2. All correction factors and the measurement procedures to obtain the values are described in the following.

Hydrogen Crossover and Electrical Short Current.—During operation, H_2 can cross over from the anode compartment through the membrane to the cathode compartment, where it is oxidized at the applied potential in a H_2/O_2 polarization curve. Hence, the measured current is lower compared to the actual ORR current due to its superposition with the HOR current, i_{H_2}, on the cathode. Additionally, a current, i_{short}, can pass through the membrane due to its finite electrical conductivity and the voltage difference between the two electrodes. Since both of these features are not driven by kinetics, the measured current, i, needs to be corrected according to Equation [34] to obtain the corrected current, i_{corr}.

$$i_{corr} = i + i_{H_2} + i_{short} \quad [34]$$

To determine the H_2 crossover current, H_2/N_2 are supplied to anode / cathode while otherwise maintaining the same conditions (cell temperature, *RH*, gas pressure) that are used to record the polarization curve. Subsequently, the cell voltage is increased in several chronoamperometric steps to record the steady state current after 2 min, as shown in Figure 24. Before execution of this measurement, the cathode gas line system needs to be free of residual O_2, since even small ORR currents disturb the measurement. Hence, a cathode purge procedure is commonly applied prior to testing. As shown in

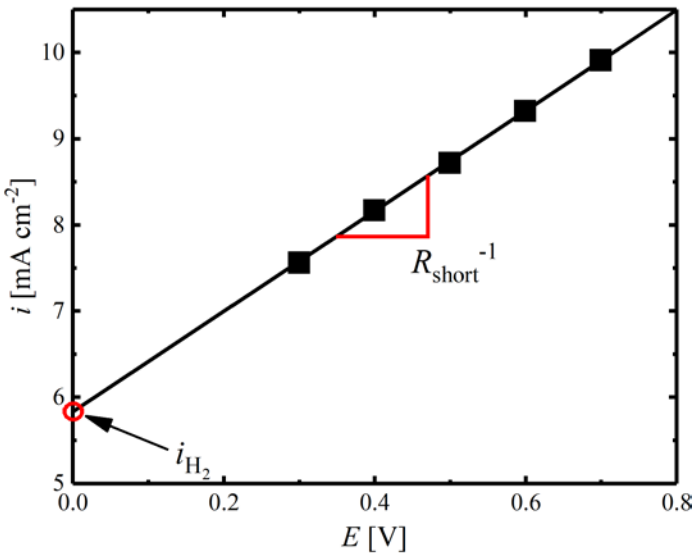

Figure 24. Measurement to determine the H_2 crossover and the electrical short current in H_2/N_2 at 150 nccm / 600 nccm, 100% *RH*, 80°C and 170 kPa_{abs} for a cathode loading of the Pt/C catalyst of 0.4 mg_{Pt} cm^{-2} (TEC10V50E, *Tanaka Kikinzoku Kogyo K.K.*, Japan, black curve). The anode loading is 0.1 mg_{Pt} cm^{-2} and the I/C ratio is 0.65 g_I g_C^{-1} on anode and cathode, using a PFSA-based ionomer and membrane (15 µm). The GDL and MPL (H14C7, *Freudenberg KG*, Germany) are the same on both sides assembled at a compression of 20%. The MEA size is 5 cm^2 and the flow fields have 7 channels with 0.5 mm lands and channels in serpentine arrangement (c.f., Figure 22a). The extracted H_2 crossover current density in this measurement is 5.9 mA cm^{-2} and R_{short} = 200 Ω cm^2, respectively.

Figure 24, a linear dependency of current and voltage is found in this measurement, where the y-axis intersect represents the H_2 crossover current (red circle) and the electrical resistance, R_{short}, is the inverse of the slope of the line. The shorting current at each applied current density of the polarization curve is calculated by dividing the measured cell voltage by the electrical resistance.

HFR Determination by EIS.—As mentioned before, the measured voltage, *E*, needs to be corrected for the ohmic drop of the cell ($i \cdot R_{HFR}$) according to the following equation.

$$E_{R_{HFR}\text{-free}} = E + i \cdot R_{HFR} \qquad [35]$$

The resistance can be easily analyzed by galvanostatic electrochemical impedance spectroscopy (GEIS) during the polarization curve (Figure 25a), adjusting the AC amplitude to 10% of the applied DC current of the load bank with a maximum of 3 A and a minimum of 0.1 A (defined by the limits of the potentiostat, Reference3000, *Gamry Instruments*, USA). The high frequency resistance, R_{HFR}, which mainly represents the membrane resistance and the electrical contact resistance between the flow fields, the GDLs,

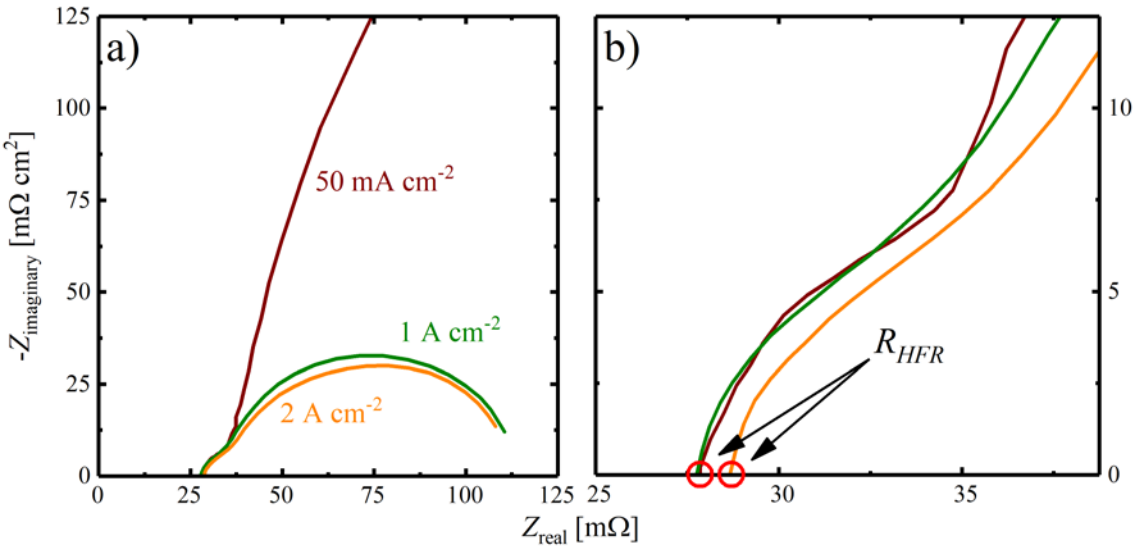

Figure 25. a) Nyquist plot for a GEIS measurement recorded between 100 kHz and 10 Hz at 80°C, 170 kPa_{abs}, 100% *RH*, applying 2000 nccm / 5000 nccm H_2/O_2 on anode / cathode employing a cathode loading of the Pt/C catalyst of 0.4 mg_{Pt} cm^{-2} (TEC10V50E, *Tanaka Kikinzoku Kogyo K.K.*, Japan, black curve). The anode loading is 0.1 mg_{Pt} cm^{-2} and the I/C ratio is 0.65 g_I g_C^{-1} on anode and cathode, using a PFSA-based ionomer and membrane (15 µm). The GDL and MPL (H14C7, *Freudenberg KG*, Germany) are the same on both sides assembled at a compression of 20%. The MEA size is 5 cm^2 and the flow fields have 7 channels with 0.5 mm lands and channels in serpentine arrangement (c.f., Figure 22a). The DC current was 50 mA cm^{-2} (brown), 1 A cm^{-2} (green) and 2 A cm^{-2} (orange), while the AC current amplitude was 5, 100 and 200 mA cm^{-2}, respectively. b) Zoom-in to determine the *HFR* as the x-axis intersect of the impedance curve.

and the catalyst layers, is determined as the x-axis intersect of the high frequency branch in a Nyquist plot (red circles in Figure 25b). The *HFR* is recorded at each applied current density of the polarization curve to evaluate changes with respect to the degree of membrane humidification (e.g., lower water content due to heating at high *i*) and to allow for a precise correction of the measured data.

Proton Conduction Resistance in the Cathode.—The voltage loss due to proton transport within the electrode has to be taken into account by correcting for the effective proton conduction resistance in the cathode. Note that proton conduction in the anode is often neglected due to the fast HOR kinetics, hence a short proton conduction path in the anode.

$$E_{\left(R_{HFR}+R^{\mathrm{eff}}_{\mathrm{H^+,cath}}\right)-\mathrm{free}} = E_{R_{HFR}-\mathrm{free}} + i \cdot R^{\mathrm{eff}}_{\mathrm{H^+,cath}} \qquad [36]$$

In this, the effective proton conduction resistance, $R^{\mathrm{eff}}_{\mathrm{H^+,cath}}$, is defined by the average proton conduction resistance in the cathode, $R_{\mathrm{H^+,cath}}$, and a correction factor, ζ, that

depends on the current density, on $R_{H^+,cath}$ and on the Tafel slope of the reaction (for a more detailed explanation, the reader is referred to Neyerlin et al.).[121]

$$R^{eff}_{H^+,cath} = \frac{R_{H^+,cath}}{3+\zeta} \quad [37]$$

The proton conduction resistance can be determined by potentiostatic electrochemical impedance spectroscopy (PEIS) in H_2/N_2 on anode / cathode, assuming a transmission line model to fit the resulting Nyquist plots shown in Figure 26a for different *RH* values.[122]

Typically, intermediate humidification yields the most reliable results for data fitting, since the individual regimes are well-separated from each other. Therefore, the data evaluation is shown exemplarily in Figure 26b for the measurement at 70% *RH*. The most accurate way is to fit the data to the equivalent circuit with a suitable software (e.g., EC-Lab), whereas the data in Figure 26b are only fitted linearly in the high- and low frequency branch. The x-axis intersect of the resulting fitting lines can be used to

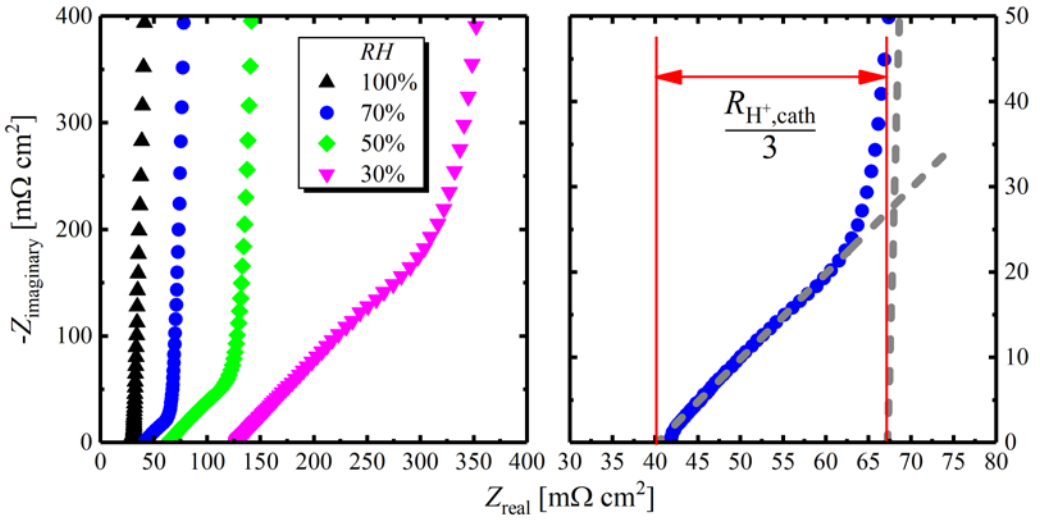

Figure 26. a) Nyquist plot for a PEIS measurement recorded between 500 kHz and 200 mHz at 0.2 V_{cell} with a peak-to-peak perturbation of 3.5 mV at 80°C, 100% (black), 70% (blue), 50% (green) and 30% *RH* (pink), while maintaining constant gas partial pressure (i.e., at cell pressures of 270, 255, 246, and 236 kPa_{abs}, respectively). The gas flow is 1000 nccm / 1000 nccm H_2/N_2 on anode / cathode employing a cathode loading of the Pt/C catalyst of 0.4 mg_{Pt} cm^{-2} (TEC10V50E, *Tanaka Kikinzoku Kogyo K.K.*, Japan, black curve). The anode loading is 0.1 mg_{Pt} cm^{-2} and the I/C ratio is 0.65 g_I g_C^{-1} on anode and cathode, using a PFSA-based ionomer and membrane (15 µm). The GDL and MPL (H14C7, *Freudenberg KG*, Germany) are the same on both sides, assembled at a compression of 20%. The MEA size is 5 cm^2 and the flow fields have 7 channels with 0.5 mm lands and channels in serpentine arrangement (c.f., Figure 22a). b) Evaluation procedure to obtain the proton conduction resistance in the cathode by fitting of the impedance data, shown for the measurement at 70% *RH*.

determine the proton sheet resistance, as shown in the graph. Clearly, the H_2/O_2 polarization curve data has to be corrected by the proton conduction resistance determined at the same humidification.

O_2 mass-transport resistance.—In addition to the losses in the H_2/O_2 polarization curve, an O_2 mass-transport overpotential arises in H_2/air polarization curves. This loss can be quantified by limiting current measurements according to the method described by Baker et al.[123] For the experiment, a high, differential-flow of O_2 in N_2 is applied to the cathode, varying the O_2 content and measuring the maximum current at low cell voltage, shown in Figure 27a at a pressure of 170 kPa_{abs}. At these conditions, the O_2 concentration in the cathode drops to zero, hence an increase of the applied cathode overpotential (i.e., a lower cell voltage) does not yield a higher current density. The O_2 mass-transport resistance, $R_{O_2}^{total}$, can subsequently be extracted from the measured limiting current, i_{lim}, at each O_2 concentration, c_{O_2}, (c.f., Figure 27b) according to Equation [38].

$$R_{O_2}^{total} = \frac{4 \cdot F}{i_{lim}} \cdot c_{O_2} \qquad [38]$$

Measuring the transport resistance as a function of pressure (Figure 27b) enables a distinction of the pressure dependent, $R_{O_2}^{PD}$, and the pressure independent fraction, $R_{O_2}^{PI}$, of the total O_2 mass-transport resistance, as there is a linear dependency of the applied pressure and $R_{O_2}^{total}$ (Figure 27c).

For the analysis, the averaged values of $R_{O_2}^{total}$ (Figure 27) are fitted vs. the pressure and extrapolated to obtain the y-axis intersect at p = 0 kPa (y = 0.17 s cm^{-1}) and the slope of the fitted line (0.003 s cm^{-1} kPa^{-1}). The pressure independent resistance can be obtained according to Equation [39],[123] and amounts to $R_{O_2}^{PI}$ = 0.32 s cm^{-1} for the measurement shown in Figure 27.

$$R_{O_2}^{PI} = \text{y} - \text{slope} \cdot p_{H_2O} \cdot \left(\frac{D_{ON}}{D_{OW}} - 1\right) + B_{ch} \frac{2 \cdot N \cdot L \cdot d}{\dot{V}_{dry}} \cdot \left(\frac{273}{T}\right) \cdot \frac{p_{H_2O}}{p_a} \frac{D_{ON}}{D_{OW}} \qquad [39]$$

In this, p_{H_2O} is the partial pressure of water in the cell (47.4 kPa at 100% *RH* and 80°C),

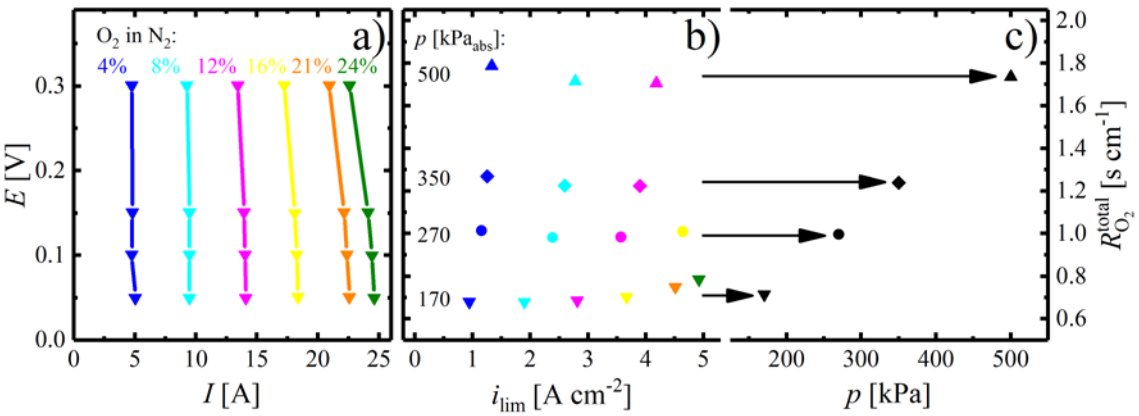

Figure 27. a) Limiting current measurement recorded at 80°C, 100% *RH*, 170 kPa_{abs}, applying 2000 nccm / 5000 nccm H_2/O_2 in N_2 (4%, 8%, 12%, 16%, 21%, 24%, respectively; colour coded) on anode / cathode at a cathode loading of the Pt/C catalyst of 0.4 mg_{Pt} cm^{-2} (TEC10V50E, *Tanaka Kikinzoku Kogyo K.K.*, Japan, black curve). The anode loading is 0.1 mg_{Pt} cm^{-2} and the I/C ratio is 0.65 g_I g_C^{-1} on anode and cathode, using a PFSA-based ionomer and membrane (15 µm). The GDL and MPL (H14C7, *Freudenberg KG*, Germany) are the same on both sides assembled at a compression of 20%. The MEA size is 5 cm^2 and the flow fields have 7 channels with 0.5 mm lands and channels in serpentine arrangement (c.f., Figure 22a). b) Extracted total O_2 mass transport resistance versus measured limiting current collected at different pressures (170, 270, 350, 500 kPa_{abs}; symbol style coded). c) Average of the O_2 mass-transport resistance at each examined pressure as a function of the absolute pressure derived from the data shown in b).

D_{ON} ($1.7 \cdot 10^{-5}$ m^2 s^{-1} at 170 kPa_{abs}) and D_{OW} ($2.2 \cdot 10^{-5}$ m^2 s^{-1} at 170 kPa_{abs}) are the binary diffusion coefficients of O_2 relative to N_2 and water vapor, respectively, B_{ch} is a dimensionless coefficient that represents the flow rate dependent part of the channel transport resistance (1.01), N is the number of parallel channels in the flow field (7 in our case), L and d are the length (68.13 mm) and the depth (0.8 mm) of the channels in the flow field, $\dot{V}_{dry}$ is the total dry gas flow rate at standard temperature and pressure (5000 nccm), T is the temperature (80°C), and p_a is the atmospheric pressure (101.3 kPa).

In contrast to the pressure dependent O_2 transport processes in the GDL, the pressure independent resistance is related to Knudsen diffusion in small pores, i.e., in the catalyst layer, or to O_2 diffusion through liquid water or through an ionomer film. Finally, the O_2 mass-transport overpotential, η_{O_2}, is calculated according to Equation [40].[124]

$$\eta_{O_2} = \frac{R \cdot T}{F} \cdot \left(\frac{1}{4} + \frac{\gamma}{\alpha}\right) \cdot \frac{p_{O_2} - \frac{R \cdot T}{4 \cdot F} \cdot R_{O_2}^{total} \cdot i}{p_{O_2}} \qquad [40]$$

In this, p_{O_2} is the partial pressure of O_2 in the feed gas, γ is the reaction order of the ORR with respect to p_{O_2} (0.54) and α is the transfer coefficient (1.0).[125]

Voltage loss analysis.—In order to analyze the measured H_2/air performance curve with respect to all known loss terms, a full voltage loss analysis is carried out, recovering the so-called unassigned losses $R_{\text{unassigned}}$. For this, the reversible cell voltage is calculated according to Equation [7] and the individual loss terms (determined according to the procedures described above) are subsequently subtracted from it to reveal the difference between the projected and the measured performance.

$$E_{\text{unassigned}} = E_{\text{rev}} - \eta_{\text{ORR}} - i \cdot R_{HFR} - R^{\text{eff}}_{\text{H}^+\,\text{cath}} - \eta_{\text{O}_2} - E_{\text{cell}} \qquad [41]$$

The individual loss terms are i) the ORR overpotential, η_{ORR} (red area in Figure 6), derived from the ORR activity (Figure 23), ii) the *iR*-drop, measured by EIS (Figure 25). For a known contact resistance ($R_{\text{contact}} \approx 15$ mΩ cm^2 in the setup described here), the R_{HFR} can be separated into the two major components, R_{contact} (blue area in Figure 6) and R_{membrane} (green area in Figure 6). Furthermore, iii) the effective proton conduction resistance in the cathode, $R^{\text{eff}}_{\text{H}^+,\text{cath}}$, (turquoise area in Figure 6) and the iv) total O_2 mass-transport resistance, $R^{\text{total}}_{\text{O}_2}$, (pink area in Figure 6). As shown by Harzer et al., the resulting unassigned loss term ($R_{\text{unassigned}}$, grey area in Figure 6) is significantly higher for low cathode *rf* values.[58]

2.3.4. H_2 Pump Measurements in PEMFCs

This section provides an overview of the procedure used for H_2 pump measurements, where both sides of the fuel cell are supplied with H_2, which is oxidized in the anodic reaction (HOR) according to Equation [42]. The protons travel through the ionomer phase to the other electrode where they are reduced to H_2 in the cathodic reverse reaction (HER) as shown in Equation [43].

$$H_2 \rightarrow 2H^+ + 2e^- \quad [42]$$

$$2H^+ + 2e^- \rightarrow H_2 \quad [43]$$

Amongst others, this technique is used to i) evaluate the HOR/HER exchange current density of different catalysts[57,94,126,127] and ii) to determine the anode contribution to the overpotential during H_2/air operation of the fuel cell.[68,128] The measurement procedure to determine the HOR/HER exchange current density is described in more detail in the following, including the use of dilute H_2 to reveal mass-transport issues.

An MEA with a high loaded counter electrode (e.g., 0.4 mg_{Pt} cm^{-2} with a 50%$_{wt.}$ Pt/C catalyst) and a super-low loading working electrode (on the order of ≈2-3 μg_{Pt} cm^{-2} with a 5%$_{wt.}$ Pt/C catalyst) is prepared and assembled according to the procedure discussed in the previous sections. The difference in electrode loading reduces the overpotential contribution of the counter electrode to the total cell voltage compared to that of the working electrode in order to obtain a sufficient measurement precision. Since weighing the decal before and after the transfer by hot pressing has a limited accuracy to determine low Pt loadings, the *ECSA* of the working electrode catalyst is evaluated prior to any kinetic measurements. However, the most common method for the evaluation of the *ECSA*, i.e., using the H_{upd} features in a CV, becomes increasingly erroneous at low *rf* values, caused by the superposition of the H_2 evolution currents. Hence, the CO stripping procedure (similar to that described in section 2.2.2 for RDE) is used to estimate the Pt surface area of the working electrode. Prior to CO stripping, the catalyst layer should be activated to clean the surface and ensure reliable results (e.g., by 20 CV cycles between 0.1 and 1.0 V_{RHE} at 200 mV s^{-1}). If the obtained value for the low loaded electrode is not within an acceptable range (±10%) compared to the *ECSA* of the same catalyst at higher loading, the MEA has to be discarded. Due to the very severe poison-

ing of many noble metals by CO at low potentials (especially Pt), the CO strip and the H_2 pump measurement have to be carried out on different fuel cell test stations, as this is a way to ensure that no measurement errors related to the intrusion of CO into the H_2 gas feed are present.

Directing H_2 to the cathode side of the fuel cell is a safety concern, since improper operation can lead to the formation of explosive mixtures with O_2 residues in the humidifier or gas lines. Therefore, H_2 is only allowed to be directed into the cell when the air supply of the test station is physically closed and the entire gas line and humidifier systems are free of O_2. To switch from regular operation (air, O_2, N_2 or 5% H_2 in Ar on the cathode side and H_2 or N_2 on the anode) to H_2 pump operation (H_2 or N_2 on both sides), a semi-automatic purging procedure can be used. First of all, O_2 at a high flow (e.g., 2000 nccm) is supplied to the cathode and the O_2 supply valve is closed, resulting in a drop of the gas line pressure until ambient pressure is reached and no gas flows through the cell anymore. Thereafter, the N_2 valve connected to the O_2 supply line is opened, purging for 5 min with inert gas and ensuring the removal of O_2. The N_2 supply in the former O_2 line remains open throughout the entire measurement phase, leaving no possibility for an introduction of O_2 into the humidifier / cell. The procedure is repeated with the air supply line in the same manner to remove all possible O_2 sources. Subsequently, the entire gas line system is purged with N_2. Finally, the 5% H_2 in Ar supply valve can be closed, opening the pure H_2 gas for this line. To prevent any misunderstanding with other users of the test station, the regular O_2 operation mode has to be reinstalled after completion of the measurement by closing the pure H_2 supply line while a H_2 flow is applied until the line pressure drops and the 5% H_2 in Ar can be opened again. Furthermore, the cathode has to be purged well with inert gas and the N_2 valves on the O_2 and air lines have to be closed to switch back to O_2 and air, respectively.

For the H_2 pump measurement, 2000 nccm of H_2 (for a 5 cm^2 active area) are directed to each side of the MEA. The high flow ensures that gas phase mass transport limitations are avoided and the use of the 7 channel flow field (Figure 22a) guarantees a low pressure drop for the applied conditions. Homogeneous humidification of the MEA can be achieved by choosing a high relative humidity of the supply gas (e.g., 90 – 100%

RH), also limiting the influence of the electroosmotic drag during the current application. For measurements in dilute H_2, the working electrode gas is mixed with N_2 to the desired concentration while the counter electrode is supplied with pure H_2. The resulting Nernst shift of the HOR/HER equilibrium potential on the WE can be calculated according to Equation [44] and is corrected for in the data treatment.

$$E = E_0^{\mathrm{HOR/HER}} + \frac{RT}{2F} \cdot \ln\left(\frac{p_{\mathrm{H_2}}^{\mathrm{ref}}}{p_{\mathrm{H_2}}}\right) \qquad [44]$$

The *HFR*, which is used to correct the potential for the *iR*-drop, is determined either at each applied current density or voltage (for steady state measurements) or at several voltage points after recording a potential sweep. In order to verify the stability of the working electrode during the H_2 pump measurements, another CO strip should be recorded at the end of test. The data analysis to obtain the HOR/HER exchange current density from the H_2 pump measurement is analogous to that in RDE experiments (c.f., section 2.2), whereas the voltage is solely corrected for the *iR*-drop and the current is only normalized to the loading of the working electrode. Finally, fitting the micro-polarization region ($\eta \leq 5$ mV) to Equation [32] or the entire polarization curve (over a minimum voltage range corresponding to one *TS* value) to the Butler-Volmer equation ([31]) yields the desired parameters.

2.3.5. Low Temperature Fuel Cell Testing

The goal of the procedure described in this section is the determination of the membrane conductivity at temperatures below the freezing point of water at a defined membrane water content (λ value given in $mol_{H_2O}\ mol^{-1}_{SO_3^-}$). Whereas the temperature control in the common fuel cell testing setup (Figure 21) is based on a rod heater and air ventilation, the cell used for freeze measurements employs a liquid cooling / heating system. The temperature regulation is achieved by a temperature control unit (FP50-HL, *Julabo GmbH*, Germany) in combination with a thermocouple that is directly placed into the flow field of the cell hardware. A 1:1 volume mixture of ethylene glycol and water is used as cooling fluid due to its low freezing (< -35°C) and high boiling point (> 110°C). The 50 cm^2 cells are assembled as described in section 2.3.2 and the setup can be used with both, AEMFCs and PEMFCs. When the temperature is lowered, ambient humidity condenses on the cell, leading to a less efficient cooling process and a higher minimum temperature of the system. Therefore, the entire cell is wrapped in a plastic bag after assembly and the interior has been continuously purged with a gentle stream of dry air. All openings of the bag should be closed as good as possible (e.g., with a zip tie), leaving only the necessary connections (cables, sensors) to the devices free.

Since *RH* control in the cell environment by dew point regulation of the inlet gas stream is not trivial at temperatures below the freezing point of water, the MEA is equilibrated in a humidified (between 20 and 100% *RH*) N_2 gas stream (500 nccm on each side) at 50°C and 150 kPa_{abs} for 70 min. Thereafter, the cell is purged for 75 s with 50 nccm dry N_2 on each side to remove humidified gas from the void volume inside the cell. The delay time between changing the gas stream until it reaches the cell flow field can, e.g., be evaluated by a mass spectrometer and is considered individually for each side. Right after completion of the dry gas purge, the gas stream is interrupted and the cell is closed with valves at the cell in- and outlets to initiate the cooling process. The valves are used to limit the dead volume before and after the cell and to avoid any interference with purge procedures in the fuel cell test station. After the minimum temperature is reached (≈-20°C), the cell is heated up in a thaw cycle to 50°C. Recording the *HFR* while knowing the contact resistance reveals the membrane conductivity.

2.4. Physical / Chemical Characterization Methods

SEM/EDX.—Scanning electron microscopy images are taken on a Jeol SEM (JCM-6000PKUS NeoScope, *Jeol GmbH*, Germany), where the sample is mounted on a sample holder with conductive carbon tape (powders are dropped directly on the tape). Energy dispersive X-ray (EDX) spectra are taken in backscattering mode.

TEM.—Transmission electron microscopy images are taken from samples on TEM grids (Formvar-supported carbon coated Cu400, *Science Services GmbH*, Germany). To deposit the catalyst on the grid, it is dispersed in a small amount of ultrapure water (≈1 mL) by sonication and subsequently dropped on the grid with a pipette. Images are typically recorded at 100 kV with a Philips machine (CM100 EM, *Royal Philips AG*, Netherlands).

XRD.—X-ray diffractograms are recorded in transmission mode on a Stadi P machine (*Stoe & Cie GmbH*, Germany) using Ge(111) monochromatized Cu $K_{\alpha 1}$ radiation (λ = 1.54059 Å, 50 kV, 30 mA) and an areal detector (Mythen 1 K, *Dectris Ltd.*, Switzerland). The samples are homogenized in a mortar and filled into glass capillaries (0.5 mm outer diameter, *Hilgenberg GmbH*, Germany). A calibration with Si is carried out prior to every measurement to account for slight shifts of the °2θ value.

TGA.—Thermogravimetric analysis (TGA) is carried out on a TGA / DSC 1 instrument coupled with a mass spectrometer for exhaust gas analysis (GC 200, *Mettler Toledo Corp.*, Switzerland). The analysis chamber of the TGA is continuously purged with 20 mL min^{-1} and an additional gas flow of O_2, air, 5% H_2 in Ar, or Ar. The gas composition, as well as the heating rate can be defined in an automated procedure and a blank is recorded prior to the first experiment, where the same type of crucible, e.g., 70 µL sapphire with lid (*THEPRO GbR*, Germany), is used without a sample.

Elemental Analysis.—The elemental composition of various catalysts can be analyzed by the central analytical laboratory of the catalysis research center of the chemistry department at the Technical University of Munich. The elements C, H, N, S are simulta-

neously detected (EURO EA analyzer, *HEKAtech GmbH*, Germany), while Pt needs to be quantified photometrically (UV 160, *Shimadzu K.K.*, Japan).

3. Published Work

The articles comprising this thesis were published in the peer-reviewed Journal of The Electrochemical Society or will be submitted to it in the near future. The first two publications presented here focus on electrocatalysis in alkaline electrolyte and on membranes for AEMFCs, starting with a fundamental study on the HOR mechanism on bimetallic Pt-Ru catalysts (see section 3.1.1). Main goal of the study is to identify whether hydroxide species on Ru participate directly in the removal of adsorbed hydrogen species on Pt during HOR. In the second manuscript (see section 3.1.2), AEMFC single cells are prepared from commercially available materials and used to evaluate the conductivity of a state-of-the-art AEM (Tokuyama A201) below the freezing point of water.

Transitioning from the alkaline to the acidic media, the next section focusses on the more established PEMFC system, in particular, the degradation of the catalyst layers under fuel cell relevant operating conditions. At first, the SUSD process, commonly known for severe cathode degradation, is investigated with regards to its impact on the anode catalyst layer (see section 3.2.1). The manuscript includes the development of a voltage cycling based AST to simulate anode ageing while maintaining the cathode unaltered in order to determine the anode overpotential by H_2 pump measurements in pure and dilute H_2. Maintaining the focus of the thesis on degradation phenomena, the subsequent publication deals with the stability of the cathode catalyst layer during PEMFC operation, taking a closer look at the effect of the cathode loading and the impact of different AST protocols on the most relevant voltage loss contributions in H_2/air PEMFCs, especially the evaluation of the O_2 mass transport (see section 3.2.2). To complement, one of the thus developed voltage cycling ASTs is applied to an in-house prepared Pt_xY/C catalyst in the subsequently described manuscript (see section 3.2.3). The synthesis method is based on a high temperature treatment in reductive atmosphere, which can be used as a roadmap for Pt alloy catalysts with other rare earth elements.

Finally, a manuscript is provided (see section 3.3.1) that is concerned with the electrodeposition of Pt on Sn from liquid electrolyte with the aim to be used as a model system for the generation of Pt on non-noble metal support materials. Special attention in this manuscript is dedicated to the role of Sn surface oxide species.

3.1. Research on AEMFCs – HOR catalysis and membrane conductivity

3.1.1. Origin of Superior HOR/HER Activity of Bimetallic Pt-Ru Catalysts in Alkaline Media Identified via Ru@Pt Core Shell Nanoparticles

In this section, the journal article "Origin of Superior HOR/HER Activity of Bimetallic Pt-Ru Catalysts in Alkaline Media Identified via Ru@Pt Core Shell Nanoparticles" is presented.[111] The article was published in March 2018 in the peer-reviewed Journal of The Electrochemical Society as an open access article distributed under the terms of the Creative Commons Attribution 4.0 License, permitting unrestricted reuse of the work in any medium, provided the original work is properly cited. The permanent web link to this article is https://doi.org/10.1149/2.0791805jes. The paper was presented by Jan N. Schwämmlein at the 230th ECS Meeting (PRiME 2016) in Honolulu, Hawaii (abstract #2779), including the publication of a conference proceedings paper in the associated journal (ECS Transactions) named "Origin of Superior Activity of Ru@Pt Core-Shell Nanoparticles towards Hydrogen Oxidation in Alkaline Media",[129] which can be retrieved at the permanent web link https://doi.org/10.1149/07514.0971ecst.

Short summary.—A topic of ongoing discussion regarding the HOR in alkaline media is the origin of the high exchange current density of bimetallic alloys (e.g., Pt-Ru) in alkaline media[103,130–135] compared to the corresponding monometallic catalysts.[101,102,127] Some researchers argued that the HOR in acidic and alkaline media is based on different reaction mechanisms, requiring hydroxide species to remove the reaction intermediate Pt-H_{ads} in alkaline media.[103] However, surface oxidation in the potential region of interest (0 mV_{RHE} ± ≈100 mV) does not occur on Pt.[136,137] In contrast, the surface of Ru is oxidized at significantly less anodic potentials. In this view, Strmcnik et al. hypothesized that Ru actively supplies hydroxide species to Pt during the HOR.[103] Other researchers pointed to varied electronic properties of Pt in the vicinity of Ru, while Ru was considered mostly inactive due to its oxidized surface.[105] Different hypothesis exist to underline this hypothesis, such as a shift of the Pt d-band center[138] and an associated lowering of the Pt-H_{ads} BE[105] or a change of the orientation of water[104] or protons[139] in the vicinity of the catalytic surface.

The study presented here aims to prove / disprove, the active participation of Ru sites in the catalytic process, i.e., support or eliminate the theory of a bifunctional mechanism. To distinguish between a bifunctional mechanism and an electronic effect, Ru@Pt core-shell nanoparticles with either partial Pt coverage, or fully Pt encapsulated Ru nanoparticles are prepared. First of all, TEM images show an increasing average particle size when depositing higher quantities of Pt on the Ru core. Furthermore, high resolution TEM qualitatively proves the existence of a core-shell structure on the analyzed particles. The images are supported by EDS line scans of individual particles featuring a submonolayer Pt shell or a fully Pt encapsulated Ru core. The exposure of Ru on the surface of Ru@Pt core-shell nanoparticles is also probed electrochemically by recording CVs in sulfuric acid, where the appearance of a cathodic peak is used as an indicator for Ru oxide species. As a result, surface Ru species are found in submonolayer Ru@Pt samples, while Ru is not exposed in samples with a thicker Pt shell. Furthermore, two different Pt species are identified by CO stripping, representing the first and subsequent Pt layers on the Ru core according to a method developed by El Sawy et al.[140] After identification of the HOR/HER transfer coefficient of one of the Ru@Pt core-shell catalysts, the activity of all samples is determined by a linear fit in the micro-polarization region of polarization curves recorded in H_2-saturated solution. In this, Ru particles with submonolayer Pt coverage show a significantly lower surface area normalized exchange current density compared to fully Pt covered core-shell nanoparticles. This clearly indicates that the participation of Ru sites on the surface of the particle is not necessary to achieve a high HOR activity, thereby rendering an electronic effect more plausible than a bifunctional mechanism. It shall be mentioned again at this point that no conclusion on the actual origin of the electronic effect (i.e., variation of the Pt-H_{ads} BE versus interfacial orientation of water or protons) can be drawn from the presented data.

Author contributions.—Ru@Pt catalysts were prepared by H.E.S. and B.M.S. Electrochemical tests and data analysis were carried out by J.N.S. and B.M.S. TEM images were taken by H.E.S. with the help of K.W. and H.D., while high resolution TEM images were provided by V.T. All authors discussed the results of the study and reviewed the manuscript that was written by J.N.S.

Origin of Superior HOR/HER Activity of Bimetallic Pt-Ru Catalysts in Alkaline Media Identified via Ru@Pt Core-Shell Nanoparticles

Jan N. Schwämmlein,[1,*,z] Björn M. Stühmeier,[1] Klaus Wagenbauer,[2] Hendrick Dietz,[2] Vasiliki Tileli,[3] Hubert A. Gasteiger,[1,] and Hany A. El-Sayed[1]**

[1] *Chair of Technical Electrochemistry, Department of Chemistry and Catalysis Research Center, Technical University of Munich, D-85748 Garching, Germany*
[2] *Walter Schottky Institute, Technical University of Munich, D-85748 Garching, Germany*
[3] *Institute of Materials, École Polytechnique Fédérale de Lausanne, CH-1015 Lausanne, Switzerland*

Compared to Pt/C, the HOR activity of Pt-Ru alloys in alkaline electrolyte is exceptionally high. Nevertheless, it remains unknown whether this enhancement is due to a bifunctional mechanism involving Pt and Ru as active sites or an electronic effect of Ru on Pt. In this study, we distinguish between those fundamental differences using Ru@Pt core-shell nanoparticles as a model system. Ru@Pt catalysts were prepared from submonolayer to multilayer Pt coverage. The exposure of Ru on the surface of the catalyst was analyzed by cyclic voltammetry, showing that Ru is solely exposed on the surface of Ru@Pt particles with low Pt-coverage. The thickness of the Pt-shell was characterized by CO stripping in H_2SO_4, allowing to distinguish between single and bilayered Ru@Pt catalysts. Determining the HOR/HER activity of these catalysts in 0.1 M NaOH revealed that fully Pt-covered Ru is more active than partially covered Ru@Pt nanoparticles. Hence, the participation of Ru as active site in a bifunctional mechanism is of minor importance with respect to the HOR/HER activity compared to its influence on the electronic structure of Pt. Similar to Pt-Ru alloys, the most active Ru@Pt core-shell nanoparticles show a 4 to 5-fold enhancement of the surface-normalized HOR/HER activity compared to Pt/C.

 [DOI: 10.1149/2.0791805jes]

Manuscript submitted January 22, 2018; revised manuscript received March 14, 2018. Published March 29, 2018. This was Paper 2779 presented at the Honolulu, Hawaii, Meeting of the Society, October 2–7, 2016.

Fuel cells are a promising technology for automotive applications, supplying electricity by converting H_2 and O_2 to H_2O in an electrochemical reaction.[1] Whereas the oxidation of H_2 on the anode side of proton exchange membrane fuel cells (PEMFCs) is facile on platinum with an exchange current density as high as $i_0^{293K} \approx 80$ mA cm_{Pt}^{-2} (extrapolated to 293 K based on H_2-pump experiments between 313–353 K),[2] the reaction rate is sluggish in alkaline environment and the exchange current density decreases by approximately 2 orders of magnitude ($i_0^{293K} \approx 0.6$ mA cm_{Pt}^{-2}).[3,4] The cause of this tremendous difference is still subject of discussion within the field of electrochemistry. Density functional theory (DFT) calculations by Nørskov et al. on the hydrogen evolution reaction (HER) activity of different monometallic surfaces revealed a volcano like relation of the exchange current density and the M-H_{ads} (M = metal) binding energy (BE).[5] Of all the investigated monometallic surfaces, Pt exhibits the highest HER activity. According to Nørskov et al., the Pt-H_{ads} binding is slightly stronger compared to the hypothesized theoretical optimum. Further studies indicated a shorter Pt-H_{ads} bond distance in alkaline vs. acid environment, hence a larger Pt-H_{ads} BE.[6–8] In accordance with this, several researchers expect the Pt-H_{ads} BE to be responsible for the low hydrogen oxidation/evolution reaction (HOR/HER) activity of common noble metals in base compared to acid.[2,4,9–11] In 2015, Sheng et al. reported a monotonic decrease of the HOR/HER activity as a function of pH, determined by RDE in buffered electrolytes. They correlated this trend to the increasing Pt-H_{ads} BE at higher pH, indicated by the potential shift of the H_{upd} process in cyclic voltammetry (CV).[11] It is a known phenomenon in chemistry that bimetallic systems (e.g. alloys) can have different electronic properties than the single metals they are composed of. This may cause a variation of the binding strength toward an adsorbate, termed electronic or ligand effect. Ruban et al. reported a downshift of the platinum d-band center for a Pt overlayer on Ru compared to pure Pt, thus a weaker Pt-H_{ads} BE.[12] In fact, the beneficial combination of Pt and Ru as catalytic system for the HOR was reported by various groups in acidic[13–15] and alkaline media.[14,16–18] In contrast to Pt-H_{ads} as a sole descriptor for the HOR/HER activity of Pt in acidic versus alkaline environment, Ledezma-Yanez et al. recently attributed the pH effect to a reorganization of interfacial water at the catalyst surface, influencing the barrier for hydrogen adsorption.[19] However, both effects, a variation of the Pt-H_{ads} BE and the reorganization of interfacial water, are closely related to the electronic properties of the catalyzing metal and are expected to differ between a monometallic and a bimetallic surface. In the further analysis of this manuscript, no disentanglement between those hypothesis is made, and both are termed "electronic effect". Furthermore, with the presented measurements, we are not able to identify the origin of the electronic modification, which could be related to an electronic interaction of ruthenium and platinum or to a strain effect as described by Adzic et al.[20]

Taking a different view, Strmcnik et al. proposed that a change of the HOR mechanism in alkaline compared to acid is the reason for the high activity of bimetallic Pt-Ru alloys.[21] In this case, dissociated H_2 is believed to be adsorbed on Pt, whereas the more oxophilic Ru adsorbs hydroxide to form water via a bifunctional mechanism.

$$0.5H_2 + Pt \rightarrow Pt - H_{ads} \quad [1]$$

$$Ru + OH^- \rightarrow Ru - OH_{ads} + e^- \quad [2]$$

$$Pt - H_{ads} + Ru - OH_{ads} \rightarrow Pt + Ru + H_2O \quad [3]$$

To date, it remains unknown whether the experimentally observed HOR/HER activity enhancement of Pt-Ru compared to pure Pt is due to a bifunctional mechanism or an electronic effect. In this study, we seek to identify the cause of the high HOR/HER activity in the bimetallic Pt-Ru system by preparing Ru@Pt core-shell nanoparticles with different Pt shell thickness (Figure 1) and determining their intrinsic HOR/HER activity in 0.1 M NaOH, complementing our previous preliminary study with a detailed microscopic analysis of the synthesized particles and with a more in-depth analysis of the HOR/HER kinetics.[22]

With respect to a bifunctional mechanism, Ru atoms are thought to actively participate in the oxidation of hydrogen by adsorbing hydroxide, and thus would need to be present on the surface of the

*Electrochemical Society Student Member.
**Electrochemical Society Fellow.
[z]E-mail: jan.schwaemmlein@tum.de

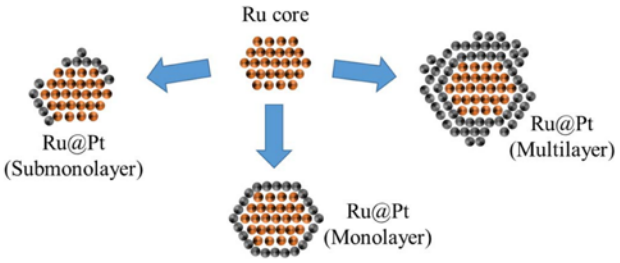

Figure 1. Schematic of Ru@Pt core-shell nanoparticles with different Pt-shell thickness on a Ru nanoparticle. Reproduced from Schwämmlein et al. with permission of The Electrochemical Society.[22]

catalytic material in the vicinity of the Pt atoms. In accordance with this, Ru@Pt core-shell nanoparticles with submonolayer Pt coverage would be expected to be highly active compared to pure Pt. The activity normalized by the noble metal surface area (in units of mA cm^{-2}_{NM}, with NM being Pt + Ru) is expected to increase with the Pt coverage within the submonolayer coverage of Pt on Ru (Ru@Pt) up to an optimized surface composition of Pt and Ru (Figure 2). In other words, the activity of each Pt atom stays constant, while the contribution of Pt to the total noble metal surface area increases when more Ru sites are covered by Pt, i.e., the activity normalized by the total noble metal surface area (Pt + Ru) increases. Depositing more Pt on the core would eventually cover more and more Ru sites, which then no longer could contribute to the reaction by supplying hydroxide. As a consequence, the expected activity of a fully Pt encapsulated Ru particle would be similar to that of pure Pt, since this is the only active site remaining on the surface of the particle.

In the case that an electronic effect were to be the main cause of the high HOR/HER activity of the Pt-Ru system, Ru@Pt particles with submonolayer Pt coverage would also show high activity compared to pure Ru. However, the total noble metal surface area normalized HOR/HER exchange current density of the catalyst would be expected to increase with increasing Pt coverage, and the HOR/HER activity maximum should occur only once at least all of the Ru core is fully encapsulated by Pt (i.e., once the Pt monolayer coverage is $\geq$1). This assumes that the HOR/HER kinetics on pure Ru are substantially

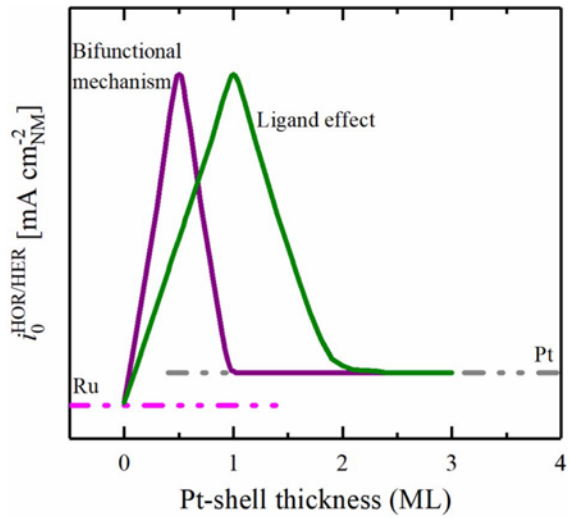

Figure 2. Theoretical trend of the HOR/HER activity (in mA cm^{-2}_{NM}) vs. Pt coverage of Ru@Pt core-shell catalysts in alkaline media for a purely bifunctional mechanism (purple line) compared to a purely electronic effect (green line). Reproduced from Schwämmlein et al. with permission of The Electrochemical Society.[22]

smaller than on pure Pt,[23,24] which indeed is the case and will be shown also in the following. Whether the hypothesized electronic effect of Ru on the Pt-H_{ads} BE is most beneficial for the first, the second, or any subsequent Pt overlayer would determine if a mono-, bi- or multi-layered Ru@Pt particle were to show the HOR/HER activity maximum. The optimum with respect to the amount of Pt overlayers depends mainly on the nature and range of the electronic effect of the Ru core and is not known so far. Nevertheless, Schlapka et al. showed by deposition of Pt on Ru(0001) that the electronic effect of Ru on the Pt-CO_{ads} BE is strongest in the first Pt monolayer (ML) and that it vanishes for ca. 3 monolayers and beyond.[25] If the same were true for the HOR/HER, we would expect an activity maximum anywhere between 1 and maximum 3 monolayers of Pt on Ru. Increasing the Pt shell thickness beyond this coverage would then have to lead to an activity decay, eventually approaching the activity of pure Pt.

In the following we will first describe briefly how the Ru@Pt catalysts with (sub-)monolayers of Pt were prepared as well as the design of the experiments. Secondly, the catalyst itself will be characterized by various physical-chemical (TEM) and electrochemical methods (CV, CO stripping) to finally determine the HOR/HER activity of all prepared Ru@Pt, Pt, and Ru catalysts via the rotating disk electrode (RDE) method in alkaline media.

Experimental

The synthesis of Ru@Pt core-shell nanoparticles, electrode, and ink preparation, as well as the setup and measurement procedure were already reported in a previous publication.[22]

Synthesis of Ru@Pt core-shell nanoparticles.—Ru was prepared from 4.2 mg $RuCl_3$ (45–55% Ru content, Sigma Aldrich Corp., Germany) and 2.1 mg Polyvinylpyrrolidone (PVP) (average $M_w \approx$ 55000 g mol^{-1}, Sigma Aldrich Corp., Germany) dissolved in 40 mL of water-free ethylene glycol (99.8%, anhydrous, Sigma Aldrich Corp., Germany), deaereated by argon (6.0-grade, Westfalen AG, Germany) and heated from room temperature to 155°C at a constant rate of 4°C min^{-1}. The temperature of the heating ramp was controlled by an automatic temperature control device (Model 310, J-KEM, Inc., USA). After keeping the temperature constant at 155°C for 90 min, the suspension was left to cool down to room temperature. Meanwhile, the respective amount (calculated according to Equation 4, using the desired monolayer equivalents of Pt and the mass of Ru, added during the synthesis) of high purity K_2PtCl_4 (99.99% [metals basis], Sigma Aldrich Corp., Germany) was dissolved in 40 mL of deaerated ethylene glycol, added at once to the Ru containing suspension at room temperature and stirred for 10 min. To deposit Pt on Ru, the mixture was heated another time to 155°C at the same rate as before and held at this temperature for 90 min. After the mixture has cooled down to room temperature, the Ru@Pt nanoparticles were added to Vulcan carbon (Tanaka Kikinzoku International K. K., Japan) dispersed in 80 mL ethylene glycol and stirred for 14 h. The amount of carbon used as support for core-shell nanoparticles was chosen to achieve a loading of 8%$_{wt}$ Ru@Pt. Subsequently, the suspension was mixed with acetone and centrifuged at 11500 rpm (10 min, 5°C) in an ultra-centrifuge (5810 R, Eppendorf GmbH, Germany) to separate the catalyst and the solvent. Then, the catalyst was washed three times with acetone, once in 2-propanol (Chromasolv Plus, 99.9%, Sigma Aldrich Corp., Germany) and finally dried at 70°C in air. For each Pt:Ru ratio to obtain various Pt shell thicknesses, the Ru core was synthesized freshly.

Electrode and ink preparation.—Glassy carbon (GC) electrodes (5 mm diameter, Pine Research Instrumentation, USA), supported by a PTFE-body (Pine Research Instrumentation, USA) were polished with 0.05 µm Al_2O_3 polishing suspension (Bühler AG, Germany), sonicated various times in ultrapure water (18.2 MΩ cm, Merck Millipore KGaA, Germany) and cleaned by subsequent dipping in 5 M KOH (99.99% purity, Semiconductor grade, Sigma Aldrich Corp., Germany), 2M $HClO_4$ (60%, Cica Reagent, Kanto Chemical Co., INC., Japan) and ultrapure water. Inks were prepared by adding

ultrapure water to the dry catalyst followed by high purity 2-propanol (Chromasolv Plus, 99.9%, Sigma Aldrich Corp., Germany). The solvent mixture consisted of 80%$_v$ 2-propanol and 20%$_v$ H_2O. The catalyst content of the ink was adjusted to achieve a very thin catalyst layer thickness of only ≈0.6 μm by choosing noble metal loadings of ≈2 μg_{NM} cm_{geo}^{-2} (corresponding to 0.022 mg_{Vulcan} cm_{geo}^{-2}, which at a packing density of ≈28 μm $(mg_{Vulcan}$ $cm_{geo}^{-2})^{-1}$ yields a thickness of ≈0.6 μm[26]) for HOR/HER kinetic measurements in alkaline electrolyte. For solely cyclic voltammetric measurements in acid electrolytes, higher loadings of ≈4.7 μg_{NM} cm_{geo}^{-2} were used, corresponding to film thickness of ≈1.5 μm. The catalyst suspension was sonicated for 30 min in a sonication bath (Elmasonic S 30 H, Elma Schmidbauer GmbH, Germany) to achieve a homogeneous dispersion. The temperature of the bath was maintained at less than 25°C to avoid evaporation of the solvent. Subsequently, Nafion (5%$_{wt}$ in lower aliphatic alcohols, 15–20% H_2O, Sigma Aldrich Corp., Germany) was added to the suspension resulting in an ionomer to carbon ratio of 0.15/1 g_I g_C^{-1}. Prior to coating, the ink was sonicated in a lower energy sonication bath (USC100T, VWR International GmbH, Germany) for at least 15 min. Finally, 7 μL of ink were dropped on a GC, covered with a small glass vial and left to dry at room temperature.

Setup and measurement procedure.—Electrolyte solutions were prepared from high purity NaOH · H_2O (99.9995% [metals basis], TraceSELECT, Sigma Aldrich Corp., Germany) or H_2SO_4 (Ultrapur, 96%, Merck Millipore KGaA, Germany) by addition of ultrapure water. Argon and hydrogen used for purging of the electrolyte were of high purity (6.0-grade, Westfalen AG, Germany); carbon monoxide (4.7-grade, Westfalen AG, Germany) was used for CO stripping voltammetry. The single-cell PTFE setup including the cleaning procedure prior to electrochemical measurements in alkaline environment was already described in an earlier work.[3] A home-made Ag/AgCl reference electrode, saturated with KCl (99.999% purity, Sigma Aldrich Corp., Germany) was used for measurements in alkaline electrolyte. For experiments in sulfuric acid, a glass cell was used with a reversible hydrogen electrode (RHE) as reference. The reference potential was calibrated in H_2-saturated electrolyte prior to every experiment using the platinum ring of the electrode. Independent of the reference electrode used during the measurement, all potentials in this publication are given with respect to RHE.

Electrochemical measurements were performed using an Autolab potentiostat (PGSTAT302N, Metrohm AG, Switzerland) and a rotator (Pine Research Instrumentation, USA) with a polyether ether ketone shaft. Prior to any activity determination measurements, catalysts were cleaned by cycling the potential 15 times between 0.05 and 0.8 V_{RHE} at 50 mV s^{-1}. Afterwards, the electrolyte solution was replaced by fresh 0.1 M NaOH and saturated with H_2. The resistance was determined by electrochemical impedance spectroscopy (EIS) from 100 kHz to 100 Hz at open circuit potential (OCP) with an amplitude of 10 mV. After fully saturating the electrolyte with H_2, polarization curves were recorded from −0.025 V_{RHE} to 0.800 V_{RHE} at 10 mV s^{-1} and 1600 rpm while the gas was set to blanketing. To calculate the exchange current density, i_0, the cathodic-going scans of the polarization curves in H_2-saturated electrolyte were evaluated. To determine the electrochemical surface area (*ECSA*), CO stripping was performed by applying a constant potential of 0.06 V_{RHE} and purging CO for 3 min. Subsequently, CO was removed from solution by Ar-purging for 20 min while the potential was kept constant. The adsorbed CO was oxidized in a CV from 0.05 to 1.00 V_{RHE} at a scan rate of 10 mV s^{-1}, starting at 0.06 V_{RHE}. The second CV was used as baseline to correct for the capacitance and the roughness factors (*rf*) were calculated from the resulting integral, using a specific charge of 420 μC cm_{NM}^{-2} (NM = noble metal).

TEM imaging.—Samples for TEM analysis were prepared by dispersing a very small amount of the catalyst in Milli-Q water and/or 2-propanol and then depositing a few drops of the dispersion on Formvar-supported carbon-coated Cu400 TEM grids (Science Services GmbH, Germany). Imaging was performed using a Philips CM100 EM operated at 100 kV and a resolution of 0.5 nm. TEM images taken with this device were used to establish a particle size distribution profile of each individual catalyst. Further high spatial resolution TEM experiments were performed on a FEI Scanning/Transmission Electron microscope equipped with a high brightness electron gun and a four segmented electron energy dispersive spectrometer (Super-X detector). Data using the high angle annular dark field (HAADF) detector in STEM mode were acquired at 300 kV with a low beam current of ≈60 pA to minimize damage/contamination effects.

Results and Discussion

Catalyst loading and TEM images.—In the course of this study, several Ru@Pt core-shell nanoparticles with varying Pt:Ru ratio were prepared via a polyol process and directly supported on Vulcan carbon. The Ru and Pt content of all samples was determined by elemental analysis via inductively coupled plasma mass spectroscopy based on two individual measurements of each element, including reference samples for Pt, Ru, and a mixture of Pt and Ru. Additionally, the carbon content of the catalysts was measured by oxidizing it to CO_2 at elevated temperatures in air. The resulting catalyst composition of all prepared Ru@Pt core-shell nanoparticles with respect to carbon, Pt and Ru content, as well as that for the plain Ru core and pure Pt, are given in Table I. The target Pt coverage or shell thickness in monolayers, termed monolayer equivalents (MLE), was achieved by controlling the molar ratio of the two noble metals in the Ru@Pt catalysts. The Pt-MLE on the Ru core was calculated according to the following equation. The derivation of this formula can be found in the appendix.

$$\mathrm{MLE} = \frac{\sqrt[3]{\frac{n_{Pt}\cdot\rho_{Ru}\cdot r_{Ru,particle}^{3}\cdot M_{Pt}}{n_{Ru}\cdot\rho_{Pt}\cdot M_{Ru}} + r_{Ru,particle}{}^{3}} - r_{Ru,particle}}{2\cdot r_{Pt,atom}} \quad [4]$$

where n is the molar quantity of either Pt or Ru determined via elemental analysis, ρ is the density of the metal (ρ_{Ru} = 12.45 g cm^{-3}, ρ_{Pt} = 21.45 g cm^{-3}), $r_{Ru,particle}$ is the radius of the Ru core formed in the synthesis, $r_{Pt,atom}$ is the radius of a single Pt atom (0.135 nm), and M is the molar mass of the respective metal (M_{Ru} = 101.1 g mol^{-1}, M_{Pt} = 195.1 g mol^{-1}). To determine the MLE of the Ru@Pt catalysts, a fully spherical Ru core with a diameter of $r_{Ru,particle}$ = 1.9 nm (corresponding to $\bar{d}_S$ in Table I) and no particle agglomeration were assumed. We would like to emphasize that the term MLE is merely a conceptual number. On the one hand, a catalyst with e.g., one MLE of Pt on Ru could consist of Ru particles with an exact diameter of 1.9 nm, covered with a single monolayer of Pt. On the other hand, the catalyst could be composed of a mixture of monolayered and bilayered Pt on Ru particles with different size, where the residual Ru surface remains uncovered. The Ru surface exposure, as well as the Pt shell composition are analyzed in more detail in a latter section of this manuscript.

Table I shows the series of prepared catalysts with increasing MLEs for Ru@Pt from 0.3 to 2.3 MLE, hence ranging from partially covered Ru nanoparticles all the way to catalysts with a sufficiently high Pt content to fully encapsulate the Ru core. The total metal content in all samples was determined to be between 7.5 and 8.6%$_{wt}$ with little deviation between the individual catalysts (see Table I). Furthermore, TEM images reveal that the catalyst is homogeneously distributed over the whole carbon support with a low degree of agglomeration between the individual catalyst particles (Figure 3a), as was observed for all of the prepared catalysts (data not shown). Based on measuring the size of more than 100 individual particles, the particle size distribution of all prepared samples was determined (Figure 4). The number-averaged ($\bar{d}_N$) and size-averaged ($\bar{d}_S$) diameters were calculated according to Equations 5 and 6:

$$\bar{d}_N = \frac{\sum_{i=1}^{n} l_i d_i}{\sum_{i=1}^{n} l_i} \quad [5]$$

Table I. Monolayer-equivalents (MLEs) for Ru@Pt catalysts calculated via the molar fraction of Pt and Ru in the catalyst by assuming a fully spherical Ru core with a diameter of 1.9 nm and a homogeneous Pt shell. The number-averaged ($\bar{d}_N$, see Equation 5) and the size-averaged ($\bar{d}_S$; see Equation 6) diameters were obtained from the TEM-based particle size distributions in Figure 4.

Catalyst	MLE [#]	Pt:Ru molar ratio	Pt content $\%_{wt}$	Ru content $\%_{wt}$	C content $\%_{wt}$	$\bar{d}_N$ nm	$\bar{d}_S$ nm
Pt	-	-	9.4	0	90.6	4.1	4.3
Ru	0	-	0	8.1	91.9	1.8	1.9
Ru@Pt	0.3	0.2	2.5	6.0	91.5	2.0	2.1
Ru@Pt	0.5	0.4	3.2	4.3	92.5	2.5	2.6
Ru@Pt	0.9	0.9	5.0	3.0	92.0	2.9	3.1
Ru@Pt	1.4	1.5	6.0	2.1	91.9	3.0	3.3
Ru@Pt	1.8	2.3	7.0	1.6	91.4	3.5	3.7
Ru@Pt	2.1	2.8	7.1	1.3	91.6	3.1	3.3
Ru@Pt	2.3	3.8	7.4	1.2	91.4	4.2	4.4

$$\bar{d}_S = \frac{\sum_{i=1}^{n} l_i d_i^3}{\sum_{i=1}^{n} l_i d_i^2} \quad [6]$$

where d_i is the measured diameter of the respective particle and l_i is the number of particles that have this diameter. The resulting diameters are listed in Table I. The TEM analysis shows that the Ru core has an average diameter of $\bar{d}_S = 1.9$ nm with a size distribution ranging from 1.2 to 2.6 nm (see upper panel of Figure 4). By depositing Pt on the Ru nanoparticles, the particle size distribution broadens (see Figure 4) and shifts toward larger diameters (see Table I).

A quantitative estimate of the Pt shell thickness on the basis of the particle size distribution is rather delicate due to various reasons. First, every synthesis of Ru@Pt was based on synthesizing a fresh batch of Ru nanoparticles on which Pt was deposited directly. Therefore, the exact particle size distribution of the Ru core might be slightly different from batch to batch, and the average diameter can also be slightly different from that given in Table I. Second, the resolution of the TEM instrument used to obtain the particle size distribution is in the order of an atomic monolayer (0.5 nm). Third, it is not known in which form Pt grows on Ru and if the Pt in the shell is already oxidized when the TEM measurement is performed. For these reasons, while the particle size distribution indicates the change in the Pt coverage/shell thickness with increasing Pt content, it is not sufficiently precise to determine the exact Pt shell thickness. Thus, in order to obtain further insight into the morphology of the prepared catalysts, high-resolution scanning transmission electron microscopy (STEM) images were taken. Figure 3b shows an image of a faceted core-shell nanoparticle of the Ru@$Pt_{0.9MLE}$ catalyst. It can be clearly observed that the particle in the focus of the STEM image shows two separate domains, a core and a shell with different brightness. Furthermore, spatially resolved energy-dispersive X-ray spectroscopy (EDS) of individual particles were collected on several samples. A comparison of the EDS profile of a Ru@Pt particle with a nominal coverage of 0.9 MLE (Figure 3c) with that with a nominal coverage of 1.8 MLE (Figure 3d) provides further evidence for an increase of the Pt content in the shell as the MLE value increases. Based on this consistency check, it is reasonable to assume that Figure 3c shows a Ru core, at least partially covered by a single Pt overlayer while Figure 3d shows a fully covered core-shell nanoparticle.

Electrochemical characterization by cyclic voltammetry.—As mentioned earlier, the determination of the surface composition of the prepared Ru@Pt core-shell nanoparticles is crucial to obtain an insight into the origin of the superior HOR/HER activity of bimetallic Pt-Ru catalysts. To distinguish between a bifunctional mechanism and an electronic effect, it has to be clarified whether Ru is exposed on the surface of the prepared particles or if it is fully encapsulated within a mono- or multilayered Pt shell. The formation and reduction of the oxide layer on the Ru metal in a CV in liquid electrolyte was used before by El-Sawy et al. to qualitatively describe the presence of Ru on the surface of partially covered Ru@Pt core-shell nanoparticles as well as fully Pt covered Ru nanoparticles.[27] Due to its oxophilicity, Ru is covered with an ad-layer of oxygenated species at potentials cathodic to those of platinum in aqueous electrolyte and no interference of the Pt oxide and Ru oxide reduction peaks is expected in a CV in base or acid electrolyte. Nevertheless, Ru oxidation and reduction in alkaline solution does not occur at a well-defined potential (see dash-dotted line in Figure 5a), distinct from the H_{upd} process on pure Pt or the Pt shell of Ru@Pt particles (Figures 5b and 5c). In contrast to this, a well-defined cathodic peak correlates with the reduction of the Ru oxide in dilute sulfuric acid at a potential of ≈280 mV_{RHE} (see solid line in Figure 5a).

Covering the Ru core with a small amount of Pt, e.g., at a level of 0.3 MLE in Ru@$Pt_{0.3MLE}$, causes a slight potential shift of the Ru oxide reduction peak to ≈320 mV_{RHE} (see black line in Figure 5b). This potential shift is tentatively assigned to the varied electronic structure of Ru nanoparticles covered with a small

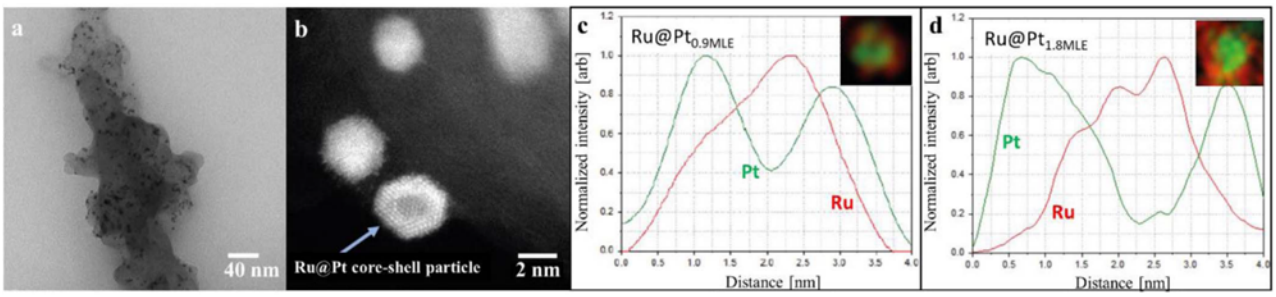

Figure 3. a) Representative TEM image of Ru@Pt, showing a catalyst with a Pt:Ru ratio of 0.9 (corresponding to the 0.9 MLE catalyst; see Table I) at a magnification of 73000x. Similar images were taken of all prepared catalysts and used to evaluate the particle size distribution of the samples. b) High resolution STEM image of a Ru@Pt catalyst with the same MLE of 0.9, showing a faceted core-shell structure. Results of an energy-dispersive X-ray spectroscopy (EDS) scan of individual catalyst particles are shown for c) Ru@$Pt_{0.9MLE}$ and d) Ru@$Pt_{1.8MLE}$.

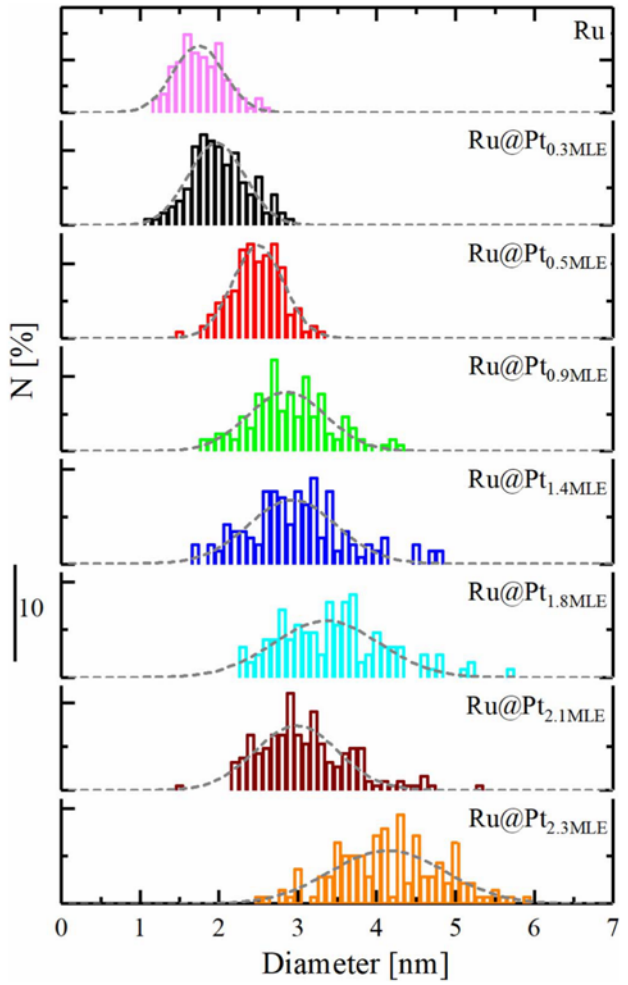

Figure 4. Particle size distribution in % of all measured particles for all prepared Ru@Pt/C catalysts, including pure Ru. The particle size distribution closely resembles a Gaussian distribution (gray dashed lines). For each catalyst, at least 100 particles were counted.

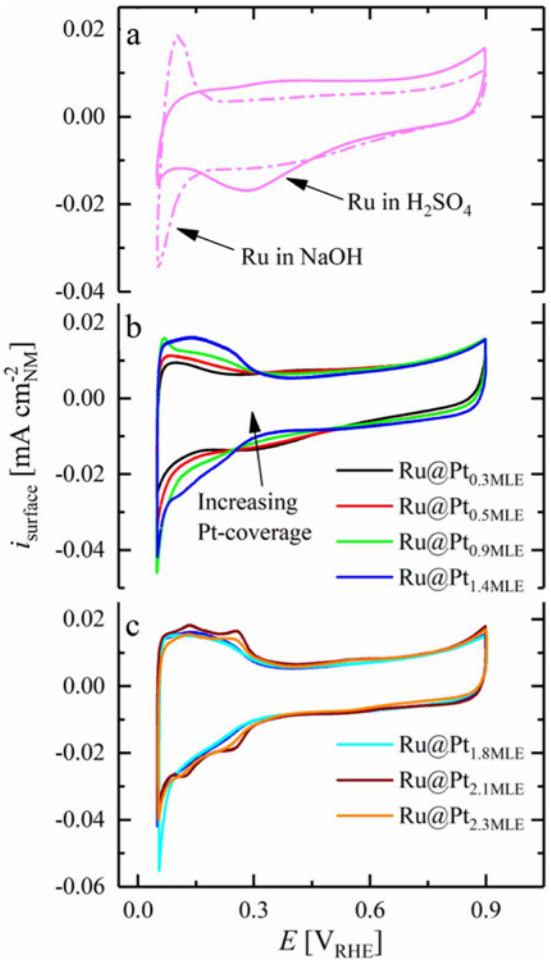

Figure 5. Cyclic voltammogram of a) Ru/C at 20 mV s^{-1} in Ar-saturated 0.1 M H_2SO_4 (solid line) and 0.1 M NaOH (dash-dotted line), respectively and of Ru@Pt/C core-shell nanoparticles with b) submonolayer and c) multilayer Pt shell in Ar-saturated 0.1 M H_2SO_4 at 20 mV s^{-1} (Pt coverages are given in the Figure in terms of their MLE values). All measurements were done at room temperature in stagnant electrolyte. The current obtained in the CV was normalized to the surface area of the catalyst, as determined by CO stripping voltammetry at the end of the CV measurements. Reproduced from Schwämmlein et al. with permission of The Electrochemical Society.[22]

amount of Pt with respect to pure Ru. The absence of a shoulder (at ≈280 mV_{RHE}) in the cathodic peak at 320 mV_{RHE} supports our initial assumption that Ru@Pt core-shell nanoparticles are free of pure Ru nanoparticles even for low Pt:Ru ratios. As the Ru core gets covered with larger amounts of Pt by increasing the Pt MLE value (i.e., the Pt:Ru ratio) of the catalysts, the surface normalized peak current density for the Ru oxide reduction decreases significantly (see Figure 5b), indicating the loss of Ru surface sites. At a Pt MLE value of 1.4 (blue line in Figure 5b), the Ru oxide reduction peak disappears entirely. The current in the cathodic scan of the CVs for Ru@Pt nanoparticles with higher Pt MLE values ($Ru@Pt_{1.8MLE}$, $Ru@Pt_{2.1MLE}$ and $Ru@Pt_{2.3MLE}$; see Figure 5c) matches well with that obtained for $Ru@Pt_{1.4MLE}$ at potentials more anodic than 390 mV_{RHE}. In accordance with this, for Ru@Pt particles with Pt MLE values of ≥1.4, no Ru surface sites can be detected any more. The threshold for completely covering the Ru core with Pt is theoretically expected to be at exactly 1 MLE for monodisperse Ru nanoparticles with a diameter of 1.9 nm, whereas 1.4 MLE was observed experimentally. This minor discrepancy, however, is likely related to the relatively broad particle size distribution of the Ru cores (from 1.2 to 2.6 nm, see Figure 4), as explained in the following. During Ru@Pt synthesis, the Pt ions, as well as the Ru nanoparticles are homogeneously distributed over the entire ethylene glycol solution. Therefore, the availability of $PtCl_4^{2-}$ ions to reductively deposit on the Ru particle surface is equal for all Ru nanoparticles. Nevertheless, the amount of Pt needed to fully cover a Ru nanoparticle depends strongly on its diameter. A small Ru particle can be easily covered by Pt, whereas the Pt precursor in the vicinity of a larger Ru particle is readily consumed when the reduction process is initiated without closing the monolayered Pt shell. Some of the excess Pt ions next to the small Ru nanoparticle can start to form a second Pt overlayer on it, since the distance to neighboring Ru particles is in some cases larger than that to the already covered nanoparticle. Hence, a Pt precursor concentration sufficient to form 1 MLE on a 1.9 nm Ru core, is not sufficient to cover larger Ru particles completely due to local starvation of Pt ions. Especially for higher Pt ion concentrations in the electrolyte which are required to prepare fully covered Ru nanoparticles, the final catalyst is expected to be a mixture of mono- and multilayered Ru@Pt core-shell nanoparticles. Despite these minor imperfections in the synthesis of Ru@Pt core-shell catalysts, we would like to emphasize that the difference between the ideally expected complete encapsulation of the Ru cores at 1 MLE of Pt and the observed complete encapsulation at 1.4 MLE of Pt is actually reasonably small considering all the experimental uncertainties.

Moreover, all CVs provided in Figure 5 correspond to steady-state measurements. The fact that the reductive peak remains absent in all CVs of fully Pt-covered Ru@Pt catalysts is a clear evidence that the core-shell structure remains intact upon potential application in the considered potential window.

With increasing Pt MLE values (i.e., increasing Pt:Ru ratios), anodic and cathodic peaks appear in the potential range from 80 to 250 mV_{RHE}, corresponding to the H_{upd} process on the Pt shell of Ru@Pt particles. Since the steep increase of the negative current at the most cathodic potential (50 mV_{RHE}) is due to the evolution of hydrogen, the maximum cathodic current at the lower potential limit in the Ar-saturated electrolyte can be used as a first indicator for the activity of the prepared Ru@Pt core-shell nanoparticles toward the HER. As shown in Figure 5c, the cathodic current at the lower potential limit increases with increasing Pt coverage, reaching a maximum at $Ru@Pt_{1.8MLE}$. At higher Pt:Ru ratios ($Ru@Pt_{2.1MLE}$ and $Ru@Pt_{2.3MLE}$), the cathodic current at the lower potential limit decreases again, thus indicating that these catalysts are less active towards the HER.

Pt shell composition by CO stripping voltammetry.—The thickness of the Pt shell of Ru@Pt core-shell nanoparticles can be determined by oxidation of CO_{ads} in deaerated liquid electrolyte, as will be outlined below, followed by a discussion of the past findings with regards to the CO stripping behavior on Pt-Ru surfaces. Bimetallic Pt-Ru alloys were used for CO oxidation by various researchers due to their high activity toward this reaction.[28–32] Studies on well-characterized alloy surfaces by Gasteiger et al. revealed that the overpotential necessary for the oxidation of CO_{ads} on Pt-Ru in 0.5 M H_2SO_4 is more than 200 mV lower compared to pure Pt, depending on the composition of the alloy.[28] Similar to others,[31,32] Gasteiger et al. attributed this effect to a bifunctional mechanism requiring the participation of both Pt and Ru surface sites in the oxidation process of CO.[28] According to the authors, the low overpotential necessary to oxidize CO on Ru frees these surface sites from CO_{ads} at comparably cathodic potentials. As mentioned earlier, Ru is oxidized at a moderate potential, thus covered by an oxide ad-layer right after the removal of CO from the surface. In the bifunctional mechanism that was proposed by the authors, the oxygen species on Ru aid the oxidation of CO_{ads} on neighboring Pt sites, hence promote the overall CO oxidation activity. Nevertheless, it remains unclear why the CO_{ads} oxidation potential on Pt-Ru alloys shifts even more cathodic with respect to that on pure Ru. In an intent to clarify this, Gasteiger et al. proposed that surface-bound oxygen species may cause a lowered overpotential for the oxidation of CO on Pt compared to a pure Ru surface.

Later on, other researchers showed that Ru@Pt core-shell nanoparticles are capable of oxidizing CO at potentials comparable to those found for Pt-Ru alloys in acid electrolyte.[13,27,33–35] For example, Ochal et al. reported a significant cathodic shift of the CO stripping peak from 0.8 V_{RHE} on pure Pt to 0.58 V_{RHE} on Ru@Pt in 0.5 M $HClO_4$.[33] Similar to Pt-Ru alloys, CO can be oxidized on Ru@Pt core-shell nanoparticles at a lower overpotential compared to pure Ru. The results of these groups indicate that the enhancement of the CO oxidation in the bimetallic Pt-Ru system is due to a modification of platinum's electronic structure by Ru rather than a bifunctional mechanism that involves both metals in the reaction mechanism. This fact also explains the finding by Gasteiger et al. that a low percentage of Ru atoms is sufficient to significantly enhance the oxidation of CO_{ads} on Pt-Ru alloys compared to pure Pt.[28] Furthermore, Ochal et al. reported a second peak in the CO stripping voltammogram at a significantly more anodic potential of 0.76 V_{RHE} and attributed it to small Pt impurities in their Ru@Pt catalyst, even though the potential is different from the CO_{ads} oxidation potential on pure Pt.[33] In 2014, El-Sawy et al. prepared a series of Ru@Pt catalysts with different Pt coverage/Pt shell thickness and utilized CO stripping voltammetry to qualitatively distinguish between $Ru@Pt_{1ML}$ and $Ru@Pt_{2ML}$.[27] They found two peaks related to the oxidation of CO_{ads}, viz., at 0.62 and 0.78 V_{RHE} in 0.5 M H_2SO_4, depending on the Pt shell composition of the Ru@Pt particles. In contrast to Ochal et al., El-Sawy et al. identified the two peaks to be associated with CO adsorbed on the first (referred to as $CO_{ads}{}^{A}$, with a peak potential at 0.62 V_{RHE}) and on the second (referred to as $CO_{ads}{}^{B}$, with a peak potential at 0.78 V_{RHE}) Pt overlayer of Ru@Pt particles. The different peak potentials for the oxidation of $CO_{ads}{}^{A}$ and $CO_{ads}{}^{B}$ on Ru@Pt can be explained by a different Pt-CO_{ads} BE on the first compared to that on the second Pt overlayer on Ru. These results are in accordance with those of Schlapka et al., who prepared a series of Pt layers on Ru(0001) with different thickness and determined their respective CO_{ads} desorption temperatures.[25] They reported the lowest CO_{ads}-desorption temperature for the first Pt overlayer on Ru and ascribed it to the electronic effect of the Ru substrate on Pt. Supported by DFT calculations, they showed that the Pt-CO_{ads} BE in subsequent Pt overlayers increases significantly, quickly approaching that of pure Pt as its coverage exceeds 2 monolayers.

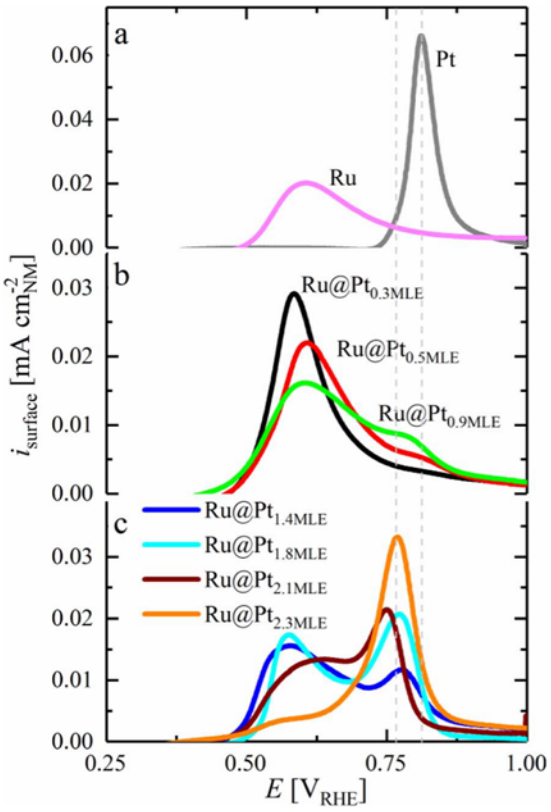

Figure 6. Baseline-corrected, surface normalized CO stripping voltammograms of different Ru@Pt/C, Ru/C and Pt/C catalysts in Ar-saturated 0.1 M H_2SO_4 at 10 mV s^{-1}. Prior to CO-stripping, CO was adsorbed at 0.06 V_{RHE} for 3 min, followed by purging the solution with Ar for 20 min. Reproduced from Schwämmlein et al. with permission of The Electrochemical Society.[22] The dashed gray lines indicate the peak potential for the oxidation of CO on pure Pt (0.81 V_{RHE}) versus the peak oxidation potential for $CO_{ads}{}^{B}$ (0.77 V_{RHE}).

In the present study, the method developed by El-Sawy et al. is used to determine the thickness of the Pt shell in Ru@Pt particles in 0.1 M H_2SO_4 and to compare it to the bare Ru core and Pt nanoparticles prepared by the same method (Figure 6a). Ru@Pt particles with a low Pt coverage of 0.3 MLE (black line in Figure 6b) show only a single anodic peak for the oxidation of $CO_{ads}{}^{A}$ on the first Pt layer on Ru. Similar to Pt-Ru alloys,[28] no additional peak is found for the oxidation of CO_{ads} on surface Ru sites for partially Pt covered Ru@Pt particles. Furthermore, no oxidation peak occurs in any of the Ru@Pt catalysts at the oxidation potential of CO adsorbed on pure Pt at 0.81 V_{RHE} (Figure 6a), confirming once more that the synthesis did not yield pure Pt particles in detectable quantities. Increasing the Pt:Ru ratio in the synthesis process towards a full Pt-MLE ($Ru@Pt_{0.5MLE}$ and $Ru@Pt_{0.9MLE}$) causes the emergence of a second peak at 0.77 V_{RHE}. According to the work of El-Sawy et al.,[27] this anodic current is

assigned to the oxidation of $CO_{ads}{}^{B}$ on the second Pt overlayer. Catalysts with higher Pt:Ru ratio (Figure 6c) show an increasing $CO_{ads}{}^{B}$:$CO_{ads}{}^{A}$ ratio, as expected due to the increasing coverage of the first Pt layer (1st monolayer) with an additional Pt overlayer (2nd monolayer). However, here it should be noted that the occurrence of $CO_{ads}{}^{B}$ on Ru@$Pt_{0.9MLE}$ particles which nominally should not yet have a fully Pt covered Ru core is due to the above discussed issue that a nominally 0.9 MLE coverage for not perfectly mono-dispersed Ru cores will lead to the partial formation of a second Pt overlayer on the smaller Ru core particles. The catalyst with the largest Pt:Ru ratio (Ru@$Pt_{2.3MLE}$) consists nearly exclusively of $CO_{ads}{}^{B}$, indicated by the very small current in the CO stripping voltammogram which is ascribed to $CO_{ads}{}^{A}$ (i.e., at 0.6 V_{RHE}). While this minor discrepancy between nominal/average and actual Pt coverage will have to be kept in mind in our further analysis, the overall agreement between the expected nominal Pt coverage and the observed Pt coverage distribution (on the order of several tenths of a monolayer) is quite reasonable. The difference of the peak positions for $CO_{ads}{}^{A}$ (≈0.60 vs 0.62 V_{RHE}) and $CO_{ads}{}^{B}$ (0.77 vs 0.78 V_{RHE}) between this study and that of El-Sawy et al.[27] may originate in parts from the accuracy of the reference electrode calibration and from slightly varied synthesis routes used to prepare the Ru core. Furthermore, since the differences in the Pt-CO_{ads} BE becomes smaller as the amount of Pt layers on Ru increases,[25] it might be experimentally difficult to resolve a difference between the second vs. the third Pt layer by CO stripping voltammetry.

HOR/HER activity in alkaline electrolyte.—The kinetics of Ru@Pt core-shell nanoparticles toward the HOR/HER were determined via the well-established RDE method in H_2-saturated 0.1 M NaOH, as described in an earlier publication.[22] While this technique does not allow the determination of the exchange current density of catalysts with intrinsically high HOR/HER kinetics (e.g., Pt in acid electrolyte) due to limitations by H_2 mass-transport resistances,[2] it was nevertheless shown that the HOR/HER exchange current densities in the low mA cm_{NM}^{-2} range can be accurately extracted using this technique.[3,9] To evaluate the kinetics of Ru@Pt catalysts precisely and reliably, the roughness factor of the used electrodes needs to be as low as possible in order to increase the ratio of kinetic/mass-transport resistance contributions to the observed voltage losses.[2] To obtain a low total noble metal content on the electrode, all samples were supported on carbon with a comparably low loading of roughly 8%$_{wt}$ and the film thickness was chosen to be ≈0.6 μm. Accordingly, the prepared coatings had an overall noble metal content of approximately 2 μg_{NM} cm_{geo}^{-2}, corresponding to roughness factors on the order of 1–2 cm_{NM}^{2} cm_{geo}^{-2} as determined by CO stripping. Despite the small film thickness, the quality of the films was sufficient for activity measurements and we did not observe limitations or artifacts due to film quality. Figure 7 shows a representative RDE data set for the HOR/HER in 0.1 M NaOH under pure H_2 at 25°C for the Ru@$Pt_{0.3MLE}$ catalyst at 1600 rpm, with a limiting current of ≈2.5 mA cm_{geo}^{-2}, as expected for these conditions[3] (essentially identical limiting current densities were obtained for all catalysts). It shall be mentioned at this point, that no difference was observed between subsequent cycles in CVs to determine the HOR/HER activity. This again underlines the previously stated stability of the prepared Ru@Pt core-shell under operating conditions.

For the determination of the exchange current density, we followed the same approach as Rheinländer et al.,[3] assuming that the HOR/HER kinetics on Ru@Pt follow the Butler-Volmer relation:

$$i_{kin} = i_0 \cdot rf \cdot \left(e^{\frac{\alpha_a \cdot F}{R \cdot T} \cdot \eta} - e^{-\frac{\alpha_c \cdot F}{R \cdot T} \cdot \eta} \right) \quad [7]$$

with the kinetic current i_{kin}, the exchange current density i_0 (in A cm_{NM}^{-2}), the roughness factor *rf*, the Faraday Constant *F*, the reaction overpotential η, the ideal gas constant *R*, the temperature *T*, and the anodic/cathodic transfer coefficients α_a and α_c, respectively. For small overpotentials, in the so-called micro-polarization region, the Butler-Volmer equation can be simplified using the mathematical approximation $e^x \approx 1 + x$ to obtain the following equation:

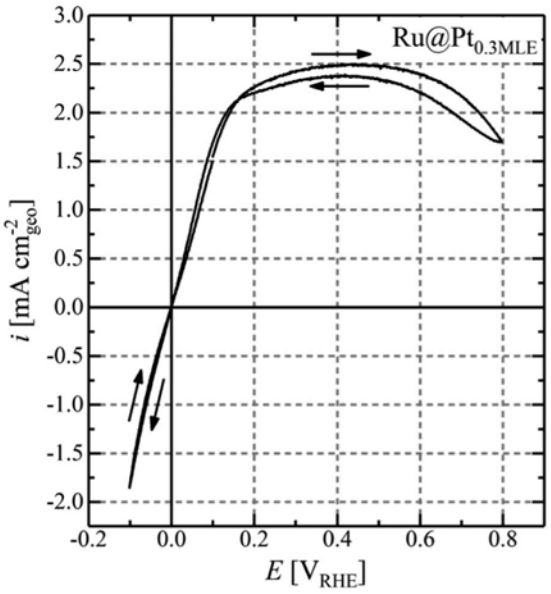

Figure 7. Anodic and cathodic scan (scan direction indicated by arrows in the graph) of a steady-state CV for Ru@$Pt_{0.3MLE}$/C in H_2-saturated 0.1 M NaOH at a scan rate of 10 mV s^{-1} and a rotation rate of 1600 rpm (25°C). The total metal (Pt+Ru) loading on the disk was 1.28 mg_{NM} cm_{geo}^{-2}. The obtained raw data was solely corrected for the reference electrode potential. The HFR determined via EIS was 40.2 Ω.

$$i_{kin} \approx i_0 \cdot rf \cdot \frac{(\alpha_a + \alpha_c) \cdot F}{R \cdot T} \cdot \eta \quad [8]$$

This linearized form of the Butler-Volmer equation can be helpful to determine the exchange current density, whereby it is also here essential that contributions from mass-transport and ohmic resistances to the measured current density have been accounted for, i.e., that the modeled current truly represents the kinetic current. The disadvantage of the kinetic analysis in the micro-polarization region (i.e., using Equation 8) is, however, that i_0 can only be extracted this way if the sum of alphas (i.e., $\alpha_a + \alpha_c$) is known. Quantification of the α-values, on the other hand, requires determination of the Tafel slope (*b*) at large anodic or cathodic overpotentials, where the exponential term for the reverse reaction can be neglected.

$$b = \frac{2.303 \cdot R \cdot T}{\alpha_{a,c} \cdot F} \quad [9]$$

For HOR/HER on carbon-supported Pt in a PEMFC, anodic and cathodic transfer coefficients of 0.5 were determined by Durst et al.[2] (between 313 and 353 K), corresponding to $\alpha_a + \alpha_c = 1$. These α-values suggest that the HOR/HER on Pt in acidic media follows the simplest possible electrochemical case of a single-electron transfer process as rate-limiting step. This assumption holds also true for the HOR/HER in alkaline electrolyte according to Sheng et al.[4] and Rheinländer et al.[3] who determined $\alpha_a = \alpha_c = 0.5$ on Pt by the RDE technique. However, depending on the catalytic material, the electrolyte, and the respective reaction, a variety of different Tafel slopes have been reported in literature, e.g., ≈60 mV dec^{-1} for the ORR on Pt and Pt based alloys in acid.[36] For this reason, the value of the transfer coefficients or at least of $\alpha_a + \alpha_c$ must be determined for a given reaction system (catalyst, electrolyte, reaction) in order to be able to extract exchange current densities from an analysis of the kinetics in the micro-polarization region.

In the following, the sum of alphas for the HOR/HER on Ru@Pt core-shell nanoparticles in alkaline media is identified by fitting the experimentally obtained polarization curve, after the appropriate mass-transport and ohmic resistance corrections, to the Butler-Volmer

equation. The Ru@$Pt_{0.3MLE}$ catalyst is used as a model for the series of prepared Ru@Pt catalysts, since its moderate activity enables fitting of the HOR/HER polarization curve to sufficiently high overpotentials, so that Tafel slopes (and thus α_a and α_c values) can be obtained. Fitting the corrected data of more active Ru@Pt catalysts (e.g., Ru@$Pt_{1.8MLE}$) to the Butler-Volmer equation cannot be carried out in a trustworthy fashion, since their high activity, even at low *rf* values, yields high current densities at already small overpotentials, so that mass-transport resistance free, kinetic currents cannot be extracted at overpotentials which would be high enough to obtain a meaningful transfer coefficient. Here it should be noted that due to the approximate nature of the RDE transport corrections, it is not sensible to extract kinetic data in a region where the measured and the transport-limited current are very similar; therefore, our kinetic data were only extracted for measured currents which are not larger than 80% of the transport-limited current, as suggested by Rheinländer et al.[3] To obtain the true HOR/HER kinetic currents from the raw data shown in Figure 7, several mass-transport and ohmic resistance corrections must be applied. Here, we will follow the approach taken by Rheinländer et al.,[3] which will be outlined briefly below.

To account for the effects of concentration gradients on the HOR/HER kinetics, the measured current needs to be modified according to Equation 10.[3]

$$i_{kin} = i_{meas} \cdot \left(1 - \frac{i_{meas}}{i_{lim}}\right)^{-m} \quad [10]$$

where the measured current is i_{meas}, where the diffusion limited current is i_{lim}, and where the reaction order of the HOR/HER is m. This equation assumes the presence of a concentration gradient, which in the case of the HOR branch of the polarization curve is caused by the depletion of dissolved H_2 near the electrode surface. However, in the case of the HER branch, this correction would only be valid, if supersaturation of H_2 in the electrolyte would occur (OH^- or H_2O transport are not limiting at the typically used current densities in RDE experiments), which was shown to not be the case;[3] therefore, currents in the HER branch are corrected by Equation 10. For poly-crystalline Pt, the dependency of the exchange current density on the H_2 concentration was reported by Rheinländer et al.[3] and in accordance with their results, m = 0.5 was used for all calculations in this study. To obtain the potential at the electrode/electrolyte interface, the resistance of the electrolyte solution in the respective setup needs to be accounted for according to Equation 11:

$$E_{iR-free} = E_{meas} - I \cdot R_{HFR} \quad [11]$$

The high frequency resistance R_{HFR} used for this calculation was determined individually for every experiment by electrochemical impedance spectroscopy (the value of R_{HFR} was on the order of ≈45 Ω). Lastly, the measured potential needs to be corrected for the shift of the reversible potential for the HOR/HER caused by the current-dependent depletion of the H_2 concentration in the vicinity of the electrode (again, this correction will only be applied to the HOR branch, as we assume that there is no supersaturation of dissolved H_2 in the HER branch[3]).

$$E_{iR-free}^{\eta_{diff}-free} = E_{iR-free} + \frac{R \cdot T}{2 \cdot F} \ln\left(1 - \frac{i_{meas}}{i_{lim}}\right) \quad [12]$$

The cathodic-going scan of the steady-state polarization curve collected for Ru@$Pt_{0.3MLE}$ in H_2-saturated alkaline electrolyte was treated accordingly and the absolute value of the HOR/HER current density was plotted on a logarithmic current scale (black crosses in Figure 8) versus $E_{iR-free}^{\eta_{diff}-free}$. As mentioned above, this analysis performed for Ru@$Pt_{0.3MLE}$ serves as a model for all prepared Ru@Pt catalysts in this study, since its moderate activity compared to the other Ru@Pt catalysts simplifies the fitting up to larger overpotentials with small error.

These kinetic data were then fitted to the Butler-Volmer equation (fitting as logarithm of the current vs. the corrected potential) in three different ways by fixing a) $\alpha_a + \alpha_c = 1$ (green line), b) $\alpha_a + \alpha_c = 2$ (red), and, c) treating α_a and α_c as individual free parameters without

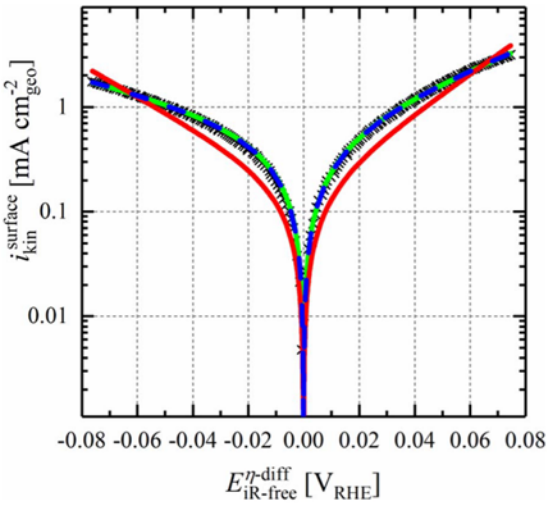

Figure 8. Tafel plot showing the kinetic currents in the cathodic-going scan (black crosses) for the HOR/HER on Ru@$Pt_{0.3MLE}$ core-shell nanoparticles in H_2-saturated 0.1 M NaOH at a scan rate of 10 mV s^{-1} and a rotation rate of 1600 rpm. All experiments were conducted at 298 K and ambient pressure. The potential was corrected for the solution resistance determined by electrochemical impedance spectroscopy (see Eq. 11), as well as for the potential shift due to the diffusion overpotential with respect to the applied current (see Eq. 12). The measured current in the HOR branch was corrected according to Equation 10. The experimentally obtained data were fitted to the Butler-Volmer equation (Equation 7) by: a) fixing the sum of alphas to 1 (green line); b) fixing the sum of alphas to 2 (red line); and, c) treating α_a and α_c as freely variable individual parameters (blue dashed line).

constraints (blue). For Ru@$Pt_{0.3MLE}$, fixing $\alpha_a + \alpha_c = 1$ resulted in an excellent fit of the measured data (green line in Figure 8) with $r^2 = 0.983$ and α-values of $\alpha_a \approx 0.6$ and $\alpha_c \approx 0.4$, indicating that the HOR possibly proceeds at a slightly faster rate than the HER on the tested catalyst. Nevertheless, these values represent a more or less symmetric HOR/HER reaction similar to pure poly-crystalline Pt.[3] No meaningful fit was obtained for $\alpha_a + \alpha_c = 2$ (red line), suggesting that the HOR/HER does not occur by a simultaneous two-electron transfer on Ru@Pt. As a proof of concept, α_a and α_c were also fitted as individual independent parameters (blue dashed line), yielding a fit which superimposes with that for which $\alpha_a + \alpha_c = 1$ was pre-defined, and also yielding values of $\alpha_a \approx 0.6$ and $\alpha_c \approx 0.4$. A HOR/HER exchange current density of $i_0^{298K} = 0.57$ mA cm_{NM}^{-2} was obtained by the fit where the sum of alphas was fixed to 1, hence comparable to that of pure Pt ($i_0^{313K} = 1.0$ mA cm_{Pt}^{-2};[10] $i_0^{293K} = 0.55$ mA cm_{Pt}^{-2};[3] $i_0^{294K} = 0.57$ mA cm_{Pt}^{-2};[4] $i_0^{313K} = 1.78$ mA cm_{Pt}^{-2};[9]). Summarizing the above analysis, we can state that the sum of alphas for the Ru@Pt core-shell nanoparticles is clearly 1, which enables an extraction of the exchange current density also from the micro-polarization region according to Equation 13.

$$i_{kin} \approx i_0 \cdot \frac{rf \cdot F}{R \cdot T} \cdot E_{iR-free}^{\eta_{diff}-free} \quad [13]$$

Thus, the exchange current density can be obtained directly by plotting the kinetic current versus the η_{diff} and iR-corrected potential between -5 and 5 mV_{RHE}. The linear fit of the data crosses the y-axis at $i = 0$ and the slope yields i_0 for the HOR/HER, since all other parameters in Equation 13 are known. Again, for the analysis of the measured data, we did not correct the HER-branch for η_{diff}.[3]

The evaluation of the micropolarization region yielded a HOR/HER exchange current density of $i_0^{298K} = 0.47 \pm 0.01$ mA cm_{Pt}^{-2} for pure Pt (Figure 9a), which is in reasonable agreement with those reported by other groups.[3,4,9,10,38,39] It was also reported before, that the HOR/HER activity of pure Ru in alkaline environment is rather poor and the current ceases quickly as the oxide is formed on the metallic

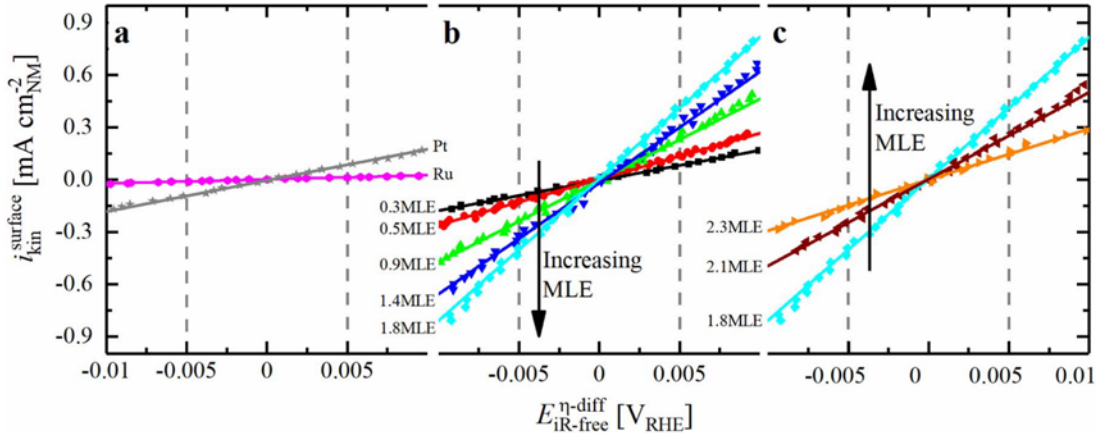

Figure 9. Cathodic-going scans (points), including linear fits (lines) in the micro-polarization region for different Ru@Pt/C, Ru/C and Pt/C catalysts at 10 mV s^{-1} in H_2-saturated 0.1 M NaOH at 1600 rpm. All measurements were carried out at 298 K, corrected for the ohmic drop and normalized to the total noble metal surface obtained from CO stripping voltammetry in NaOH. a) Reference catalysts, b) catalysts with increasing and c) decreasing HOR/HER activity. The most active catalyst (Ru@Pt$_{1.8\mathrm{MLE}}$) is shown in b) and c). Reproduced from Schwämmlein et al. with permission of The Electrochemical Society.[22]

surface.[17] Covering Ru with a fraction of a Pt-ML (Ru@Pt$_{0.3\mathrm{MLE}}$) increases the HOR/HER current significantly compared to pure Ru (Figure 9b), and a decrease of the HOR current density due to oxide formation is not noted until >0.4 V (see Figure 7). Similar to the exchange current density obtained by fitting the data to the Butler-Volmer equation, evaluation of the micro-polarization region yields an exchange current density of $i_0^{298\mathrm{K}} = 0.54 \pm 0.12$ mA cm$^{-2}_{\mathrm{NM}}$ (using Equation 13), consistent with the above presented fitting procedure. The HOR/HER exchange current densities obtained from the micro-polarization region for all of the here tested materials as well as for some comparable materials from the literature are summarized in Figure 10 (normalized to the total metal surface area (a), the total mass of noble metal (b), or the mass of Pt (c)). The high HOR/HER activity of Ru@Pt$_{0.3\mathrm{MLE}}$ despite the small amount of Pt in this catalyst confirms reports on the beneficial effect of Pt adatoms on a Ru surface with respect to the HOR/HER activity.[16] Furthermore, the high activity of the Ru@Pt$_{0.3\mathrm{MLE}}$ catalyst is similar to that reported for both partially covered Ru@Pt core-shell nanoparticles and Pt-Ru alloys.[17,18,37] It is especially noteworthy that the total surface area normalized exchange current density for the Ru@Pt$_{0.3\mathrm{MLE}}$ catalyst with only ≈30% Pt coverage (the absence of bi-layered Pt is supported by the above CO stripping analysis) is essentially the same as that of pure Pt (solid black square vs. solid gray asterisk is Figure 10a), demonstrating that each Pt surface atom in the Ru@Pt$_{0.3\mathrm{MLE}}$ catalyst is ≈3-4 times more active than Pt surface atoms in pure Pt.

Increasing the Pt:Ru ratio leads to an increase of the surface normalized HOR/HER activity of Ru@Pt catalysts, with a maximum exchange current density of 2.14 ± 0.05 mA cm$^{-2}_{\mathrm{NM}}$ for Ru@Pt$_{1.8\mathrm{MLE}}$ (light blue diamond in Figure 10a), that has a fully closed Pt shell. This is in good agreement with the statement that Pt is roughly 4 times more active if it is deposited on Ru compared to a pure Pt particle ($i_0^{298\mathrm{K}} = 0.47 \pm 0.01$ mA cm$^{-2}_{\mathrm{Pt}}$; solid gray asterisk in Figure 10a). The HOR/HER activity of catalysts with larger Pt:Ru ratio (Ru@Pt$_{2.1\mathrm{MLE}}$ and Ru@Pt$_{2.3\mathrm{MLE}}$) decreases with respect to the most active Ru@Pt catalysts (see Figure 1a). The fact that a fully Pt covered Ru core, where Ru is not exposed to the surface of the particle, has the highest HOR/HER exchange current density if normalized to the total metal surface area in conjunction with the absence of a HOR/HER activity drop after the completion of the first Pt overlayer (i.e., for Ru@Pt catalysts with Pt-MLE ≥ 1.4) clearly proves that the participation of Ru as active surface site in the catalysis of the HOR/HER is not the major reason for the high activity of the bimetallic Pt-Ru system. Hence, the presented data reveal that the HOR/HER on bimetallic Pt-Ru catalysts does not follow a bifunctional mechanism and that the activity enhancement with respect to Pt must be caused by an electronic effect of Ru on Pt.

In addition to this finding, it is of great interest to identify whether the first or the second Pt overlayer on Ru is most active towards

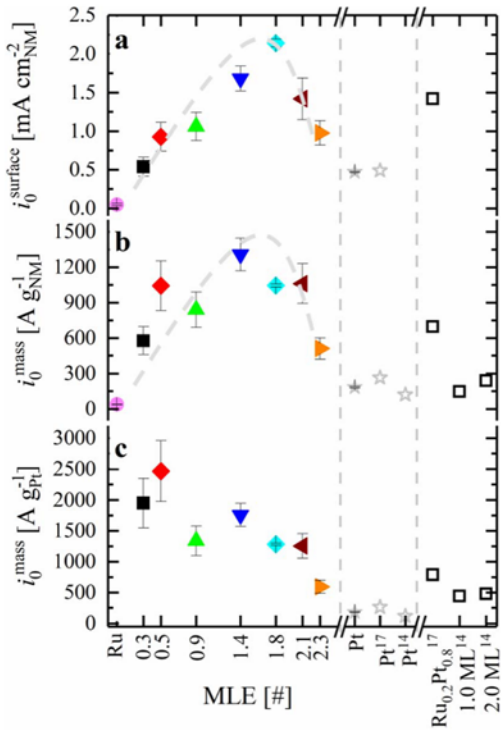

Figure 10. HOR/HER activity, obtained by linear fitting in the micro-polarization region (Eq. 13) for Ru@Pt/C with varying Pt-shell thickness, Ru/C and Pt/C catalysts in 0.1 M NaOH with respect to a) surface area of noble metals obtained by CO stripping, b) total mass of noble metals and c) mass of Pt. Hollow symbols show data published in the literature (the respective article references are marked by the superscripts). All values are based on at least three independent measurements of different coatings of the same catalyst, while error bars indicate the standard deviation of the individual values. The gray dashed line in a) is simply a guide-to-the-eye line.

the HOR/HER. However, CO stripping showed that the most active catalyst of this study (Ru@$Pt_{1.8MLE}$) is composed of a mixture of mono- and multilayered Pt on Ru. Nevertheless, the low activity of Ru@$Pt_{2.1MLE}$ (i_0 = 1.4 ± 0.3 mA cm_{NM}^{-2}) and Ru@$Pt_{2.3MLE}$ (i_0 = 1.0 ± 0.2 mA cm_{NM}^{-2}) compared to Ru@$Pt_{1.8MLE}$ (2.1 ± 0.1 mA cm_{NM}^{-2}) indicates that the first Pt overlayer on Ru is more active than subsequent ones, since especially Ru@$Pt_{2.3MLE}$ is basically exclusively composed of multilayered Pt on Ru with a very small fraction of monolayered Pt. Also Schlapka et al. reported that the electronic effect of Ru on a Pt overlayer is strongest for the first layer, followed by the second one and largely vanishes for more than three layers.[25] While they studied the temperature dependent desorption of CO_{ads} from the Pt surface, a very different process compared to the HOR/HER reactions studied in this publication, the lower overpotential needed for both processes on Pt-Ru compared to Pt seems to be caused by a downshift of the platinum d-band center by nearby Ru atoms and an associated lower binding energy toward the adsorbate. In comparison with the HOR/HER exchange current density of Pt-Ru alloys in alkaline media, e.g., an $Ru_{0.2}Pt_{0.8}$ alloy prepared by St. John et al., Ru@$Pt_{1.8MLE}$ core-shell nanoparticles exhibit slightly superior activity, while both systems are within a similar range (Figure 10a).[17] This provides further evidence that the activity enhancement of Pt-Ru alloys towards the HOR/HER in alkaline media is due to an electronic effect of Ru on Pt, similar to that hypothesized above for our Ru@Pt core-shell nanoparticles. The fact that the HOR/HER surface area normalized activity of Ru@Pt is slightly superior to that of an alloy may originate from the missing Ru surface sites in a core-shell nanoparticles since Ru contributes to the total noble metal surface area while having a low HOR/HER activity. All in all, this shows the advantage of a core-shell configuration compared to a bimetallic alloy with respect to the catalytic activity.

Normalizing the measured HOR/HER activity to the mass of Pt or to the total mass of noble metal can provide further insights into the catalysts properties and the distinction between a bifunctional mechanism and an electronic effect, whereas the analysis of this data is somewhat more complex. In an idealized scenario, Pt would grow homogeneously on perfectly monodispersed Ru cores and a second Pt layer would form only after the first Pt monolayer is completed. For such idealized surfaces and for a reaction mechanism based on an electronic effect, the HOR/HER activity normalized to the mass of platinum of the Ru@Pt core-shell particles (in A g_{Pt}^{-1}) would be expected to be identical for all catalysts composed of a partial up to a full Pt monolayer on Ru, since the activity per Pt surface atom in the first monolayer would be constant. Upon formation of a second Pt layer, the Pt mass activity would have to decrease, since the Pt atoms in the first monolayer, which are covered, cannot contribute to the HOR/HER, whereas their mass is taken into account for the normalization. In addition, based on the low HOR/HER activity of Ru@$Pt_{2.1MLE}$ (i_0 = 1.4 ± 0.3 mA cm_{NM}^{-2}) and Ru@$Pt_{2.3MLE}$ (i_0 = 1.0 ± 0.2 mA cm_{NM}^{-2}) shown in Figure 10a, Pt atoms in the second layer are significantly less active compared to those in the first layer, enhancing the activity decrease when a second Pt overlayer is being formed on the first one. Assuming that the electronic effect decreases further in the third Pt layer, an additional activity decrease with respect to the mass of Pt is expected for multilayered Ru@Pt catalysts. Comparing this idealized scenario to the data shown in Figure 10c, the two catalysts with the lowest Pt coverage (Ru@$Pt_{0.3MLE}$ and Ru@$Pt_{0.5MLE}$) show the highest Pt mass activity for the HOR/HER in this study (i_0 = 1950 ± 400 A g_{Pt}^{-1} and i_0 = 2470 ± 490 A g_{Pt}^{-1}). Furthermore, the activity of these catalysts is reasonably similar with respect to the error of the measurement, as expected for submonolayer Ru@Pt catalysts. In contrast to this, the activity of Ru@$Pt_{0.9MLE}$ is considerably lower (i_0 = 1340 ± 240 A g_{Pt}^{-1}), even though for a purely electronic effect an equally high Pt mass activity would have been expected for this catalyst with a nominal MLE of less than 1. At this point, however, the imperfection of the synthesis process needs to be taken into account, i.e., the polydisperse particle size distribution of the Ru core causes a partial growth of the second Pt layer on the Ru@$Pt_{0.9MLE}$ catalyst before the first overlayer is completed (refer to green lines in Figures 5b and 6b). According to the above given rationale, the growth of a second Pt layer leads to a significant decrease of the Pt mass activity, which we believe is the reason for the observed low Pt mass activity of the Ru@$Pt_{0.9MLE}$. catalyst. Since the Ru core is not fully covered by Pt in the Ru@$Pt_{0.9MLE}$ catalyst, the overall Pt mass activity can be increased by covering the remaining uncovered Ru sites, hence increasing the amount of monolayered Pt atoms in the catalyst compared to bilayered Pt atoms. Accordingly, a slightly larger exchange current density normalized to the mass of Pt was found for Ru@$Pt_{1.4MLE}$ (i_0 = 1760 ± 190 A g_{Pt}^{-1}), which is the first catalyst in the series that does not expose Ru on its surface (blue line in Figure 5b). As the MLE increases further, the first Pt layer gets gradually covered, leading to a decrease of the Pt mass activity.

In a similar fashion, an idealized scenario can be developed with respect to a normalization of the HOR/HER activity by the total mass of noble metal (A g_{NM}^{-1}), i.e., Pt + Ru. On the one hand, the activity is expected to increase with the amount of Pt deposited on Ru for (sub-)monolayer Ru@Pt catalysts, since the fraction of active Pt compared to inactive Ru increases. Hence, the maximum activity with respect to the total noble metal content should be found for a Ru particle which is fully encapsulated by a Pt monolayer. On the other hand, an activity decay takes places when the growth continues and bilayered Ru@Pt forms, according to the same reasoning described earlier: the second layer is less active and covers the first one, thus hindering its participation in the HOR/HER while contributing to the total weight of the catalyst. Compared to a normalization to the Pt mass alone, the activity decrease due to the formation of the second overlayer is expected to be less pronounced when normalizing to the total mass of noble metal, since the constant weight of the Ru core is also taken into account. As a consequence, the activity trend is expected to be similar to that in Figure 10a, where the exchange current density is normalized to the total surface area of the catalyst. We essentially find this, when looking at Figure 10b (i_0 in A g_{NM}^{-1}), with the difference that the maximum is found for Ru@$Pt_{1.4MLE}$ (1309 ± 138 A g_{NM}^{-1}) instead of Ru@$Pt_{1.8MLE}$ (1045 ± 14 A g_{NM}^{-1}), what we tentatively ascribe to a minor fraction of multilayered Pt in Ru@$Pt_{1.8MLE}$. Similar to the emergence of the second Pt overlayer on the first one, the third layer renders the Pt that it covers inactive since it is not exposed on the surface, eventually causing a slight decrease of the overall activity. It is stated here as a reminder, that the "hidden" Pt layers are not taken into account when normalizing the activity to the total surface of the catalyst, as Ru and Pt atoms that are not exposed will not participate in the CO stripping.

To summarize, the presented data conclusively shows that the actual origin of the high HOR/HER activity in the bimetallic Pt-Ru system is mainly due to an electronic effect rather than a bifunctional mechanism, rationalized by the observation that the most active catalysts (Figure 10a, blue triangle and turquoise diamond) with respect to the surface area (mA cm_{NM}^{-2}) do not expose Ru on their surface (Figure 5b, blue and turquoise lines). Compared to the only other study on the HOR/HER activity of Ru@Pt core-shell nanoparticles in alkaline media by Elbert et al. (Figures 10b and 10c, hollow, black squares), the most active catalyst in this study shows a more than fivefold higher activity with respect to the total mass of noble metal (1309 ± 138 A g_{NM}^{-1} for Ru@$Pt_{1.4MLE}$ compared to 240 A g_{NM}^{-1} for Ru@Pt_{2ML}) as well as with respect to the mass of Pt (2466 ± 493 A g_{Pt}^{-1} for Ru@$Pt_{0.5MLE}$ compared to 480 A g_{Pt}^{-1} for Ru@Pt_{2ML}) in Ru@Pt catalysts, while the activity of the Pt reference reported by Elbert et al. (Figure 10c, hollow, gray asterisk) is only 30% lower (120 A g_{Pt}^{-1} vs. 182 ± 7 A g_{Pt}^{-1}) than that reported here (Figure 10c, filled, gray asterisk).[14]

Conclusions

The evaluation of the HOR/HER activity of Ru@Pt core-shell catalysts with varying Pt shell thickness in H_2-saturated 0.1 M NaOH by RDE voltammetry provided fundamental insights into the HOR/HER in alkaline media. By comparing the surface normalized HOR/HER

activity of partially covered Ru@Pt particles with fully Pt encapsulated Ru, the bifunctional mechanism involving Ru as active site in the HOR/HER mechanism was found to be of minor importance compared to the modification of the electronic properties of Pt by Ru. A comparison of the Ru@Pt core-shell nanoparticles prepared in this study with the HOR/HER activity Pt-Ru alloys from the literature revealed the transferability of this concept to the bimetallic Pt-Ru system. Even though, we cannot disentangle between a variation of the Pt-H_{ads} BE and other electronic effects that influence the catalytic properties of Pt, the results presented here clearly show that a bifunctional mechanism cannot explain the high HOR/HER activity of the bimetallic Pt-Ru system. Recent results by Li et al. indeed suggest that a variation of the Pt-H_{ads} BE may not be the governing effect with respect to the HOR/HER reactivity in alkaline media.[40] Nevertheless, the so-called "experimental prove" for a bifunctional mechanism given by this group, that Ru sites on the surface of Pt-Ru alloys are at least partially covered with oxidic species in the potential range relevant for HOR/HER must not intrinsically be related to a bifunctional mechanism, since the role of these species in the actual catalytic mechanism remains unclear. In conclusion, and based on the presented results, we suggest that the close vicinity of Ru and Pt promotes the HOR/HER in alkaline due to a variation of the electronic structure of Pt, which can e.g., relate to the lowering of the hydrogen adsorption barrier, proposed by Ledezma-Yanez et al.[19]

Acknowledgment

At first, the work of the micro-analytical laboratory at TUM is acknowledged for the spent effort to obtain the desired elemental analysis quickly and reliably, especially by Ulrike Ammari. The work on TEM images and SED patterns by Marianne Hanzlik is also appreciated, as well as the work of Anqi Li to synthesize an early stage of the catalyst. Financial support in the frame of the CATAPULT project (FCH JU, GA 325268) is acknowledged.

Appendix

The calculation of the MLE of Pt on the Ru core is based solely on the basic physical properties of the two metals. First of all, the radius of the Ru@Pt core-shell particle ($r_{Ru@Pt}$) is the radius of the Ru core ($r_{Ru,particle}$) plus the radius of the Pt shell composed of twice the radius of a Pt atom ($r_{Pt,atom}$) per MLE.

$$r_{Ru@Pt} = r_{Ru,particle} + 2 \cdot r_{Pt,atom} \cdot \text{MLE} \quad [A1]$$

The volumes of Ru (V_{Ru}) and Ru@Pt ($V_{Ru@Pt}$) can be calculated assuming spherical particles.

$$V_{Ru} = \frac{4}{3}\pi \cdot r_{Ru,particle}{}^3 \quad [A2]$$

$$V_{Ru@Pt} = \frac{4}{3}\pi \cdot r_{Ru@Pt}{}^3 \quad [A3]$$

The volume of Pt (V_{Pt}) is simply the difference between the two volumes.

$$V_{Pt} = V_{Ru@Pt} - V_{Ru} \quad [A4]$$

Furthermore, the amount of substance of Ru (n_{Ru}) and Pt (n_{Pt}) can be calculated from the respective volumes, densities (ρ_{Ru}, ρ_{Pt}) and molar masses (M_{Ru}, M_{Pt}).

$$n_{Ru} = \frac{V_{Ru} \cdot \rho_{Ru}}{M_{Ru}} \quad [A5]$$

$$n_{Pt} = \frac{V_{Pt} \cdot \rho_{Pt}}{M_{Pt}} \quad [A6]$$

The ratio of the molar masses yields the following equation:

$$\frac{n_{Pt}}{n_{Ru}} = \frac{V_{Pt} \cdot \rho_{Pt} \cdot M_{Ru}}{V_{Ru} \cdot \rho_{Ru} \cdot M_{Pt}} \quad [A7]$$

Inserting Equations A1–A4 into Equation A7 and solving for MLE finally yields Equation 4.

ORCID

Jan N. Schwämmlein https://orcid.org/0000-0001-8902-4508

References

1. A. Veziroglu and R. Macario, *Int. J. Hydrogen Energ.*, **36**, 25 (2011).
2. J. Durst, C. Simon, F. Hasché, and H. A. Gasteiger, *J. Electrochem. Soc.*, **162**, F190 (2015).
3. P. J. Rheinländer, J. Herranz, J. Durst, and H. A. Gasteiger, *J. Electrochem. Soc.*, **161**, F1448 (2014).
4. W. Sheng, H. A. Gasteiger, and Y. Shao-Horn, *J. Electrochem. Soc.*, **157**, B1529 (2010).
5. J. K. Nørskov, T. Bligaard, A. Logadottir, J. R. Kitchin, J. G. Chen, S. Pandelov, and U. Stimming, *J. Electrochem. Soc.*, **152**, J23 (2005).
6. A. B. Anderson, R. A. Sidik, J. Narayanasamy, and P. Shiller, *J. Phys. Chem. B*, **107**, 4618 (2003).
7. Y. Cai and A. B. Anderson, *J. Phys. Chem. B*, **108**, 9829 (2004).
8. T. Zhang and A. B. Anderson, *J. Phys. Chem. C*, **111**, 8644 (2007).
9. J. Durst, C. Simon, A. Siebel, P. J. Rheinländer, T. Schuler, M. Hanzlik, J. Herranz, F. Hasché, and H. A. Gasteiger, *ECS Trans.*, **64**(3), 1069 (2014).
10. J. Durst, A. Siebel, C. Simon, F. Hasché, J. Herranz, and H. A. Gasteiger, *Energy Environ. Sci.*, **7**, 2255 (2014).
11. W. Sheng, Z. Zhuang, M. Gao, J. Zheng, J. G. Chen, and Y. Yan, *Nat. Commun.*, **6**, 5848 (2015).
12. A. Ruban, B. Hammer, P. Stoltze, H. Skriver, and J. Nørskov, *J. Mol. Catal. A: Chem.*, **115**, 421 (1997).
13. L. Zhang, J. Kim, H. M. Chen, F. Nan, K. Dudeck, R.-S. Liu, G. A. Botton, and J. Zhang, *J. Power Sources*, **196**, 9117 (2011).
14. K. Elbert, J. Hu, Z. Ma, Y. Zhang, G. Chen, W. An, P. Liu, H. S. Isaacs, R. R. Adzic, and J. X. Wang, *ACS Catal.*, **5**, 6764 (2015).
15. J. X. Wang, Y. Zhang, C. B. Capuano, and K. E. Ayers, *Sci. Rep.*, **5**, 12220 (2015).
16. S. St. John, R. W. Atkinson, K. A. Unocic, R. R. Unocic, T. A. Zawodzinski, and A. B. Papandrew, *ACS Catal.*, **5**, 7015 (2015).
17. S. St. John, R. W. Atkinson, R. R. Unocic, T. A. Zawodzinski, and A. B. Papandrew, *J. Phys. Chem. C*, **119**, 13481 (2015).
18. Y. Wang, G. Wang, G. Li, B. Huang, J. Pan, Q. Liu, J. Han, L. Xiao, J. Lu, and L. Zhuang, *Energy Environ. Sci.*, **8**, 177 (2015).
19. I. Ledezma-Yanez, W. D. Z. Wallace, P. Sebastián-Pascual, V. Climent, J. M. Feliu, and M. T. M. Koper, *Nat. Energy.*, **2**, 17031 (2017).
20. R. R. Adzic, J. Zhang, K. Sasaki, M. B. Vukmirovic, M. Shao, J. X. Wang, A. U. Nilekar, M. Mavrikakis, J. A. Valerio, and F. Uribe, *Top. Catal.*, **46**, 249 (2007).
21. D. Strmcnik, M. Uchimura, C. Wang, R. Subbaraman, N. Danilovic, Dennis van der Vliet, A. P. Paulikas, V. R. Stamenkovic, and N. M. Markovic, *Nat. Chem.*, **5**, 300 (2013).
22. J. N. Schwämmlein, H. A. El-Sayed, B. M. Stühmeier, K. F. Wagenbauer, H. Dietz, and H. A. Gasteiger, *ECS Trans.*, **75**(14), 971 (2016).
23. H. A. Gasteiger, N. M. Markovic, and P. N. Ross, *J. Phys. Chem.*, **99**, 8290 (1995).
24. N. Danilovic, R. Subbaraman, D. Strmcnik, A. P. Paulikas, D. Myers, V. R. Stamenkovic, and N. M. Markovic, *Electrocatal.*, **3**, 221 (2012).
25. A. Schlapka, M. Lischka, A. Gross, U. Kasberger, and P. Jakob, *Phys. Rev. Lett.*, **91**, 16101 (2003).
26. W. Gu, D. R. Baker, Y. Liu, and H. A. Gasteiger, in *Handbook of Fuel Cells: Advances in Electrocatalysis, Materials, Diagnostics and Durability*, 1st ed., W. Vielstich, H. Yokokawa, and H. A. Gasteiger, Editors, p. 631, John Wiley & Sons Ltd, Chichester (2009).
27. El Sawy, E. N., H. A. El-Sayed, and V. I. Birss, *Chem. Commun.*, **50**, 11558 (2014).
28. H. A. Gasteiger, N. Markovic, P. N. Ross, and E. J. Cairns, *J. Phys. Chem.*, **98**, 617 (1994).
29. H. N. Dinh, X. Ren, F. H. Garzon, Piotr Zelenay, and S. Gottesfeld, *J. Electroanal. Chem.*, **491**, 222 (2000).
30. J. S. Spendelow, G. Q. Lu, P. Kenis, and A. Wieckowski, *J. Electroanal. Chem.*, **568**, 215 (2004).
31. C. Roth, A. J. Papworth, I. Hussain, R. J. Nichols, and D. J. Schiffrin, *J. Electroanal. Chem.*, **581**, 79 (2005).
32. M. Watanabe and S. Motoo, *J. Electroanal. Chem. Interfac.*, **60**, 267 (1975).
33. P. Ochal, J. L. Gomez de la Fuente, M. Tsypkin, F. Seland, S. Sunde, N. Muthuswamy, M. Rønning, D. Chen, S. Garcia, S. Alayoglu, and B. Eichhorn, *J. Electroanal. Chem.*, **655**, 140 (2011).
34. D. Bokach, J. L. Gomez de la Fuente, M. Tsypkin, P. Ochal, I. C. Endsjø, R. Tunold, S. Sunde, and F. Seland, *Fuel Cells*, **11**, 735 (2011).
35. N. Muthuswamy, J. L. Gomez de la Fuente, D. T. Tran, J. Walmsley, M. Tsypkin, S. Raaen, S. Sunde, M. Rønning, and D. Chen, *Int. J. Hydrogen Energ.*, **38**, 16631 (2013).
36. H. A. Gasteiger, S. S. Kocha, B. Sompalli, and F. T. Wagner, *Appl. Catal. B*, **56**, 9 (2005).
37. S. St. John, R. W. Atkinson, A. Roy, R. R. Unocic, A. B. Papandrew, and T. A. Zawodzinski, *J. Electrochem. Soc.*, **163**, F291 (2016).
38. S. Dessources, C. Morais, T. W. Napporn, and K. B. Kokoh, *ChemPhysChem*, **17**, 3964 (2016).
39. M. D. Woodroof, J. A. Wittkopf, S. Gu, and Y. S. Yan, *Electrochem. Commun.*, **61**, 57 (2015).
40. J. Li, S. Ghoshal, M. K. Bates, T. E. Miller, V. Davies, E. Stavitski, K. Attenkofer, S. Mukerjee, Z.-F. Ma, and Q. Jia, *Angew. Chem. Int. Ed.*, **56**, 15594 (2017).

3.1.2. Through-Plane Conductivity of Anion Exchange Membranes at Sub-Freezing Temperatures – Hydroxide vs. (Bi–)Carbonate Ions

The following section presents the manuscript “Through-Plane Conductivity of Anion Exchange Membranes at Sub-Freezing Temperatures – Hydroxide vs. (Bi–)Carbonate Ions”, which will be submitted to the peer-reviewed Journal of The Electrochemical Society in the near future.

Short summary.—AEMFC single cell tests are used to evaluate the suitability of a state-of-the-art AEM for operation at sub-zero temperatures and to compare its conductivity to the more commonly used PEMs. AEMs suffer from the lower ionic mobility of hydroxide ions compared to protons.[106] Additionally, they are susceptible to the displacement of hydroxide by carbonate and bicarbonate ions upon exposure to ambient air in a neutralization reaction of OH^- anions with CO_2, significantly decreasing the overall conductivity.[110] This study aims to determine the conductivity of a commercially available AEM between -20°C and 50°C as a function of the conducting species (hydroxide vs. (bi–)carbonate) and the *RH*.

First of all, an experimental setup is developed and verified with a commonly used perfluorinated membrane (Nafion 212) to enable reliable conductivity measurements below the freezing point of water at a defined membrane water content. In this, the MEA is equilibrated at the desired *RH* at 50°C in N_2 atmosphere, the humidified gas is removed by a dry purge and the cell is closed. The *HFR* is measured by GEIS while the cell temperature decreases, followed by a thaw-cycle to ensure that the membrane water content remains unaltered. The membrane conductivity is extracted by subtraction of the contact resistance from the *HFR*. For this, the electrical resistance of the cell setup is measured as a function of the applied pressure in an ex-situ experiment. The same approach is then applied to MEAs with a hydrocarbon based PEM and an alkaline Tokuyama A201 membrane. AEMFCs are converted to the hydroxide form by applying a low cell voltage in H_2/O_2 and transferred to (bi–)carbonate form by exposure to ambient air.[141]

As a result of this study, both, the hydrocarbon based membrane and the alkaline membrane show inferior conductivity compared to Nafion at all conditions. The lower conductivity of the hydrocarbon membrane with sulfonic acid based cation exchange

groups is mainly related to the lower degree of phase separation between hydrophilic and hydrophobic domains. The AEM provides an approximately three times lower conductivity compared to Nafion, partially originating from the lower ionic mobility of the hydroxide ion and partially from the not yet well-optimized membrane structure. When converted to the (bi–)carbonate form, the conductivity of the AEM decreases significantly, mainly originating from the low mobility of the (bi–)carbonate ions. This difference is most pronounced at low *RH*, where the (bi–)carbonate form provides a very poor conductivity, while a certain fraction of the conductivity can be retained in hydroxide form. This is related to the bulky carbonate and bicarbonate ions, which require a well-connected network of hydrophilic conduction channels to be mobile within the ionomer phase. At lower temperatures, the conductivity of all membranes decreases significantly, and we conclude that large voltage losses are expected for freeze start-up of AEMFCs with current membranes, even for intermediate humidification of the AEM in its hydroxide form. This would be especially challenging for systems previously exposed to ambient air, where (bi–)carbonate is present within the membrane and a freeze start-up of the AEMFC system may be difficult due to excessive ion conduction losses.

In addition to these findings, an Arrhenius analysis shows that the activation energy for the conduction of hydroxide ions in AEMs increases significantly below the freezing point of water, which is similar to the observations made for protons in PEMs. Furthermore, higher activation energies are found at low *RH*, ascribed to the partial loss of the hydrophilic network. When transferred to the (bi–)carbonate form, ion conduction in AEMs generally shows higher activation energies and the absence of a change of slope when transitioning below the freezing point of water. We hypothesize that the missing transition originates from the more demanding nature of the (bi–)carbonate ions for a well-connected hydrophilic network, hence a more dominant vehicular transport under these conditions.

Author contributions.—M.E., T.M. and J.N.S. developed the setup for the measurements. L.B. prepared the hydrocarbon membrane, while N.L.T.P. and J.N.S. performed the measurements and analyzed the data. The manuscript was written by J.N.S. and was reviewed by all authors.

Through-Plane Conductivity of Anion Exchange Membranes at Sub-Freezing Temperatures – Hydroxide vs. (Bi)Carbonate Ions

Jan N. Schwämmlein,[1,z] Nhat Long T. Pham,[1] Thomas Mittermeier,[1,2] Masamitsu Egawa,[1] Lukas Bonorand,[3] and Hubert A. Gasteiger[1]

[1]*Chair of Technical Electrochemistry, Department of Chemistry and Catalysis Research Center, Technical University of Munich, D-85748 Garching, Germany*
[2]*Present address: e.GO:REX GmbH, Aachen, Germany*
[3]*Present address: SMT Energy AG, 8952 Zurich-Schlieren, Switzerland*
[z]*E-mail: jan.schwaemmlein@tum.de*

Anion exchange membrane fuel cells (AEMFCs) are considered as potential future alternative for proton exchange membrane fuel cells (PEMFCs) due to their potential to not require platinum. However, many properties of alkaline ionomers/membranes are not yet well-characterized. The goal of this study is to evaluate the suitability of current AEMs for application in a wide range of operating conditions, especially at temperatures below the freezing point of water. For this, a method was developed to reversibly convert the counter ion of the cationic group in the membrane electrode assembly (MEA) from (bi-)carbonate to hydroxide and vice versa. Subsequently, the through-plane membrane conductivity in an AEMFC was evaluated by electrochemical impedance spectroscopy at different temperatures (-20 to 50°C) and water contents, whereby the electrical resistance contribution (contact and through-plane) to the high frequency resistance of the cell was determined in an ex-situ experiment. The results obtained in this study were compared to a standard PEM (Nafion 212) and to a sulfonic acid based membrane with a hydrocarbon backbone. The here acquired conductivity data suggest that the conductivity of the evaluated anion exchange membrane, particularly in its (bi-)carbonate form, would be too low at sub-zero temperature to meet automotive freeze start requirements.

For the envisaged transition to decarbonize the fuel cycle, H_2 powered fuel cells are a promising candidate to play a major role, e.g., for automotive applications. Proton exchange membrane fuel cells (PEMFCs) are currently being rolled-out to the (mass) market by multiple car manufacturers.[1–3] However, a major hurdle for a widespread implementation of PEMFCs is their need for noble metal catalysts to drive the hydrogen oxidation reaction (HOR) and the oxygen reduction reaction (ORR). While the high HOR kinetics enable ultra-low Pt loadings in PEMFCs,[4] the sluggish kinetics of the ORR on platinum or platinum alloy catalysts,[5,6] require the utilization of at least 100 $\mu g_{Pt}\,cm^{-2}$.[7] In contrast to the acidic environment in PEMFCs, several more abundant and affordable metals, such as Ag[8,9] or Ni,[10] exhibit sufficient stability as well as ORR activity in alkaline media, therefore enabling a wider choice of cathode catalysts.[11] On the other hand, the only sufficiently active catalysts for the HOR in alkaline media are platinum and platinum group metals (PGMs), but their HOR kinetics are approximately two orders of magnitude lower in alkaline compared to acidic medium, so that ultra-low PGM loadings cannot be used in fuel cells based on alkaline electrolytes.[12–16] Nevertheless, H_2-based fuel cells operating in alkaline media are an interesting technological concept and therefore a subject of frequent studies.[17,18]

An increased interest in this technology was triggered by the development of membranes carrying cationic groups to conduct hydroxide ions instead of protons, enabling the construction of alkaline fuel cells using anion exchange membranes (AEMs) instead of an aqueous alkaline electrolyte. A general overview on different AEM types was presented by Merle et al.,[19] and the most recently developed materials are summarized by Gottesfeld et al.[18] and Fan et al.[20] Even though significant progress has been made to improve the properties of AEMs, their conductivity is still significantly lower compared to conventional PEMs,[18] in part due to the roughly 2-fold lower mobility of hydroxide ions ($20.6 \cdot 10^{-8}\,m^2\,s^{-1}\,V^{-1}$) compared to protons ($36.2 \cdot 10^{-8}\,m^2\,s^{-1}\,V^{-1}$) in dilute aqueous solutions at 25°C.[21] Especially when exposed to ambient air containing CO_2, the ionic conductivity of anion exchange membranes decrease significantly upon the reaction of the hydroxide ions with CO_2 to (bi-)carbonate,[18,21–23] consistent with the roughly 3-4 times lower mobility of carbonate ($7.5 \cdot 10^{-8}\,m^2\,s^{-1}\,V^{-1}$) and bicarbonate ($4.6 \cdot 10^{-8}\,m^2\,s^{-1}\,V^{-1}$) ions compared to hydroxide ions. Up to now, the conductivity of alkaline membranes was subject of various studies with respect to the conducting species,[23,24] the

relative humidity (*RH*)[23,25] and the temperature[22,24] within the typical operating range of a fuel cell, especially focusing on temperatures between 60 – 80°C. With respect to automotive applications, however, starting-up of the fuel cell system at ambient or sub-zero degree temperatures is important and was thoroughly studied for PEMs,[26] but to the best of our knowledge never looked into for AEMs.

Hence, the focus of the present study is to evaluate the conductivity of an anion exchange membrane at sub-freezing conditions in both its hydroxide and its (bi-)carbonate form. To enable the exchange of the ionic group between hydroxide and (bi-)carbonate, a measurement methodology was developed where the membrane was hot-pressed with two symmetrical electrodes based on Pt/C and assembled in a conventional single fuel cell testing setup consisting of the MEA, sandwiched between gas diffusion layers (GDLs), flow fields, and end plates. To change the water content of the membrane in a defined and reproducible manner, the MEAs were equilibrated at 50°C with gases humidified at different relative humidities. Subsequently, the wet gas atmosphere was removed by a short purge (75 s) with dry gas, after which the cell was sealed and subjected to a freeze cycle down to ca. -15°C (starting at 50°C) followed by a thaw cycle (back up to 50°C). During these freeze/thaw cycles, the high frequency resistance (*HFR*) was measured; the membrane resistivity was determined by subtracting the ex-situ determined electronic resistance from the *HFR* and by dividing the resulting membrane resistance by the dry membrane thickness (membrane conductivity is thus the reciprocal of this number). The removal of liquid water from the gas flow channels by a short purge (short enough to not significantly change the water content in the membrane) is crucial to avoid water condensation in the flow field channels and to obtain a defined water content in the membrane (as described in the Experimenal section). To validate the here described method to obtain low-temperature membrane conductivities for water contents defined by equilibration at 50°C, the conductivity of a well-known PEM (Nafion 212) was evaluated between +50°C and -20°C, comparing the obtained values with those reported in the literature. Subsequently, this measurement method was applied to a sulfonic acid based membrane with a hydrocarbon backbone (furtheron referred to as HC-PEM) as comparison and finally to a commercially available AEM (Tokuyama A201) in both its hydroxide and (bi-)carbonate form.

Experimental

All potentials given in this manuscript refer to the measured voltage versus the counter/reference electrode (i.e., 100% H_2 on a dry gas basis) if not otherwise stated. Pressures are given as absolute pressures, measured and controlled at the inlet of the fuel cell. All gasses were of high purity (grade 5.0), supplied by *Westfalen AG* (Germany). Gas flows are given in nccm, referenced to 0°C at a pressure of 101.3 kPa.

MEA preparation.— All fuel cell tests were executed with 50 cm^2 active-area MEAs, fabricated by the decal transfer method. PEM-based MEAs consisted of a standard Pt/C catalyst at a loading of 100 $\mu g_{Pt}\ cm^{-2}$ on each side, and an ionomer to carbon (I/C) ratio of $\approx 1/1\ g_I \cdot g_C^{-1}$, applying a standard Nafion ionomer. Details regarding hot pressing of PEM-based MEAs can be obtained from earlier publications (155°C, 0.11 kN cm^{-2}, 3 min).[27,28] MEAs consisting of a Nafion 212 membrane (50 µm thickness, 1.0 meq g^{-1}, QuinTech e.K., Germany) and of the sulfonic acid based membrane with a hydrocarbon-based backbone (HC-PEM, 30 µm thickness, 1.6 – 1.7 meq g^{-1}) were prepared the same way.

The preparation of the HC-PEM was based on the radiation grafting technique and involved three steps, viz., irradiation, grafting, and sulfonation. A 25 µm thick ethylene-co-tetrafluoroethylene base film (ETFE, Tefzel LZ-100, *Du Pont Corp.*, USA) was electron irradiated (2.5 MeV, *Leoni AG*, Switzerland) with a dose of 15 kGy and subsequently stored at -80°C until used. Grafting was carried out at a temperature of 55°C in a solution of 30%$_v$ monomer, 55%$_v$ isopropanol (technical, *Merck Millipore KGaA*, Germany), and 15%$_v$ ultrapure water (18.2 MΩ cm, *Merck Millipore KGaA*, Germany) for 24 hours. The monomer was a mixture of α-methylstyrene (99%, *Sigma Aldrich Corp.*, Germany) and acrylonitrile (≥ 99%, *Sigma Aldrich Corp.*, Germany) with a molar ratio of 2.5 to 1.0. Sulfonation of the grafted films was carried out in a solution of 10%$_v$ chlorosulfonic acid (99%, *Sigma Aldrich Corp.*, Germany) in dichloromethane (technical, *Merck Millipore KGaA*, Germany) at room temperature for 6 hours, followed by hydrolysis of the sulfonyl chloride groups in deionized water at 80°C for 8 hours. The ion exchange capacity was determined via titration and the water uptake was determined based on the difference in mass between the wet and the dry membrane. To ensure that all ionic groups within the hydrocarbon membrane carried protons, MEAs prepared with the HC-PEM were treated in 5%$_v$ H_2SO_4 at 80°C for

12 h, followed by repeated cleaning (3 times, at least 1 h, each) with ultrapure water. Thereafter, the MEAs were left to dry in ambient air and stored in dry state until assembled.

AEMs consisted of a Tokuyama A201 membrane (28 µm thickness, ca. 1.7 meq g^{-1}, *Tokuyama Corp.*, Japan), a commercial 50%$_{wt.}$ Pt/C catalyst (TEC10V50E, *Tanaka Kikinzoku Kogyo K.K.*, Japan) and the FAA-3 ionomer (solid ionomer sheet in the Br^- ion form, *Fumatech GmbH*, Germany) at an I/C ratio of 0.8/1.0 $g_I \cdot g_C^{-1}$. Catalyst inks for AEMs were prepared by mixing the catalyst with the pre-dissolved ionomer dispersion, comprised of 10%$_{wt}$ H_2O and 90%$_{wt}$ 2-propanol (Chromasolv Plus, 99.9%, *Sigma Aldrich Corp.*, Germany). The catalyst, followed by the solvent mixture, was added into a 15 mL capped bottle (HDPE), already containing 15 g of ZrO_2 beads (5 mm, *Glen Mills Inc.*, USA) in N_2 atmosphere. To obtain a suitable viscosity for the coating process, the carbon content of the ink was adjusted to 50 mg_C mL^{-1}, resulting in a total solid content of ≈15%$_{wt}$. The inks were mixed by placing the bottles onto a roller-mill (60 rpm) for 24 h at room temperature. Thereafter, the ink was coated on etched FEP (extruded, *Angst+Pfister GmbH*, Switzerland) using the Mayer rod technique with the appropriate bar on an automated coating machine. AEM-based MEAs were prepared by hot pressing the membrane between two electrode decals at 110°C for 10 min with an applied force of 1 kN cm^{-2}, using a polymer foil (Kapton, *Du Pont Corp.*, USA) to protect the MEA and foamed PTFE (Gylon Style 3545 Soft, *Garlock GmbH*, USA) to distribute the pressure equally over the entire MEA area. The platinum content of the two electrodes was determined by weighing the decals before and after the hot pressing procedure. Both electrodes in the MEAs were identical with a loading of 400 ± 40 μg_{Pt} cm^{-2}. To assure a complete exchange of the anion exchange membrane/ionomer with (bi-)carbonate ions, the MEAs were ion exchanged three times in 1 M Na_2CO_3 (anhydrous, for analysis, *Sigma Aldrich Corp.*, Germany) solution for at least 24 h each, and subsequently washed three times by placing them in ultrapure water for at least 30 min. Thereafter, the MEAs were left to dry in ambient air and stored in dry state until assembled.

Electrical resistance measurements.— The electrical areal resistance ($R_{electr.}$) of the cell assembly, used for the determination of the membrane conductivity, was acquired by a four-point probe measurement in the absence of a membrane. The schematic setup is depicted in Figure 1, composed

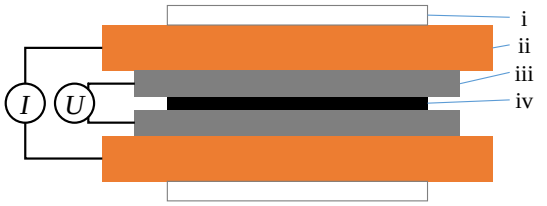

Figure 1. Experimental setup for the determination of the electronic resistance of the cell assembly by a four-point probe measurement. While the current (I) was applied to the copper plates (ii), the resulting voltage drop (U) was measured directly at the graphite flow fields (iii). The assembly, placed into a hydraulic press, was isolated by expanded PTFE sheets (i), and two gas diffusion layers with microporous layers facing each other (iv) were placed between the flow fields.

of (i) isolating, expanded PTFE (Gylon Style 3545 Soft, *Garlock GmbH*, USA), providing a homogeneous pressure distribution; (ii) two polished copper plates; (iii) two graphite flow fields (*Fuel Cell Technologies, Inc.*, USA) with 0.79 mm wide and 1.02 mm deep channels separated by 0.80 mm wide lands, and arranged in 10 serpentines with 4 channels each; and, (iv) two 50 cm^2 GDLs (Sigacret 25BC, *SGL Carbon GmbH*, Germany) with the microporous layers (MPLs) facing each other. To measure the electrical resistance of this configuration, a constant current of I = 3 A was applied via a standard laboratory power supply connected to the polished copper plates (ii in Figure 1), and the resulting voltage drop, U, was measured by a digital voltmeter (Fluke 289, *Fluke Corp.*, USA) at additional contacts inserted into the graphite flow fields (iii in Figure 1). Thus, the electrical areal resistance was calculated as $R_{\text{electr.}} = \frac{U}{I} \cdot 50\ \text{cm}^2$. To determine the pressure dependency of $R_{electr.}$, the pressure was increased by a hydraulic platen press (modified P 200 PM, *Dr. Collin GmbH*, Germany) in several steps until a total pressure of 2 MPa was reached (based on the total active area, i.e., 10 kN for the 50 cm^2 GDLs). All measurements to determine the electrical resistance were performed at 30°C, whereby the temperature was assumed to be negligible (experiments, not shown here, between 30 – 80°C at 2 MPa compression indicated a linear behavior of $R_{electr.}$ with temperature corresponding to 0.04 mΩ cm^2 $°C^{-1}$, which is negligible over the here considered temperature range). To evaluate the pressure distribution in the actual cell setup, a cell was assembled with all components (including an MEA), placing pressure sensitive dye paper (Prescale Super Low, *Fujifilm Corp.*, Japan) directly on top of the MEA.

Cell conditioning and conductivity measurements.— The measurements to determine the membrane conductivity at different temperatures and different membrane humidification were performed on an in-house manufactured single-cell 50 cm^2 hardware, whereby the endplates were fitted with internal coolant channels to enable a uniform thermal control of the cell with a coolant (1:1 mixture of ethylene glycol and deionized water) whose temperature was controlled by an external thermostat (FP50-HL, Julabo GmbH, Germany). Commercial graphite flow fields (0.787 mm channel and 0.800 mm land width; see above) were used with anode and cathode gases directed in counter-flow configuration. The GDL (see above) compression was adjusted to 20 ± 1% by PTFE-coated quasi-incompressible fiberglass gaskets (Fiberflon, Fiberflon GmbH & Co. KG, Germany), and the cell was assembled at a torque of 12 Nm (for details see Simon et al.).[29] Cell conditioning and conductivity tests were performed on automated test stations (G60, Greenlight Innovation Corp., Canada) equipped with a potentiostat (Reference3000, Gamry Instruments, USA) to conduct electrochemical impedance spectroscopy (EIS). After an initial conditioning procedure (see below), impedance spectra were recorded on N_2 purged cells (i.e., both electrodes under N_2, furtheron referred to as N_2/N_2 configuration) at zero DC current, with an AC current perturbation of 3 mA cm^{-2} from 500 kHz to 100 Hz. The HFR was extracted as x-axis intersect in a Nyquist plot and multiplied with the active area of 50 cm^2 to obtain an areal resistance. For measurements which did not show an x-axis intersect at the highest frequency (e.g., at -15°C, Figure 2), the straight line at high frequencies was extrapolated to Z_{imag} = 0 mΩ cm^2. The exemplary Nyquist data shown in Figure 2 for the case of an AEMFC equilibrated at 50°C and 80% RH exhibits a slope of ≈45° at high frequencies, bending off towards a more vertical direction at low frequencies. This represents the initial part of a purely capacitive transmission line model for the proton conduction in the electrodes in the absence of reactive gas. Details about the transmission line model can be found elsewhere (e.g., Liu et al.).[30]
The conductivity of all membranes was determined between approximately -20°C and +50°C, after the MEAs had been equilibrated at 50°C with humidified N_2 (between 20 - 100% *RH*) flowing through both cell compartments (500/500 nccm N_2/N_2 at 150 kPa_{abs}) for 70 min (Figure 3, phase I). Before initiating the resistance measurements, liquid water in the gas channels of the cell was removed by a 75 s long dry gas purge (Figure 3, phase II) with N_2/N_2 at a flow rate of

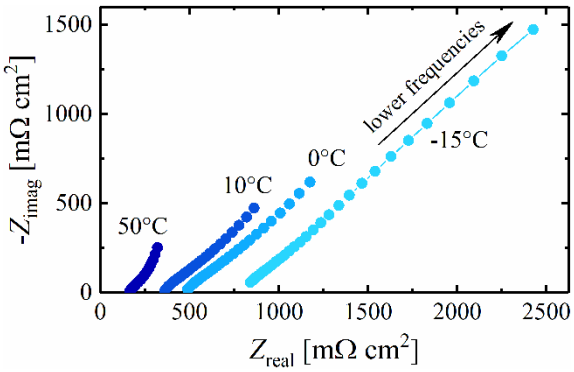

Figure 2. Exemplary Nyquist plot showing the negative imaginary part of the impedance ($-Z_{imag}$) versus the real part (Z_{real}) for an MEA comprising a Tokuyama A201 membrane in the hydroxide form recorded at different temperatures, after the MEA had been equilibrated at 50°C and 80% *RH*. The impedance spectra were recorded with both electrodes under N_2 (i.e., in N_2/N_2 configuration) at zero DC current, with an AC current perturbation of 3 mA cm^{-2} from 500 kHz to 100 Hz.

50 nccm on each side; as will be outlined below, the total amount of N_2 flowing through the cell during this period was chosen such that the amount of membrane dry-out is negligible. Directly after this purge, the gas supply and outlet valves of the cell were closed and the gas stream was interrupted. Then, the cell was subjected to a freeze cycle, slowly cooling it from +50°C to the desired temperatures (Figure 3, phase III), followed by a thaw cycle during which the temperature is gradually increased again to +50°C (Figure 3, phase IV). The heating period consisted of several intermediate target temperatures, (resulting in similar freeze- and thaw times. The EIS was measured periodically throughout the entire freeze-thaw cycle and the temperature change during the measurement (<30 s per EIS measurement) can be neglected.. Finally, the cell was maintained at +50°C to measure the conductivity after an entire freeze-thaw cycle, allowing for a comparison with the initial value (Figure 3, phase V).
In the following, we will estimate the maximum error of the membrane water content introduced by the dry gas purge step performed after each equilibration at 50°C with N_2 humidified at different *RH* values. The maximum water uptake from the membrane into the gas volume during the purge procedure can be calculated according to the definition of relative humidity (Equation [1]) for the applied total N_2 flow rate (100 nccm, i.e., 50 nccm on each side) and purge time (75 s). Assuming that the *RH* at the exit of the cell has a

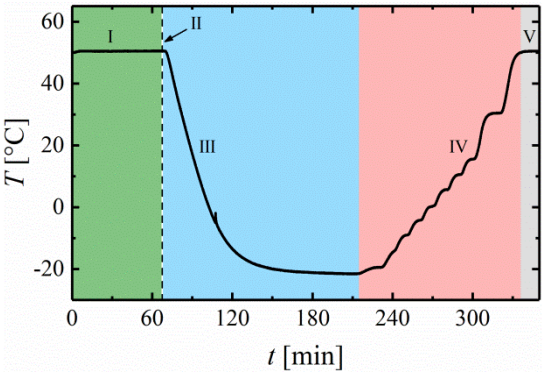

Figure 3. Exemplary profile of the cell temperature, *T*, versus time, *t*, showing a full freeze-thaw cycle after equilibration of the MEA at 50°C. Phase I: equilibration of the MEA (green area); phase II: dry gas purge (dashed line); phase III: freeze cycle (blue area); phase IV: thaw cycle (red area); phase V, constant temperature phase for reference (grey area).

maximum value equal to the *RH* adjusted during the preceding equilibration phase (Figure 3, phase I), i.e., assuming that the membrane water content and the gas flow are always in equilibrium (representing the maximum loss of water from the membrane), the *RH* can be linked to a maximum water loss during the dry gas purge:

$$RH = \frac{p_{\mathrm{H_2O}}}{p^{\mathrm{sat}}_{\mathrm{H_2O}}} = \frac{n_{\mathrm{H_2O}}}{n_{\mathrm{H_2O}} + n_{\mathrm{dry}}} \cdot \frac{p}{p^{\mathrm{sat}}_{\mathrm{H_2O}}} \qquad [1]$$

In this, $n_{\mathrm{H_2O}}$ is the molar quantity of water in the N_2 gas exiting the cell, $p^{\mathrm{sat}}_{\mathrm{H_2O}}$ is the vapor saturation pressure of water (12.34 kPa at 50°C), n_{dry} is the dry gas quantity calculated from the nitrogen flow rate and purge time (n_{dry} = 5.6 mmol) and p is the gas pressure during the purge (150 kPa_{abs}). Equation [1] can be solved for $n_{\mathrm{H_2O}}$, which represents the maximum total amount of water which will be removed from the membrane (strictly speaking from the MEA) during the dry gas purge period.

$$n_{H_2O} = n_{dry} \cdot \frac{p^{\mathrm{sat}}_{\mathrm{H_2O}} \cdot RH}{p - p^{\mathrm{sat}}_{\mathrm{H_2O}} \cdot RH} \qquad [2]$$

For example, at an *RH* of 100% at 50°C ($p_{\mathrm{H_2O}}$ = 12.35 kPa), the water content in a Nafion membrane can be calculated according to Equation 1 from Mittelsteadt and Liu,[31] resulting in a membrane water content of λ = 10 (with λ defined as $mol_{H_2O}\ mol^{-1}_{SO_3^-}$). For a membrane area of 50 cm^2, a thickness of 50 µm, a density of 2 g cm^{-3}, and an ion exchange capacity of ≈1 meq g^{-1}, the total amount of H_2O contained in the membrane at λ = 10 is 5 mmol. On the other hand, the maximum water uptake into the gas stream according to Equation [2] is ≈0.5 mmol, which is minor compared to the amount of water stored in the membrane. Analogously, at an *RH* = 20%, the calculated maximum water loss through the dry gas purge is n_{H_2O} ≈ 0.1 mmol compared to 1 mmol of H_2O, initially stored in the membrane (based on a membrane water content of λ = 2 at 50°C and 20% *RH*).[31] Hence, the λ value reached during the equilibration phase can be considered to remain approximately constant (with a maximum loss of membrane water content of ≈10%) over the course of the dry gas purge, rendering the here presented method suitable to determine the conductivity of membranes with a well-controlled water content at temperatures below the freezing point of water. The same estimates can be made for the AEM and for the HC-PEM, resulting in similar maximum water loss fractions, as the membranes have a similar thickness and essentially the same ion exchange capacity when reference to membrane volume (i.e, in terms of meq cm^{-3}). During cool-down (and subsequent thaw), the water content can be safely assumed to remain constant, due to the limited locked-in gas volume in the cell (≈2.8 cm^3) and low saturation vapor pressure, as already discussed by Tajiri et al.[32]

In experiments with AEM based MEAs, the membrane and ionomer was converted from the (bi-)carbonate form into the hydroxide form via an electrochemical pre-treatment prior to equilibration at 50°C and at the desired *RH*. For this, the cell was operated with 500/500 nccm of H_2/O_2 at 80% *RH*, 150 kPa_{abs}, and 50°C for ≈1 min at a cell voltage of 100 mV. The associated current allowed to convert the entire ionomer in the MEA into the hydroxide form by migration of all contained (bi-)carbonate species to the anode and releasing them as CO_2 via the exhaust gas. Afterwards, the cell conditioning and the *HFR* measurements were performed as described above. For measurements in the carbonate form, following the initial H_2/O_2 conditioning, air at the respective humidity of the subsequent measurement was flown on both sides of the cell for ≈2 h (note that the H_2 compartment was initially purged with N_2 to avoid damage due to gas fronts of H_2 and air), whereby the CO_2 content in the air (≈400 ppm) is sufficiently high to convert essentially all hydroxide ions into (bi-)carbonate ions.[33] Subsequently, the gases were switched to N_2/N_2 in order to equilibrate the water content of the MEA prior to initiating the freeze-thaw cycle.

Results and Discussion

Electrical Resistance.— A common measure for the ohmic resistance of a fuel cell setup is the so-called *HFR*, which can be determined from the intersect of the impedance with the real axis of a Nyquist plot obtained by EIS (Figure 2). As the *HFR* is a measure of the total ohmic resistance in the PEMFC, it is commonly expressed as the sum of the contact/bulk electronic resistance of flow fields, GDLs and electrodes ($R_{electr.}$) plus the ionic resistance of the membrane ($R_{membrane}$). $R_{electr.}$ is mainly dependent on the chosen experimental setup (e.g., applied contacting pressure, flow field, and GDL type) and is essentially independent of the ionic resistance of the membrane, which strongly depends on *RH* and, to a lesser degree on temperature. Therefore, in order to obtain the resistance contribution from the membrane, $R_{electr.}$ needs to be subtracted from the *HFR*; from the thus obtained value for $R_{membrane}$, the conductivity of the membrane can be calculated. Since an in-situ determination of the electronic resistance is challenging, an ex-situ experiment was conducted to determine its magnitude. In this four-point probe setup, a constant current (3 A) was applied to the current collectors and the voltage was measured at the flow fields (Figure 1). To determine the dependency of the electronic resistance on the applied pressure, the setup was placed in a hydraulic press and exposed to a compression/expansion cycle at 30°C, with a maximum effective pressure of 2 MPa (i.e., 10 kN applied on the 50 cm^2 GDL area). As shown in Figure 4b, the measured electronic resistance decreased with increasing applied pressure, reaching a minimum of ≈12 mΩ cm^2 (at 2 MPa); this compression dependence of $R_{electr.}$ is well-documented in the literature (e.g., Mathias et al.).[34] A hysteresis of $R_{electr.}$ was found when the pressure was reduced again, with the measured resistance at the lowest compression being clearly lower than what was obtained prior to the first compression process. $R_{electr.}$ during the second compression cycle coincides closely with that obtained during the first compression release cycle, indicating that irreversible compression (in the literature referred to as residual strain) was triggered mostly during the initial compression process. To determine the approximate electronic resistance in the actual cell assembly with which the conductivity measurement are conducted (i.e., the same assembly but with the MEA inserted between the GDLs), the pressure in the actual cell setup used for freeze/thaw conductivity measurements was evaluated by a pressure distribution test using pressure sensitive dye paper. As shown in Figure 4a, the

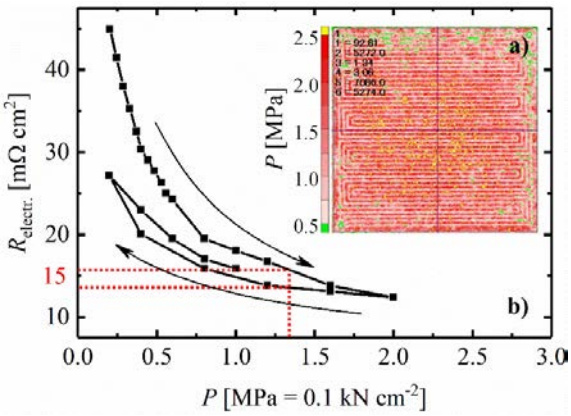

Figure 4. a) Ex-situ pressure distribution determined for the cell configuration shown in Figure 1. **b)** Electronic resistance, $R_{electr.}$, as a function of the pressure, *P*, applied onto the end plates, showing a first compression cycle and a first compression release cycle (marked by arrows), as well as a second compression cycle (data in between the first compression and the first compression release cycle). The measurement was conducted with a four-point probe in DC mode at 30°C (see Figure 1).

pressure distribution over the entire active area (i.e., the GDL area) reflects the flow field structure with higher compressive stress under the land areas than under the channels. The average value over the total 50 cm^2 was determined to be ≈1.3 MPa (the images were scanned with a Epson Perfection V33 and analyzed with the provided software), where Figure 4b reveals a value of $R_{electr.}$≈15 ± 3 mΩ cm^2. Therefore, the electronic resistance $R_{electr.}$ which we used to correct all *HFR* values in order to obtain $R_{membrane}$ was 15 mΩ cm^2 (cf., Equation [3]); considering that this value is ≈7 times lower than the lowest *HFR* values measured in our entire study (≈90 mΩ cm^2; see Figure 5), we consider the error produced by the estimated variation in the actual $R_{electr.}$ value of ca. ±3 mΩ cm^2 to be negligible.

Conductivity measurement method verification with Nafion 212.—Prior to evaluating the conductivity of membranes of interest, we will first validate our here proposed method to quantify the low-temperature through-plane membrane con ductivity at various well-defined membrane humidification levels. This will be done by means of comparative measurements with a Nafion 212 membrane whose conductivity is well-known over a wide range of temperatures. The Nafion 212 MEAs were equilibrated at 50°C with N_2 flowing through both sides of the cell (N_2/N_2 at

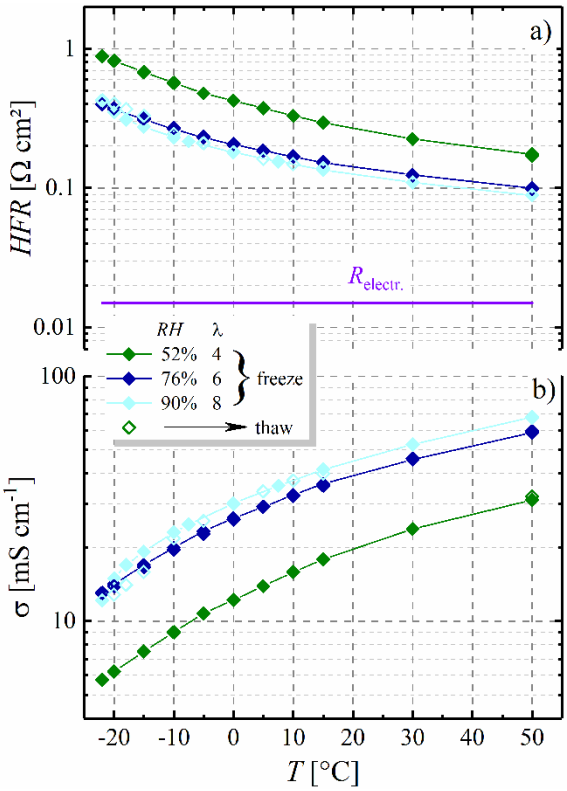

Figure 5. a) *HFR* of an MEA with a Nafion 212 membrane as a function of temperature and water content, defined by equilibration of the MEA at 50°C in humidified N_2 streams (RH values of 52%, 76%, and 90%, corresponding to λ = 4, 6, and 8, respectively). The freeze cycle is shown as full symbols and hollow symbols represent the thaw cycle (note that these are mostly overlapping). The estimated electronic resistance, $R_{electr.}$, for the cell set-up is given for comparison by the horizontal purple line (within the accuracy of these measurements it is assumed to be independent of *RH* and temperature). **b)** Through-plane conductivity of the membrane as a function of the temperature, calculated by subtraction of $R_{electr.}$ from the measured *HFR* and by normalization to the thickness of the membrane (50 µm), according to Equation [3].

500/500 nccm) that was humidified at 52%, 70%, and 90% *RH*, which corresponds to membrane water contents of and λ = 4, 6, and 8, respectively (based on the correlation by Mittelsteadt and Liu).[31] After this membrane equilibration, followed by a short dry N_2 gas purge and subsequent sealing of the cell under N_2/N_2, the cell temperature was first decreased to -22°C (freeze cycle) and then increased again (thaw cycle) to the initial value of +50°C. During the freeze/thaw cycles, the *HFR* was determined at different temperatures from the high frequency intercept of the impedance spectra with the x-axis in a Nyquist plot (see, e.g., Figure 2). These data are shown in Figure 5a for the freeze cycle (solid symbols) and for the thaw cycle (hollow symbols) for an MEA utilizing a conventional Nafion 212 membrane. As mentioned above, the ex-situ estimated electrical resistance contribution ($R_{electr.}$, drawn as a purple line in Figure 5a and considered to be independent of *RH* and temperature within the accuracy of these measurements) is substantially smaller than the lowest *HFR* of 90 mΩ cm^2 measured in this study (namely for the Nafion 212 MEA equilibrated at 50°C and 80%RH (≡ λ = 8); see light blue line in Figure 5a). Therefore, the here described measurement methodology is considered sufficiently accurate to evaluate the ionic resistance of the membrane by means of subtracting the electronic resistance from the *HFR*. However, it has to be mentioned that the thus determined membrane resistance and conductivity are most precise for high *HFR* values, hence at low temperatures and/or *RH*. Owing to the strong temperature and *RH* dependence of the membrane resistance,[31] the measured *HFR* increases substantially with decreasing temperature and *RH*. No significant differences are observed between the *HFR* values determined during the freeze cycle (closed symbols in Figure 5a) compared to those obtained during the subsequent thaw cycle (open symbols; indeed, the data points are mostly overlapping), confirming that the water content of the membrane remained unchanged during the entire freeze-thaw cycle experiment.

After subtraction of the electronic resistance contribution of $R_{electr.} \approx 15$ mΩ cm^2, the conductivity of the membrane can be calculated according to Equation [3], where σ is the conductivity (in S cm^{-1}) and *d* is the thickness of the membrane (in the dry state).

$$\sigma = \frac{d}{HFR - R_{electr.}} \qquad [3]$$

The thus obtained conductivities of the Nafion 212 membrane are shown in Figure 5b and can be compared to the values reported by Thompson et al.[35] for a Nafion 117 membrane with the same ion exchange capacity. At 20°C, these authors report conductivies ranging from 15 – 30 mS cm^{-1} at λ = 6 and from 35 – 45 mS cm^{-1} at λ = 8 and 20°C,[35] which are slightly lower, but in a comparable range as the ≈39 mS cm^{-1} at λ = 6 and the ≈45 mS cm^{-1} at λ = 8 shown in Figure 5b. At -20°C and λ = 8, Thompson et al. report an average value of ≈12 mS cm^{-1}, which is also only slightly lower than the ≈14 mS cm^{-1} obtained in

our experiments at the same conditions. Based on this, we conclude that our method to determine the membrane conductivity at low temperatures and under defined humidification conditions a valid approach; the slight differences to the literature might be due to the fact that the membrane resistance measured by Thompson et al. is based on in-plane measurements while ours is based on through-plane measurements.

Conductivity of an HC-PEM.—As comparison for the conductivity measurements performed later on with an alkaline membrane, the conductivity of a sulfonic acid based membrane with a hydrocarbon backbone (referred to as HC-PEM) was evaluated by the method validated above with Nafion 212. This is shown in Figure 6, and as before no difference in the conductivity values obtained during the freeze cycle (solid symbols) and during the thaw cycle (open symbols) is observed. While Nafion is composed of a fully perfluorinated polymer backbone, having pendent aliphatic side chains, hydrocarbon-based sulfonic acid membranes typically consist of non-fluorinated polyaromatic units, containing hydrogen endgroups.[36] In general, hydrocarbon-based membranes are considered as an alternative for the commonly applied perfluorinated membranes due their lower production cost, a lower permeability towards H_2 and O_2, and possibly due to a higher creep resistance at high temperature. First of all, the conductivity of the here investigated hydrocarbon-based membrane at 50°C and high *RH* is almost 2-fold lower (37 mS cm^{-1} for membrane equilibrated at 50°C and 95% *RH*; light blue line in Figure 6) compared to the perfluorinated Nafion 212 membrane (68 mS cm^{-1} for membrane equilibrated at 50°C and 90% *RH*; light blue line in Figure 5b). This is even more pronounced at lower humidification levels, where the conductivity at 50°C of the HC-PEM is ≈6-fold lower (5 mS cm^{-1} for membrane equilibrated at 50°C and 60% *RH*; green line in Figure 6) compared to Nafion 212 membrane (30 mS cm^{-1} for membrane equilibrated at 50°C and an even slightly lower *RH* of 52%; light blue line in Figure 5b).[37] Even more extreme differences develop when comparing the conductivities at -15°C at lower humidify cation levels, where HC-PEM conductivity (0.45 mS cm^{-1} for membrane equilibrated at 50°C and 60% *RH*; green line in Figure 6) is ≈17-fold lower than that of Nafion 212 (7.5 mS cm^{-1} for membrane equilibrated at 50°C and an even slightly lower *RH* of 52%; light blue line in Figure 5b). We assume that this is due to the fact that hydrocarbon membranes are commonly known to show a lower degree of phase separation between

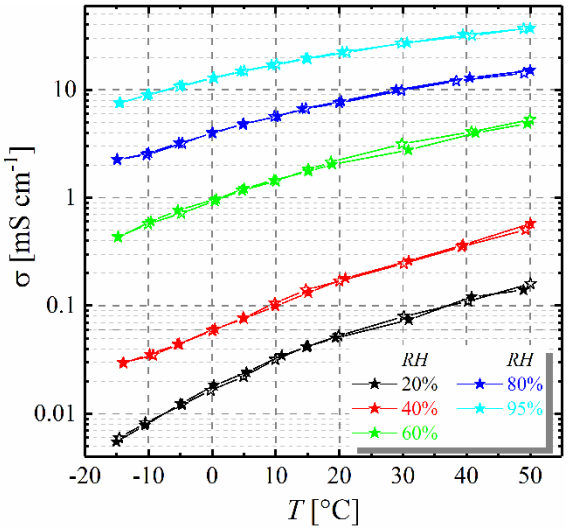

Figure 6. Through-plane conductivity, σ, of a hydrocarbon based membrane as function of temperature, *T*. σ was calculated by subtraction of $R_{electr.}$ from the measured *HFR* and normalization to the thickness of the membrane (30 µm), according to Equation [3]. The freeze cycle is shown as full symbols, while hollow symbols represent the thaw cycle.

hydrophilic and hydrophobic domains due to (i) the lower hydrophobicity of the hydrocarbon backbone, (ii) the lower hydrophilicity of the sulfonic acid group on account of its lower acidity, and, (iii) the smaller flexibility of the aromatic structure due to steric hindrances (dependent on the type of hydrocarbon).[36] Therefore, the proton conducting hydrophilic network in hydrocarbon-based sulfonic acid membranes is more tortuous with narrower conduction channels and more dead-ends, causing a lower overall conductivity. This becomes especially evident at low water content (corresponding to low *RH* levels during the equilibration procedure at 50°C), which leads to a decrease of the network connectivity and therefore a strong decrease in conductivity, as illustrated by the above comparison. The lack of phase separation in hydrocarbon-based membranes was also reported by other researchers, e.g., by Ahn et al. who showed excellent H_2/air fuel cell performance at high humidity, but strong limitations for air supplied with an *RH* of 40%.[37] The origin of the apparently more significant decrease of the conductivity of the HC-PEM with temperature compared to Nafion 212 (most pronounced for low water content, as illustrated above) is, however, still unknown.

Conductivity of an AEM.— In contrast to the sulfuric acid group, commonly employed in

PEMs, anion exchange membranes apply alkaline end groups on the side chain, e.g., based on quaternary ammonium ions, to conduct hydroxide ions through the ionomer phase of the AEMFC.[18,20,21] While pure O_2 is generally used for diagnostic purposes, the relevant cathode gas for practical fuel cell applications would be ambient air, which, however, contains approximately 400 ppm CO_2.[38] The latter was shown to react with the hydroxide ions in the ionomer phase to form (bi-)carbonate species.[21–23]

$$CO_2 + OH^- \rightarrow HCO_3^- \qquad [4]$$
$$HCO_3^- + OH^- \rightarrow CO_3^{2-} + H_2O \qquad [5]$$

In equilibrium with ambient air, the main ionic species present as counter ions of the anion exchange groups are carbonate and bicarbonate, with estimated mole fractions of 2/3 and 1/3, respectively.[39] For the remainder of this manuscript, the equilibrated mixture of carbonate and bicarbonate ions in the anion exchange membrane ionomer will be referred to as "(bi-)carbonate form" of the AEM. Since the neutralization of AEMs is inevitable upon exposure to ambient air, all alkaline MEAs were prepared directly in the carbonate form by exchanging all ionic groups in 1 M Na_2CO_3 solution. Compared to hydroxide ions ($20.6 \cdot 10^{-8}$ m^2 s^{-1} V^{-1}), the mobility of carbonate ($7.5 \cdot 10^{-8}$ m^2 s^{-1} V^{-1}) and bicarbonate ions ($4.6 \cdot 10^{-8}$ m^2 s^{-1} V^{-1}) is rather low,[21] hence, membranes comprising mainly carbonate and bicarbonate ions provide a very limited ionic conductivity.[22,40]

In accordance, the *HFR* of an MEA directly after assembly and equilibration at 50°C and an *RH* of 80% (while supplying H_2 and O_2 to anode and cathode, respectively) was as high as 604 mΩ cm^2 (Figure 7, blue hollow square). Upon drawing a large current, the membrane can be converted from carbonate to hydroxide form, since carbonate ions migrate to the anode side where they are released into the exhaust stream of the AEMFC as CO_2. As shown in Figure 7 (brown line), the current increased rapidly to a maximum of ≈1 A cm^{-2} when the cell voltage was set to 100 mV under these conditions. This current (± 10%) was reproducibly reached in all experiments presented here; MEAs that suffered damage during testing, i.e., that provided a lower H_2/O_2 performance when setting the potential to 100 mV (termed "carbonate purge"), were not considered for the evaluation of the membrane conductivity. The *HFR* measured directly after the carbonate purge (Figure 7, blue circles) was significantly lower (≈130 mΩ cm^2) compared to that measured after assembly, confirming the exchange of carbonate with hydroxide ions. No difference in the *HFR* was observed when the duration of the carbonate purge was prolonged (not shown), hence a short carbonate purge time of ≈1 min was chosen to avoid MEA degradation during the high current density application. A slight increase of the *HFR* was observed in the 30 min following the carbonate purge, which subsequently remained constant for another 90 min. We attribute the initial increase of the *HFR* after the carbonate purge to the equilibration of the membrane to the relative humidity condition supplied by the H_2/O_2 flows (80% *RH* in this figure), considering that the membrane water content during the high current density drawn during the carbonate purge is expected to be higher than in the absence of current. Furthermore, the fact that the *HFR* remained constant for more than 90 minutes verifies that the cell setup utilized for the experiments presented here is sufficiently sealed from ambient air, preventing the gradual change of the membrane from hydroxide to (bi-)carbonate form which would occur upon ambient air intrusion. To convert the

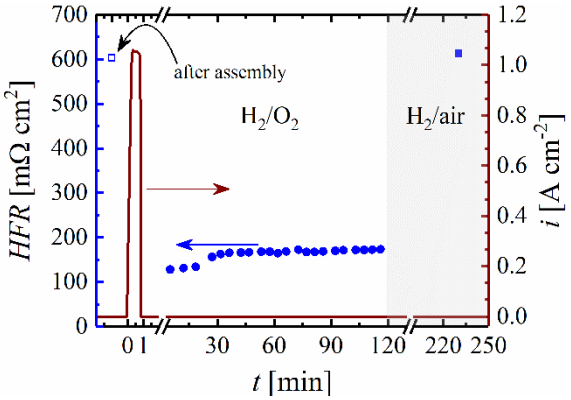

Figure 7. *HFR* of an MEA based on a Tokuyama A201 membrane (28 µm) in (bi-)carbonate form measured either directly after cell assembly with the carbonate exchanged membrane (labeled "after assembly", hollow blue square) or after the "carbonate purge" (see below) and a subsequent exposure to air (blue filled square). The carbonate purge which converts the (bi-)carbonate ions to hydroxide ions consists of applying a cell voltage of 100 mV in H_2/O_2 (at 500/500 nccm, 150 kPa$_{abs}$, 50°C, 80% *RH*) for ≈1 min (the brown line shows the current drawn during this period); the subsequently measured *HFR* in the hydroxide form is shown by the blue circles. The supplied gases, as marked in the figure, are either H_2/O_2 (directly after cell assembly and until t = 120 min) or H_2/air (starting at t = 120 min and continuing until t=250 min; also at 500/500 nccm, 150 kPa$_{abs}$, 50°C, 80% *RH*).

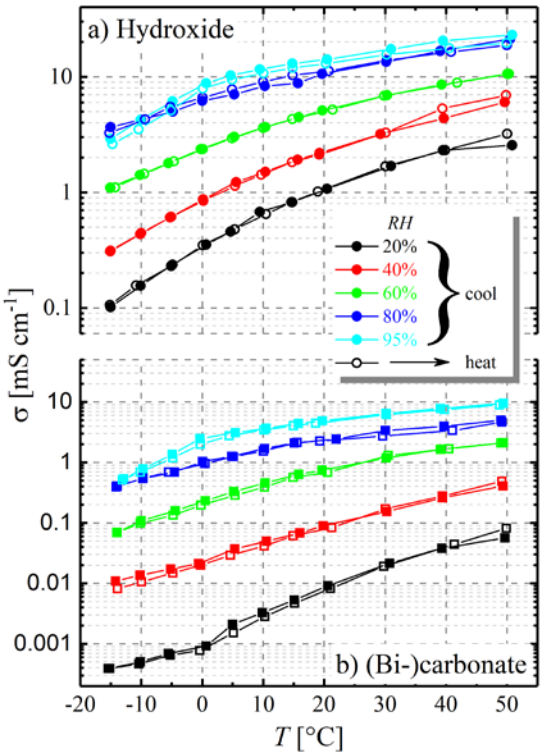

Figure 8. Through-plane conductivity, σ, of an MEA consisting of a Tokuyama A201 membrane equilibrated at 50°C with N_2/N_2 humidified at different *RH* values (as marked in the figure) as function of temperature, *T*, determined either in **a)** the hydroxide form (circles) or in **b)** the (bi-)carbonate form (squares). σ was calculated by subtraction of $R_{electr.}$ from the measured *HFR* and normalization to the thickness of the membrane (28 µm), according to Equation [3]. The freeze cycle is shown as full symbols, while hollow symbols represent the thaw cycle. The hydroxide form was obtained by the carbonate purge approach described in Figure 7, while the (bi-)carbonate form was obtained by a subsequent exposure to air/air.

membrane back to the (bi-)carbonate form in a controlled experiment, the oxygen supply was replaced by ambient air (containing ≈400 ppm CO_2). After an equilibration period of approximately two hours, the *HFR* increased to the same value as was obtained directly after assembly (compare solid and open blue squares in Figure 7), confirming the full conversion into the (bi-)carbonate form. Hence, measurements of the membrane conductivity in the (bi-)carbonate form were performed in the following order: carbonate purge to ensure that the MEA yielded the desired performance, followed by an exchange to the (bi-)carbonate form by air exposure in the fuel cell system for two hours. Apart from the ion exchange procedure, conductivity measurements of AEMs were conducted according to the procedure developed for Nafion 212.

As expected, the conductivity of the Tokuyama A201 membrane was significantly lower in the (bi-)carbonate (Figure 8b) compared to the hydroxide form (Figure 8a), e.g., at 50°C it is 5 mS cm^{-1} compared to 19 mS cm^{-1} for the membrane equilibrated at 50°C and 80% *RH* (dark blue lines). The approximately 3-4 times higher conductivity of the hydroxide compared to the carbonate form is in good alignment with that expected from the difference of the ionic mobility (≈3.2, assuming 2/3 carbonate and 1/3 bicarbonate), and similar factor which had been reported previously based on in-plane conductivity measurements of the membrane in liquid water.[22] This again confirms that the measurements aiming to determine the conductivity of the membrane in the hydroxide form were not influenced by the intrusion of CO_2 from the outside. Compared to Nafion 212 at 50°C (59 mS cm^{-1} for the membrane equilibrated at 50°C and 76% *RH*; dark blue line in Figure 5b), the conductivity of the Tokuyama A201 is ≈3-fold lower (19 mS cm^{-1} for the membrane equilibrated at 50°C and 80% *RH*), which can at least partially be ascribed to the difference of the ionic mobility between the hydroxide ion and the proton (factor of ≈1.8). Furthermore, we assume that the general structure/morphology of alkaline membranes is not yet fully optimized due to their novelty compared to the well-established Nafion 212 membrane. These structural/morphological differences could also be the reason for the similar conductivity of the Tokuyama A201 membrane and the here examined sulfonic acid membrane with a hydrocarbon backbone (15 mS cm^{-1} for the membrane equilibrated at 50°C and 80% *RH*, see Figure 6, red lines), underlining the importance of a well-optimized membrane structure/morphology. Compared to the HC-PEM, the conductivity of the alkaline membrane in the hydroxide form decreases less strongly when lowering the *RH* below 50% (e.g., 6 mS cm^{-1} vs. 0.5 mS cm^{-1} at 50°C for membranes equilibrated at 40% *RH* and 50°C). The reasonably high conductivity at low *RH* is an indicator for an upkeep of the desired phase separation to maintain well-percolating ion conduction pathways. Nevertheless, converting the hydroxide into the (bi-)carbonate form results in a much stronger decrease of the conductivity under these low *RH* conditions (0.6 mS cm^{-1} at 50°C, see Figure 8b, red lines), again comparable to the above values for the HC-PEM. The fact that the membrane conductivity in the (bi-)carbonate form is one order of magnitude smaller compared to the hy

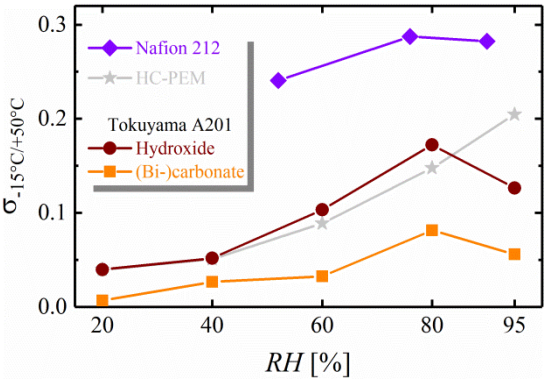

Figure 9. Ratio of the conductivity values measured at -15°C vs. +50°C, $\sigma_{-15°C/+50°C}$, for Nafion 212, HC-PEM, and Tokuyama A201 in hydroxide and (bi-)carbonate form. All membranes were equilibrated at 50°C with N_2/N_2 humidified at different *RH* values, which are depicted in the figure (x-axis). σ was calculated by subtraction of $R_{electr.}$ from the measured *HFR* and normalization to the thickness of the membrane according to Equation [3]. The hydroxide form was obtained by the carbonate purge approach described in Figure 7, while the (bi-)carbonate form was obtained by a subsequent exposure to air/air.

droxide form at low water content might be a hint that the phase separation inside the Tokuyama A201 membrane is less effective in the (bi-)carbonate form compared to the hydroxide form.

The general trend of significantly decreasing conductivity with decreasing temperatures was comparable to that observed for PEMs. For example, for membranes equilibrated at 50°C and ≈80% *RH*, the conductivity decrease from 50°C to -15°C for Nafion 212 was from 60 to 16 mS cm^{-1} (Figure 5b, dark blue diamonds), for the HC-PEM it decreased from 15 to 2.2 mS cm^{-1} (Figure 6, dark blue circles), and for the Tokuyama A201 membrane it decreased from 20 to 3.5 mS cm^{-1} for the hydroxide form (Figure 8a, dark blue circles) and from 4.6 to 0.4 mS cm^{-1} for the (bi-)carbonate form (Figure 8a, dark blue circles). At a humidification level close to saturation, i.e., for equilibration at 50°C and 95% *RH*, a bend in the trend of decreasing conductivity was observed for both, the hydroxide and carbonate form (see light blue lines in Figure 8a and b). We suspect that the more severe decrease of conductivity at ≈0°C in those measurements originates from freezing of liquid water in the membrane, causing, e.g., a blockage of ionic conduction pathways.

One interesting aspect is the much larger conductivity loss with temperature for the HC-PEM and the AEM (in the hydroxide form, and most pronouncedly in the (bi-)carbonate form), if compared to the Nafion 212 membrane. This is illustrated in Figure 9, showing the ratio of the membrane conductivities at -15°C over that at +50°C ($\sigma_{-15°C}/\sigma_{+50°C}$) vs. the *RH* value at which the membranes were equilibrated at 50°C. Quite clearly, $\sigma_{-15°C}/\sigma_{+50°C}$ is significantly larger for the Nafion 212 membrane compared to the other membranes, meaning that its conductivity loss with decreasing temperature is less. This becomes particularly pronounced as the membrane water content decreases, i.e., for membrane equilibration at 50°C at ≤60% *RH*. For example, for membranes equilibrated at 50°C and 60% RH, the loss of conductivity when lowering the temperature from +50°C to -15°C is ≈4-fold for Nafion 212 while it is ≈9-fold for the HC-PEM and for the AEM in the hydroxide form, and even ≈20-fold for the AEM in the (bi-)carbonate form. The origin of this behavior is unclear at this point, but it certainly points out the critical aspect of low temperature conductivity for HC-PEMs and for AEMs, particularly in their (bi-)carbonate form.

Activation energy of ion conduction.— To obtain some more insights into the conduction properties of the different membranes at a given water content (adjusted by equilibration at +50°C at different *RH* values), the activation energy for ionic conduction was determined from the slope of a plot showing the logarithm of the product of conductivity and measurement temperature versus the inverse of the temperature, according to Equation [6].

$$\ln(\sigma T) = \ln(\sigma_0) - \frac{E_A}{k_B} \cdot \frac{1}{T} \qquad [6]$$

where σ is the conductivity (in S cm^{-1}), T is the temperature (in K), σ_0 is the pre-exponential factor, k_B is the Boltzmann constant ($8.617 \cdot 10^{-5}$ eV K^{-1}) and E_A is the activation energy (in eV). This is shown in Figure 10a for Nafion 212 (diamonds) and in Figure 10b for the hydrocarbon-based HC-PEM (stars); the resulting E_A values of all tested membranes are shown in Table 1. Since no significant difference was found between the conductivity obtained during the freeze and during the thaw cycle for the chosen range of membrane water content (a hysteresis is commonly only observed for $\lambda \geq 12$),[26,35] only the freeze cycle conductivities are displayed in Figure 10.

The data collected for Nafion 212 were fitted to a linear regression line, divided into one regime above 0°C and another one at lower temperatures, since a clear change of slope was observed below

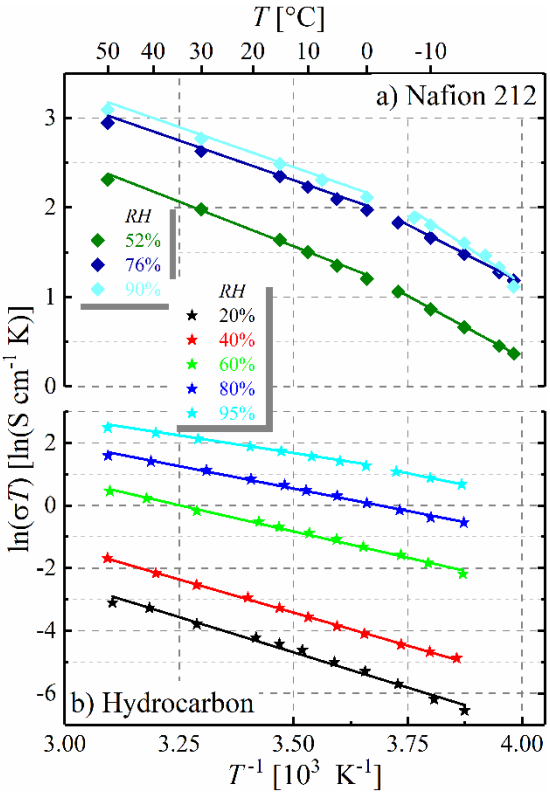

Figure 10. Arrhenius plot showing the logarithm of the product of temperature, *T*, and conductivity, σ, versus the inverse of the temperature (multiplied with 1000) for a) Nafion 212 and b) a hydrocarbon-based membrane at different *RH*. The plot contains solely data from the freeze cycle.

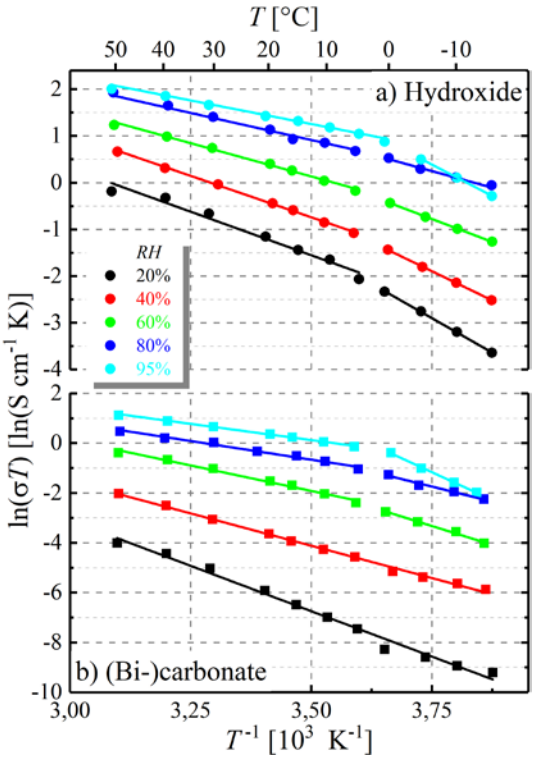

Figure 11. Arrhenius plot showing the logarithm of the product of temperature and conductivity versus the inverse of the temperature (multiplied with 1000) for a Tokuyama A201 membrane in a) hydroxide and b) carbonate form at different *RH*. The plot contains solely data from the freeze cycle.

the freezing point of water. Even though this change in slope is clearly visible at 0°C for the Nafion 212 data shown in Figure 10a, it has to be mentioned that the demarcation of two different conduction regimes has been made at temperatures near but not exactly at 0°C by other authors.[35] Considering the linear fit above 0°C, we found a slightly increasing activation energy with decreasing water content for Nafion 212 (0.15, 0.15, and 0.17 eV at λ = 8, 6, and 4, respectively; see Table 1), which is in good agreement with data presented in the literature (e.g., Thompson et al. found 0.19 and 0.22 eV at λ = 8 and 6, respectively).[35] Thompson et al. attributed the increasing activation energy for proton conduction at lower water content to a gradual change of the conduction mechanism from proton hopping according to the so-called Grotthus mechanism (similar to dilute acids), to a vehicular transport, requiring partial side-chain rearrangement. Similar to other researchers, we also observed an increase of the activation energy for the temperature regime below the freezing point of water (here between -6 and -23°C), being most significant at high λ values (e.g., for equilibration at +50°C and 90% RH (λ = 8) from a value of 0.15 eV above the freezing point to 0.29 eV in the sub-freezing regime; see Table 1). This again indicates a shift of the conduction mechanism due to the decreasing mobility in the ionomer phase as the water phase solidifies, while different transition temperatures for this process were reported in the literature.[35,41,42] However, it is commonly reported that the transition temperature shifts to lower values as the water content in the membrane decreases, explaining the less significant increase of E_A at lower water content (e.g., 0.23 eV at λ = 4, obtained by equilibration at +50°C and 52% RH; see Table 1). In general, the trend of increasing E_A with decreasing *RH* was also observed for the hydrocarbon-based HC-PEM, with values ranging in a similar order compared to Nafion 212, i.e., from 0.19 to 0.39 eV for membranes equilibrated at +50°C with N_2/N_2 humidified between 95 and 20% *RH* (see Table 1). In contrast to Nafion 212, however, no difference in the slopes between temperatures above and below 0°C were observed, apart for equilibration at the highest *RH*

Table 1. Activation energy for the ionic membrane conduction (in units of eV) for different membrane water contents obtained by equilibration of the membranes at +50°C with N_2/N_2 humidified at the below specified different *RH* values (in %). Subsequently, the membranes were cooled down at the established membrane water content to different temperatures for conductivity (σ) measurement (data only shown for freeze cycles), whereby σ was calculated by subtraction of $R_{electr.}$ from the measured *HFR* and by normalization to the thickness of the membrane according to Equation [3]. The activation energy (E_A) was extracted either over the entire temperature region (values displayed in the middle) or by fitting all values above and below the freezing point of water separately (values on the left and right, respectively).

Nafion 212			**HC-PEM**			**Tokuyama A201 (OH^-)**			**Tokuyama A201 (HCO_3^-)**		
RH	E_A [eV]		*RH*	E_A [eV]		*RH*	E_A [eV]		*RH*	E_A [eV]	
			20	0.39		20	0.32	0.51	20	0.63	
			40	0.36		40	0.31	0.43	40	0.45	
52	0.17	0.23	60	0.29		60	0.25	0.34	60	0.35	0.52
76	0.15	0.22	80	0.25		80	0.20	0.25	80	0.26	0.42
90	0.15	0.29	95	0.19	0.25	95	0.17	0.47	95	0.22	0.77

(95%), where the activation energy increased from 0.19 eV at high temperature to 0.25 eV below the freezing point of water, similar to the behavior observed for Nafion 212. We hypothesize that the missing transition for most water contents for this type of membrane originates from a lower degree of phase separation even at comparably high *RH*, hence a less significant (or even absent) change of the conduction mechanism as the temperature decreases. This finding is in good agreement with the previously reported lower conductivity of this membrane, especially at lower *RH*, where we assume that the proton conduction is strongly hindered.

Table 1: Activation energy for the ionic membrane conduction (in units of eV) for different membrane water contents obtained by equilibration of the membranes at +50°C with N_2/N_2 humidified at the below specified different *RH* values (in %). Subsequently, the membranes were cooled down at the established membrane water content to different temperatures for conductivity (σ) measurement (data only shown for freeze cycles), whereby σ was calculated by subtraction of $R_{electr.}$ from the measured *HFR* and by normalization to the thickness of the membrane according to Equation [3]. The activation energy (E_A) was extracted either over the entire temperature region (values displayed in the middle) or by fitting all values above and below the freezing point of water separately (values on the left and right, respectively).

The activation energy extracted from the conductivity data of the AEM in hydroxide form (Figure 11a) also shows two different temperature regimes, roughly separated by the freezing point of water. Furthermore, the measured E_A is similar to that of Nafion, increasing in the high-temperature regime from 0.17 to 0.32 eV as the water content decreases (set by equilibration at +50°C with N_2/N_2 humidified at 95% to 20% *RH*), and increasing in the low temperature region and from 0.47 to 0.51 eV as the water content decreases (see Table 1). First of all, these results indicate that the ion conduction mechanism is similar in the alkaline membrane and Nafion 212, i.e., at reasonably high water content, hydroxide ions in the AEM can be transported by a mechanism similarly efficient as proton hopping in PEMs (while probably not completely analogous).[43] We conclude from the data, that this ion transport mechanism is impaired by vehicular transport as the water content decreases, indicated by the gradual increase of E_A, resulting in a lower conductivity at these conditions (Figure 8a). This is also in line with the previously reported absence of a conductivity breakdown in the AEM for the hydroxide form at low *RH* (evident for the hydrocarbon-based membrane), where we assume that an interconnected network of the water phase can be reasonably well-maintained and that only a gradual change in the transport mechanism is present. Similar to Nafion 212, the activation energy increase when entering the low temperature regime is most significant for the highest water content, where the freezing of water in the membrane seems to strongly limit the mobility of the ionic species.

In contrast to the similarities between Nafion 212 and the Tokuyama A201 AEM in hydroxide form, the Arrhenius plot for the AEM in carbonate form (Figure 11b) resembles a different picture. Similar to the hydrocarbon-based HC-PEM, a separation into two different regimes was only visible at high water contents (for equilibration at +50°C at $RH \geq 60\%$), with no change of slope below the freezing point of water at lower water content. This might either be due to a less distinct separa-

tion of hydrophilic and hydrophobic domains in carbonate form, similar to that observed for the hydrocarbon-based HC-PEM or to a generally higher need for a connected hydrophilic network to conduct carbonate and (bi-)carbonate ions compared to hydroxide ions or protons. While we cannot disprove either of the two hypothesis, we believe that the intrinsically lower mobility of (bi-)carbonate ions requires more well-connected ionic pathways for high membrane conductivity, which likely causes the absence of a transition temperature, rather than a change of the hydrophilicity in the same membrane when exchanging hydroxide with carbonate. Therefore, we conclude that the vehicular conduction mechanism plays a more significant role for AEMs in the carbonate form compared to an ion hopping mechanism, which is unlikely to occur for the rather bulky (bi-)carbonate ions. Nevertheless, the trend of increasing E_A with decreasing water content (i.e., with decreasing equilibration *RH*) was also found for the (bi-)carbonate form, with E_A increasing from 0.22 and 0.63 eV (95% and 20% *RH*) in the high temperature regime. In the low temperature regime below the freezing point of water, the activation energy at any given water content is substantially larger (see Table 1); the very large activation energy observed in this region is of course reflected in the dramatic conductivity loss between +50°C and -15°C (≈20-fold) which is shown in Figure 9.

Implications of AEM conductivity for automotive applications.— While the conductivity of the here examined AEM (Tokuyama A201) in the hydroxide form at 50°C and high relative humidity (≈20 mS cm^{-1} at 95% RH, see Figure 8a) is ≈3.5-fold lower than that of Nafion 212 (≈70 mS cm^{-1} at 90% RH, see Figure 5b), it would still afford a reasonably small voltage loss for a ≈10 µm thick membrane (a thickness used in today's PEM fuel cells for vehicles), namely ≈50 mV at 1 A cm^{-2}. More of a concern, however, is the dramatic conductivity loss for AEMs at sub-freezing conditions, which is much larger than for Nafion 212 (see Figure 9), which might be critical for freeze-starting a fuel cell, particularly since this is generally preceded by equilibrating the fuel cell at low *RH* conditions in order to avoid the condensation of liquid water in the electrodes, diffusion media, and flow-fields. Exemplarily, one can estimate the membrane resistance losses at a fuel cell freeze start-up from -15°C at a current density of 0.1 A cm^{-2} (certainly a lower limit for a reasonable start-up power) from the conductivities obtained at -15°C and intermediate water content for Nafion 212 (≈7 mS cm^{-1}; equilibrated at +50°C and 52% *RH*), the HC-PEM (≈0.4 mS cm^{-1}; equilibrated at +50°C and 60% *RH*) and the alkaline membrane in hydroxide (≈1 mS cm^{-1}; equilibrated at +50°C and 60% *RH*) or (bi-)carbonate form (≈0.07 mS cm^{-1}; equilibrated at +50°C and 60% *RH*), as shown in Figures 5b, 6, and 8. For ≈10 µm thick membranes, the associated voltage drop would be roughly 0.01, 0.25, 0.10, and 1.4 V for Nafion 212, the HC-PEM, and the AEM in hydroxide or (bi-)carbonate form, respectively. A voltage loss of ≈1.4 V essentially means that a current of even 0.1 A cm^{-2} at -15°C could not be drawn for the Tokuyama A201 membrane in its (bi-)carbonate form, likely preventing a successful freeze start-up; on the other hand, a freeze start-up at under these conditions would theoretically be achievable for in the hydroxide form. This implies that it would either be necessary to improve the conductivity of anionic membranes in the (bi-)carbonate form, or that one would have to assure that the AEM would remain in its hydroxide form during the shut-down and during extended shut-down times.

Summary and Conclusions

In this study, we presented a method for the in-situ adjustment of the water content of fuel cell membranes by equilibration of the membranes at +50°C with N_2/N_2 humidified at different *RH* values, followed by a brief dry-gas purge which removes liquid water from the flow-field without significantly changing the membrane waer content. This way, the conductivity of membranes can be determined for a defined water content at low and sub-freezing temperatures by quantifying the electrical resistance and measuring the high frequency resistance (*HFR*). After validation of this methodology with a commercially available Nafion 212 membrane, the conductivity of a hydrocarbon-based PEM (HC-PEM) and of an AEM (Tokuyama A201) were determined. To disentangle the (bi-)carbonate and hydroxide form in the AEM, the MEA was subjected to an electrochemical pre-treatment followed by equilibration in the appropriate gas atmosphere.

The measurements showed that the conductivity of the here examined AEM and of the HC-PEM not only decreases significantly when the membrane water content decreases, but that their conductivity drops much more rapidly with decreasing temperature than that of a Nafion 212 membrane, particularly at intermediate and low water content. The latter effect is most strongly pronounced for the AEM in its (bi-)carbonate form,

which has significant implications for the freeze start-up capability of alkaline membrane fuel cells.

Acknowledgements

The supply of an alkaline membrane as comparison to the commercially available Tokuyama A201 by Kenneth Charles Neyerlin from the National Renewable Energy Laboratory (Denver, USA) is highly appreciated.

References

1 Hyundai Motor Co. (accessed 10/18/2018), https://www.hyundai.com/content/dam/hyundai/ww/en/images/footer/downloads/eco/e-brochure/nexo-fe-lhd-ebrochure-2019.pdf.
2 Toyota Motor Co. (accessed 01/04/2019), https://www.toyota.com/content/ebrochure/2018/mirai_FuelCellTech.pdf.
3 Honda Motor Co. (accessed 10/18/2018), https://automobiles.honda.com/-/media/Honda-Automobiles/Vehicles/2017/Clarity-Fuel-Cell/Brochure/MY18_Clarity_FCV_Flyer.pdf.
4 J. Durst, C. Simon, F. Hasché and H. A. Gasteiger, *J. Electrochem. Soc.* **162,** F190 (2015).
5 U. A. Paulus, T. J. Schmidt, H. A. Gasteiger and R. J. Behm, *J. Electroanal. Chem.* **495,** 134 (2001).
6 B. Han, C. E. Carlton, A. Kongkanand, R. S. Kukreja, B. R. Theobald, L. Gan, R. O'Malley, P. Strasser, F. T. Wagner and Y. Shao-Horn, *Energy Environ. Sci.* **8,** 258 (2015).
7 A. Kongkanand and M. F. Mathias, *J. Phys. Chem. Lett.* **7,** 1127 (2016).
8 N. Wagner, M. Schulze and E. Gülzow, *J. Power Sources.* **127,** 264 (2004).
9 S. Gamburzev, K. Petrov and A. J. Appleby, *J. Appl. Electrochem.* **32,** 805 (2002).
10 M. Schulze and E. Gülzow, *J. Power Sources.* **127,** 252 (2004).
11 J. R. Varcoe and Slade, R. C. T., *Fuel Cells.* **5,** 187 (2005).
12 W. Sheng, H. A. Gasteiger and Y. Shao-Horn, *J. Electrochem. Soc.* **157,** B1529 (2010).
13 J. Durst, C. Simon, A. Siebel, P. J. Rheinländer, T. Schuler, M. Hanzlik, J. Herranz, F. Hasché and H. A. Gasteiger, *ECS Trans.* **64,** 1069 (2014).
14 J. Durst, A. Siebel, C. Simon, F. Hasché, J. Herranz and H. A. Gasteiger, *Energy Environ. Sci.* **7,** 2255 (2014).
15 P. J. Rheinländer, J. Herranz, J. Durst and H. A. Gasteiger, *J. Electrochem. Soc.* **161,** F1448 (2014).
16 M. D. Woodroof, J. A. Wittkopf, S. Gu and Y. S. Yan, *Electrochem. Commun.* **61,** 57 (2015).
17 G. F. McLean, T. Niet, S. Prince-Richard and N. Djilali, *Int. J. Hydrogen Energ.* **27,** 507 (2002).
18 S. Gottesfeld, D. R. Dekel, M. Page, C. Bae, Y. Yan, P. Zelenay and Y. S. Kim, *J. Power Sources.* **375,** 170 (2018).
19 G. Merle, M. Wessling and K. Nijmeijer, *J. Membr. Sci.* **377,** 1 (2011).
20 J. Fan, S. Willdorf-Cohen, E. M. Schibli, Z. Paula, W. Li, T. J. G. Skalski, A. T. Sergeenko, A. Hohenadel, B. J. Frisken, E. Magliocca, W. E. Mustain, C. E. Diesendruck, D. R. Dekel and S. Holdcroft, *Nature communications.* **10,** 2306 (2019).
21 J. R. Varcoe, P. Atanassov, D. R. Dekel, A. M. Herring, M. A. Hickner, P. A. Kohl, A. R. Kucernak, W. E. Mustain, K. Nijmeijer, K. Scott, T. Xu and L. Zhuang, *Energy Environ. Sci.* **7,** 3135 (2014).
22 A. Filpi, M. Boccia and H. A. Gasteiger, *ECS Trans.* **16,** 1835 (2008).
23 N. Ziv, A. N. Mondal, T. Weissbach, S. Holdcroft and D. R. Dekel, *J. Membr. Sci.* **586,** 140 (2019).
24 K. N. Grew, X. Ren and D. Chu, *Electrochem. Solid-State Lett.* **14,** B127 (2011).
25 Q. Duan, S. Ge and C.-Y. Wang, *J. Power Sources.* **243,** 773 (2013).
26 E. L. Thompson, W. Gu and H. A. Gasteiger, *Handbook of Fuel Cells*, 1st ed., W. Vielstich, H. Yokokawa and H. A. Gasteiger, p. 699, John Wiley & Sons Ltd., Chichester (2009).
27 G. S. Harzer, J. N. Schwämmlein, A. M. Damjanović, S. Ghosh and H. A. Gasteiger, *J. Electrochem. Soc.* **165,** F3118 (2018).
28 J. N. Schwämmlein, G. S. Harzer, P. Pfändner, A. Blankenship, H. A. El-Sayed and H. A. Gasteiger, *J. Electrochem. Soc.* **165,** J3173 (2018).
29 C. Simon, F. Hasché and H. A. Gasteiger, *J. Electrochem. Soc.* **164,** F591 (2017).
30 Y. Liu, M. W. Murphy, D. R. Baker, W. Gu, C. Ji, J. Jorne and H. A. Gasteiger, *J. Electrochem. Soc.* **156,** B970 (2009).
31 C. K. Mittelsteadt and H. Liu, *Handbook of Fuel Cells*, 1st ed., W. Vielstich, H. Yokokawa and H. A. Gasteiger, p. 345, John Wiley & Sons Ltd., Chichester (2009).
32 K. Tajiri, Y. Tabuchi and C.-Y. Wang, *J. Electrochem. Soc.* **154,** B147 (2007).
33 S. Watanabe, K. Fukuta and H. Yanagi, *ECS Trans.* **33,** 1837 (2010).
34 M. F. Mathias, J. Roth, J. Fleming and W. Lehnert, *Handbook of Fuel Cells*, 1st ed., W. Vielstich, A. Lamm and H. A. Gasteiger, p. 517, John Wiley & Sons Ltd., Chichester (2009).
35 E. L. Thompson, T. W. Capehart, T. J. Fuller and J. Jorne, *J. Electrochem. Soc.* **153,** A2351 (2006).
36 K. D. Kreuer, *Handbook of Fuel Cells*, 1st ed., W. Vielstich, A. Lamm and H. A. Gasteiger, p. 420, John Wiley & Sons Ltd., Chichester (2009).
37 W.-J. Ahn, S.-D. Yim, Y.-W. Choi, Y.-J. Sohn, S.-H. Park, Y.-G. Yoon, G.-G. Park, T.-H. Yang and K.-B. Kim, *Electrochim. Acta.* **56,** 7732 (2011).
38 S. Sitch, C. Huntingford, N. Gedney, P. E. Levy, M. Lomas, S. L. Piao, R. Betts, P. Ciais, P. Cox, P. Friedlingstein, C. D. Jones, I. C. Prentice and F. I. Woodward, *Global Change Biol.* **14,** 2015 (2008).
39 T. D. Myles, K. N. Grew, A. A. Peracchio and W. K.S. Chiu, *J. Power Sources.* **296,** 225 (2015).
40 T. Kimura and Y. Yamazaki, *Electrochemistry.* **79,** 94 (2011).
41 M. Cappadonia, J.W. Erning and U. Stimming, *J. Electroanal. Chem.* **376,** 189 (1994).
42 M. Cappadonia, J. W. Erning, S. M. Saberi Niaki and U. Stimming, *Solid State Ionics.* **77,** 65 (1995).
43 M. E. Tuckerman, D. Marx, M. Parrinello and M. E. Tuckerman, *Nature.* **417,** 925 (2002).

3.2. Electrode degradation in PEMFCs

3.2.1. Anode Aging During PEMFC Start-Up and Shut-Down: H_2-Air Fronts vs. Voltage Cycles

The following section presents the publication “Anode Aging During PEMFC Start-Up and Shut-Down: H_2-Air Fronts vs. Voltage Cycles”, published in December 2018 in the peer-reviewed Journal of the Electrochemical Society as an open access paper.[128] The article is based on a publication in the conference proceedings journal, ECS Transactions, with the title “Anode Aging through Voltage Cycling Induced by H_2-Air Fronts during System Start-Up and Shut-Down”.[68] This work was presented by Jan N. Schwämmleinat the 232nd ECS Meeting (2017) in National Harbor, Maryland (abstact #1588). The ECS transactions can be found at https://doi.org/10.1149/08008.0927ecst.

Short summary.—After discontinuation of fuel cell operation for a certain amount of time, both sides of the cell, the anode and the cathode, are filled with air due to the imperfect sealing of the stack. To start the PEMFC, the anode needs to be supplied with H_2, causing the coexistence of H_2 and air in the same compartment for a limited amount of time (similar for shut-down). As the H_2-air front propagates through the anode, high potentials are reached at the cathode, where the associated carbon corrosion causes significant performance losses (see section 1.3).[142] However, the change of gas atmosphere also causes the anode potential to shift between the OCVs of the associated reactions, i.e., between 0 V_{RHE} (H_2 filled) and ≈1 V_{RHE} (air filled).[84] This change of potential causes the Pt surface to be oxidized or reduced and a frequent repetition of this process results in catalyst ageing.[71,143–146] In this publication, the SUSD induced degradation on the cathode is studied alongside with the anode for a short H_2-air front retention time, describing the phenomenon of anode ageing during SUSD for the first time in a low temperature PEMFC system. The overall performance losses are analyzed in H_2/O_2 and H_2/air polarization curves, complemented by the development of the *ECSA* on the anode and cathode during the ageing procedure. In the second part, an AST based on a quasi-square wave (4 V s^{-1}) potential profile between 0.05 and 1.05 V_{RHE} (E-cycles) is developed to simulate the anode degradation during SUSD while leaving the cathode catalyst layer intact. The *ECSA* development on the anode during this AST is compared to that

of the cathode, and the HOR overpotential is determined by H_2 pump measurements in pure and dilute H_2. In addition, the thickness of the aged electrodes is characterized via SEM imaging of cross-sections to obtain an indication on the role of carbon corrosion for the ageing procedures. The publication concludes with a projection of the impact of SUSD on low loaded anodes, where degradation phenomena are more prominent due to a low *rf* at BOT and high HOR overpotentials after ageing.

As a result of the study, a significant anode *ECSA* loss of ≈40% compared to 75% on the cathode after 3200 SUSD cycles is identified. Furthermore, a preferential dissolution of Pt(110)-like facets and the concurrent formation of Pt(100) sites is observed as a result of the rapid potential changes on the anode during SUSD. Even though the voltage cycling AST is also based on a rapid potential change, the anode faceting cannot be observed in this AST, while the *ECSA* degradation is comparable (65% after 3200 E-cycles) to SUSD. The HOR overpotential of the anode in pure H_2, determined by H_2 pump measurements after voltage cycling, is in agreement with the kinetic overpotential calculated from the *ECSA*-loss. In contrast, diluting the anode H_2 feed to 70% shows that additional H_2 mass-transport overpotentials are already present in pristine electrodes, and a severe increase is detected after 3200 E-cycles. Finally, cross-sectional measurements of aged MEAs provide an indication that the mass-transport overpotential is a result of carbon corrosion on the anode during E-cycling. Our concluding analysis shows that anodes with a low Pt loading of 25 $\mu g_{Pt}\ cm^{-2}$, which are expected to be used in the future, would provide an unacceptable kinetic HOR overpotential after ageing. Hence, automotive PEMFC stacks require mitigation strategies for the anode, alongside with those commonly considered to mitigate cathode degradation.

Author contributions.—K.T.F., Y.C., P.J.R. and J.N.S. collected and analyzed the data for this study. All authors discussed the results and reviewed the manuscript that was written by J.N.S. and P.J.R. To this work, J.N.S. and P.J.R. have contributed equally as first authors.

Anode Aging during PEMFC Start-Up and Shut-Down: H_2-Air Fronts vs Voltage Cycles

J. N. Schwämmlein, P. J. Rheinländer, Y. Chen, K. T. Freyer, and H. A. Gasteiger**

Chair of Technical Electrochemistry, Technical University of Munich, D-85748 Garching, Germany

Start-up and shut-down (SUSD) events in proton exchange membrane fuel cells (PEMFCs) are a major source of cathode degradation, causing a loss of electrochemical surface area (*ECSA*) and carbon corrosion. Our study reveals that also the anode suffers significant damage during SUSD, dominated by the loss of *ECSA*, induced by potential cycling between ≈0 and ≈1 V upon the passage of H_2/air fronts. Furthermore, we demonstrate the analogy of SUSD-induced anode degradation and that originating from quasi-square wave potential cycling between 0.05 and 1.05 V_{RHE}. The performance penalties arising from a decrease of the kinetics of the hydrogen oxidation reaction (HOR) and growing H_2 mass-transport resistances are measured via H_2-pump experiments. The thus projected anode voltage losses for low anode Pt loadings (25 μg_{Pt} cm^{-2}) predict HOR kinetic losses of ≈40 mV at 80°C and 3 A cm^{-2} for aged anode catalyst layers, suggesting that anode degradation by SUSD could be a significant durability issue in future PEMFC systems with ultra-low Pt loadings and with more stable cathode catalyst carbon supports. Moreover, SUSD-induced H_2 mass-transport related overpotentials were identified and attributed to carbon corrosion, indicated by a thinning of the anode catalyst layer upon aging.

 [DOI: 10.1149/2.0611816jes]

Manuscript submitted October 4, 2018; revised manuscript received November 24, 2018. Published December 19, 2018. This was Paper 1588 presented at the National Harbor, Maryland Meeting of the Society, October 1–5, 2017.

Proton exchange membrane fuel cells (PEMFCs) present themselves as viable alternative to internal combustion engines for automotive applications, and are currently at the edge of commercialization, as evidenced by the recent launch of PEMFC powered vehicles by Hyundai,[1] Toyota,[2] and Honda.[3] Nevertheless, the key to a large-scale implementation in fuel cell electric vehicles (FCEVs) is a reduction of cost and an enhancement of system durability, both of which are intimately related to the design of the membrane electrode assembly (MEA). A major issue causing rapid MEA failure is system start-up or shut-down (SUSD), whereby the hydrogen atmosphere on the anode side is replaced by air (shut-down) or vice-versa (start-up), hence effecting the passage of H_2/air fronts through the anode compartment of the PEMFC.[4] The underlying degradation mechanism was initially reported and described in 2005 by Reiser et al.[5] as the "reverse current" concept. During the passage of a H_2/air front, a part of each cell acts as a fuel cell (H_2 in the anode and air in the cathode compartment), while the other part acts as a galvanic cell (with air on both sides). The former supplies power to the latter, whereby the oxygen reduction reaction (ORR) occurring in the air-filled part of the anode compartment shifts the potential in the adjacent cathode electrode to ≈1.5 V vs the reversible hydrogen electrode (RHE) potential, high enough to lead to significant oxygen evolution and carbon oxidation currents. The electrochemical oxidation of the carbon electrode to CO_2 according to Equation 1 is thermodynamically possible at potentials >0.2 V_{RHE},[6] but due to its slow kinetics significant carbon oxidation rates are only reported at potentials ≥0.9 V.[7–9]

$$C + 2H_2O \rightarrow CO_2 + 4e^- + 4H^+ \quad [1]$$

Accordingly, the carbon catalyst supports used exclusively in today's PEMFC systems are subject to severe degradation during SUSD events, leading to so-called cathode thinning, i.e., a loss of void volume within the cathode catalyst layer and a concomitant decrease in cathode layer thickness, observable, e.g., by scanning electron microscopy (SEM).[9–11] Since this void volume is crucial for the transport of O_2 through the electrode to the Pt surface, thinning directly results in O_2 mass-transport related overpotentials, particularly at high current densities. Therefore, the degradation of the cathode catalyst layer during SUSD was subject to many studies, including various conditions, such as cathode gas humidification,[12–14] cell temperature,[15,11] gas front residence time,[16] and the degree of graphitization of the cathode catalyst support.[11,17]

In contrast to the frequently investigated degradation of the cathode during a SUSD event, the anode stability over the course of SUSD cycles was only rarely examined[11,10] and generally neglected. However, Engl et al. recently showed that SUSD in high temperature phosphoric acid fuel cells leads to significant amounts of carbon corrosion on the anode, along with a loss of Pt electrochemical surface area (*ECSA*), a finding which the authors attributed to the change of the anode potential upon switching the gas atmosphere between H_2 and air.[18] To the best of our knowledge, no study apart from our previously published ECS Transaction exists that is mainly focused on the degradation of the anode in low-temperature PEMFC systems.[19] While the performance decay from SUSD-induced anode degradation is rather negligible compared to cathode degradation when high anode loadings are used (≥100 μg_{Pt} cm^{-2}), it may start to become significant in future PEMFC systems, for which ultra-low anode loadings (≈25 μg_{Pt} cm^{-2}) and the use of more stable graphitized cathode carbon supports are envisaged in combination with system mitigation strategies which restrict the occurrence of H_2/air front events to room temperature, where cathode carbon support oxidation is strongly suppressed.[11]

To obtain a more quantitative understanding on the extent of anode vs cathode degradation, we will examine the PEMFC performance degradation induced by SUSD cycling by determining the loss of cell performance over the course of extended SUSD cycling and compare the concomitant *ECSA*-loss on anode and cathode. In order to quantify the voltage losses due to anode degradation, we will first compare the anode *ECSA*-loss during SUSD cycling with that observed during square-wave voltage-cycling of the anode potential between 0.05 and 1.05 V_{RHE} (with the anode catalyst layer exposed to N_2 and the cathode catalyst layer of the MEA exposed to H_2, serving as counter and reference electrode), which mimics the potential profile experienced by the anode catalyst during the passage of a H_2/air front. In the latter case, the cathode catalyst layer remains intact during the simulated SUSD test on the anode, so that losses in the HOR kinetics and increases in the H_2 mass-transport resistance on the anode can be quantified. These data will be used to project the anode related voltage losses induced by SUSD cycles for future PEMFCs with ultra-low Pt loadings.

Experimental

The design of the experiments, the experimental set-up, as well as the detailed description of the electrochemical measurements were

=These authors contributed equally to this work.
*Electrochemical Society Student Member.
**Electrochemical Society Fellow.
zE-mail: jan.schwaemmlein@tum.de

already reported in previous publications.[19–21] For the reader's convenience, an abridged description is given below.

Set-up, hardware, and materials.—All measurements were performed on single cells consisting of commercial 50 cm^2 MEAs (Gore Primea Mesga, A510.1/M715.18/C580.4, W. L. Gore & Associates, Inc., USA) with anode/cathode platinum loadings of 100/400 μg_{Pt} cm^{-2} on a conventional carbon support and an 18 µm reinforced perfluorsulfonic acid membrane, sandwiched between two gas diffusion layers (GDLs) from Freudenberg & Co. KG, Germany (H15CX483 with an uncompressed thickness of ≈185 µm). Flow-fields machined from graphite plates were custom made and then pyro-sealed (Poco Graphite, Entegris GmbH, Germany) according to the 50 cm^2 flow-field design provided by Kongkanand and Mathias,[22] featuring 14 serpentine channels at a width and depth of 0.5 and 0.8 mm, respectively, separated by 0.5 mm wide lands. A contact pressure of 0.4 MPa was adjusted by quasi-incompressible, PTFE-coated fiberglass gaskets (Fiberflon, Fiberflon GmbH & Co. KG, Germany), assembled at a torque of 12 Nm (for details regarding the cell setup see Simon et al.).[23] The low contact pressure in this study resulted in a contact resistance of ≈30 mΩ cm^2, approximately 20 mΩ cm^2 higher compared to a contact pressure of ≈2 MPa. The pressure was evaluated by assembling a regular cell and placing pressure sensitive dye paper (Prescale Ultra Low, Fujifilm Corp., Japan) between cathode flow-field and GDL. The electrical contact resistance was determined by a four-point probe measurement with two GDLs (MPLs facing each other), sandwiched between flow-fields, copper current collectors and foamed PTFE (Gylon Style 3545 Soft, Garlock GmbH, USA) as pressure distribution medium. To determine the resistance, a constant current of 3 A was directed through the current collectors and the voltage was measured at the flow-fields.

PEMFC testing was executed on customized G60 fuel cell test stations (Greenlight Innovation Corp., Canada) equipped with impedance capable potentiostats (Reference3000, Gamry Instruments, USA) using commercial fuel cell hardware (Fuel Cell Technologies, Inc., USA). All potentials are given versus the H_2 anode potential (pure H_2, i.e., corresponding to the reversible hydrogen electrode (RHE) potential) if not stated otherwise (i.e., V refers to V vs RHE). Furthermore, all area normalized values refer to the electrode area of the MEA (cm^2), unless otherwise specified by a subscript (e.g., cm^2_{Pt} if referenced to the active Pt surface area of the electrode). Gases at a grade of 5.0 were supplied by Westfalen AG (Germany).

SUSD and E-cycling conditions.—SUSD cycling was carried out at 80°C, a relative humidity (*RH*) of 66%, and at 12 kPa_g inlet gauge pressure. The time between start-up and shut-down events was 60 s, using a constant H_2 or air flow rate at the anode of 980 nccm (nccm referenced at T_0 = 273.15 K and p_0 = 101.3 kPa_{abs}), and a cathode air flow rate of 980 nccm. The resulting H_2/air front residence time of 0.1 s can be calculated by Equation 2,[11]

$$t_{\text{residence}} = \frac{V^{\text{FF}} + V^{\text{GDL}}}{\dot{V}^{\text{wet}}_{T,p,RH}} = \frac{V^{\text{FF}} + V^{\text{GDL}}}{\dot{V}^{\text{dry}}_{0} \cdot \frac{p_0}{p_{\text{gas}}} \cdot \frac{T}{T_0}} \quad [2]$$

where V^{FF} equals the internal flow-field volume (V^{FF} = 1.88 cm^3), V^{GDL} is the void volume of the compressed gas diffusion layer (V^{GDL} = 0.65 cm^3), and $\dot{V}^{\text{wet}}_{T,p,RH}$ is the anode wet gas flow rate at the given temperature, *RH*, and cell pressure p_{cell}. The latter is calculated from the applied dry gas flow rate ($\dot{V}^{\text{dry}}_0$ in nccm), the water saturation pressure $p_T^{H_2O,\text{sat}}$, and the ideal gas law, whereby $p_{\text{gas}} = p_{\text{cell}} - p_{H_2O} = p_{\text{cell}} - RH \cdot p_T^{H_2O,\text{sat}}$.

To simulate the effect of SUSD cycles on the anode catalyst layer, quasi-square wave potential voltammetry (termed E-cycles in this manuscript) between 0.05 and 1.05 V at a scan rate of 4 V s^{-1}, and a hold time of 60 s at each potential was executed on the working electrode (anode compartment) under N_2 atmosphere, applying a fixed flow of 980 nccm N_2, while supplying 980 nccm pure H_2 to the counter/reference electrode (cathode compartment), both at an *RH* of 66%, a cell temperature of 80°C, and 12 kPa_g inlet gauge pressure. The value of 1.05 V for the upper potential limit was chosen based on the reported potential of a platinum catalyst in an air/air cell,[24] while the lower potential limit of 0.05 V, i.e., above the expected potential of ≈0 V was chosen to avoid excessive H_2 evolution which would occur under N_2-flow; the voltage transient rate of 4 V s^{-1} was the maximum applicable scan rate with our 30 A booster, mimicking the fast transient originating from the H_2/air front in an actual SUSD experiment.

MEA conditioning, CVs, polarization curves, and H_2-pump measurements.—Prior to every experiment, MEAs were conditioned at 80°C, an inlet gauge pressure of 70 kPa_g and fully humidified flows of 1400 nccm H_2 (anode) and 3300 nccm air (cathode); nccm refer to a volumetric flow rate in units of cm^3 min^{-1}, referenced to a pressure of 101.3 kPa and at temperature of 273 K. Gases were supplied to anode and cathode in counter flow mode in all measurements. MEA conditioning consisted of eight cycles, each with three potentiostatic steps: i) 45 min at 0.6 V, ii) 5 min at 0.95 V, and iii) 10 min at 0.85 V. Preceding the polarization curves, cyclic voltammograms (CVs) on the anode electrode (200 and 100 mV s^{-1}) and on the cathode electrode (100 mV s^{-1}) were recorded at 40°C and 50 kPa_g, with a flow of 50 nccm dry N_2 at the working electrode and 500 nccm fully humidified H_2 at the counter/reference electrode. Full CVs were recorded between a lower limit of 0.07 or 0.08 V and an upper limit of 1.00 V, while additional CVs with a limited potential range (0.07/0.08 V to 0.55 V) were used to extract the *ECSA* by integration of the charge corresponding to the hydrogen underpotential deposition (H_{upd}) and the associated anodic H-desorption. The *ECSA* was calculated from the mean value of adsorption and desorption charge and averaged over all MEAs at the same aging stage.

H_2/air and H_2/O_2 polarization curves as well as H_2-pump measurements were carried out at 80°C, 100% *RH* and 70 kPa_g. The flow rate for H_2/air and H_2/O_2 polarization curves was 2000/5000 nccm. For H_2-pump measurements with pure H_2, 2000 nccm H_2 was fed to both anode and cathode; on the other hand, when conducting H_2-pump experiments with dilute H_2 to examine H_2 mass-transport resistances, the anode dry gas feed was mixed with N_2 to achieve a mixture of 70% H_2 and 30% N_2, while the cathode served as counter/reference electrode operated with pure H_2. The difference in the reversible potential for hydrogen oxidation/evolution between pure and dilute H_2 was corrected for by calculating the potential shift according to the Nernst equation (at constant pH):

$$\Delta E_{\text{Nernst}} = -\frac{R \cdot T}{n \cdot F} \ln\left(\frac{p_{H_2}}{p^{\text{ref}}_{H_2}}\right) \quad [3]$$

where ΔE_{Nernst} is the Nernstian shift in V, *R* is the ideal gas constant (8.314 J mol^{-1} K^{-1}), *T* is the temperature in K, *n* is the number of transferred electrons per H_2 molecule (i.e., 2), *F* is the Faraday constant (96485 A s mol^{-1}), and $p^{\text{ref}}_{H_2}$ and p_{H_2} are the partial pressures of H_2 in the reference and working electrode, respectively. Each polarization curve was recorded after a 10 min recovery step, applying 0.6 V before H_2/air curves, and drawing 1.5 A cm^{-2} before H_2/O_2 curves as well as H_2-pump measurements. Thereafter, a galvanostatic curve was collected from low to high current densities, recording the potential after 10 min at the respective current density. The high frequency resistance (*HFR*) was determined from the intersect of the high frequency branch with the x-axis in a Nyquist plot obtained by galvanostatic electrochemical impedance spectroscopy (GEIS) from 100 kHz to 10 Hz at each current density (the amplitude was adjusted to 10% of the applied current with a minimum/maximum of 0.1/3.0 A).

Design of experiment.—In order to allow for a sufficient averaging of the experimental results, a test plan was carried out for SUSD aging (Table I), where the end-of-test (EoT) of the first MEA was at 100 SUSDs and subsequent MEAs went through 100 × 2^n SUSDs, up to 3200 SUSD (n = 1,...,5). CVs and H_2/air polarization curves

Table I. Experimental design, where each individual measurement is marked in the 1st column with the respective number of SUSDs. Columns 2 to 8 denote the individual steps throughout the measurement series for each MEA. At steps marked by an X, CVs at anode and cathode as well as H_2/air and H_2/O_2 polarization curves were taken; at steps marked by an O, only CVs at anode/cathode and H_2/air polarization curves were measured. All measurements, such as *ECSA*, H_2/air and H_2/O_2 polarization curves, corresponding to a particular number of excecuted SUSD cycles were averaged, e.g., the BoT H_2/air polarization curves of all measurements (regardless of their specific EoT). Modified from Schwämmlein et al. with permission of The Electrochemical Society.[19]

	Step [# SUSD]						
Total # SUSD	BoT	100	200	400	800	1600	3200
100	X	X					
200	X	O	X				
400	X	O	O	X			
800	X	O	O	O	X		
1600	X	O	O	O	O	X	
3200	X	O	O	O	O	O	X

were recorded at beginning-of-test (BoT; after MEA conditioning), after each aging stage, and at EoT. Additionally, H_2/O_2 polarization curves were taken at BoT and EoT. Thus, several data points could be recorded for the same aging stage, except for EoT data of the H_2/O_2 polarization curves. All data for a given aging stage were averaged over the series (error bars in the graphs represent the standard deviation).

Analogous to the above described SUSD aging procedure, the same amount of MEAs was tested using E-cycles, recording CVs and H_2-pump polarization curves in pure H_2 after each aging stage. In addition, a H_2-pump measurement in dilute H_2 at BoT and after 3200 E-cycles was carried out exemplarily on one MEA.

SEM imaging.—SEM was used to determine the thickness of anode and cathode of the 50 cm^2 MEAs (from SUSD & E-cycles). 5 samples (≈1 cm diameter) were punched out from each MEA, one at each corner and one in the center (Figure 1). The punch-outs also included the GDL/MPL-layers, except for the pristine MEA. The samples were then embedded in a polymer resin (EpoThin 2 resin and hardener) at reduced pressure to remove gas bubbles, hardened at 40°C overnight, ground (CarbiMet S, P280) and polished to a mirror finish surface (MicroPolish II, Alumina, 1 µm, all purchased at ITW Test & Measurement GmbH, Germany). The thickness was measured using a benchtop scanning electron microscope (JCM-6000PLUS NeoScope, JEOL GmbH, Germany), operated in backscattering mode at an acceleration voltage of 15 kV and a magnification of 2000x. Each punch-out was evaluated at ten different spots to obtain an average thickness for each punch-out position (A-E in Figure 1) and its standard deviation. Here, the thickness at each position for a given MEA was determined from the area divided by the length to obtain a more precise average, whereby the area integration was executed semi-automatically based on the contrast between Pt rich electrodes and their less dense neighboring materials using the program ImageJ (as described by Harzer et al.).[20] Furthermore, high resolution field-emission SEM images were taken to compare the morphology of the MEA cross-section (JSM-7500F, JEOL GmbH, Germany).

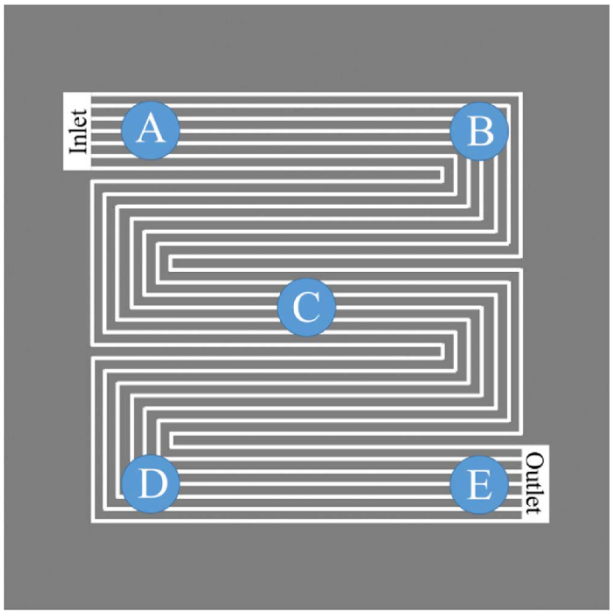

Figure 1. Schematic representation of the five punch-out positions for 50 cm^2 MEAs, showing the flow-field pattern, as well as the cathode gas inlet and outlet manifolds. The same flow-field was used on the anode and the gas was supplied in counter-flow mode. Please note that the scheme is not drawn to scale.

Results and Discussion

In the following, we will first examine the H_2/air and H_2/O_2 performance loss as well as the anode and cathode *ECSA*-loss over extended SUSD cycles. This will then be compared to the anode *ECSA* loss during voltage-cycling of the anode catalyst layer, simulating the voltage-cycling experienced by the anode catalyst layer during SUSD events. The latter will allow to quantify the performance loss of the anode catalyst layer during SUSD cycling.

Cathode degradation during SUSD.—To analyze the commonly reported SUSD-induced performance decay due to degradation of the cathode catalyst layer, Figure 2a shows the H_2/air performance curves of a Gore MEA at BoT (after conditioning) and after the respective number of SUSD cycles. The ≈50 mV lower BoT performance at 2 A cm^{-2} in Figure 2a compared to the data shown by Simon et al. using the same MEA (see Figure 8b in Simon et al.)[23] is due to the approximately 20–25 mΩ cm^2 lower *HFR* in the latter study, originating from the lower contact resistance (for details see Experimental section). In general, the MEA performance decreases compared to their BoT with increasing number of SUSD cycles. The observed voltage decay is most pronounced at high current densities ($i \geq 1$ A cm^{-2}), where overpotentials are predominantly caused by O_2 mass-transport losses, amounting to, e.g., ≈420 mV at 1 A cm^{-2} after 3200 SUSD. As outlined earlier, the corrosion of the carbon support occurs at high potentials during SUSD events, accompanied by a loss of void volume in the cathode catalyst layer and the so-called "cathode thinning".[9] Since O_2 is transported across the electrode through its void volume fraction, the collapse of the carbon structure upon carbon oxidation causes increasing O_2 mass-transport resistances, which are the more pronounced the higher the current density. According to Gasteiger et al., a decrease of the electrode's total carbon inventory by solely 7–10%$_{wt}$ leads to a ≈70% lower current density at 0.5 V in H_2/air polarization curves.[25] Due to the rapid performance decay after 400 SUSD cycles (see Figure 2a), we conclude that such a structural collapse of the carbon structure occurs after an exposure to somewhere between 400 and 800 SUSD cycles under the here applied SUSD conditions.

In addition to the O_2 mass-transport resistance induced voltage losses observed in the H_2/air performance, the *HFR* (see Figure 2b) at each of the measured current densities nearly doubles from BoT (≈55 mΩ cm^2) to after 1600 and 3200 SUSD cycles (≈100 mΩ cm^2). In general, the *HFR* is composed mostly of the proton conduction resistance of the membrane as well as of the cell compression dependent electrical contact resistances at the flow-field/GDL and at the GDL/catalyst layer interface. Since significant membrane degradation is not expected within these relatively short experiments (less than 200 h for the longest experiment with 3200 SUSD cycles) under conditions which should minimize membrane degradation (i.e., with fully humidified reactants),[26,27] the observed rise in *HFR* points towards an

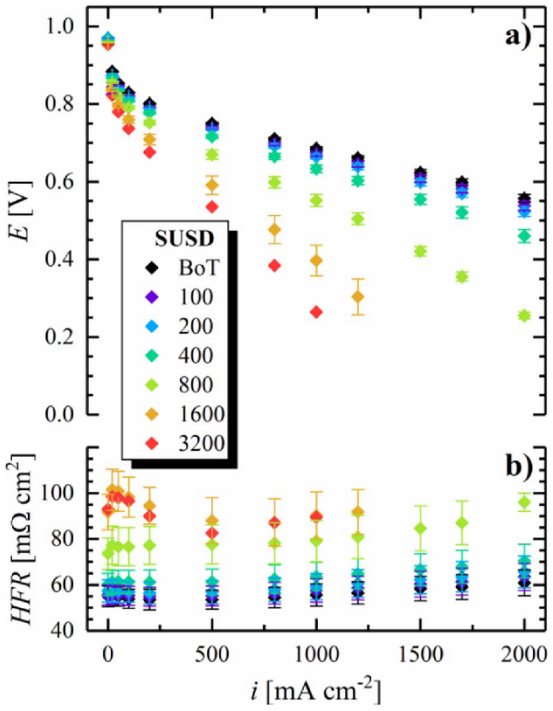

Figure 2. a) Differential flow H_2/air (2000/5000 nccm) polarization curves at BoT (after conditioning) and after the indicated number of SUSD cycles for 50 cm^2 Gore MEAs recorded at 80°C, 100% *RH*, and 70 kPa_g. b) *HFR* determined at each current density via GEIS. Error bars represent the standard deviation from independent repeat measurements (as indicated in Table I, 6 for BoT and after 100 SUSD cycles, 5 after 200 SUSD cycles, etc.). Based on the data by Schwämmlein et al.[19]

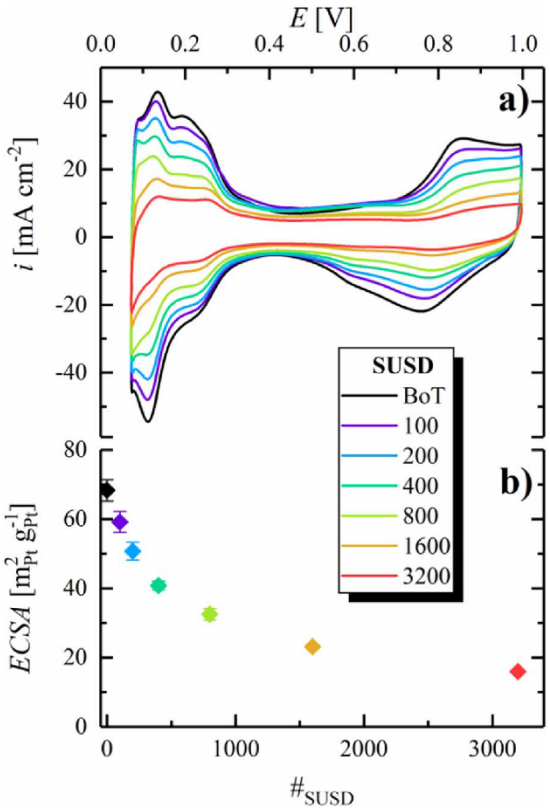

Figure 3. a) CVs of the cathode catalyst layer after different numbers of SUSD cycles, recorded between 0.07–1.00 V at a scan rate of 100 mV s^{-1} at 40°C, using a constant flow of 50 nccm dry N_2 in the cathode compartment and 500 nccm fully humidified H_2 in the anode compartment, at a pressure of 50 kPa_g. b) *ECSA* vs number of SUSD cycles, evaluated from the averaged H_{upd} charge from CVs with a limited potential window of 0.07–0.55 V under otherwise equal conditions (error bars represent the standard deviation from independent repeat measurements (as indicated in Table I, 6 for BoT and after 100 SUSD cycles, 5 after 200 SUSD cycles, etc.). Reproduced from Schwämmlein et al. with permission of The Electrochemical Society.[19]

increase in contact resistance. For the here utilized cell setup, based on a strain-controlled cell assembly (see Experimental section), the ≈7 µm cathode thinning after ≥1600 SUSD cycles (cf. Figure 9) leads to a lowering of the compressive strain of the GDL by ≈2% (based on two GDLs, each with 185 µm uncompressed thickness). As the contact pressure of 0.4 MPa in this study is already relatively low at BoT (reflected by the rather high *HFR* value of ≈55 mΩ cm^2, compared to ≈30 mΩ cm^2 which one would usually find under these operating conditions with this type of MEA),[23] and as the contact resistance rises dramatically at low compressive forces,[28] the lowering of the compressive strain of the GDL upon cathode thinning is the most likely explanation for the observed *HFR* increase after extended SUSD cycles.

In addition to the described voltage losses at high current densities, the H_2/air performance also decreases substantially with SUSD cycling in the low current density region (e.g., 70 mV at 50 mA cm^{-2} after 3200 SUSD cycles), where the contribution from O_2 mass-transport resistances should be negligible. This voltage loss is indicative of kinetic losses, i.e., of a decrease of the cathode *ECSA* with SUSD cycling. To monitor the development of the *ECSA*, we recorded cathode CVs at BoT and after each aging stage, shown exemplarily in Figure 3a for a single MEA over the course of 3200 SUSD cycles. In the course of aging, the charge in the Pt oxide formation/reduction region ($E > 0.5$ V), in the double layer region (approximately between 0.4 and 0.5 V), and in the H_{upd} region ($E < 0.4$ V) decreases significantly, whereas the qualitative shape of the CV remains largely unaltered. While the double layer charge originates largely from capacitive processes on the carbon surface, the decay of the H_{upd} and the Pt oxidation/reduction charge is associated with a decrease of the Pt surface area due to SUSD-induced cathode degradation.

To quantify the loss of Pt surface area, the *ECSA* was calculated from the average of the integrated hydrogen ad-/desorption charge in the potential range between ≈80 and ≈400 mV of CVs recorded with a limited upper inversion potential of 550 mV (not shown) to mitigate the superposition of the H_{upd} process with currents originating from the delayed reduction of Pt oxide in the cathodic scan. Figure 3b shows an exponential-like decrease of the cathode *ECSA* over the course of SUSD aging, with a strong initial decay during the first 800 SUSD cycles, followed by a more gradual *ECSA*-loss over the residual cycles. During SUSD, several contributions lead to a loss of *ECSA*: The aforementioned corrosion of the carbon support causes a physical detachment of Pt nanoparticles from the support material, rendering them inactive due to electrical insulation from the electrode. Additionally, repetitive oxidation during the SUSD events and partial reduction of the Pt surface leads to dissolution of Pt ions into the electrolyte phase. Even though these Pt ions can partially be re-deposited into larger particles,[29–31] this so-called Ostwald ripening plays only a minor role in the loss of *ECSA* on the cathode due to the rather high potential in air. In contrast, Pt dissolved in the electrolyte phase can diffuse towards the membrane to eventually be reduced by H_2 crossing over from the anode compartment, leading to electrically insulated Pt particles within the membrane, manifested by a Pt deposition band as was also observed for extended OCP (open circuit potential) holds.[32] Initially, the electrode comprises Pt nanoparticles with a certain size distribution and an average diameter around 3 nm. Considering that the extent of Pt dissolution is highest for small Pt particles, the *ECSA*-loss is expected to be initially dominated

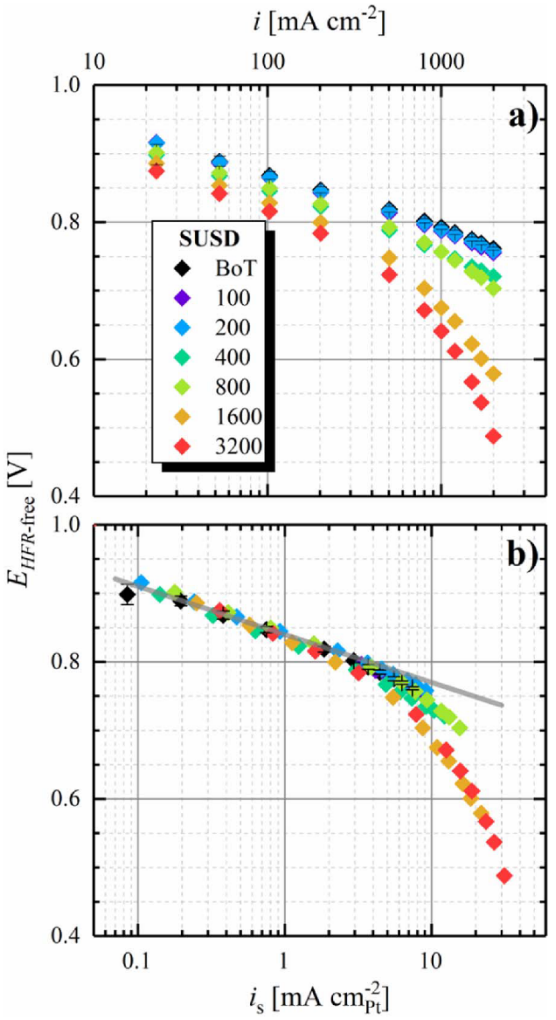

Figure 4. a) Tafel plot representation for differential-flow H_2/O_2 (2000/5000 nccm) polarization curves of 50 cm^2 Gore MEAs at 80°C, 100% *RH*, and 70 kPa_g. The current density (*i*) was corrected for the H_2-crossover measured in N_2 atmosphere under otherwise identical conditions; the potential was corrected for the *HFR* determined via GEIS measurements at the respective current density. b) Tafel plot representation based on the Pt specific current density (i_s), obtained from the *ECSA* values measured at each individual aging step. The gray line represents the ideal Tafel slope of 70 mV dec^{-1}. Reproduced from Schwämmlein et al. with permission of The Electrochemical Society.[19]

by the dissolution of smaller Pt particles, which have a higher relative contribution to the total Pt surface area.[31,33] This causes the observed steep decrease of the *ECSA* in the beginning, followed by a less pronounced loss in the remainder of the aging cycles.

To obtain further insights into the loss of performance and the development of the ORR overpotential with SUSD aging, polarization curves in pure O_2 were recorded, in which case O_2 mass-transport related voltage losses are typically negligible. Here, the measured current density was corrected for the H_2 crossover current (≈3 mA cm^{-2}), and the voltage was corrected by the *HFR* (determined via GEIS measurements at the respective current density). The Tafel slope of the recorded polarization curves was determined by fitting the corrected data in the current density region between 50 and 500 mA cm^{-2} (corresponding to approximately 0.2 to 2.0 mA cm^{-2}_{Pt} at BoT), resulting in a slope of 69 ± 1 mV dec^{-1} at BoT, in accordance with the theoretical value of 70 mV dec^{-1} based on a cathodic transfer coefficient of 1, and in good agreement with values reported for Pt/C and Pt(pc)in the literature.[34–37]

According to the Tafel equation, the available active surface area of the cathode, i.e., the roughness factor (*rf*), is directly correlated to the kinetic ORR overpotential (η, given in mV).

$$\eta = TS \cdot \left[\lg\left(\frac{i}{i_0} \cdot \frac{1}{rf}\right)\right] = TS \cdot \left[\lg\left(\frac{i}{i_0} \cdot \frac{1}{10 \cdot ECSA \cdot L_{Pt(ca)}}\right)\right] \quad [4]$$

In Equation 4, *TS* is the Tafel slope in mV dec^{-1}, *i* is the H_2-crossover corrected current density in mA cm^{-2}, i_0 is the exchange current density of the ORR in mA cm^{-2}_{Pt}, and *rf* is the roughness factor in cm^2_{Pt} cm^{-2}; the latter corresponds to 10 times the product of *ECSA* (in m^2_{Pt} g^{-1}_{Pt}) and cathode Pt loading ($L_{Pt(ca)}$ in mg_{Pt} cm^{-2}). According to Equation 4, a decrease of the cathode's *rf* by a factor of ten should results in an increase of the ORR overpotential by approximately one *TS* (neglecting minor changes of i_0 with Pt particle size), i.e., by ≈70 mV. In agreement with this, the H_2/O_2 performance decreases with the number of SUSD cycles (Figure 4a), reflecting the loss of the cathode *ECSA*. This kinetic offset between the performance of aged MEAs and that at BoT is well visible in the low current density region ($i \leq 200$ mA cm^{-2}), where O_2 mass-transport losses are negligible.

In order to clarify the correlation between *rf* and the kinetic ORR overpotential, the corrected polarization curves were normalized to the cathode *rf* and plotted against the Pt specific current density (i_s), yielding a superposition of the H_2/O_2 polarization curves at reasonably low current densities for all aging stages (Figure 4b). This demonstrates that the voltage loss at low current densities can be fully ascribed to a kinetic penalty arising from the loss of cathode *ECSA* according to Equation 4. Even though these polarization curves were recorded in pure O_2, the strong performance decay at high current densities along with an increase of the Tafel slope in the course of aging, eventually reaching 95 mV dec^{-1} after 3200 SUSDs (limiting the fit to a maximum current density of 200 mA cm^{-2}, i.e., ≈3.2 mA cm^{-2}_{Pt}) is indicative for additional mass-transport related overpotentials even in pure O_2. Moreover, the fact that a significant voltage loss in the high current density region is solely observed for MEAs exposed to >400 SUSD cycles is in accordance with the aforementioned collapse of the carbon support structure.

Anode degradation during SUSD.—During the above described SUSD aging experiments, we also monitored the loss of anode *ECSA* via CVs in inert atmosphere (Figure 5a), utilizing the H_2-filled cathode compartment as counter/reference electrode. Similar to the cathode catalyst layer, all CV features gradually decrease over the course of SUSD aging. As reported by Engl et al. for high temperature phosphoric acid fuel cells,[18] this *ECSA*-loss can be attributed to the passage of H_2/air fronts through the anode compartment during SUSD. This change of gas atmosphere effectively results in a step-change of the anode potential from the OCP under H_2 (0 V) to the OCP in air (≈1.05 V in the case of a PEMFC)[24] during shut-down and vice versa during start-up. According to a broad spectrum of literature focusing on the voltage-cycling stability of PEMFCs under various conditions,[38–45] it is well-known that repetitive potential scanning leads to degradation of the electrode, namely a loss of *ECSA* and, if the upper potential is sufficiently high, also to carbon support corrosion. Therefore, the observed exponential-like decay of the anode *ECSA* with the number of SUSD cycles (Figure 5b) qualitatively agrees with that observed under conventional voltage-cycling protocols in PEMFCs.

Following the same reasoning already outlined in the previous section, the exponential shape of the *ECSA* development is due to a selective dissolution of small Pt particles in the voltage-cycling induced aging process. In contrast to the cathode, Ostwald ripening is expected to be the major *ECSA*-loss mechanism on the anode during start-up (purging an air-filled anode compartment with H_2), as Pt

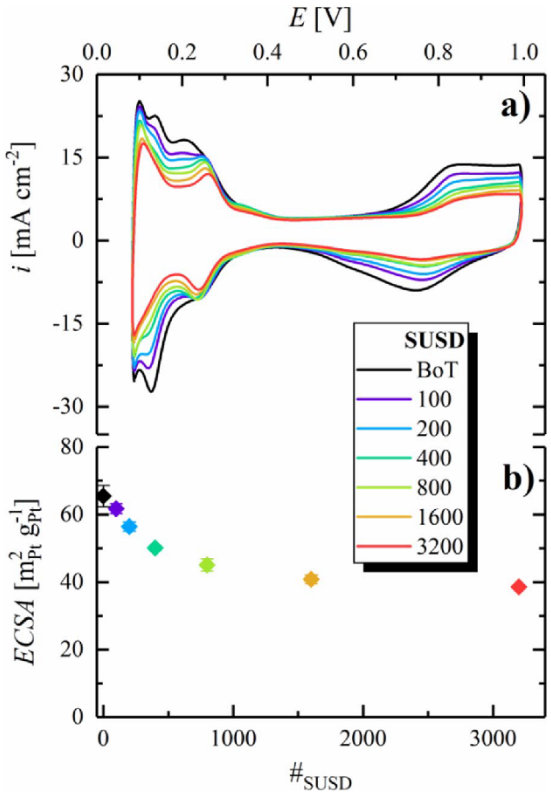

Figure 5. a) CVs of the anode catalyst layer at 40°C after different numbers of SUSD cycles, recorded between 0.08–1.00 V at a scan rate of 200 mV s^{-1}, using a constant flow of 50 nccm dry N_2 in the anode compartment and 500 nccm fully humidified H_2 in the cathode compartment, a pressure of 50 kPa_g. b) Anode *ECSA* vs number of SUSD cycles, evaluated from the averaged H_{upd} charge in CVs with a limited potential range of 0.08–0.55 V under otherwise same conditions (error bars represent the standard deviation from independent repeat measurements (as indicated in Table I, 6 for BoT and after 100 SUSD cycles, 5 after 200 SUSD cycles, etc.). Reproduced from Schwämmlein et al. with permission of The Electrochemical Society.[19]

dissolved during the potential transient will immediately re-deposit at the low potential. On the other hand, during a shut-down the released Pt ions can diffuse into the membrane phase, where they are reduced to electrically isolated Pt particles (visible in the respective SEM micrograph in Figure 8b) by H_2 dissolved in the aqueous phase of the membrane. Besides the different cycling window of the anode (≈0–1.05 V) vs that of the cathode (≈0.9–1.5 V) during SUSD, this is the likely reason for the smaller *ECSA*-loss of the anode vs the cathode during SUSD aging (≈40% vs ≈75% after 3200 SUSD for anode (Figure 5a) and cathode (Figure 3a), respectively).

Interestingly, the H_{upd} features in the anode CVs change not only with respect to the total charge from BoT to EoT, but also with respect to their shape. While the main H_{upd} feature around ≈0.13 V undergoes severe degradation, the H_{upd} processes occurring at more anodic potentials denote a less significant decrease, eventually forming a separate feature at ≈0.25 V. Derived from measurements on low-index Pt single crystals in liquid electrolyte,[46,47] and confirmed later on by experiments including an ionomer film on a polycrystalline Pt electrode,[48] the latter feature can be attributed to Pt(100) facets, while that at ≈0.13 V represents Pt(110)-like sites. Consequently, the CVs point at a preferential dissolution of Pt(110)-like sites and concurrent formation of Pt(100) facets on the anode, which is in accordance with the results presented by other researchers, showing a reconstruction of polycrystalline Pt surfaces when exposed to fast voltage scans or voltage steps in liquid electrolyte.[49–51] With respect to Pt nanoparticles, commonly regarded as cubo-octahedra with Pt(111) and Pt(100) facets, and with Pt(110)-like H_{upd} features originating from the Pt atoms located on edges and corners, the evolution of the anode CVs with SUSD aging indicates a strong faceting of the Pt particles in the anode.

Estimation of the anode voltage losses during SUSD cycles.— Since the loss of anode *ECSA* during SUSD cycles is modest, one might expect that the increase in HOR kinetic losses are rather small. At the same time, however, it is unclear whether the noticeable thinning of the anode catalyst layer (shown later on in Figure 9b) will lead to H_2 mass-transport resistances in a real PEMFC system, where the N_2 concentration in the anode compartment can be substantial. For example, based on the N_2 permeability of a Nafion membrane at 80°C and 100% *RH* ($9 \cdot 10^{-14}$ mol cm cm^{-2} s^{-1} kPa^{-1}),[52] the N_2 flux through a state-of-the-art 12 µm thick membrane at 70 kPa_g cell pressure (≡96 kPa N_2 partial pressure) is ≈4.5-6.7 $\cdot 10^{-9}$ mol cm^{-2} s^{-1} (for 7–36 kPa N_2 in the anode, corresponding to 6–30% on a dry gas basis), which for a H_2 utilization of 99% would translate to steady state N_2 concentrations of ≈30% (dry gas basis) at 0.2 A cm^{-2} (roughly the average current density of an automotive PEMFC) and of ≈6% (dry gas basis) at 2 A cm^{-2} (roughly the maximum current density of an automotive PEMFC). These estimates are based on assuming sufficiently high anode recycle flows, and are in good agreement with the study by Kocha et al.[53] Thus, in an up-transient of the PEMFC system, the N_2 concentration in the anode gas would be on the order of 30%, raising the question about the significance of H_2 mass-transport resistances in a mixture of 70% H_2 and 30% N_2, particularly after SUSD-induced damage of the anode catalyst layer. Unfortunately, the possible increase of anode overpotential due to kinetic and H_2 mass-transport losses cannot be determined experimentally from the SUSD cycled MEAs, as the substantial damage of the cathode catalyst layer prevents any meaningful diagnostic tests. Hence, an accelerated aging test to simulate SUSD-induced anode degradation while maintaining the cathode undamaged is required to estimate the extent of voltage losses induced at the anode by SUSD cycling.

Therefore, to simulate the anode degradation during SUSD cycling, we have employed a voltage-cycling procedure which mimicks the potential perturbations experienced by the anode electrode during SUSD events: a quasi square-wave perturbation between the OCP of the anode under H_2 (i.e., ≈0 V) and the anode potential in a cell filled with air on both sides (≈1.05 V),[24] with a ramp rate of 4 V s^{-1} between these two potentials (representing a short H_2/air front residence time) and a hold time of 60 s at each potential (as was used in the above SUSD tests). A square-wave protocol was chosen to simulate the constant potential phases on the anode during OCV periods in H_2 or air in SUSD events, including the fast transition from one to the other potential. Here, the cathode was used as counter/reference electrode supplied with H_2, while N_2 was fed to the anode compartment. The lower potential limit was chosen to be 50 mV higher than the reversible potential in pure H_2 in order to limit the H_2 evolution rate on the working electrode in N_2 atmosphere. Even though, the anode voltage profile in the course of multiple SUSD events might slightly change due to electrode degradation, the employed AST test is based on a fixed E-cycle throughout the entire measurement to enable comparability between different experiments and laboratories. After different numbers of E-cycles, CVs were recorded on anode and cathode to quantify their *ECSA* via integration of the H_{upd} charge.

As expected, the *ECSA* of the cathode remains essentially constant during the anode voltage-cycling experiment (hollow symbols in Figure 6b), while the anode *ECSA* decreases substantially with voltage-cycling (filled symbols in Figure 6b). Similar to the trend observed for cathodes (Figure 3b), as well as anodes (Figure 5b) exposed to the SUSD test protocol, the anode *ECSA* shows an exponential-like decay over the course of E-cycling. The total *ECSA*-loss after 3200 E-cycles (≈65% loss compared to BoT, see Figure 6b) is significantly larger than that observed after 3200 SUSD events (≈40% loss compared to BoT, see Figure 5b). This is most likely related to differences in the extent of Pt loss from the anode into the membrane phase in

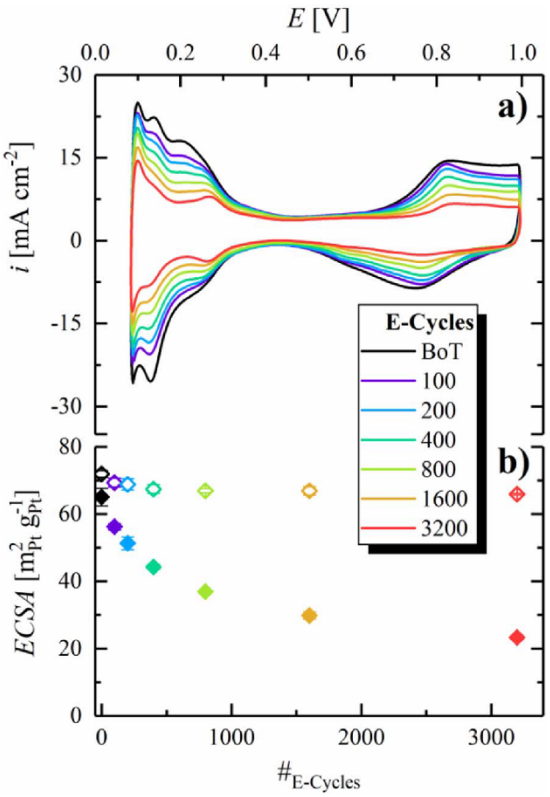

Figure 6. Voltage-cycling test of the anode catalyst layer designed to mimick the SUSD degradation of the anode, using a quasi square-wave perturbation between 0.05 and 1.05 V with a voltage ramp rate of 4 V s^{-1} between these two potentials and a hold of 60 s at each potential. a) CVs of the anode catalyst layer at 40°C after different numbers of E-cycles and at BoT (after MEA conditioning), recorded between 0.08–1.00 V at 200 mV s^{-1}, using a constant flow of 50 nccm dry N_2 in the anode compartment and 500 nccm fully humidified H_2 in the cathode compartment, at a pressure of 50 kPa_g. b) *ECSA* vs number of E-cycles for the anode (filled symbols) and the cathode catalyst layer (hollow symbols), evaluated from the averaged H_{upd} charge in CVs with a limited potential range of 0.08–0.55 V under otherwise identical conditions (as indicated in Table I, 6 for BoT and after 100 SUSD cycles, 5 after 200 SUSD cycles, etc.).

SUSD cycles compared to the voltage-cycling test. In the latter, particularly for thin electrodes, the majority of the Pt loss is due to the formation of electrically isolated Pt particles in the membrane phase,[39] which will happen for both up- and down-transients of the potential, as H_2 is only present in the membrane phase (permeating through the membrane from the H_2-filled counter electrode) due to the fact that the working electrode compartment is being purged with N_2. On the other hand, in the case of SUSD cycling, any Pt dissolved during the SUSD start-up part (purging an air-filled anode compartment with H_2) will immediately re-deposit at the low potential, so that the loss of Pt into the membrane phase should be minimized during start-up and should only be occurring during the shut-down part of the SUSD test, during which dissolved Pt ions can diffuse into the membrane phase, where they can precipitate during the subsequent start-up. This is probably the most likely explanation for the higher anode *ECSA*-loss during the E-cycling test compared to an actual SUSD test.

Although the anode *ECSA*-loss during SUSD is lower than during anode voltage-cycling, the latter allows to quantify the loss in anode kinetics and changes in H_2 mass-transport resistance induced by anode *ECSA*-loss, since the cathode catalyst layer remains intact throughout the entire measurement (shown in Figure 6b).

HOR overpotential caused by anode E-cycling.—Due to the very fast HOR/HER kinetics on Pt, their quantification can only be done using the H_2-pump method, first introduced by Neyerlin et al.[54] In this, H_2 is supplied to both sides of the MEA, and a current is applied to oxidize H_2 on the anode side while the cathode serves as counter/reference electrode, providing a reductive current via the HER. In order to evaluate the HOR overpotential on the anode, the contribution of the HER on the cathode to the overall voltage needs to be comparably small in the current density region of interest (tested herein up to 2 A cm^{-2}) and, more importantly, should not change significantly over the course of the experiment. Compared to the ORR,[37] the HOR on Pt is faster by several orders of magnitude with an exchange current density of ≈250 mA cm^{-2}_{Pt} at 80°C and 100 kPa H_2 partial pressure.[54–57] Here, the overpotential for the HOR/HER was shown to follow the Butler-Volmer equation

$$i = i_0 \cdot rf \cdot \left[e^{\frac{\alpha_a \cdot F \cdot \eta}{R \cdot T}} - e^{\frac{-\alpha_c \cdot F \cdot \eta}{R \cdot T}} \right] \quad [5]$$

where i is the kinetic current density in mA cm^{-2}, i_0 is the HOR/HER exchange current density in mA cm^{-2}_{Pt}, η is the overpotential in V, F is the Faraday constant, R is the gas constant, T is the temperature (in K), and α_a and α_c are the anodic and cathodic transfer coefficients, respectively. Using the above given exchange current density and the values of $\alpha_a = \alpha_c = 0.5$ determined by Durst et al.,[57] an HOR overpotential of only 4 mV is predicted at a current density of 2 A cm^{-2} at the anode *rf* of 65 cm^2_{Pt} cm^{-2} at BoT in our case (0.1 mg_{Pt} cm^{-2} loading at a specific surface area of 65 m^2_{Pt} g^{-1}_{Pt}). In fact, the high HOR exchange current density has been proven to enable Pt loadings in the anode catalyst layer of as little as 50 μg_{Pt} cm^{-2} without significant loss in the H_2/air performance compared to higher anode loadings (400 μg_{Pt} cm^{-2}).[34] For the HER occurring at our cathode in the H_2-pump experiments (*rf* ≈ 260 cm^2_{Pt} cm^{-2}), the calculated overpotential at 2 A cm^{-2} is $\eta_{HER} \approx 1$ mV. Due to this rather small contribution of the cathode and the fact that the cathode does not age during anode E-cycling (see Figure 6b), the cathode overpotential is neglected herein. Hence, the following analysis of the HOR overpotential can be directly correlated to the contribution of the anode in H_2/air and H_2/O_2 polarization curves.

Figure 7a shows a measured $E_{HFR+Nernst\text{-}free}$ potential (corresponding to η_{HOR}) of 3 ± 4 mV at 2 A cm^{-2} at BoT (black diamonds), agreeing well with the above estimate based on the published HOR/HER kinetics, thereby confirming the absence of other voltage losses in the H_2-pump configuration. Note that the large error bars are due to the very low overpotentials and to errors in determining the *HFR* (≈5%); this is the reason why for precise measurements of the HOR/HER kinetics, very low Pt loadings are required.[54,57] The anode *ECSA*-loss of ≈65% after 3200 E-cycles translates into an additional kinetic overpotential of 7 mV at 2 A cm^{-2} according to the Butler-Volmer equation based estimate using the above given kinetic parameters, which is again perfectly consistent with the measured 10 ± 3 mV at 2 A cm^{-2} (red diamonds). The agreement between calculated and measured η_{HOR} gains upon anode *ECSA*-loss requires that the HOR/HER exchange current density is invariant with *ECSA*, which previously was shown to be the case for catalysts with largely different m^2_{Pt} g^{-1}_{Pt} values.[55]

As discussed above, under automotive operating conditions with a H_2 utilization of 99% and with an anode recycle loop, the N_2 concentration in the anode flow-field can be as high as ≈30% at low current densities of 0.2 A cm^{-2}. Thus, to obtain insights into the anode overpotential arising under such operating conditions, experiments with dilute feed gas (70% H_2 in N_2) were carried out. In addition to kinetic overpotential losses, these experiments with dilute H_2 will also yield information with respect to the H_2 mass-transport properties of the anode before (Figure 7, black, hollow circles) and after aging (Figure 7, red, hollow circles). Due to the lower concentration of H_2 in the gas feed, the equilibrium potential of the anode shifts with respect to the counter/reference electrode operated under pure H_2, which is corrected for in Figure 7 by subtracting the calculated Nernst shift (5.4 mV at 80°C and 70% H_2) from the measured potential.

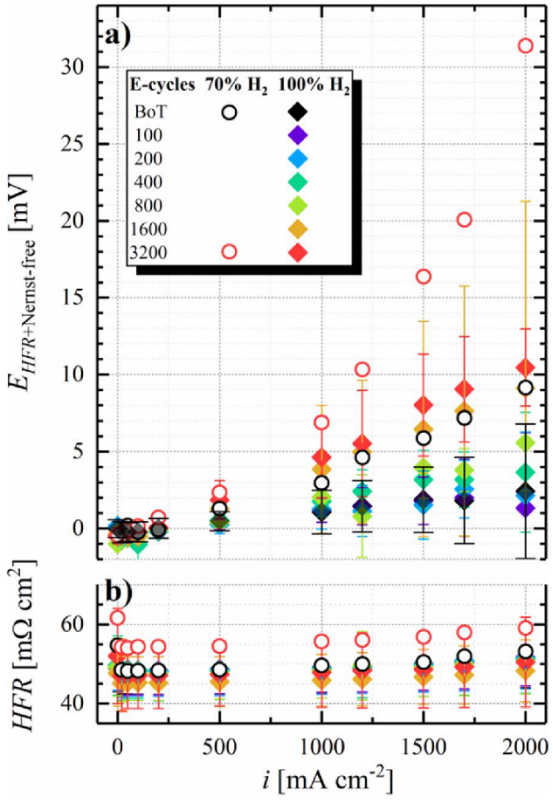

Figure 7. a) H_2-pump polarization curves of a 50 cm^2 Gore MEA at 80°C, 100% *RH*, and 70 kPa_g at a fixed flow rate of 2000 nccm H_2 on the cathode and 2000 nccm H_2 (diamonds) or 70% H_2 in N_2 (circles) on the anode, respectively. b) *HFR* determined via GEIS measurements at the respective current density. The potential ($E_{HFR+Nernst\text{-}free}$) was corrected for the *HFR* and in case of the 70% H_2 data (circles) for the Nernstian shift. Error bars represent the standard deviation from independent repeat measurements (analogous to the SUSD protocol shown in Table I, 6 for BoT and after 100 E-cycles, 5 after 200 E-cycles, etc.).

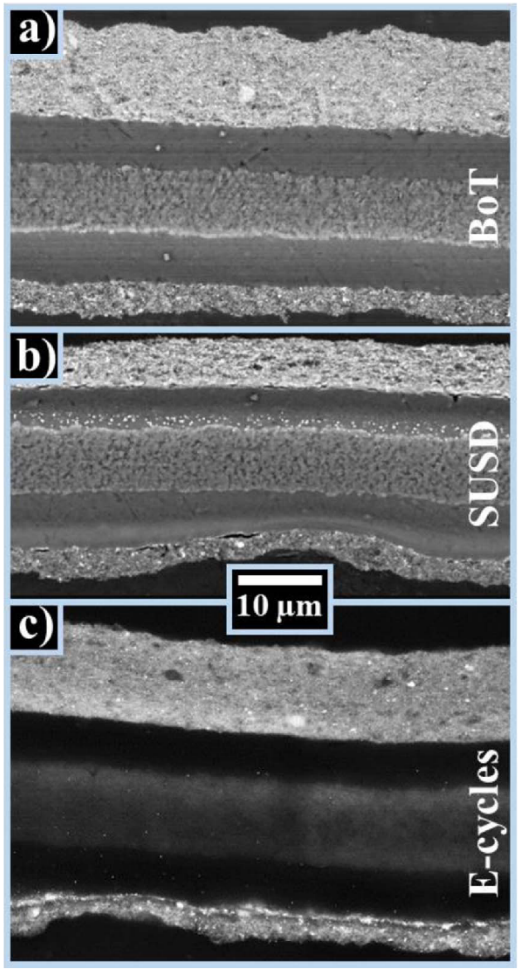

Figure 8. High-resolution SEM images of cross-sectioned embedded MEAs at a) BoT, b) after 3200 SUSD cycles, and, c) after 3200 E-cycles. From top to bottom, the layers are cathode, membrane (with PTFE reinforcement), and anode for each image. SEM images were taken at a magnification of 1500x and an acceleration voltage of 10 kV (a and b) or 25 kV (c).

Furthermore, reducing the concentration of H_2 in the anode feed is expected to cause a small offset in the kinetic HOR overpotential compared to pure H_2 (5 mV in dilute H_2 compared to 4 mV in pure H_2 at 2 A cm^{-2} and a *rf* of 65 cm^2_{Pt} cm^{-2}) due to the slower apparent kinetics at the lower H_2 partial pressure, following a 0.5-order dependence[58] (i.e., $i_0^{70\%} = (\frac{70}{100})^{0.5} \cdot i_0^{100\%}$). However, the anode overpotential measured in 70% H_2 at BoT of ≈9 mV at 2 A cm^{-2} (black circles in Figure 7a) is larger than that determined in pure H_2 (3 ± 4 mV at 2 A cm^{-2}), which must originate from an overpotential induced by H_2 mass-transport to the Pt surface, likely due to the lower H_2 diffusion coefficient in the N_2 containing mixture. After 3200 E-cycles, the total anode overpotential in 70% H_2 in N_2 increases to ≈31 mV (red circles in Figure 7a), much larger than the ≈8 mV predicted by the HOR/HER kinetics for the decreased anode *ECSA* after 3200 E-cycles. Hence, we attribute this additional overpotential to a significantly increased H_2 mass-transport resistance produced by E-cycling. As outlined in the analysis of SUSD-induced cathode degradation, such mass-transport overpotentials are typically caused by a loss of void volume in the electrode, originating from the oxidation of the carbon support to high potentials. In the case of SUSD-induced cathode degradation, the cathode potential can reach ≈1.5 V, where carbon support corrosion is very fast, and where it leads to the well-known effect of "cathode thinning". Quite clearly, cycling the electrode potential to only 1.05 V in the case of our anode E-cycling protocol, much less carbon support corrosion is expected, but as shown by Borup et al.,[8] it is not negligible. Evidence for corrosion of the anode carbon support during SUSD was presented by Engl et al., who reported significant carbon oxidation on the anode electrode during SUSD in high temperature phosphoric acid fuel cells.[18]

MEA thickness after SUSD/E-cycles.—To determine whether one can indeed observe a thinning of the anode catalyst layers upon extended SUSD cycles or E-cycles, cross sections of pristine and aged MEAs were prepared and analyzed via SEM. MEAs after 3200 SUSD cycles (Figure 8b) show a clear deposition of Pt inside the membrane, close to the cathode electrode, originating from the reduction of Pt ions by H_2 permeating from the anode compartment, as outlined earlier. On the other hand, the SEM image after 3200 E-cycles presented in Figure 8c shows a clearly brighter contrast at the membrane/anode interface compared to BoT (Figure 8a), consistent with the above stated hypothesis that voltage-cycling on the anode leads to an accumulation of Pt precipitates in this region.

Due to the relatively inhomogeneous electrode thickness, already in their pristine state, and especially on the anode side (cf. Figure 8a), the electrode thickness was obtained by dividing the respective catalyst layer's cross section area by their length within the imaged MEA section. The calculated mean layer thicknesses were double-checked with ordinary thickness measurements in the center of each micrograph. All MEAs were investigated at five different positions along

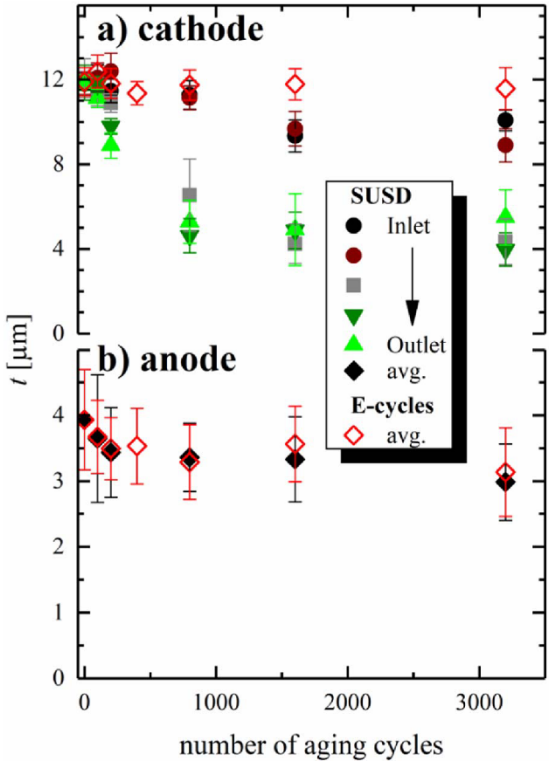

Figure 9. Thickness of a) the cathode and b) the anode at the respective number of aging cycles, determined via SEM analysis of embedded MEA cross-sections. Thickness values are averaged from measurements at 5 different locations (see Figure 1) with 10 measurements at each location, with the error bars representing their standard deviation. For SUSD cycled cathodes, thickness values are given for the 5 different locations along the anode gas flow, i.e., from the anode gas inlet (black, brown) via the center of the MEA (gray) to the outlet (olive, green). Owing to the small thickness changes, thickness values for SUSD aged anodes and anodes/cathodes aged by E-cycles are shown as average of all locations (error bars representing the standard deviation of 50 measurements).

the anode gas flow direction (see Figure 1) to resolve local differences in the thinning profile from inlet to outlet, which is commonly observed for SUSD-aged cathodes.[59] At each of these five locations, ten micrographs were taken to obtain statistically significant results. As expected, local disparities were only observed for cathodes aged by SUSD (Figure 9a, solid symbols), i.e., a moderate thinning by about 20% within 1600 SUSD cycles close to the anode inlet, while the cathode layer thickness at the center of the cathode active area and the region facing the outlet of the anode flow-field decreased by at least 50% of their original thickness. This much higher degradation near the cathode outlet can be assigned to the so-called pseudo-capacitive effect, which mitigates the carbon oxidation reaction (COR) during the reverse current event via capacitive charging of the electrodes during potential transients.[16] Since the effectiveness of this mitigation is stronger during shut-down compared to start-up, cathode corrosion in the vicinity of the anode inlet, which is mainly occurring during shut-down, is more strongly suppressed, leading to the observed thinning profile. This pattern is expected whenever the H_2/air front residence time is short, as is the case in our experiments (≈0.1 s), because capacitive effects can more effectively provide the reverse current at fast potential transients. Assuming that the volume of the fully humidified ionomer in the cathode is roughly the same as that of the carbon (i.e., an ionomer to carbon weight ratio of ≈0.6), and based upon the packing density of 18% for conventional carbons,[60] the void volume fraction amounts to about 60% in the pristine cathode at 100% *RH*. Since electrode thinning is caused by carbon structure collapse after the corrosion of only 7–10%$_{wt}$ of the total carbon mass,[25] the loss of electrode volume is at the expense of the electrode's void volume fraction. Consequently, the observed thickness reduction of 20 and 50% is indicative of a drop in void volume by 1/3 and 5/6, respectively, resulting in the unacceptably high O_2 mass-transport penalties observed in the corresponding H_2/air curves discussed above (Figure 2a).

In contrast to the clearly observable thinning of the cathode during SUSD, a much more subtle thinning of the anode upon SUSD/E-cycling is indicated by the measurements provided in Figure 9b (black and red diamonds), with rather large error bars compared to the overall changes. As no trend with respect to the sampling location (see Figure 1) could be determined at the five imaged positions, all anode thicknesses measurements on a given MEA were averaged. The results show a ≈25% anode thinning for both aging protocols, even though it must be noted that the respective error bars largely overlap for all measurements between BoT and 3200 aging cycles. Nevertheless, these relatively large error bars are mainly due to the high thickness variations of the anode electrodes in the pristine MEA (Figure 8a), so that the general trend of a ≈25% anode thinning over the course of 3200 SUSD or E-cycles is still significant. For an anode, for which the ionomer to carbon weight ratio is typically close to one, this translates into a more than 50% loss in void volume fraction, which suggests that the large non-kinetic overpotentials after 3200 E-cycles observed in H_2-pump experiments conducted with 70% H_2 at the anode side (red circles in Figure 7a) are indeed due to a H_2 mass-transport resistance caused by anode carbon corrosion during voltage-cycling (and, by extension, during SUSD cycles). Finally, as expected, anode aging via E-cycles does not lead to a thinning of the cathode (red diamonds in Figure 9a).

Implications for low-loaded anodes.—Even though the here observed kinetic HOR overpotentials were small both at BoT and after aging of the MEAs via E-cycling (see data in pure H_2, Figure 7a), the targeted anode Pt loadings for commercially viable MEAs are on the order of 50 μg_{Pt} cm^{-2} (compared to 100 μg_{Pt} cm^{-2} in this study) at current densities up to 3 A cm^{-2}.[22] For example, in order to meet the current DoE target of 125 μg_{Pt} cm^{-2} total Pt loading in the MEA,[61] and considering the large O_2 mass-transport resistance when using cathode loading of less than 100 μg_{Pt} cm^{-2},[62,63] anode loadings likely will need to be further reduced to as little as 25 μg_{Pt} cm^{-2}. For such extremely low anode loadings, the HOR kinetic losses may become significant and anode *ECSA*-losses upon SUSD events can be expected to gain relevance.

To enable a comparison of the expected contribution of the HOR to the overall fuel cell performance with respect to the anode loading and the SUSD-induced anode *ECSA*-loss, Figure 10 shows the kinetic overpotential as a function of the anode roughness factor, calculated via the Butler-Volmer equation (see Equation 5), using an HOR/HER exchange current density of 240 mA cm$_{Pt}^{-2}$ and of 120 mA cm$_{Pt}^{-2}$ at 80°C and 40°C, respectively, anodic/cathodic transfer coefficients of $\alpha_{a/c} = 0.5$, and a H_2 partial pressure of 100 kPa. As verified experimentally by the H_2-pump measurements discussed in the previous section, the high anode roughness factor of ≈65 cm$_{Pt}^2$ cm^{-2} (based on 100 μg_{Pt} cm^{-2} with a BoT specific surface area of 65 m$_{Pt}^2$ g$_{Pt}^{-1}$) leads to minor kinetic overpotentials, estimated to be only ≈6 mV even at a current density as high as 3 A cm^{-2} at 80°C (black line in Figure 10). For an anode catalyst with the same *ECSA* applied at a loading of 50 μg_{Pt} cm^{-2}, the *rf* decreases to ≈32 cm$_{Pt}^2$ cm^{-2}, while the kinetic HOR overpotential remains relatively low at ≈12 mV at 3 A cm^{-2} and 80°C, underlining the observation made by Gasteiger et al., that the overall fuel cell performance in H_2/air is not noticeably affected when lowering the anode loading from 400 μg_{Pt} cm^{-2} to 50 μg_{Pt} cm^{-2}.[34] However, considering a future employment of anodes with a decreased Pt loading of 25 μg_{Pt} cm^{-2}, the *rf* for the same catalyst would decrease to ≈16 cm$_{Pt}^2$ cm^{-2}, in which case the HOR overpotential would increase to ≈23 mV at 3 A cm^{-2}. While PEMFC testing is most commonly studied at a constant temperature of 80°C, applied systems will at least partially operate at lower temperatures,

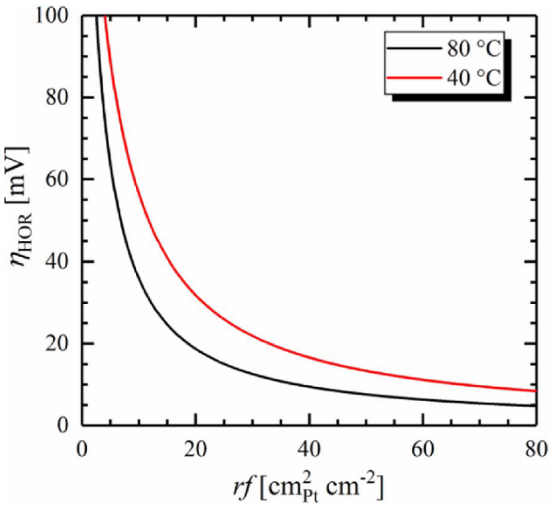

Figure 10. Kinetic overpotential for the HOR at 3 A cm^{-2} as a function of the anode roughness factor, calculated for an exchange current density of i_0 = 240 mA cm^{-2}_{Pt} or 120 mA cm^{-2}_{Pt} at 80°C or 40°C, respectively, for a H_2 partial pressure of 100 kPa, and for anodic and cathodic transfer coefficients of $\alpha_{a/c}$ = 0.5.

e.g., after starting the system or at low ambient temperatures, leading to a more pronounced contribution of the anode HOR overpotential of ≈38 mV at 3 A cm^{-2} and 40°C for these ultra-low anode loadings (red line in Figure 10).

While anode overpotentials in this order of magnitude are already at the limit of a tolerable voltage loss for practical applications, aging of the anode catalyst layer due to SUSD cycles, resulting in a reduction of the *ECSA* on the order of 50% will lead to non-tolerable increases of the anode overpotential, e.g., an increase at 3 A cm^{-2} to more than 40 mV at 80°C and more than 65 mV at 40°C. In conclusion, the degradation not only of the cathode, but also of the anode during SUSD needs to be taken into consideration in order to obtain a durable PEMFC system when reducing the Pt content on the anode to meet future loading targets.

Conclusions

In this manuscript, the effect of SUSD not only on the cathode, but also on the anode side of PEMFCs was shown. While the degradation of the cathode followed the expected pattern and was observable with respect to a decrease of *ECSA*, an associated increase in the kinetic overpotential, as well as an increase of the O_2 mass-transport resistance, anode degradation was found to occur as also a combination of carbon corrosion, distinctive in the form of electrode thinning, and *ECSA*-loss. While the loss of *ECSA* can be simply monitored by recording CVs in the course of SUSD cycling, the development of an AST based on voltage-cycling between ≈0 and ≈1 V was necessary to determine the effect of carbon corrosion in a H_2-pump measurement under dilute H_2 on the working electrode. As outlined by our final analysis of the kinetic HOR overpotential as a function of anode *rf*, the implementation of ultra-low loaded anodes (i.e., 25 μg_{Pt} cm^{-2}), necessary in the future to meet cost requirements for a widespread commercialization of PEMFC systems in automotive applications, requires to largely mitigate anode degradation. Among different strategies to mitigate SUSD-induced degradation, simply limiting the amount of SUSD events addresses both, cathode and anode deterioration and therefore is the strategy of choice with respect to our findings. Such system management-based approaches are e.g., to maintain the anode compartment filled with H_2 during longer lasting idle times, or to consume the O_2 in the cathode compartment before a full shut-down of the system. If this could decrease the number of SUSD events to ≤100 cycles throughout the lifetime of a vehicle, the *ECSA*-losses on both electrodes (<20%), as well as the associated H_2/air performance loss would be tolerable, even for the target total Pt loading of 0.125 mg_{Pt} cm^{-2}.

Acknowledgment

The authors of this study acknowledge the work of Nhat Long Tran Pham and David Fischermeier for providing some help in an early phase of this study. Furthermore, the expert work of Katia Rodewald to obtain SEM images of MEA cross sections is greatly appreciated. Finally, Greenerity GmbH is acknowledged for funding through a subcontract co-funded by the German Federal Ministry for Economic Affairs and Energy (BMWi; project "HyMotion5-Brennstoffzellenstapel" under the project support number 03ET2058C).

ORCID

J. N. Schwämmlein https://orcid.org/0000-0001-8902-4508
P. J. Rheinländer https://orcid.org/0000-0002-0018-065X

References

1. *Hyundai Motor Co. (accessed* 09/18/2018), https://www.hyundai.com/worldwide/en/eco/ix35-fuelcell/highlights.
2. *Toyota Motor Co. (accessed* 09/18/2018), https://ssl.toyota.com/mirai/fcv.html.
3. *Honda Motor Co., Ltd. (accessed* 09/18/2018), https://automobiles.honda.com/clarity-fuel-cell.
4. Y. Yu, H. Li, H. Wang, X.-Z. Yuan, G. Wang, and M. Pan, *J. Power Sources.*, **205**, 10 (2012).
5. C. A. Reiser, L. Bregoli, T. W. Patterson, J. S. Yi, J. D. Yang, M. L. Perry, and T. D. Jarvi, *Electrochem. Solid-State Lett.*, **8**, A273 (2005).
6. S. G. Bratsch, *J. Phys. Chem. Ref. Data.*, **18**, 1 (1989).
7. J. P. Meyers and R. M. Darling, *J. Electrochem. Soc.*, **153**, A1432 (2006).
8. R. L. Borup, D. D. Papadias, R. Mukundan, D. Spernjak, D. A. Langlois, R. Ahluwalia, K. L. More, and S. Grot, *ECS Trans.*, **69**, 1029 (2015).
9. J. Zhang, R. N. Carter, P. T. Yu, W. W. Gu, F. T. Wagner, and H. A. Gasteiger, in *Encyclopedia of Electrochemical Power Sources*, 1st ed., J. Garche, C. Dyer, P. Moseley, Z. Ogumi, D. Rand, and B. Scrosati, p. 626, Elsevier, Amsterdam (2009).
10. Y. Yu, Z. Tu, H. Zhang, Z. Zhan, and M. Pan, *J. Power Sources.*, **196**, 5077 (2011).
11. T. Mittermeier, A. Weiß, F. Hasché, G. Hübner, and H. A. Gasteiger, *J. Electrochem. Soc.*, **164**, F127 (2017).
12. J. H. Kim, E. A. Cho, J. H. Jang, H. J. Kim, T. H. Lim, I. H. Oh, J. J. Ko, and S. C. Oh, *J. Electrochem. Soc.*, **157**, B104 (2010).
13. J. H. Kim, Y. Yeon Jo, E. A. Cho, J. H. Jang, H. J. Kim, T.-H. Lim, I.-H. Oh, J. J. Ko, and I. J. Son, *J. Electrochem. Soc.*, **157**, B633 (2010).
14. T. Mittermeier, A. Weiß, F. Hasché, and H. A. Gasteiger, *submitted*.
15. Y. Y. Jo, E. Cho, J. H. Kim, T.-H. Lim, I.-H. Oh, S.-K. Kim, H.-J. Kim, and J. H. Jang, *J. Power Sources.*, **196**, 9906 (2011).
16. W. Gu, R. N. Carter, P. T. Yu, and H. A. Gasteiger, *ECS Trans.*, **11**, 963 (2007).
17. P. T. Yu, W. Gu, R. Makharia, F. T. Wagner, and H. A. Gasteiger, *ECS Trans.*, **3**, 797 (2006).
18. T. Engl, L. Gubler, and T. J. Schmidt, *Energy Technol.*, **4**, 65 (2016).
19. J. N. Schwämmlein, P. J. Rheinländer, Y. Chen, K. T. Freyer, and H. A. Gasteiger, *ECS Trans.*, **80**, 927 (2017).
20. G. S. Harzer, J. N. Schwämmlein, A. M. Damjanović, S. Ghosh, and H. A. Gasteiger, *J. Electrochem. Soc.*, **165**, F3118 (2018).
21. J. N. Schwämmlein, G. S. Harzer, P. Pfändner, A. Blankenship, H. A. El-Sayed, and H. A. Gasteiger, *J. Electrochem. Soc.*, **165**, J3173 (2018).
22. A. Kongkanand and M. F. Mathias, *J. Phys. Chem. Lett.*, **7**, 1127 (2016).
23. C. Simon, F. Hasché, and H. A. Gasteiger, *J. Electrochem. Soc.*, **164**, F591 (2017).
24. R. Makharia, S. Kocha, P. Yu, M. A. Sweikart, W. Gu, F. Wagner, and H. A. Gasteiger, *ECS Trans.*, **1**, 3 (2006).
25. H. A. Gasteiger, W. Gu, B. Litteer, R. Makharia, B. Brady, M. Budinski, E. Thompson, F. T. Wagner, S. G. Yan, and P. T. Yu, in *Mini-Micro Fuel Cells*, 1st ed., S. Kakaç, A. Pramuanjaroenkij, and L. Vasiliev, p. 225, Springer Netherlands, Dordrecht (2008).
26. Y. H. Lai and D. A. Dillard, in *Handbook of Fuel Cells*, 1st ed., W. Vielstich, H. Yokokawa, and H. A. Gasteiger, p. 403, John Wiley & Sons Ltd., Chichester (2009).
27. A. B. LaConti, M. Hamdan, and R. C. McDonald, in *Handbook of Fuel Cells*, 1st ed., W. Vielstich, A. Lamm, and H. A. Gasteiger, p. 647, John Wiley & Sons Ltd., Chichester (2009).
28. M. F. Mathias, J. Roth, J. Fleming, and W. Lehnert, in *Handbook of Fuel Cells*, 1st ed., W. Vielstich, A. Lamm, and H. A. Gasteiger, p. 517, John Wiley & Sons Ltd., Chichester (2009).
29. I. M. Lifshitz and V. V. Slyozov, *J. Phys. Chem. Solids.*, **19**, 35 (1961).

30. Y. Shao-Horn, P. Ferreira, G. J. La O', D. Morgan, H. A. Gasteiger, and R. Makharia, *ECS Trans.*, **1**, 185 (2006).
31. Y. Shao-Horn, W. C. Sheng, S. Chen, P. J. Ferreira, E. F. Holby, and D. Morgan, *Top. Catal.*, **46**, 285 (2007).
32. J. Zhang, B. A. Litteer, W. Gu, H. Liu, and H. A. Gasteiger, *J. Electrochem. Soc.*, **154**, B1006 (2007).
33. R. M. Darling and J. P. Meyers, *J. Electrochem. Soc.*, **150**, A1523 (2003).
34. H. A. Gasteiger, J. E. Panels, and S. G. Yan, *J. Power Sources.*, **127**, 162 (2004).
35. P. D. Beattie, V. I. Basura, and S. Holdcroft, *J. Electroanal. Chem.*, **468**, 180 (1999).
36. H. A. Gasteiger, S. S. Kocha, B. Sompalli, and F. T. Wagner, *Appl. Catal., B.*, **56**, 9 (2005).
37. K. C. Neyerlin, W. Gu, J. Jorne, and H. A. Gasteiger, *J. Electrochem. Soc.*, **153**, A1955 (2006).
38. A. P. Young, J. Stumper, and E. Gyenge, *J. Electrochem. Soc.*, **156**, B913 (2009).
39. P. J. Ferreira, G. J. la O', Y. Shao-Horn, D. Morgan, R. Makharia, S. Kocha, and H. A. Gasteiger, *J. Electrochem. Soc.*, **152**, A2256 (2005).
40. R. L. Borup, J. R. Davey, F. H. Garzon, D. L. Wood, and M. A. Inbody, *J. Power Sources.*, **163**, 76 (2006).
41. C. H. Paik, G. S. Saloka, and G. W. Graham, *Electrochem. Solid-State Lett.*, **10**, B39 (2007).
42. S. Arisetty, X. Wang, R. K. Ahluwalia, R. Mukundan, R. Borup, J. Davey, D. Langlois, F. Gambini, O. Polevaya, and S. Blanchet, *J. Electrochem. Soc.*, **159**, B455 (2012).
43. R. K. Ahluwalia, S. Arisetty, J.-K. Peng, R. Subbaraman, X. Wang, N. Kariuki, D. J. Myers, R. Mukundan, R. Borup, and O. Polevaya, *J. Electrochem. Soc.*, **161**, F291 (2014).
44. K. Yu, D. J. Groom, X. Wang, Z. Yang, M. Gummalla, S. C. Ball, D. J. Myers, and P. J. Ferreira, *Chem. Mater.*, **26**, 5540 (2014).
45. P. Zihrul, I. Hartung, S. Kirsch, G. Huebner, F. Hasché, and H. A. Gasteiger, *J. Electrochem. Soc.*, **163**, F492 (2016).
46. N. M. Marković, B. N. Grgur, and P. N. Ross, *J. Phys. Chem. C.*, **101**, 5405 (1997).
47. N. Marković, H. A. Gasteiger, and P. N. Ross, *J. Electrochem. Soc.*, **144**, 1591 (1997).
48. R. Subbaraman, D. Strmcnik, V. Stamenkovic, and N. M. Marković, *J. Phys. Chem. C.*, **114**, 8414 (2010).
49. J. C. Canullo, W. E. Triaca, and A. J. Arvía, *J. Electroanal. Chem. Interfacial. Electrochem.*, **175**, 337 (1984).
50. R. M. Cerviño, W. E. Triaca, and A. J. Arvia, *J. Electrochem. Soc.*, **132**, 266 (1985).
51. C. L. Perdriel, W. E. Triaca, and A. J. Arvia, *J. Electroanal. Chem.*, **205**, 279 (1986).
52. C. K. Mittelsteadt and H. Liu, in *Handbook of Fuel Cells*, 1st ed., W. Vielstich, H. Yokokawa, and H. A. Gasteiger, p. 345, John Wiley & Sons Ltd., Chichester (2009).
53. S. S. Kocha, J. Deliang Yang, and J. S. Yi, *AIChE J.*, **52**, 1916 (2006).
54. K. C. Neyerlin, W. Gu, J. Jorne, and H. A. Gasteiger, *J. Electrochem. Soc.*, **154**, B631 (2007).
55. J. Durst, C. Simon, A. Siebel, P. J. Rheinländer, T. Schuler, M. Hanzlik, J. Herranz, F. Hasché, and H. A. Gasteiger, *ECS Trans.*, **64**, 1069 (2014).
56. J. Durst, A. Siebel, C. Simon, F. Hasché, J. Herranz, and H. A. Gasteiger, *Energy Environ. Sci.*, **7**, 2255 (2014).
57. J. Durst, C. Simon, F. Hasché, and H. A. Gasteiger, *J. Electrochem. Soc.*, **162**, F190 (2015).
58. P. J. Rheinländer, J. Herranz, J. Durst, and H. A. Gasteiger, *J. Electrochem. Soc.*, **161**, F1448 (2014).
59. W. Gu, P. T. Yu, R. Makharia, and H. A. Gasteiger, in *Modeling and Diagnostics of Polymer Electrolyte Fuel Cells*, 1st ed., U. Pasaogullari and C.-Y. Wang, p. 45, Springer, New York (2010).
60. W. Gu, D. R. Baker, Y. Liu, and H. A. Gasteiger, in *Handbook of Fuel Cells*, 1st ed., W. Vielstich, H. Yokokawa, and H. A. Gasteiger, p. 631, John Wiley & Sons Ltd., Chichester (2009).
61. *U.S. Department of Energy (accessed* 10/16/2017), https://energy.gov/eere/fuelcells/downloads/fuel-cell-technologies-office-multi-year-research-development-and-22.
62. T. A. Greszler, D. Caulk, and P. Sinha, *J. Electrochem. Soc.*, **159**, F831 (2012).
63. N. Nonoyama, S. Okazaki, A. Z. Weber, Y. Ikogi, and T. Yoshida, *J. Electrochem. Soc.*, **158**, B416 (2011).

3.2.2. Cathode Loading Impact on Voltage Cycling Induced PEMFC Degradation: A Voltage Loss Analysis

Here, the journal article “Cathode Loading Impact on Voltage Cycling Induced PEMFC Degradation: A Voltage Loss Analysis” is presented,[58] published in March 2018 in the Journal of The Electrochemical Society as an open access article distributed under the terms of the Creative Commons Attribution 4.0 License, permitting unrestricted reuse of the work in any medium, provided the original work is properly cited. The permanent web link for this article is https://doi.org/10.1149/2.0161806jes.

Short summary.—As outlined in the previous section, a frequent change of the potential at the catalyst layer in the MEA is a major source of degradation. During dynamic operation, e.g., load cycling in automotive applications, the cathode is subjected to a frequent potential variation.[70] As detailed in section 1.3, this induces an oxidation / reduction of the Pt surface, leading to Pt dissolution which in turn causes Ostwald ripening and a loss of *ECSA*. Furthermore, the most commonly applied support material, i.e., carbon black, is thermodynamically not stable at potentials positive of 0.2 V_{RHE}, even though the sluggish kinetics of the COR enable the use of carbon up to ≈1 V_{RHE}.[78]

Since a large variety of ASTs is described in the literature,[77,124,147–150] one aim of this study is to compare different voltage cycling procedures with respect to their impact on PEMFC key performance indicators, such as *ECSA*, ORR activity, H^+-conduction resistance and O_2-mass transport resistance. Amongst others, square waves (SW) between 0.6 and 1.0 V_{RHE} and triangular waves (TW) at a scan rate of 50 mV s^{-1} in the same potential region are compared. To determine the influence of the fast potential transient versus the holding period in SWs, the rapid potential change is replaced by a scan at 50 mV s^{-1}, termed as triangular wave-hold profile (TW-H). Moreover, the impact of the potential range is evaluated by lowering the upper potential limit of the triangular wave protocol to 0.85 V_{RHE} (TW-LUPL). To investigate the influence of a loss of pore volume in the cathode catalyst layer on the O_2 mass-transport resistance, MEAs are exposed to a high cathode potential hold (CP), specifically degrading the cathode carbon support structure, while maintaining a reasonably high *rf*. In addition to differences in the applied AST protocol, it is well known that severe voltage losses occur when the *rf*

of the cathode decreases below a certain value, e.g., for low loaded electrodes or after electrode ageing.[60–62,151,152] To investigate the correlation of the Pt specific O_2 mass-transport resistance and the ageing stage of the cathode, electrodes with high and low initial Pt loading are prepared and aged by various ASTs.

In alignment with previous reports in the literature, the SW ageing protocol is more damaging than the TW protocol, both, for high and low-loaded electrodes. A comparison of the *ECSA* after ageing between the TW-H and the SW profile shows that the rapid potential transient has an insignificant influence on the ageing behavior of the cathode (considering degradation per cycle), which is mainly determined by the high potential phase. Furthermore, a stronger ageing of low compared to high loaded catalyst layers is discovered and related to the smaller initial Pt particle size in the different catalysts. By comparing the O_2 mass-transport resistances of electrodes aged according to SW, TW, TW-H and CP profiles, we are able to identify that carbon corrosion has a minor impact on the loss of performance in ASTs with a maximum voltage of 1.0 V_{RHE}. On the other hand, we conclude that lowering the *rf* (either at BOT or after ageing) induces a non-linear increase of the Pt specific O_2 mass-transport resistance which significantly impacts the performance of low loaded cathodes. A comparison of the O_2 mass-transport resistance for pristine low loaded electrodes and aged high loaded cathodes shows that the pressure independent O_2 mass-transport resistance after the AST consisted of the Pt specific fraction and an additional resistance originating from catalyst layer ageing. Moreover, lowering the upper potential limit of the AST to 0.85 V_{RHE} results in full retention of the BOT H_2/air performance after 30000 ageing cycles, hence provides a clear path for the development of highly durable, automotive PEMFC systems. Finally, a correction of the measured H_2/air polarization curves for all known loss terms shows that a large fraction of unaccounted losses occurs on electrodes which suffer from high Pt specific O_2 mass transport resistances, rendering the currently applied in-situ diagnostic toolset questionable.

Author contributions.—In this study, A.M.D. acquired the data and analyzed it together with G.S.H. and J.N.S. All authors discussed the results and reviewed the manuscript that was written by G.S.H. and J.N.S. To this work, G.S.H. and J.N.S. have contributed equally as first authors.

JES Focus Issue on Proton Exchange Membrane Fuel Cell (PEMFC) Durability

Cathode Loading Impact on Voltage Cycling Induced PEMFC Degradation: A Voltage Loss Analysis

Gregor S. Harzer,[1,=,*,z] Jan N. Schwämmlein,[1,=,*] Ana Marija Damjanović,[2] Sourov Ghosh,[1] and Hubert A. Gasteiger[1,]**

[1] *Chair of Technical Electrochemistry, Department of Chemistry and Catalysis Research Center, Technical University of Munich, D-85748 Garching, Germany*
[2] *Faculty of Chemical Engineering and Technology, University of Zagreb, 10000 Zagreb, Croatia*

This study focuses on voltage cycling induced degradation of cathodes with different loading (0.4 and 0.1 mg_{Pt}/cm^2) when applying square wave or triangular wave based accelerated stress tests (ASTs) between 0.6 and 1.0 V_{RHE}. The degradation of the H_2/O_2 and H_2/air performance upon extended voltage cycling (up to 30000 cycles) was analyzed in terms of the voltage loss contributions from ORR kinetics, O_2 mass transport resistances and proton conduction resistances in the cathode. The extent of cathode thinning due to carbon support corrosion was determined by post mortem electrode thickness measurements. Square waves were found to cause a more rapid loss of *ECSA* and mass activity compared to triangular waves, which was shown to be due to the longer hold periods at high potentials rather than to the rate of the potential transient. The observed increase of the O_2 mass transport resistance with voltage cycling was found to mainly depend on the available Pt surface area, while mass transport resistances due to carbon corrosion were found to be insignificant. Finally, it was shown that by lowering the upper potential limit to 0.85 V_{RHE}, low-loaded catalyst layers can sustain 30000 potential cycles without degradation of the H_2/air performance.
 [DOI: 10.1149/2.0161806jes]

Manuscript submitted December 27, 2017; revised manuscript received February 28, 2018. Published March 14, 2018. *This paper is part of the JES Focus Issue on Proton Exchange Membrane Fuel Cell (PEMFC) Durability.*

Currently, proton exchange membrane fuel cells (PEMFCs) are on the verge of widespread commercialization as an alternative power source for the automotive market, impressively demonstrated by the launch of PEMFC based vehicles by Toyota,[1] Hyundai,[2] and Honda[3] in recent years. The major hurdle for a significant market penetration of PEMFC vehicles in the near future is the reduction of system cost and the amount of platinum, while meeting long-term durability targets.[4,5] Despite remarkable achievements in lowering the Pt loading of the cathode catalyst layer in state-of-the-art membrane electrode assemblies (MEAs) down to ≈0.1 mg_{Pt}/cm^2,[6–8] recent studies have shown that additional overpotentials occur at low loadings and high current density.[8–11] Even though the exact origin of these losses is subject to ongoing discussions in the literature, its occurrence was directly correlated to the available Pt surface area in the cathode, i.e., to the cathode roughness factor (*rf*, defined as Pt surface area per geometric surface area in units of cm^2_{Pt}/cm^2), so that it is often referred to as Pt specific O_2 mass transport resistance ($R^{Pt}_{O_2}$).[8–10] Additionally, it is well-known that MEAs degrade under the dynamic load-cycles relevant for automotive applications due to the associated voltage cycles. This made extended voltage cycling tests a frequently applied accelerated stress test (AST) to probe the durability of the cathode catalyst layer. Despite various reports in the literature employing different aging protocols, such as applying square wave (SW) potential perturbations or constant high potential phases, the most commonly applied aging protocol is based on triangular wave (TW) potential perturbations between cell voltages of 0.6 and 1.0 V at a scan rate of typically 50 mV/s.[12–21]

Thermodynamically, the carbon black support for the noble metal catalyst in the MEA is not stable under fuel cell operating conditions, since the equilibrium potential of the carbon oxidation reaction (COR) is only 0.2 V_{RHE} (considering CO_2 as reaction product).[22] Fortuitously, the sluggish kinetics of the COR prevent the oxidation of carbon at potentials < 0.9 V_{RHE}, i.e., within the typical fuel cell operating range,[17,23,24] and therefore enable its use in the cathode catalyst layer. On the other hand, high voltage periods, occurring for example during system start-up or shut-down, can oxidize the carbon structure in the catalyst layer, eventually leading to a loss of void volume and a thinning of the electrode (often referred to as "cathode thinning").[25–27] Since a sufficiently large void volume is crucial for the transport of O_2 through the cathode catalyst layer, significant corrosion of the carbon support causes an increase of the O_2 mass transport resistance and a decrease of PEMFC performance. In addition, carbon corrosion was found to cause a detachment of Pt from the carbon support, leaving the Pt nanoparticles electrically disconnected from the electrode, which decreases the available electrochemical surface area (*ECSA*) of Pt. Another source of *ECSA* loss during ASTs are repetitive changes of the cathode potential, leading to oxidation and reduction of the Pt surface.[13,14,20] Upon its reduction/oxidation, Pt surface atoms can dissolve from the nanoparticle into the electrolyte as ionic species, eventually redepositing on existing Pt nanoparticles via a process referred to as Ostwald ripening, resulting in an increase of the average Pt particle size and an associated *ECSA* loss.[28,29] Furthermore, as long as the electrode is held at high potentials, Pt ions can diffuse in the electrolyte phase towards the membrane where they can react with cross-over hydrogen to form electrically insulated Pt deposits within the membrane phase.[30] Since these Pt deposits can no longer contribute to the electrochemical processes in the cathode catalyst layer, a significant decrease of the *ECSA* is observed.

To gain a better understanding of the aging processes occurring during voltage cycling ASTs, high-loaded (0.4 mg_{Pt}/cm^2) and low-loaded (0.1 mg_{Pt}/cm^2) MEAs were exposed to different potential cycling profiles: square waves, triangular waves, and triangular waves with an upper and lower potential hold (TW–H). The associated losses of *ECSA* and ORR mass activity were quantified by cyclic voltammetry and by differential flow H_2/O_2 performance measurements, respectively. Furthermore, the performance degradation of differential flow H_2/air polarization curves was analyzed by quantifying the proton conduction resistance via electrochemical impedance spectroscopy (EIS) and by determining the oxygen transport resistance via limiting current diagnostics. The comparison of MEA performance vs *ECSA* over the course of extended voltage cycling provides insights into the voltage cycling induced increase of the O_2 transport resistance. In addition, by deliberately corroding the carbon support through a high-potential hold of the cathode, where substantial carbon corrosion occurs (1.2 V_{cell} for 8 h), resulting in pronounced cathode thinning at a

=These authors contributed equally to this work.
*Electrochemical Society Student Member.
**Electrochemical Society Fellow.
zE-mail: gregor.harzer@tum.de

reasonable *ECSA* retention, we were able to distinguish between the impact of carbon corrosion and *ECSA* loss on the limiting current measurements. Comparing the various voltage cycling protocols, it could be shown that the higher degradation observed for square wave compared to triangular wave modulation were due to the extended time at high potentials in the former rather than to the voltage ramp rate between upper and lower potential. Our analysis also showed that the oxygen transport resistances developing over the course of voltage cycling ASTs predominantly depends on the specific current density (in units of A/cm^2_{Pt}), independent of the initial Pt loading of the MEAs.

Experimental

Comprehensive experimental details on MEA preparation and fuel cell testing are given in our previous publication,[11] but the most pertinent information is given below. All potentials referred to in cyclic voltammograms and in voltage cycling experiments are referenced to the reversible hydrogen electrode (RHE) potential at a nominal H_2 pressure of 100 kPa_{abs} (V_{RHE}). This was obtained by correcting for the Nernstian shift of the hydrogen anode if the H_2 partial pressure was different from 100 kPa_{abs}. For the voltage cycling tests conducted under H_2/N_2 (anode/cathode) at 100 kPa_{abs}, 80°C, 100% *RH*, the different applied potential limits of 0.60, 0.85, and 1.00 V_{RHE} correspond to cell voltage limits of 0.59, 0.84, and 0.99 V_{cell}. If not stated otherwise, area-normalized currents (e.g., cm^2) refer to the geometric area of the electrode. Furthermore, note that all pressures were measured and controlled at the inlet of the fuel cell and are stated as absolute pressures.

Membrane electrode assembly preparation.—All fuel cell tests were conducted with 5 cm^2 MEAs, fabricated by the decal transfer method. Catalyst inks were prepared by mixing the catalyst with a low equivalent weight ionomer in a water-solvent dispersion (Asahi Kasei, 700 EW). To realize the same electrode thickness (identical carbon loading of 0.4 mg_C/cm^2), two catalysts with different Pt/C ratio were used. For low-loaded catalyst layers, a 20%$_{wt}$ Pt/Vulcan catalyst (TEC10V20E, Tanaka Kikinzoku Kogyo K.K., TKK) and for high-loaded catalyst layers, a 50%$_{wt}$ Pt/Vulcan (TEC10V50E, TKK) was used. The ink components were added into a 15 mL capped bottle (HDPE), already containing 16.5 g of 5 mm ZrO_2 beads as grinding medium in the following sequence: catalyst, water, 1–propanol, and finally the ionomer dispersion. The water concentration of the ink was 10%$_{wt}$, while the solid content was 0.03 g/mL_{ink} to obtain a suitable viscosity for the coating process. The ionomer to carbon weight ratio (I/C) was 0.65. The inks were mixed by placing the bottles onto a roller-mill (60 rpm) for 18 h at room temperature. Thereafter, the inks were coated on virgin PTFE using the mayer rod technique with the appropriate bar on a coating machine. The same type of anode was used for all experiments, namely 0.1 mg_{Pt}/cm^2 consisting of 20%$_{wt}$ Pt/C (TEC10V20E, TKK) with an I/C ratio of 0.65. The MEAs were assembled by hot pressing a 15 µm membrane (Asahi Kasei) placed between the anode and cathode decals at 155°C for 3 min with an applied force of 0.11 kN/cm^2. The cathode loadings were 0.1 mg_{Pt}/cm^2 and 0.4 mg_{Pt}/cm^2, with a maximum deviation of ±5%, as determined by weighing the decals before and after the catalyst layer transfer. For each aging procedure, two independent fuel cell measurements were conducted and subsequently averaged with error bars corresponding to the mean absolute deviation.

Fuel cell testing equipment.—Electrochemical measurements were performed on an in-house manufactured, single-cell hardware, using commercial graphite flow fields (0.5 mm lands/ channels; manufactured by Poco Graphite according to our design).[31] Gas diffusion layers (GDLs) were supplied by Freudenberg (H14C7) and the GDL compression was adjusted to 20 ± 1% by PTFE coated, incompressible fiberglass gaskets, assembled at a torque of 12 Nm (for details see Simon et al.).[32] Fuel cell tests were performed on automated test stations (G60, Greenlight Innovation) equipped with a potentiostat (Reference3000, Gamry) to conduct electrochemical impedance spectroscopy (EIS).

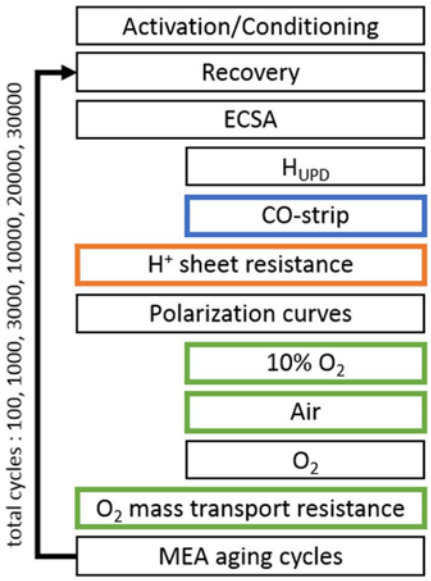

Figure 1. Overview of the experimental procedure for MEA aging. Complete MEA characterization (differential flow H_2/O_2 and H_2/air curves, cyclic voltammetry, CO stripping, limiting current measurements, and EIS) was performed at beginning-of-test (BOT) and end-of-test (EOT). The color of the boxes indicates the type of MEA characterization after specific MEA aging cycles: after every aging cycle (black); only at BOT and EOT (orange); after 10000 and 20000 cycles (blue), after 10000 cycles (green).

Voltage cycling procedure and diagnostic measurements.—The experimental testing procedure is depicted in Figure 1. All MEAs were conditioned prior to testing, using a voltage-controlled ramp-in procedure (H_2/air flows of 1390/3320 nccm at 80°C, 100% relative humidity (*RH*), and 150 kPa_{abs}): 0.6 V for 45 min, 5 min at OCV, and 10 min at 0.85 V. This sequence was repeated 10 times, after which constant performance was reached. Before each set of differential flow polarization curves and diagnostic measurements, an MEA recovery step was implemented, which consisted of a hold time in H_2/air (2000 nccm/5000 nccm) at 0.3 V for 2 h at 40°C, 270 kPa_{abs}, and 100% *RH*. The purpose of this procedure is to recover reversible losses prior to catalyst layer characterization.

Cyclic voltammograms (CVs) of the cathode electrode were recorded between 0.07 and 1.00 V_{RHE} at a scan rate of 150 mV/s, at 40°C and ambient pressure, while the *ECSA* was evaluated from CVs with a limited upper potential of 0.6 V_{RHE} by averaging the H-desorption and H-adsorption charge (using a specific charge of 210 $\mu C/cm^2_{Pt}$). The counter/reference electrode was fed with 200 nccm of fully humidified 5% H_2 in N_2, and the working electrode was initially purged with dry N_2 at 50 nccm, while interrupting the gas flow to record the CVs.

CO stripping was done by adsorbing CO (10% CO in N_2, 100 nccm) for 10 min at 40°C and 150 kPa_{abs} while maintaining the cathode potential at 0.1 V_{RHE}. Subsequently, residual CO was removed from the cell and the gas lines by purging with nitrogen for ≈1.5 h. A CV from the holding potential to 1.2 V_{RHE} at a scan rate of 100 mV/s was performed to oxidize the adsorbed CO. Two additional sweeps were recorded to verify the full oxidation and removal of CO from the electrode and the gas feed system. The *ECSA* was determined by integrating the area of the first anodic scan with the subsequent sweep as baseline, using a specific charge of 420 $\mu C/cm^2_{Pt}$.

The proton conduction resistance of the cathode, $R^{cath}_{H^+}$ (in units of $\Omega \cdot cm^2$), was determined from AC impedance spectra recorded in H_2/N_2 (anode/cathode) at 0.2 V_{cell} with a peak-to-peak perturbation of

3.5 mV between 500 kHz and 0.2 Hz (20 points per decade), according to a procedure reported in the literature,[33,34] based on a transmission line model.[35] In order to ensure reproducibility, the measurement was repeated three times at each condition: 100, 70, 50, and 30% *RH*, while maintaining constant gas partial pressures (i.e., at cell pressures of 270, 255, 246, and 236 kPa_{abs}, respectively) under differential flow conditions (H_2/N_2 at 1000/1000 nccm) at 80°C. The proton resistivity, $\rho_{H^+}^{cath}$ (in units of $\Omega \cdot cm$), was calculated by dividing $R_{H^+}^{cath}$ by the cathode thickness.

Differential flow polarization curves were recorded in current-control mode at 80°C, 170 kPa_{abs} inlet-controlled pressure, 100% *RH* for both reactants, and constant flows of 2000 nccm of H_2 on the anode and 5000 nccm of O_2, air, or 10% O_2 (balanced with N_2) on the cathode. Anode and cathode were operated in counter flow mode. At these conditions, the inlet to outlet pressure drop in anode and cathode was about 2 and 22 kPa_{abs}, respectively. Prior to recording a polarization curve from low to high current densities, the cathode potential was held at 0.75 V for 15 min to reduce Pt-oxides; each current density point was held constant for at least 10 min and the resulting voltage was averaged over the final 30 s. The ORR kinetics (mass activity, specific activity, and Tafel slopes) were determined from H_2/O_2 polarization curves after application of two corrections: i) the potential was corrected for the *iR*-drop, using the high frequency resistance (*HFR*) obtained from the x-axis intersect in the Nyquist plot measured by galvano electrochemical impedance spectroscopy (GEIS) in the frequency range from 100 kHz to 10 Hz at each current density (applying a 10% AC amplitude with respect to the current, limited to a minimum/ maximum of 0.1/3.0 A); ii) the current was corrected for the ohmic short of the membrane, as well as for the H_2 crossover, both determined in H_2/N_2 (150/600 nccm) at 170 kPa_{abs}, 80°C, and 100% *RH* by applying a constant potential of 0.2, 0.3, 0.4, 0.5, 0.6 and 0.7 V for 2 min each.

The total mass transport resistance ($R_{O_2}^{total}$) was extracted from limiting current measurements at 80°C and 100% *RH* under differential flow conditions (2000 nccm of H_2 and 5000 nccm of O_2/N_2 mixtures).[15,36,37] The dry mole fraction of oxygen was altered from 4 to 24% O_2 in N_2, while the cell potential was set to 0.30, 0.15, 0.10, and 0.05 V for 2 min each. To quantify pressure-independent and pressure-dependent oxygen transport resistances, limiting current measurements were also conducted at 170, 270, 350, and 500 kPa_{abs}.

Aging of the cathode electrodes was performed at 100 kPa_{abs}, 80°C, 100% RH and H_2/N_2 flows of 200 nccm/75 nccm on anode/cathode, respectively. In voltage cycling ASTs, various potential profiles were examined that are depicted in Figure 2: triangular wave modulation between a lower potential of 0.6 V_{RHE} and an upper potential of either 1.0 V_{RHE} (referred to as "TW", a) or a lower upper potential limit of 0.85 V_{RHE} (referred to as "TW–LUPL", d) at 50 mV/s; square wave (SW, b) modulation between 0.6 and 1.0 V_{RHE}; and triangular wave modulation with a potential hold at the lower (0.6 V_{RHE}) and upper (1.0 V_{RHE}) potential (referred to as "TW–H", c). Voltage cycling ASTs were controlled by a potentiostat (Reference3000, Gamry). To avoid reductive currents during potential cycling, all residual O_2 was removed from the humidifier and gas line system by a N_2 purging procedure, lasting about 45 min. The scan rate for all TW procedures was 50 mV/s, while the potential step in the SW procedure was completed in less than 0.1 seconds (corresponding to an average rate of >4 V/s). The hold times of 8 s at the vertex potentials in the SW procedure was chosen such that it is identical to the overall time required for one TW cycle (compare Figures 2a and 2b).

Electrode thickness determination by SEM.—The thicknesses of pristine (BOT), as well as aged MEAs (EOT) were determined from cross-section images, obtained by scanning electron microscopy (SEM). To get a more accurate comparison between BOT/EOT and to exclude any effects of cell assembly on the catalyst layer thickness, the pristine MEAs were assembled in a cell and operated at 80°C, 100% RH and 500 nccm N_2/N_2 flows at ambient pressure for 24 h before determining their initial thickness. The MEAs were cut in quarters, using one quarter close to the gas inlet and one close to

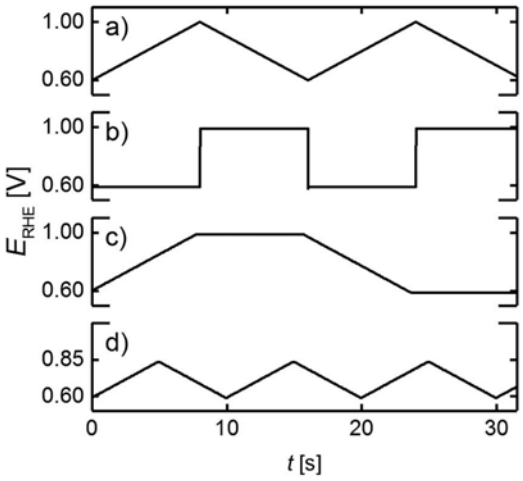

Figure 2. Voltage profiles used in voltage cycling ASTs performed at 100 kPa_{abs}, 80°C, 100% *RH* and H_2/N_2 flows of 200 nccm/75 nccm on anode/cathode, respectively. a) triangular wave modulation ("TW") between 0.6 and 1.0 V_{RHE} (corresponding to 0.59 and 0.99 V_{cell}) at a scan rate of 50 mV/s; b) square wave modulation ("SW"), applying a hold time of 8 s at the lower (0.6 V_{RHE}) and upper (1.0 V_{RHE}) potential; c) triangular wave modulation at a scan rate of 50 mV/s with 8 s potential hold at the lower (0.6 V_{RHE}) and upper (1.0 V_{RHE}) limits ("TW–H"); d) triangular wave modulation at 50 mV/s between 0.6 V_{RHE} and a lowered upper potential limit ("TW–LUPL") of 0.85 V_{RHE} (≡0.84 V_{cell}). The combination of an anodic and a cathodic scan is referred to as one cycle in this study.

outlet of the cell. The samples were fixed in a Teflon holder and embedded in epoxy resin (EpoThin 2 resin and hardener, Buehler Ltd.) at reduced pressure to remove gas bubbles. After hardening overnight at 40°C, the resin block was removed from the holder, ground on SiC (CarbiMet S, P280, Buehler Ltd.) under constant water flow and thoroughly cleaned by ultrasonification in water. SEM (JCM-6000PLUS NeoScope, Jeol) images were taken in backscattering mode at 15 kV accelerating voltage and a magnification of 2000x at ten arbitrarily chosen locations for each quarter of an MEA, generating 20 images per MEA. The thickness of the electrode was determined by integration of the electrode area with ImageJ (version 1.51j8) and dividing by the length of the image as shown in Figure 3. This way, the entire image is evaluated, which provides a more accurate measure of the catalyst layer thickness compared to a single point measurement.

The thickness of pristine electrodes was used to calculate the packing density of the Vulcan carbon based electrodes. The obtained packing density of 22 ± 4 $\mu m/(mg_C/cm^2)$ is in reasonable agreement with values in the literature.[38] The BOT thickness for all tested MEAs was

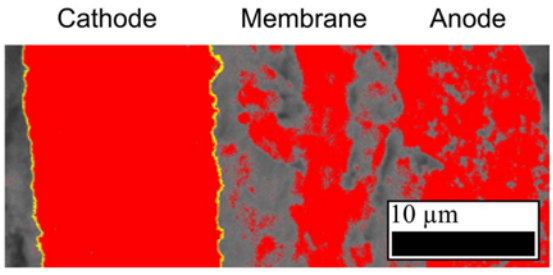

Figure 3. Cross-sectional SEM image of an MEA embedded in epoxy resin and taken at an acceleration voltage of 15 kV and a magnification of 2000x. The cathode edges are marked in yellow and the integrated area in between is shown in red, based on the grayscale of the image. Red areas outside the cathode are not included in the evaluation.

calculated from the transferred weight of carbon in the hot pressing process and the packing density.

Results and Discussion

In this study, we present the aging behavior of MEAs exposed to different voltage cycling protocols, with the respective voltage transients shown in Figure 2. The most commonly used AST is a potential scan between 0.6 and 1.0 V_{RHE} at a scan rate of 50 mV/s and 80°C in inert gas atmosphere, termed TW in this manuscript (Figure 2a). In addition, many researchers reported the aging behavior of MEAs exposed to square wave (SW) voltammetry (Figure 2b), since the combination of fast potential transients and hold periods has proven to accelerate catalyst layer degradation.[39,40] However, it is not well-understood yet, whether the holding time at the respective potential or the fast transient from one to the other potential is the dominating factor for the observed electrode degradation. To deconvolute between TW and SW modulations, triangular scans were combined with a potential hold period (TW–H) in order to eliminate the fast potential step while maintaining the effect of the hold time (Figure 2c). Furthermore, electrode aging by a TW modulation between 0.6 and 1.0 V_{RHE} will be compared to a TW modulation with the same lower voltage limit but with a lowered upper potential limit of 0.85 V_{RHE} (TW-LUPL), where carbon support corrosion can safely be assumed to be negligible and where Pt dissolution rates are expected to be reduced (Figure 2d). Finally, our study is complemented by a potential hold experiment at 1.2 V_{cell} for 8 h (under N_2 at 95°C, 100% *RH*, and 100 kPa_{abs}) to degrade the carbon support structure via COR, while maintaining a reasonably high electrode roughness factor. All of the aging procedures were conducted on high-loaded (0.4 mg_{Pt}/cm^2) and low-loaded cathodes (0.1 mg_{Pt}/cm^2) to identify similarities and/or differences in the aging behavior with respect to the *ECSA* and mass activity originating from different catalyst layer loadings. Moreover, changes of the cathode O_2 mass transport resistance upon aging, especially with respect to the local O_2 mass transport resistance which is commonly observed to be a function of the electrode *rf* was of major interest in this study.[9,10,41] The utilization of high- and low-loaded catalyst layers enables a comparison over a wide range of *rf*, i.e., to compare low Pt specific current densities (A/cm^2_{Pt}) for high-loaded MEAs (high *rf*) to high specific current densities after aging of low-loaded cathodes (low *rf*). However, to establish a valid comparison of the total mass transport resistance, the same catalyst layer thickness was maintained (≈10 μm) for all MEAs at BOT by utilizing a 50%$_{wt}$ Pt/C catalyst for high-loaded and a 20%$_{wt}$ Pt/C catalyst for low-loaded electrodes.

ECSA evaluation: H_{UPD} vs CO stripping.—To evaluate the degradation of the Pt surface area over the course of MEA aging, CVs were recorded after each aging stage, exemplarily shown in Figure 4a for a single low-loaded MEA (0.1 mg_{Pt}/cm^2) exposed to SW aging between 0.6 and 1.0 V_{RHE} (see Figure 2b). To determine the *ECSA* by integration of the H_{UPD} charge, additional CVs with a limited upper potential (0.6 V_{RHE}) were recorded (not shown) to avoid a contribution of charge originating from the reduction of the Pt surface.[42] Due to the above outlined Pt dissolution/redistribution mechanisms, the H_{UPD} features of the CV degrade significantly, i.e., a decrease of the cathode *rf* is observed over the course of extended voltage cycling. In general, the evaluation of the *ECSA* via integration of the pseudo-capacitive H_{UPD} current is influenced by a superimposed faradaic current at low potentials, originating from the hydrogen evolution reaction (HER). This superposition is especially dominant at low *rf*, as the rate of the HER above 0 V_{RHE} in cyclic voltammetry is mostly thermodynamically controlled (i.e., it does not depend significantly on the active Pt surface area), whereas the pseudo-capacitive H_{UPD} charge scales directly with the available Pt surface area. Hence, the strong decrease of the *rf* in the course of the voltage cycling AST renders the determination of the *ECSA* via the H_{UPD} method increasingly erroneous, requiring the implementation of CO stripping to reliably determine the remaining Pt surface area for very low *rf* values,[43] i.e., towards the end of the aging protocol.

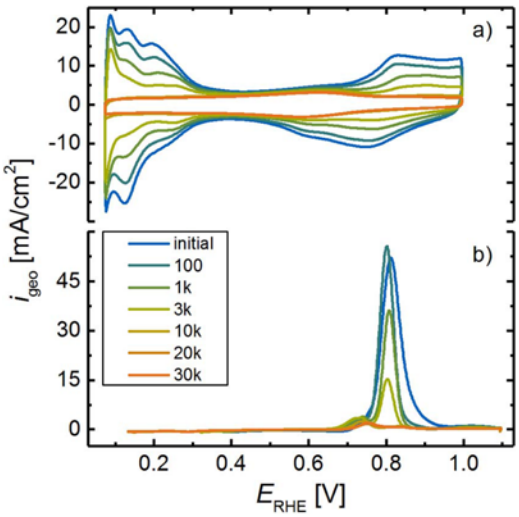

Figure 4. a) CVs of the cathode after different aging stages during a SW-based AST between 0.6 and 1.0 V_{RHE} (see Figure 2b). CVs were conducted at a scan rate of 150 mV/s from 0.07 to 1.00 V_{RHE} at ambient pressure and 40°C (the anode was supplied with 200 nccm of 5% H_2 (in N_2) and the cathode N_2 flow was 50 nccm (set to zero flow when recording the CVs)). b) CO stripping voltammograms after subtraction of the subsequent anodic sweep, recorded at a scan rate of 100 mV/s to 1.1 V_{RHE} at 150 kPa_{abs} and 40°C (constant flows of 200 nccm 5% H_2 on the anode and 5 nccm N_2 on the cathode). CO was adsorbed for 10 min at a flow rate of 100 nccm prior to the CV, maintaining the potential at 0.1 V_{RHE}. To remove residual CO gas from the cell and the test station, a purging procedure with N_2, lasting approximately 1.5 h was executed.

Representative CO stripping measurements are shown in Figure 4b after subtraction of the second anodic scan. The peak for CO oxidation occurs at ≈0.81 V_{RHE}, which is consistent with reports by other researchers for CO oxidation on Pt nanoparticles,[44] mainly dominated by CO oxidation on Pt(111) facets.[45,46] Furthermore, a second peak at ≈0.74 V_{RHE} is observed, representing Pt(110)-like planes.[47] Since those facets are less prone to dissolution upon surface oxidation/reduction, this peak becomes more dominant upon potential cycling. Consistent with the decrease in H_{UPD} features, the charge associated with the oxidation of CO_{ads} decreases significantly during cathode aging. Since *ECSA* determination via H_{UPD} is reasonably accurate for high *rf* values, the charge ratio between H_{UPD} and CO stripping remains constant ($\frac{ECSA_{H_{UPD}}}{ECSA_{CO}} \approx 0.8$) throughout the first phase of aging (up to ≈3000 cycles). As the H_{ad} formation is not quantitative in the applied potential range (≥ 0.07 V_{RHE}), the *ECSA* determined by the H_{UPD} method is slightly underestimated compared to the *ECSA* determined from CO stripping, hence their ratio is below unity.[48] In the course of potential cycling, the ratio decreases significantly ($\frac{ECSA_{H_{UPD}}}{ECSA_{CO}} < 0.1$ after 10000 cycles), as the electrode *rf* approaches very low values where the H_{UPD} currents are small compared to the capacitive current contributions from the carbon support. As CO stripping was only implemented for electrodes with a considerably low *rf*, and H_{UPD} was the preferred method for *ECSA* determination (due to its experimental simplicity), comparability of these two techniques was assured by introducing a scaling factor. The scaling factor was calculated as the ratio of *ECSA* determined by H_{UPD} and CO stripping at BOT and was used to correct the values determined by CO stripping to an "H_{UPD}-derived" *ECSA* at low *rf* (denoted by open symbols in figures showing *ECSA* data in this manuscript).

ECSA evolution during voltage cycling ASTs.—A decrease of the *ECSA* with increasing number of voltage cycles for each cathode loading and aging protocol is given in Figure 5, eventually reaching similarly low *ECSA* values on the order of 5–10 m^2_{Pt}/g after

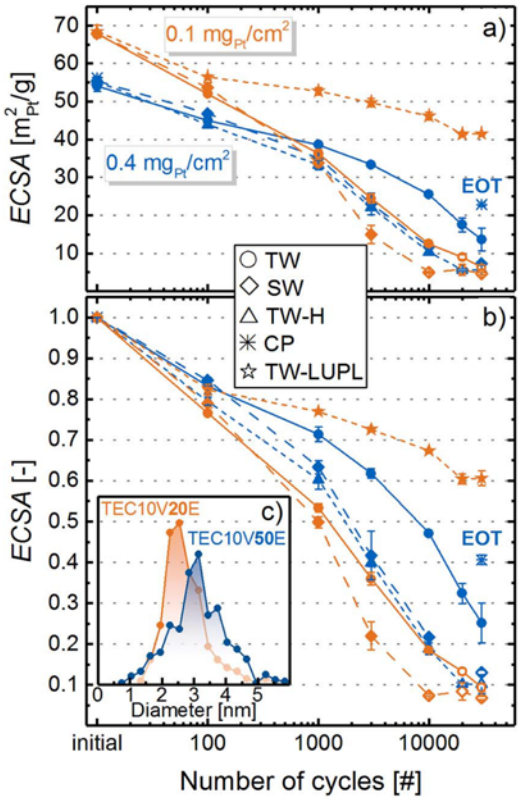

Figure 5. a) Cathode *ECSA* of all tested MEAs with cathode loadings of 0.4 mg_{Pt}/cm^2 (blue symbols) and 0.1 mg_{Pt}/cm^2 (orange symbols), recorded for TW cycling between 0.6 and 1.0 V_{RHE} (s. Figure 2a; solid lines, circles) as well as SW cycling between 0.6 and 1.0 V_{RHE} (s. Figure 2b; long-dashed lines, diamonds). For 0.4 mg_{Pt}/cm^2 loadings, also a TW-H profile (s. Figure 2c; short-dashed lines, triangles) was examined, while for 0.1 mg_{Pt}/cm^2 loadings a triangular cycle with a lowered upper potential limit of 0.85 V_{RHE} (s. Figure 2d; short-dashed lines, stars) was tested. The single point labeled CP (blue star symbol placed at 30000 cycles) depicts the *ECSA* after an 8 hour hold at 1.2 V_{cell}, (under N_2 at 95°C, 100% *RH*, and 100 kPa_{abs}), where substantial carbon support oxidation occurs. For high *rf* values, the *ECSA* was evaluated from the integration of the H_{upd} area, shown by a full symbol in the graph; for low *rf* values, the *ECSA* was determined by CO stripping and corrected by the scaling factor to allow comparability with the *ECSA* determined from H_{UPD} (denoted by open symbols). b) *ECSA* evolution over voltage cycling normalized to its initial value. The error bars represent the mean absolute deviation between two independently conducted experiments for each AST. c) Particle size distribution for the 20%$_{wt}$ Pt/C catalyst (orange) and the 50%$_{wt}$ Pt/C catalyst (blue).

30000 cycles (apart from the TW-LUPL and CP protocols). Since the change of potential in the applied ASTs results in a repetitive reduction/oxidation of the Pt surface, Ostwald ripening and a loss of Pt into the ionomer phase are expected to be the major contributors to the overall loss of active surface area. The gradual stabilization of the *ECSA* after extended voltage cycling, also observed in previous studies,[49] is likely due to the higher thermodynamic stability of larger Pt particles against dissolution. In contrast to the similar trend of decaying *ECSA* for all tested samples, its evolution with respect to the aging protocol and the cathode loading differs widely. First of all, it is noteworthy that the *ECSA* at BOT is higher for low-loaded cathodes (68 ± 1 m^2_{Pt}/g) compared to those with a higher loading (55 ± 1 m^2_{Pt}/g). As mentioned earlier, the electrode thickness was maintained constant for all tested MEAs (≈10 µm), which required a catalyst with 20%$_{wt}$ Pt content to prepare low-loaded catalyst layers, whereas 50%$_{wt}$ Pt/C was used for high-loaded electrodes. Even though both catalysts were obtained from the same supplier, Pt nanoparticles are commonly more homogeneously dispersed on the carbon support at low Pt to carbon ratio. This leads to a lower degree of Pt agglomeration, hence a lower average particle size and higher *ECSA*.[50] In fact, an evaluation of the particle size distribution (Figure 5c) by counting ≈400 individual particles (in TEM images) revealed a number averaged diameter of 2.8 ± 0.8 nm and 3.2 ± 1.0 nm for 20%$_{wt}$ and 50%$_{wt}$ Pt/C, respectively. As reported frequently by other researchers, Ostwald ripening is more pronounced for small particles compared to larger ones due to their intrinsically lower stability versus dissolution upon oxidation/reduction.[19] In accordance with this, for any given aging protocol, a faster decay of the *ECSA* is observed for low-loaded (orange colored in Figure 5) compared to high-loaded cathodes (blue colored in Figure 5). In summary, the observed relatively stronger *ECSA* fade for lower catalyst layer loadings in this study is not primarily caused by the cathode loading itself, but is most likely due to the different aging behavior of Pt nanoparticles with different size and different degrees of agglomeration.

Comparing different aging protocols, the *ECSA* loss is more pronounced for MEAs subjected to SW aging (long-dashed lines) compared to TW aging (solid lines), resulting in a dramatically low *ECSA* already after 10000 square wave cycles between 0.6 and 1.0 V_{RHE} (11 m^2_{Pt}/g for high-loaded and 5 m^2_{Pt}/g for low-loaded cathodes). The accelerated degradation caused by square wave compared to triangular wave aging has frequently been observed for PEMFCs,[40] as well as in liquid electrolyte.[39] There are four possible hypotheses to rationalize the faster degradation during SW cycling: i) a more significant carbon corrosion due to an extended hold period at high potential, eventually resulting in Pt particle detachment, accompanied by a thinning of the cathode catalyst layer; ii) the fast potential transient of the square wave modulation (>4 V/s) could induce more severe Pt dissolution forced by a fast reconstruction of the Pt surface from an oxidized to a reduced state; iii) the holding time at high potential induces a growth of the oxide, resulting in a stronger dissolution in the subsequent cathodic scan;[51] or, iv) the hold time at high anodic potentials provides more time for Pt dissolution and diffusion through the ionomer phase. As was shown by Cherevko et al., polycrystalline Pt in 0.1 M H_2SO_4 dissolves at constant anodic potential during about 600 s which is in the same order of magnitude as the dissolution during a potential transient.[52] The constantly released Pt ions can diffuse towards the membrane, where they are reduced by H_2 permeating through the membrane from the anode, causing a redeposition of electrically disconnected Pt particles within the ionomer phase.[20] The following analysis will shed some light onto the origin of the different aging of MEAs exposed to SW or TW potential profiles as well as at the degradation caused by holding at high potential to deliberately corrode the carbon support.

To investigate whether significant carbon support corrosion takes place over the course of the various voltage cycling protocols, which should lead to cathode thinning, MEA cross sections were prepared at EOT and imaged by SEM. Since the initial thickness of the electrodes at BOT could not be determined by SEM without damaging the MEA, the packing density of high-loaded and low-loaded catalyst layers was evaluated by measuring the thickness and catalyst loading of pristine MEAs (amounting to 22 ± 4 µm/(mg_C/cm^2), see experimental section), from which the initial thickness of each MEA could be calculated by its measured catalyst weight. The catalyst layers exposed to TW or SW aging between 0.6 and 1.0 V_{RHE} (Figures 6a/6b/6d/6e) show no catalyst layer collapse compared to a pristine MEA (Figure 6c), eliminating carbon corrosion as a likely contributor to the overall degradation. Interestingly, the catalyst layers depicted in Figures 6a/6b and 6d/6e show a bright area at the cathode/membrane interface, representing an accumulation of Pt in the membrane phase, caused by precipitation of dissolved Pt in the ionomer phase.[20,30] However, due to the rather qualitative nature of such SEM images, no conclusion on the quantitative differences between the amount of deposited Pt during TW and SW cycling can be drawn, even though the larger *ECSA* loss in the SW protocol points towards a higher amount of disconnected Pt. The absence of cathode thinning was also confirmed for all other

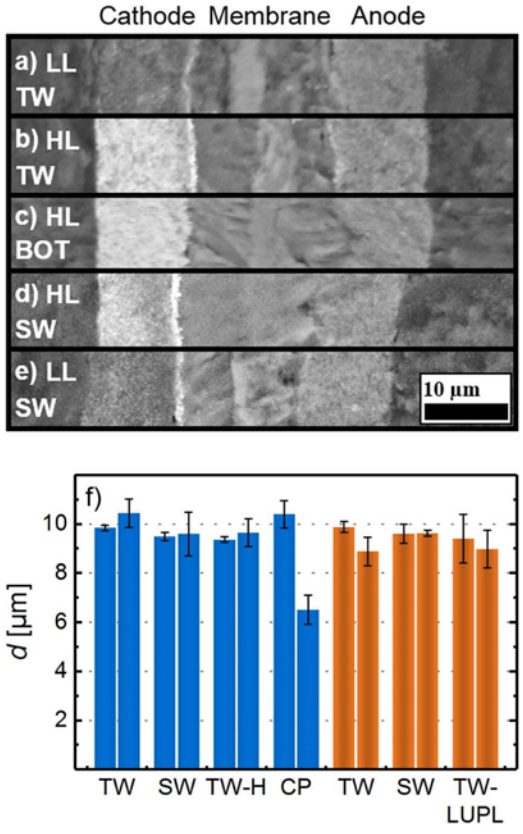

Figure 6. SEM cross-section images of MEAs at BOT and after 30000 potential cycles: low-loaded MEAs (0.1 mg_{Pt}/cm^2) after TW (a) and SW (e) aging between 0.6 and 1.0 V_{RHE}. High-loaded catalyst layers (0.4 mg_{Pt}/cm^2) of a pristine MEA (c), an MEA after 30000 TW cycles and c) an MEA after SW cycles between 0.6 and 1.0 V_{RHE}. Images were taken by SEM at a magnification of 2000x in electron back-scattering mode. f) Average cathode thickness of MEAs subjected to different aging protocols both at BOT (left-hand bars in each group) and at EOT (right-hand bars in each group), with high-/ and low-loaded cathodes shown in blue/orange color, respectively. The error bars represent the standard deviation between two independently conducted experiments for each aging protocol; voltage cycling aging protocols are described in Figure 2 and CP refers to cathodes subjected to an 8 hour potential hold at 1.2 V_{cell} (under N_2 at 95°C, 100% *RH*, and 100 kPa_{abs}).

cathode electrodes which had been subjected to voltage cycling tests, whose thicknesses was found not to change between EOT and BOT, as is shown in Figure 6f. Quite clearly, carbon support corrosion must be rather minor over 30000 voltage cycles between 0.6 and 1.0 V_{RHE} since any significant carbon corrosion is accompanied by cathode thinning (noticeable once ca. 5–7% carbon are corroded).[53] However, we cannot fully exclude the possibility that a small extent of carbon corrosion might occur (small enough to not lead to cathode thinning), which then could contribute to the observed *ECSA* degradation by a particle detachment mechanism. To determine the effect of substantial carbon support corrosion on the *ECSA*, cathodes were held for 8 hours at 1.2 V_{cell} (under N_2 at 95°C, 100% *RH*, and 100 kPa_{abs}), which resulted in a decrease of the catalyst layer thickness by ≈40%; despite the large extent of carbon corrosion, the *ECSA* remained at a reasonably large value of ≈22 m^2_{Pt}/g (blue asterisks in Figure 5).

To obtain further insights into the origin of the faster degradation upon SW aging, seeking to differentiate between *ECSA* loss caused by the holding time at high potential which might enhance Pt loss into the membrane phase and that originating from the fast Pt oxidation/reduction transient in SW cycling, the potential step in the SW protocol was replaced by a potential sweep with the same scan-rate as in the TW protocol (Figure 2c). This voltage cycling AST is referred to as TW–H. As shown in Figure 5, the decrease of the cathode *ECSA* over the course of SW (blue long-dashed line, diamonds) and TW-H (blue short-dashed line, triangles) is identical, indicating that the rapid potential transient has no influence on the *ECSA* degradation and that it is rather the holding time at each potential that is the controlling factor. This can either be explained by the higher oxide coverage of Pt formed at longer holds at high potential, which Gilbert et al. hypothesized to lead to a larger extent of Pt dissolution during a subsequent step to lower potentials at which the oxide is reduced, leading to faster *ECSA* losses for SW profiles.[51,39] An alternative explanation is that the holding time at high potentials allows for a longer time of Pt dissolution and subsequent diffusion in the ionomer phase towards the cathode/membrane interface, where it can deposit as electrically insulated particles by reduction with cross-over hydrogen. The latter mechanism would explain the apparently higher accumulation of Pt at the cathode/membrane interface for the SW compared to the TW modulation suggested qualitatively by the above SEM analysis (compare Figures 6a/6b and 6d/6e). Therefore, our experiments suggest that the faster degradation by SW cycling is caused by a more severe Pt dissolution and simultaneously allowing sufficient time for Pt diffusion towards the cathode/membrane interface and its deposition as electrically insulated particles, rather than by carbon support corrosion or the fast voltage transient. It shall be mentioned that the aging per time interval was in fact smaller for TW-H compared to SW, since both methods showed a similar degradation per cycle while one scan in the TW-H procedure required double the time (32 sec) compared to SW (16 sec). However, the cathode potential remains below 0.9 V_{RHE} for a substantial fraction of the time, while we believe that higher potentials are most detrimental for the *ECSA*.

To probe the degradation at lower potentials, a triangular scan procedure with a lower upper potential limit (TW-LUPL) of 0.85 V_{RHE} (orange star symbols and short-dotted lines in Figure 5) was tested. In this case, carbon corrosion most certainly will not play a role, so that aging from Pt detachment from the carbon support can surely be excluded (the above analysis suggests, carbon corrosion is not a major contributor to *ECSA* loss even for upper potentials as high as 1.0 V_{RHE}). In addition, Pt dissolution/redeposition effects should also decrease substantially, since the degree of Pt surface oxidation is limited, leading to less Pt dissolution, hence to a smaller overall *ECSA* loss (40% after 30000 aging cycles).[20] Since the *ECSA* loss during TW-LUPL is comparatively low, we conclude that most of the additional time during TW-H compared to SW is non-damaging, e.g. below 0.85 V_{RHE}. We therefore believe that the lower amount of *ECSA* loss per time (not per cycle) in the TW-H procedure can be mainly attributed to the additional time at these low, non-damaging potentials. In the light of the rather small *ECSA* loss when limiting the upper potential to 0.85 V_{RHE} (TW-LUPL) compared to the TW aging protocols with an upper potential limit of 1.0 V_{RHE} for which *ECSA* losses of ≈90% over 30000 cycles are observed, avoiding high voltages (e.g., OCV) appears highly advisable to maximize PEMFC durability.

AST induced ORR activity changes.—Assuming simple Tafel kinetics for the ORR according to Equation 1, lowering the cathode *rf* over the course of ASTs should directly cause an increase of the ORR overpotential according to:[6,54]

$$\eta = TS \cdot \left[\lg \left(\frac{i}{i_0} \cdot \frac{1}{rf} \right) \right] \qquad [1]$$

where η denotes the ORR overpotential in mV, *TS* is the Tafel slope in mV/dec, *i* denotes the current density in A/cm^2, i_0 is the exchange current density in A/cm^2_{Pt}, and *rf* denotes the roughness factor in cm^2_{Pt}/cm^2.

In Figure 7a, differential flow H_2/O_2 polarization curves at 80°C and 100% *RH* are shown for all AST protocols at BOT and after 30000 aging cycles. First of all, a voltage offset is observed in the initial polarization curves of low-loaded (solid orange lines) compared to high-loaded (solid blue lines) cathodes at BOT. Based on simple Tafel

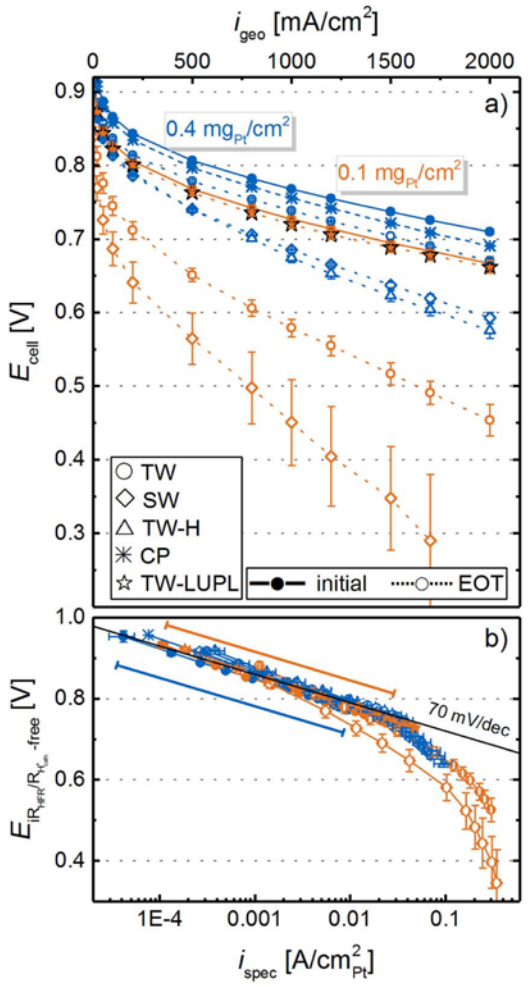

Figure 7. Differential flow H_2/O_2 (2000/5000 nccm) performance for MEAs with 0.4 mg$_{Pt}$/cm^2 (blue lines/symbols) and 0.1 mg$_{Pt}$/cm^2 (orange lines/symbols) cathodes at BOT (solid lines and filled symbols) and at EOT, i.e., after 30000 voltage cycles or an 8 hour hold at 1.2 V_{cell} (dotted lines or hollow symbols). a) Measured cell voltage curves at a pressure of 170 kPa$_{abs}$, a temperature of 80°C, and an *RH* of 100%. b) Tafel plot representation normalized to the *ECSA*, corrected by the *HFR*, the effective proton conduction resistance, as well as by the H_2 crossover and electrical short current. BOT polarization curves of all tested MEAs were averaged and error bars represent the standard deviation of all tested MEAs. Error bars for EOT curves represent the mean absolute deviation between two measurements. The two slanted lines in b) indicate the specific current density region for high-loaded (blue) and low-loaded (orange) MEAs at BOT.

kinetics (Equation 1) and an ORR Tafel slope of 70 mV/dec, four times lower Pt cathode loadings should result in an approximately four times lower roughness factor (as the catalyst *ECSA* is very similar) and thus to an additional overpotential of ≈42 mV at the same current density, which is in excellent agreement with the observed offset between high- and low-loaded MEAs (e.g., 737 ± 3 mV vs 695 ± 8 mV at 1.5 A/cm^2 (42 ± 11 mV) for high- and low-loaded electrodes, respectively).

Over the course of 30000 voltage cycles (≡ EOT condition), the polarization curves of all tested MEAs degrade significantly, with a more severe performance decay for low-loaded MEAs (e.g., 214 mV loss at 2 A/cm^2 for the TW protocol) compared to high-loaded MEAs (39 mV loss at 2 A/cm^2). When comparing polarization curves from different aging protocols, the previously identified higher *ECSA* loss for SW compared to TW cycling correlates well with the observed performance difference in the O_2 polarization curve at EOT for both loadings. Furthermore, a similar performance decay is observed for the TW-H and SW protocol, e.g., a voltage of 593 ± 8 mV for SW and 575 ± 1 mV for TW-H at 2 A/cm^2 and EOT, which is in accordance with the comparable loss of *ECSA*. In contrast to the other AST protocols, EOT polarization curves for the TW-LUPL protocol do not show any degradation compared to BOT, reflecting the comparably low degradation of the *ECSA*.

To determine the specific ORR activity for each MEA, the polarization curves were corrected by the *HFR* (R_{HFR}), the H_2 crossover current ($i_{H_2-cross}$, on the order of ≈4 mA/cm^2), the shorting current (i_{short}), the effective proton conduction resistance in the cathode catalyst layer ($R_{H^+}^{cath,eff}$), and were normalized to the Pt surface area (Figure 7b). As expected for H_2/O_2 polarization curves dominated by kinetic overpotentials, all data points fall on a straight line, with a BOT Tafel slope of 70 ± 3 mV/dec for high-loaded and 73 ± 3 mV/dec for the low-loaded MEAs. After 30000 voltage cycles, the apparent Tafel slope of high-loaded MEAs, determined in the low current density region (50–500 mA/cm^2), increases to 79 ± 1 mV/dec for TW aged MEAs and more significantly (≈90 mV/dec) for the SW and TW–H aging protocols. Tafel slopes of around 120–160 mV/dec were observed for low-loaded MEAs subjected to 30000 TW and SW cycle protocols, while the Tafel slope remained unchanged over the course of the TW-LUPL voltage cycling AST. An increasing Tafel slope upon aging was also observed by other researchers,[21] and is attributed to additional, non-kinetic overpotentials, such as O_2 mass transport or proton transport losses which apparently increase with extended voltage cycling. Since the electrode thickness remained unchanged (Figure 6f), even for the most damaging aging protocols (SW and TW-H), a hindrance of the gas phase mass transport caused by a deterioration of the overall catalyst layer structure can be excluded. Although, slight corrosion of the catalyst support and a concomitant slight decrease of the available pore volume cannot be fully excluded, cathode thinning was clearly not observed by SEM in any of our experiments. Additionally, changes of the Tafel slope due to loss or restructuration of the ionomer can be excluded as the proton transport resistance did not change significantly upon voltage cycling (not shown) and major chemical degradation of the ionomer can be excluded due to the absence of oxygen in the largest fraction of the experimental time.[56]

We would like to emphasize that these measurements were performed with pure O_2, where gas phase O_2 transport resistances can be excluded as possible cause for the increasing apparent Tafel slopes. It is also worth noting that these severe and unassigned mass transport overpotentials occur at similar values of the Pt specific current density (near ≈0.05 A/cm$^2_{Pt}$) in all H_2/O_2 polarization curves. At high Pt specific current densities, caused by ultra-low *rf* values, additional voltage losses have also been observed by other researchers.[9,10,55] Since this overpotential occurs at high geometric current densities and low cathode *rf* values, i.e., at high local oxygen flux to the Pt surface, we hypothesize that it is related to oxygen transport limitations at the catalyst/ionomer interface. Suggestions for the observed voltage losses at high Pt-specific currents by other research groups include a limited dissolution of oxygen into the ionomer phase,[57] an intrinsically high transport resistance of the thin ionomer phase,[58] a limited effective ionomer surface,[10,37] or a decrease of the ORR kinetics at low potential.[59] Although we cannot exclude any one of these effects, a Pt/ionomer specific resistance appears most reasonable to explain the observed voltage losses at high Pt-specific currents, as the voltage profile shows a shape resembling a mass transport limitation, rather than a kinetic phenomenon.

A linear regression of the measured data in the current density range from 50 to 500 mA/cm^2 and extrapolation to 0.9 V_{RHE} yields the kinetic ORR activity at 0.9 V_{RHE} (at 120 kPa$_{abs}$ O_2 partial pressure), commonly used to compare the catalytic activity of platinum. It can either be normalized to the measured *ECSA* to yield the specific current density for the ORR at 0.9 V_{RHE} ($i_{0.9\,V}^{spec}$, Figure 8b) or to the mass of Pt in the cathode catalyst layer to yield the mass activity for the ORR at 0.9 V_{RHE} ($i_{0.9\,V}^{mass}$, Figure 8a) to enable comparability between all experiments. In general, the here determined ORR

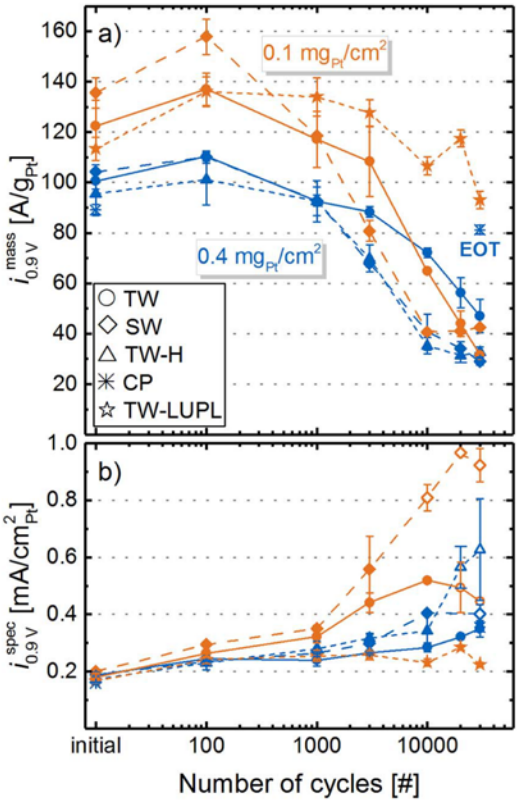

Figure 8. a) ORR mass activity at 0.9 V ($i^{mass}_{0.9\,V}$) and b) ORR specific activity at 0.9 V ($i^{spec}_{0.9\,V}$) extracted from Figure 7 for MEAs with 0.4 mg$_{Pt}$/cm^2 (blue lines/symbols) and 0.1 mg$_{Pt}$/cm^2 (orange lines/symbols) cathodes over the course of various ASTs. The exchange current density at 0.9 V was obtained by a linear regression of fully corrected polarization curves in O_2 between 50 and 500 mA/cm^2.

mass activities at BOT (≈110–140 A/g$_{Pt}$ for the 20%$_{wt}$ Pt/V catalyst and ≈85–105 A/g$_{Pt}$ for the 50%$_{wt}$ Pt/V catalyst) compare well with those reported by other researchers for Pt supported on Vulcan type carbon.[7,60,61] In accordance with the severe *ECSA* loss in most of the here examined aging protocols, the overall surface available for the ORR decreases significantly from BOT to EOT (low-loaded TW, SW and TW-H: ≈90% *ECSA* loss), there is also a significant loss of $i^{mass}_{0.9\,V}$ over the course of aging for all loadings and aging procedures (see Figure 8a). Comparing TW (solid lines, circles) and SW (long-dashed lines, diamonds), the decrease of $i^{mass}_{0.9\,V}$ as a function of cycle number is more pronounced for SW profiles, which is directly correlated to the stronger *ECSA* loss (see Figure 5). To clarify, the accelerated decrease of $i^{mass}_{0.9\,V}$ by SW compared to TW modulations most likely represents a true change in the ORR kinetics, as interference from O_2 mass transport resistances in pure O_2 in the low current density region (data evaluation was restricted to a maximum current density of 500 mA/cm^2) should be negligible. This assumption is reasonably justified since only a slight increase in the *apparent* Tafel slope was observed upon aging (e.g., 70 ± 3 mV/dec at BOT increases to 86 ± 2 mV/dec at EOT for high-loaded SW cycled cathodes) and since we eliminated regions at high specific current density (where local transport resistances could be important) from the analysis. As expected from our preceding analysis of the *ECSA* development (see Figure 5), the mass activity of electrodes aged by TW-H cycles is essentially identical to those aged by SW cycles (compare blue triangle and diamond symbols in Figure 8a), underlining our previous hypothesis that the potential hold phase is the dominating factor for MEA degradation during square wave aging. Finally, the ORR mass activity loss over the TW–LUPL procedure (orange stars) is significantly lower compared to the other protocols, which again is in accordance with the lower *ECSA* loss.

It is interesting to note that in contrast to the overall trend of decreasing ORR mass activity, $i^{mass}_{0.9\,V}$ reaches a maximum after 100 cycles, particularly noticeable for low-loaded MEAs. This could be ascribed to an activation of the catalyst particles due to cleaning of the Pt surface, which might overcompensate the *ECSA* loss of ≈20% in the initial 100 cycles. If true, this would mean that the initial activation procedure (see experimental section) was not sufficient to fully activate the cathode catalyst layer. Alternatively, there is the possibility that the measurement sequence (described in Figure 1) might influence the observed small variation of the measured ORR activity. While the O_2 polarization curves at BOT as well as at 10000, and at 30000 cycles were recorded after polarization curves in 10% O_2 and in air (each approximately 3.5 h), all other O_2 polarization curves were recorded directly after a recovery step. Thus, it is possible that after these two polarization curves without an intermediate recovery step, a certain extent of reversible degradation (i.e., Pt poisoning) might have occurred,[62] resulting in a lower ORR mass activity. Evidence for this behavior can be seen for the low-loaded MEAs tested with the TW-LUPL procedure (orange stars in Figure 8a), where ORR mass activities were always higher when measured directly after a recovery step (i.e., at 100, 1000, 3000 and 20000 cycles), while reproducibly lower values were obtained in the absence of a directly preceding recovery step (at BOT as well as at 10000 and 30000 cycles). Since the overall degradation rate induced by the TW-LUPL procedure is rather small (≈40% loss in *ECSA* and $i^{mass}_{0.9\,V}$ after 30000 cycles), this presumably testing procedure related inaccuracy of ≈10% in the quantification of $i^{mass}_{0.9\,V}$ might have become apparent. Nevertheless, this minor uncertainty in ORR mass activity values is of no consequence to the conclusions drawn from these data.

Further insights into the aging process can be obtained by examining the specific ORR activity at 0.9 V_{RHE}, $i^{spec}_{0.9\,V}$, as shown in Figure 8b. It is well-known that small Pt nanoparticles have a lower specific ORR activity due to their relatively larger amount of edge and corner sites compared to larger nanoparticles.[63] Amongst others, Mayrhofer et al. found an increase of the specific activity of Pt particles by a factor ≈2 when going from 1 nm sized particles to 5 nm.[64] In our case, the determined specific ORR activities of low-loaded (182 ± 18 μA/cm$^2_{Pt}$) and high-loaded MEAs (177 ± 16 μAcm$^2_{Pt}$) at BOT are essentially identical, consistent with the very similar average particle size of the two catalysts (2.8 ± 0.8 nm for 20%$_{wt}$ Pt/C and 3.2 ± 1.0 nm for 50%$_{wt}$ Pt/C). In the course of aging, the specific activity increases for all tested MEAs due to the constantly growing fraction of larger particles. The highest observed ORR activity (≈1 mA/cm$^2_{Pt}$) was found for low-loaded catalyst layers with the most significant *ECSA* loss (Figure 5) due to the harsh SW aging protocol. However, it shall be noted that the determination of the catalyst activity is slightly impaired by an increased Tafel slope for MEAs with a very small *rf* value, hence the calculation of $i^{spec}_{0.9\,V}$ becomes increasingly erroneous for strongly aged catalyst layers due to difficulties in determining kinetic parameters accurately.

AST induced H$_2$/air and H$_2$/10%O$_2$ performance losses.—To obtain further information about mass transport related overpotentials induced by the different aging protocols, polarization curves in air and 10% O_2 (to simulate conditions at the cathode outlet of a PEMFC stack operated at an air stoichiometry of ≈1.75) were measured at several aging stages (Figure 9). The solid lines are the average BOT performance of MEAs with 0.4 mg$_{Pt}$/cm^2 (blue) and 0.1 mg$_{Pt}$/cm^2 (orange) cathode loadings at the here investigated operating conditions of 170 kPa$_{abs}$, 80°C, and 100% *RH* (error bars represent the standard deviation across all measured MEAs, indicating the excellent reproducibility of the performance at BOT). Similarly to polarization curves in O_2 (Figure 7a), a clear offset between high-loaded and low-loaded cathodes, resulting from a different cathode *rf*, is observed for BOT polarization curves in air (e.g., 689 ± 3 mV vs 634 ± 10 mV at 1.5 A/cm^2 for high- and low-loaded electrodes, respectively) and 10% O_2 (e.g., 620 ± 10 mV vs 496 ± 9 mV at 1.5 A/cm^2 for high- and

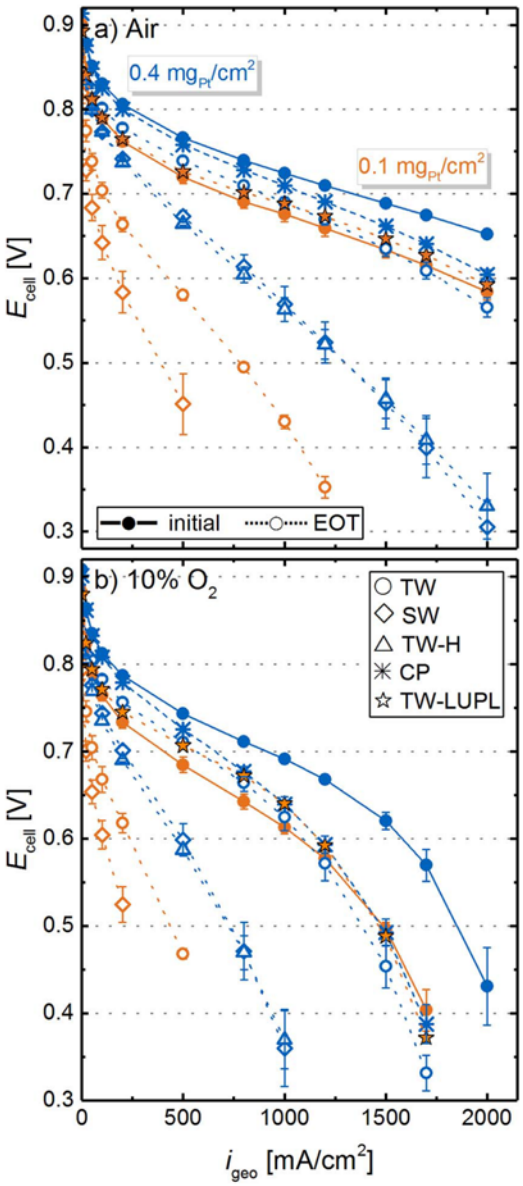

Figure 9. Differential flow a) H_2/air and b) H_2/10% O_2 (2000/5000 nccm) performance (170 kPa_{abs}, 80°C, and 100% *RH*) for MEAs with 0.4 mg_{Pt}/cm^2 (blue lines/symbols) and 0.1 mg_{Pt}/cm^2 (orange lines/symbols) cathodes at BOT (solid lines and filled symbols) and at EOT, i.e., after 30000 voltage cycles or an 8 hour hold at 1.2 V_{cell} (dotted lines or hollow symbols). BOT polarization curves of all tested MEAs were averaged and error bars represent the standard deviation of all measurement points. At EOT, error bars represent the mean absolute deviation of two measurements.

low-loaded electrodes, respectively). In contrast to pure O_2, where the offset perfectly matched the increase of η_{ORR} predicted by Equation 1, the voltage loss for low-loaded MEAs in air (e.g., 55 ± 13 mV at 1.5 A/cm^2) and 10% O_2 (e.g., 124 ± 19 mV at 1.5 A/cm^2) was much higher than the kinetically expected penalty. The additional voltage loss for low-loaded cathodes in air, being even more pronounced in 10% O_2, is an initial hint on a mass transport overpotential related to the *rf* value of the cathode. Several other researchers reported the occurrence of such a Pt surface area specific O_2 mass transport resistance (termed $R_{O_2}^{Pt}$ in this manuscript) for pristine cathodes with different loadings and showed its substantial increase with decreasing cathode *rf* values by limiting current measurements.[8–10,41]

High-loaded MEAs aged by the SW and TW-H protocol (open blue diamonds and triangles in Figure 9) show a similar performance at EOT, which was significantly lower compared to MEAs aged by the TW protocol (open blue circles). This is in accordance with the above discussed O_2 polarization curves (Figure 7a) and *ECSA* losses (Figure 5a). Even though the overall performance losses are rather dramatic for the low-loaded MEAs, they also show the same increased aging when subjected to SW rather than TW voltage cycling (open orange diamonds and circles). However, as one might have hoped based on the *ECSA* (Figure 5) and ORR mass activity (Figure 8a) data, even with low-loaded cathodes no voltage cycling induced performance losses occur over 30000 cycles when using the TW-LUPL protocol with a lowered upper voltage limit of 0.85 V_{RHE}, neither in H_2/air nor in H_2/10% O_2 (orange stars in Figure 9).

An interesting insight into the *rf* dependent $R_{O_2}^{Pt}$ induced losses can be gained by comparing the H_2/air EOT performance of the high-loaded cathode subjected to TW cycling (open blue circles) and the low-loaded cathode subjected to TW-LUPL cycling (orange stars). At EOT, the high-loaded cathode has a slightly higher roughness factor (56 ± 12 cm^2_{Pt}/cm^2) compared to the low-loaded cathode (42 ± 2 cm^2_{Pt}/cm^2), so that one would expect a similar or an even lower $R_{O_2}^{Pt}$ value for the former. At the same time, the specific ORR activity at 0.9 V_{RHE} for the high-loaded cathode (350 ± 29 $\mu A/cm^2_{Pt}$) is substantially larger than that for the low-loaded cathode (224 ± 7 $\mu A/cm^2_{Pt}$). Since the product of ($i_{0.9\,V}^{spec} \cdot rf$), equating to 19.6 mA/cm^2_{Pt} for the high-loaded and 9.2 mA/cm^2_{Pt} for the low-loaded cathode, is proportional to ($i_0 \cdot rf$) under the same operating conditions, the η_{ORR} difference predicted by Equation 1 is ≈23 mV, suggesting that the kinetically predicted EOT performance of the high-loaded cathode subjected to TW cycles should be ≈23 mV higher than that of the low-loaded cathode subjected to TW-LUPL cycles. This is consistent with the higher H_2/O_2 performance of the former (see Figure 7a) and also its superior low current density performance in H_2/air or H_2/10%O_2 (see Figure 9). However, despite its higher EOT roughness factor, the TW-aged high-loaded cathode exhibits a larger (unassigned) mass transport loss, evident by its lower H_2/air or H_2/10%O_2 performance at current densities above ≈1 A/cm^2 (see Figure 9). Since no significant differences in the effective proton conduction resistance (measured by EIS) were observed between these two electrodes, an apparently larger oxygen transport resistance, which is not simply related to the cathode *rf* value and produced by voltage cycling, must exist. Its origin is unclear at the moment, but it may be related to the morphological changes and redistribution of Pt within the cathode electrode caused by voltage cycling.

O_2 transport resistance evaluation.—In order to disentangle mass transport resistances originating from gas transport in the flow fields and the GDL from those in the catalyst layer, and to identify resistances dependent on the cathode *rf* value, limiting current measurements were executed according to the method developed by Baker et al.[36] In this approach, the concentration of O_2 (dry gas fraction in N_2) in the feed gas is varied from 4% to 24%, while a low potential between 0.05 and 0.30 V is applied to obtain the limiting current, where the O_2 concentration at the Pt surface decreases to zero and the current-voltage profiles at different O_2 concentrations resemble a vertical line (see Figure 10a). For each concentration, the O_2 mass transport resistance is calculated and plotted versus the respective limiting current density, as illustrated in Figure 10b for the low-loaded cathode MEAs at BOT and after 30000 SW cycles (for details on the analysis see Simon et al.).[32]

For all cathodes at BOT, the total oxygen mass transport resistance, $R_{O_2}^{total}$, is essentially independent of the limiting current density at all pressures (see triangles in Figure 10b and its inset), as is expected under these conditions for the Freudenberg GDL.[65] Furthermore, the determination of the limiting current density at various pressures enables the separation of $R_{O_2}^{total}$ into a pressure dependent ($R_{O_2}^{PD}$) and a pressure independent ($R_{O_2}^{PI}$) oxygen mass transport resistance via a linear regression of $R_{O_2}^{total}$ versus the absolute pressure (Figure 10c).

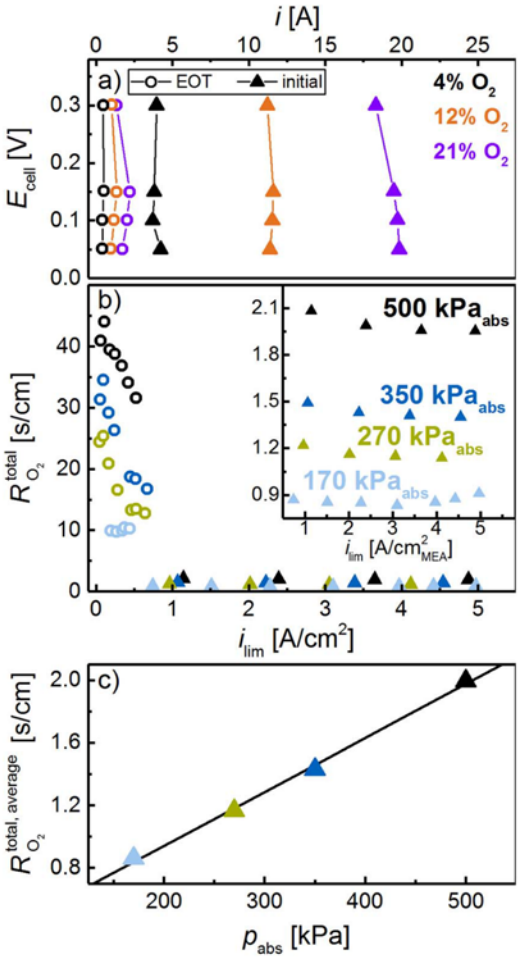

Figure 10. a) Limiting current measurement in the potential range between 0.30 and 0.05 V at O_2 concentrations of 4%, 12%, and 21%, comparing a 0.1 mg_{Pt}/cm^2 cathode at BOT (triangles) and after 30000 SW cycles (circles). Measurements were performed at 80°C, 100% *RH*, and 170 kPa_{abs} (using 2000 nccm H_2 and 5000 nccm O_2 in N_2). b) Total O_2 mass transport resistance vs limiting current density at 170, 270, 350 and 500 kPa_{abs} (O_2 concentration between 4% and 24%); the inset is a zoom into the low $R_{O_2}^{total}$ region at high limiting current densities. c) $R_{O_2}^{total}$ of the BOT cathode averaged over all O_2 concentrations at the respective pressure; the shown linear regression line is used to deconvolute $R_{O_2}^{total}$ into $R_{O_2}^{PD}$ and $R_{O_2}^{PI}$.

Nevertheless, a severe decrease of the limiting current is observed for low-loaded cathodes after extended TW or SW cycling, exemplarily shown in Figure 10a for the SW protocol (BOT ≡ triangles; EOT ≡ circles). At EOT, the limiting current density (circles in Figure 10a) is significantly lower, and the resulting $R_{O_2}^{total}$ values are more than an order of magnitude larger than at BOT and change severely with limiting current density, especially at higher pressures (circles in Figure 10b). We attribute this unsteady transport resistance at higher pressures to a local catalyst layer/GDL flooding (at an inlet *RH* of 100%) due to the low limiting current, at which no significant through-plane temperature gradient between MEA and flow field can be established, thereby hampering product water removal through the gas phase. This hypothesis is underpinned by the fact that the transport resistance is strongly decreasing with increasing current density, i.e., at a higher temperature gradient. The effect of flooding is even more pronounced at higher applied pressures, analogous to what is generally observed.[66] As the evaluation of $R_{O_2}^{total}$ at higher pressure is not reliable in cases like the one shown in Figure 10b (circles), a deconvolution of $R_{O_2}^{total}$ into $R_{O_2}^{PD}$ and $R_{O_2}^{PI}$ is not trustworthy, hence only the total transport resistance at 170 kPa_{abs} is considered in these instances. The origin of this effect is yet unclear, but as will be shown in the following, it is not related to carbon support corrosion.

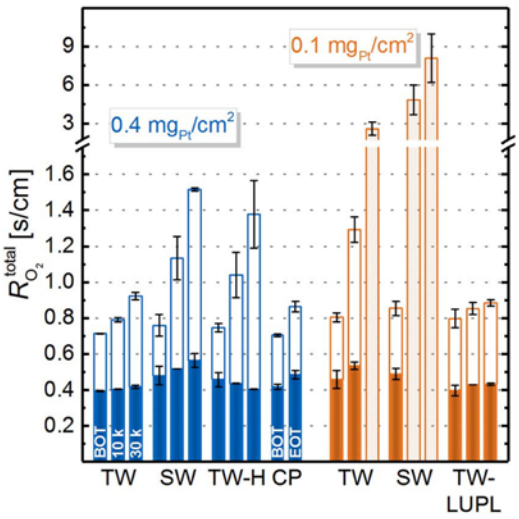

Figure 11. Total oxygen mass transport resistance ($R_{O_2}^{total}$) determined at 80°C, 100% *RH*, and 170 kPa_{abs} (differential flow of hydrogen and 4% - 21% O_2 (balance N_2) for high-loaded (blue) and low-loaded (orange) cathodes tested by different ASTs (for each, left bars are at BOT, middle bars at 10000 cycles, and right bars 30000 cycles). $R_{O_2}^{total}$ was also separated into pressure dependent ($R_{O_2}^{PD}$, solid bar) and pressure independent ($R_{O_2}^{PI}$, open bar) oxygen mass transport resistance contributions. For certain experiments, the deconvolution of $R_{O_2}^{total}$ was not reliable, thus only the total transport resistance at 170 kPa_{abs} is plotted as a dotted bar. Error bars correspond to the mean absolute deviation of two repeat experiments with different MEAs.

The total oxygen mass transport resistance at different stages of the aging protocol is shown for high-loaded (blue) and low-loaded (orange) cathodes in Figure 11, separated into pressure dependent, $R_{O_2}^{PD}$ (solid bars), and pressure independent, $R_{O_2}^{PI}$ (hollow bars) contributions, according to the above described analysis. All high-loaded (average of 0.73 ± 0.09 s/cm), as well as all low-loaded cathodes (average of 0.82 ± 0.10 s/cm) show a similar $R_{O_2}^{total}$ at BOT, demonstrating a reproducible MEA fabrication. In general, low-loaded cathodes show a slightly higher transport resistance than high-loaded electrodes at BOT, as already indicated by the observed voltage losses in H_2/air (Figure 9a) and H_2/10% O_2 polarization curves (Figure 9b). The pressure dependent transport resistance associated with the GDL is, as expected, essentially identical for high- ($R_{O_2}^{PD}$ = 0.44 ± 0.05 s/cm) and low-loaded ($R_{O_2}^{PD}$ = 0.45 ± 0.05 s/cm) cathodes at BOT. Therefore, the differences in $R_{O_2}^{total}$ originate from a higher pressure independent transport resistance, due to their lower cathode *rf* values ($R_{O_2}^{PI}$ high-loaded: 0.29 ± 0.04 s/cm; $R_{O_2}^{PI}$ low-loaded: 0.37 ± 0.05 s/cm).

Over the course of catalyst layer aging, the pressure dependent transport resistance remains reasonably constant, considering that the observed fluctuations are within the experimental accuracy. At the same time, $R_{O_2}^{PI}$ increases significantly. In general, $R_{O_2}^{PI}$ is composed of various contributions, namely Knudsen diffusion in small pores, diffusion in the ionomer and in water, as well as of the so-called Pt surface specific resistance ($R_{O_2}^{Pt}$). Since the ionomer content and the overall electrode thickness was constant in all experiments, we ascribe the higher $R_{O_2}^{PI}$ of low-loaded electrodes to a *rf* specific mass transport resistance. An increase of $R_{O_2}^{PI}$ was also observed by other researchers who conducted limiting current measurements for MEAs with different loading.[9,10,37,55] In accordance with the *ECSA* trends presented in Figure 5, $R_{O_2}^{PI}$ increases with decreasing *ECSA* values in all aging protocols. Consistently, the highest transport resistances

were obtained for procedures which showed the most severe *ECSA* losses, namely SW and TW-H for high-loaded cathodes as well as TW and SW for low-loaded cathodes. Comparing the transport resistance evolution for high-loaded catalyst layers, TW aging leads to less significant increases of $R_{O_2}^{PI}$ compared to SW and TW-H aging, which in turn show a similar transport resistance at each aging interval. Taking the similar *ECSA* decrease and the same performance in polarization curves of TW-H and SW into account, it is evident that the potential transient during aging is of minor importance, while the hold time at high potentials is the main contributor to electrode degradation. As described earlier, for degraded cathodes with ultra-low *rf* values (low-loaded cathodes subjected to 30000 TW cycles or to ≥10000 SW cycles), the deconvolution of pressure dependent and pressure independent resistance is not reliable, hence only the total transport resistance at 170 kPa_{abs} is shown in Figure 11.

To disentangle the effect of low *rf* values on the observed increase of the total transport resistance from possible transport limitations originating from carbon corrosion, cathodes were exposed to a constant potential hold (CP) of 1.2 V_{cell} for 8 h at 95°C and 100% *RH*. This procedure results in a thinning of the catalyst layer by approximately 40%, while maintaining a reasonably high *rf* value (from 222 ± 10 at BOT to 90 ± 2 cm^2_{Pt}/cm^2 at EOT). Despite the fact that the catalyst layer structure collapses in this experiment, the total transport resistance increases only moderately from 0.70 ± 0.01 to 0.86 ± 0.01 s/cm (see Figure 11). On the one hand, the slight increase of the pressure independent resistance can be attributed to the loss of *ECSA*, comparable to the other testing procedures which lead to lower *rf* values. On the other hand, since $R_{O_2}^{PD}$ is mostly associated with the transport resistances in the flow-field, the GDL, and the in the void volume within the catalyst layer, it would be reasonable to expect that it increases upon cathode thinning. Nevertheless, since the pressure dependent part of the transport resistance increases solely by 0.07 ± 0.04 s/cm (Figure 11), this hypothesis cannot be proven within the limited accuracy of this method. Considering that no thinning was observed for electrodes exposed to voltage cycling, the changes of $R_{O_2}^{total}$, and especially $R_{O_2}^{PI}$ in the course of aging are clearly not attributed to carbon corrosion. In other words, the much larger increase of $R_{O_2}^{total}$ and $R_{O_2}^{PI}$ over the course of all voltage cycling protocols (with the exception of the TW–LUPL protocol) where no cathode thinning was observed, must be related to phenomena other than carbon corrosion. Consistent with the essentially identical BOT and EOT performance of low-loaded cathodes subjected to TW-LUPL cycling, there is also essentially no increase of the total oxygen mass transport resistance.

As a comparison to the data in literature,[9] the pressure independent part of the O_2 mass transport resistance was plotted as a function of the *rf* in Figure 12. The clear trend of strongly increasing $R_{O_2}^{PI}$ with decreasing platinum surface area (i.e., *rf* < 50 cm^2_{Pt}/cm^2) presented here, was also observed by Greszler et al. and underlines the previously stated hypothesis that the high O_2 mass transport resistance is a strong function of the cathode *rf*. The fact that aged, high-loaded electrodes show a similar $R_{O_2}^{PI}$ (e.g., after 30000 TW cycles) compared to low-loaded cathodes at BOT further clarifies that the *rf* is indeed a major influencing factor on the O_2 mass transport. However, a disentanglement of $R_{O_2}^{PI}$ into a fraction caused by the AST and another contribution, originating solely from the *rf* of the cathode, cannot be drawn unambiguously with respect to the accuracy of the measurement.

Voltage loss analysis of aged cathodes.—Using the total oxygen mass transport resistance at BOT and EOT (Figure 11), the corresponding air polarization curves were corrected for all voltage loss contributions that are currently accessible by in situ measurement techniques, according to a preceding publication[11] and are shown in Figure 13. In short, corrections of the potential include the *HFR*, the effective cathode proton conduction resistance, and the total oxygen mass transport resistance, while the current density was corrected

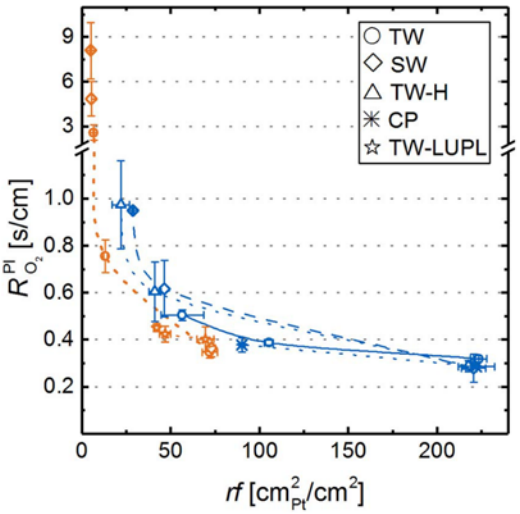

Figure 12. Pressure independent oxygen mass transport resistance, $R_{O_2}^{PI}$, as a function of the electrode's roughness factor, *rf*, for high-loaded (blue) and low-loaded (orange) MEAs at BOT and the respective aging intervals. If the EOT transport resistance could not be separated into pressure dependent and independent contributions (see open bars in Figure 11), the total transport resistance at 170 kPa_{abs} is given in this figure.

for H_2 crossover, electrical short current and was normalized to the cathode's *ECSA*.

For BOT, all H_2/air polarization curves coincide with a Tafel slope of ≈73 mV/dec for high-loaded and ≈80 mV/dec for low-loaded catalyst layers. We attribute the higher Tafel slope in air compared to pure O_2 to unaccounted mass transport limitations, which increase as the O_2 concentration decreases. Upon aging, a strong deviation from the theoretical 70 mV/dec slope is observed at high current density, similar to the limitations observed in pure O_2 (deviations from a straight $E_{corrected}$ vs log(*i*) line at EOT occur at ≈30 mA/cm^2_{Pt} for all aged cathodes, except for the low-loaded cathode subjected to SW cycling). However, the deviation from a straight $E_{corrected}$ vs log(*i*) line at EOT occurs earlier in air, viz., at ≈10 mA/cm^2_{Pt} (again, with the exception of the low-loaded cathode subjected to SW cycling, which deviates much earlier), which one would expect in case of significant oxygen transport resistances. The here observed deviation was also seen by other research groups at specific current densities ranging from 5–50 mA/cm^2_{Pt} in fully corrected air polarization curves with aged MEAs or at very low cathode *rf* values, commonly attributed to a local oxygen diffusion resistance.[9,10,12] Although a correction for the mass transport was applied to these measurements, it seems that the deviation at high Pt specific current density is not accounted for by the transport resistance determined by the limiting current method. Indeed, the conditions of the MEA during the limiting current measurement (local MEA temperature and *RH* due to a high heat production rate at <0.3 V) are not identical to the operating conditions during the polarization curve (lower heat production rate at voltages of ≈0.6–0.5 V) where the corrections are applied, which certainly introduces an error. Furthermore, due to changes in temperature or local *RH*, the utilization of the Pt surface area may change, increasing the oxygen flux to the remaining Pt surface or altering the ORR kinetics.[59,67] While we cannot prove one or the other hypothesis, we consider the limitations of the oxygen mass transport determination method to be a probable cause of at least part of the observed deviations at high current density. However, whatever the origin of these unaccounted transport resistances may be, they clearly scale with the specific current density.

After full correction of the recorded H_2/air polarization curves for all known voltage loss contributions (namely the *HFR*, the effective cathode proton conduction resistance, and the total oxygen mass

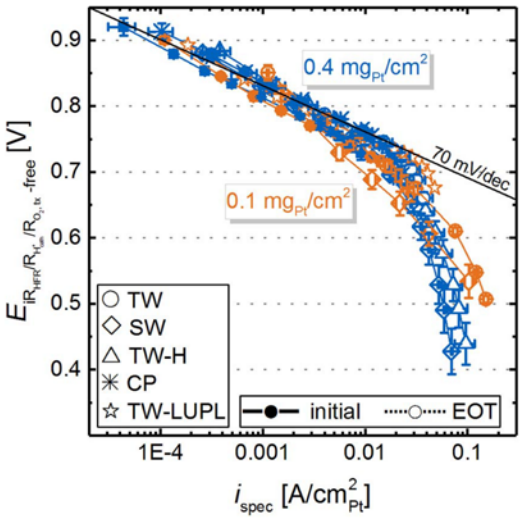

Figure 13. Transport-corrected differential flow H_2/air polarization curves at 80°C, 100% *RH*, and 170 kPa$_{abs}$ at BOT (full symbols) and EOT (open symbols) for high-loaded (blue) and low-loaded (orange) MEAs. The potential is corrected for the *HFR*, effective cathode proton conduction resistance, and the total oxygen mass transport resistance, while the current is corrected for the H_2 crossover and ohmic shorting currents, and is normalized to the cathode *ECSA*. The two slanted lines indicate the specific current density region for high-loaded (blue) and low-loaded (orange) MEAs at BOT. BOT polarization curves of all tested MEAs were averaged and error bars symbolize the standard deviation over all MEAs. Error bars for EOT curves represent the mean absolute deviation between two measurements.

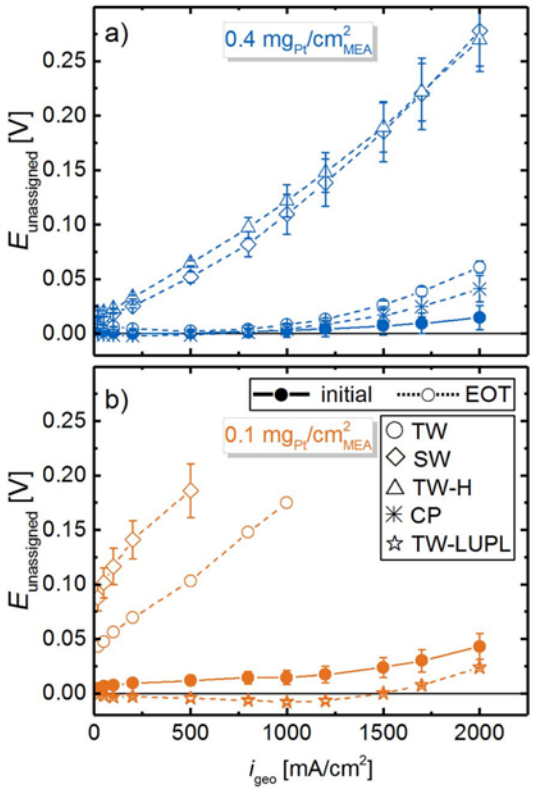

Figure 14. Unaccounted voltage losses between a theoretical, kinetically limited H_2/air polarization curve calculated from the measured ORR mass activity (assuming simple Tafel kinetics with an intrinsic Tafel slope of 70 mV/dec) and polarization curves recorded in H_2/air (differential flow, 170 kPa$_{abs}$, 80°C, and 100% *RH*), where the potential is corrected for the *HFR*, effective cathode proton conduction resistance, and the total oxygen mass transport resistance for a) high-loaded and b) low-loaded cathode catalyst layers at BOT (full symbols) and EOT (open symbols).

transport resistance), the H_2/air polarization curves can be compared to the theoretical, kinetically limited polarization curve, constructed from the experimentally determined ORR mass activities (see Figure 8a) and assuming simple Tafel kinetics with an intrinsic Tafel slope of 70 mV/decade. The remaining unaccounted voltage losses are shown in Figure 14a for high-loaded and in Figure 14b for low-loaded catalyst layers at BOT (solid lines) and EOT for all aging protocols.

An analysis of Figure 14a reveals an almost quantitative account of all voltage losses for high-loaded MEAs at BOT (blue solid line), with only minor unaccounted losses at 2 A/cm^2 (15 ± 11 mV). Upon catalyst layer aging over 30000 TW cycles (open blue circles), the unaccounted voltage losses at higher current density (>1 A/cm^2) increase, pointing to the fact that not all voltage losses can be assessed by the current in situ diagnostic measurements. This discrepancy is even more pronounced for the MEAs exposed to SW and TW-H aging, where unaccounted voltage losses on the order of 250 mV were observed at 2 A/cm^2. In accordance with the previously described evolution of the *ECSA*, the ORR mass activity, and the total oxygen mass transport resistance, both aging protocols (SW and TW-H) lead to identical unaccounted losses. In contrast, the corrosion of the carbon support (CP aging) does not lead to a significant increase of the unaccounted losses (e.g., 41 ± 12 mV at 2 A/cm^2) and therefore cannot explain the high, unaccounted voltage losses for SW and TW-H cycling.

The unaccounted voltage losses for low-loaded MEAs (Figure 14b) at BOT are slightly higher compared to high-loaded MEAs, and are in reasonably good agreement with our previous voltage-loss analysis with the same catalyst.[11] After aging by the TW or SW procedure, rather dramatic unaccounted voltage losses are already observed at low geometric current densities and become increasingly larger with current density. Considering the SW and TW-H aged, high-loaded catalyst layers, the significant unaccounted voltage losses of all these measurements suggest that the quantitative evaluation of voltage loss contributions is impaired when using cathodes with low *rf* values, i.e. at a high Pt specific current density. This hypothesis is further validated by the TW-LUPL voltage cycling test applied to the 0.1 mg$_{Pt}$/cm^2 cathodes: even after 30000 potential cycles, the unaccounted voltage losses were substantially less compared to all other aging protocols, being as little as 24 ± 1 mV at 2 A/cm^2 at EOT, where the roughness factor is 42 ± 2 cm$^2_{Pt}$/cm^2. A very intriguing observation is that this roughness factor is only ≈2–fold larger than the EOT roughness factor of the high-loaded cathodes subjected to SW cycling (29 ± 1 cm$^2_{Pt}$/cm^2), while the unaccounted voltage losses of the latter are >250 mV at 2 A/cm^2. Quite clearly, the currently available in situ diagnostics do not capture the critical voltage loss phenomena which must be related to the morphological changes with regards to Pt particle size and location within the electrode.

Conclusions

To better understand the influence of voltage cycling based ASTs on the development of mass transport resistances and on the extent to which they can be captured by currently available in situ diagnostics (ORR kinetics in H_2/O_2, cathode proton conduction resistance by impedance, oxygen transport resistance via limiting current measurements), we conducted a comprehensive voltage loss analysis on MEAs with high- and low-loaded cathodes (0.4 and 0.1 mg$_{Pt}$/cm^2) over the course of ASTs based on different voltage cycling protocols. These include triangular wave (TW) and square wave (SW) cycles between 0.6 and 1.0 V_{RHE}, TW cycles between 0.6 and a lowered upper potential limit of 0.85 V_{RHE} (TW–LUPL), as well as a combination of a triangular sweeps between 0.6 and 1.0 V_{RHE}, with potential hold periods at the upper and lower potential (TW–H), all conducted in H_2/N_2 (anode/cathode) at ambient pressure, 80°C, and 100% *RH*.

A comparison of the *ECSA* and the O_2 mass transport resistance evolution of MEAs aged by SW cycles leads to considerably faster degradation compared to TW cycles. To identify whether the fast potential transients or the potential hold phase is responsible for the faster degradation rates during SW aging, an additional procedure, consisting of a triangular potential scan followed by potential hold phase (TW-H) was tested. A comparison of the evolution of the cathode's *ECSA*, mass activity, and mass transport resistance revealed that the potential hold rather than the rate of the potential transient is the main contributor to cathode aging in voltage cycling ASTs, so that SW and TW–H cycling profiles lead to identical aging rates with respect to the number of cycles.

For all ASTs, the magnitude of assignable and unassigned O_2 mass transport resistances scaled predominantly with the cathode roughness factor, increasing with decreasing roughness factor, whereby the pressure dependent O_2 transport resistance remained essentially constant. At the same time, ex situ cathode thickness measurements indicated the absence of cathode thinning and thus of significant carbon support corrosion. These results were further compared to an aging procedure which consisted of a constant potential hold at 1.2 V_{cell} for 8 h (at 95°C and 100% *RH*), leading to significant carbon corrosion and concomitant cathode thinning, while maintaining a reasonably high cathode roughness factor. This analysis showed that the impact of carbon corrosion on the O_2 mass transport resistance is minor compared to its increase with decreasing roughness factor.

While 30000 TW or SW cycles between 0.6 and 1.0 V_{RHE} dramatically decrease the H_2/air performance of low-loaded MEAs, it shows negligible degradation over 30000 cycles when a lowered upper potential limit of 0.85 V_{RHE} is applied (TW–LUPL). This provides a guideline to limit cathode degradation under automotive conditions, namely by eliminating high potential periods (e.g., OCV).

Acknowledgment

The authors of this work would like to guide special thanks to Christoph Simon for insightful discussions about limiting current measurements and mass transport resistances. We would also like to thank Daniel Herein and Annett Reichl for fruitful discussions and valuable suggestions. Furthermore, the effort of Hany A. El-Sayed to acquire high quality TEM images is greatly appreciated.

ORCID

Gregor S. Harzer https://orcid.org/0000-0002-1830-1931
Jan N. Schwämmlein https://orcid.org/0000-0001-8902-4508

References

1. *Toyota Motor Co. (accessed* 05/18/2017), http://newsroom.toyota.co.jp/en/detail/4198334/.
2. *Hyundai Motor Co. (accessed* 05/18/2017), http://globalpr.hyundai.com/prCenter/news/newsView.do?dID=1581.
3. *Honda Motor Co., Ltd. (accessed* 10/13/2017), http://hondanews.com/honda-automobiles/channels/clarity-fuel-cell-press-releases/releases/southern-california-customers-take-delivery-of-new-2017-honda-clarity-fuel-cell-sedan.
4. M. F. Mathias, R. Makharia, H. A. Gasteiger, J. J. Conley, T. J. Fuller, C. J. Gittleman, S. S. Kocha, D. P. Miller, C. K. Mittelsteadt, T. Xie, S. G. Yan, and P. T. Yu, *Electrochem. Soc. Interface*, **14**, 24 (2005).
5. A. Veziroglu and R. Macario, *Int. J. Hydrogen Energ.*, **36**, 25 (2011).
6. H. A. Gasteiger, J. E. Panels, and S. G. Yan, *J. Power Sources*, **127**, 162 (2004).
7. H. A. Gasteiger, S. S. Kocha, B. Sompalli, and F. T. Wagner, *Appl. Catal., B.*, **56**, 9 (2005).
8. A. Kongkanand and M. F. Mathias, *J. Phys. Chem. Lett.*, **7**, 1127 (2016).
9. T. A. Greszler, D. Caulk, and P. Sinha, *J. Electrochem. Soc.*, **159**, F831 (2012).
10. J. P. Owejan, J. E. Owejan, and W. Gu, *J. Electrochem. Soc.*, **160**, F824 (2013).
11. A. Orfanidi, P. Madkikar, H. A. El-Sayed, G. S. Harzer, T. Kratky, and H. A. Gasteiger, *J. Electrochem. Soc.*, **164**, F418 (2017).
12. P. Zihrul, I. Hartung, S. Kirsch, G. Huebner, F. Hasché, and H. A. Gasteiger, *J. Electrochem. Soc.*, **163**, F492 (2016).
13. C. H. Paik, G. S. Saloka, and G. W. Graham, *Electrochem. Solid-State Lett.*, **10**, B39 (2007).
14. R. Mukundan, G. James, J. Davey, D. Langlois, D. Torraco, W. Yoon, A. Z. Weber, and R. Borup, *ECS Trans.* **41**, 613 (2011).
15. S. Jomori, N. Nonoyama, and T. Yoshida, *J. Power Sources*, **215**, 18 (2012).
16. R. K. Ahluwalia, S. Arisetty, J.-K. Peng, R. Subbaraman, X. Wang, N. Kariuki, D. J. Myers, R. Mukundan, R. Borup, and O. Polevaya, *J. Electrochem. Soc.*, **161**, F291 (2014).
17. A. P. Young, J. Stumper, and E. Gyenge, *J. Electrochem. Soc.*, **156**, B913 (2009).
18. R. L. Borup, J. R. Davey, F. H. Garzon, D. L. Wood, and M. A. Inbody, *J. Power Sources*, **163**, 76 (2006).
19. K. Yu, D. J. Groom, X. Wang, Z. Yang, M. Gummalla, S. C. Ball, D. J. Myers, and P. J. Ferreira, *Chem. Mater.*, **26**, 5540 (2014).
20. P. J. Ferreira, G. J. la O', Y. Shao-Horn, D. Morgan, R. Makharia, S. Kocha, and H. A. Gasteiger, *J. Electrochem. Soc.*, **152**, A2256 (2005).
21. S. Arisetty, X. Wang, R. K. Ahluwalia, R. Mukundan, R. Borup, J. Davey, D. Langlois, F. Gambini, O. Polevaya, and S. Blanchet, *J. Electrochem. Soc.*, **159**, B455 (2012).
22. R. G. Compton and G. H. W. Sanders, in *Electrode potentials*, Oxford University Press, Oxford, New York (1996).
23. J. P. Meyers and R. M. Darling, *J. Electrochem. Soc.*, **153**, A1432 (2006).
24. R. L. Borup, D. D. Papadias, R. Mukundan, D. Spernjak, D. A. Langlois, R. Ahluwalia, K. L. More, and S. Grot, *ECS Trans.* **69**, 1029 (2015).
25. C. A. Reiser, L. Bregoli, T. W. Patterson, J. S. Yi, J. D. Yang, M. L. Perry, and T. D. Jarvi, *Electrochem. Solid-State Lett.*, **8**, A273 (2005).
26. Y. Yu, H. Li, H. Wang, X.-Z. Yuan, G. Wang, and M. Pan, *J. Power Sources*, **205**, 10 (2012).
27. J. N. Schwämmlein, P. J. Rheinländer, Y. Chen, K. F. Freyer, and H. A. Gasteiger, *ECS Trans.* **80**, 927 (2017).
28. C. Wagner, *Z. Elektrochem. (Zeitschrift für Elektrochemie).*, **65**, 581 (1961).
29. R. M. Darling and J. P. Meyers, *J. Electrochem. Soc.*, **150**, A1523 (2003).
30. J. Zhang, B. A. Litteer, W. Gu, H. Liu, and H. A. Gasteiger, *J. Electrochem. Soc.*, **154**, B1006 (2007).
31. C. Simon, F. Hasché, D. Müller, and H. A. Gasteiger, *ECS Trans.* **69**, 1293 (2015).
32. C. Simon, F. Hasché, and H. A. Gasteiger, *J. Electrochem. Soc.*, **164**, F591 (2017).
33. R. Makharia, M. F. Mathias, and D. R. Baker, *J. Electrochem. Soc.*, **152**, A970 (2005).
34. Y. Liu, M. W. Murphy, D. R. Baker, W. Gu, C. Ji, J. Jorne, and H. A. Gasteiger, *J. Electrochem. Soc.*, **156**, B970 (2009).
35. M. Eikerling and A. A. Kornyshev, *J. Electroanal. Chem.*, **475**, 107 (1999).
36. D. R. Baker, D. A. Caulk, K. C. Neyerlin, and M. W. Murphy, *J. Electrochem. Soc.*, **156**, B991 (2009).
37. N. Nonoyama, S. Okazaki, A. Z. Weber, Y. Ikogi, and T. Yoshida, *J. Electrochem. Soc.*, **158**, B416 (2011).
38. W. Gu, D. R. Baker, Y. Liu, and H. A. Gasteiger, in *Handbook of Fuel Cells*, 1st ed., W. Vielstich, H. Yokokawa, and H. A. Gasteiger, p. 631, John Wiley & Sons Ltd, Chichester (2009).
39. J. A. Gilbert, N. N. Kariuki, X. Wang, A. J. Kropf, K. Yu, D. J. Groom, P. J. Ferreira, D. Morgan, and D. J. Myers, *Electrochimica Acta*. **173**, 223 (2015).
40. M. Uchimura and S. S. Kocha, *ECS Trans*. **11**, 1215 (2007).
41. A. Ohma, T. Mashio, K. Sato, H. Iden, Y. Ono, K. Sakai, K. Akizuki, S. Takaichi, and K. Shinohara, *Electrochim. Acta.*, **56**, 10832 (2011).
42. R. N. Carter, S. S. Kocha, F. Wagner, M. Fay, and H. A. Gasteiger, *ECS Trans*. **11**, 403 (2007).
43. T. R. Garrick, T. E. Moylan, V. Yarlagadda, and A. Kongkanand, *J. Electrochem. Soc.*, **164**, F55 (2017).
44. T. J. Schmidt, H. A. Gasteiger, G. D. Stäb, P. M. Urban, D. M. Kolb, and R. J. Behm, *J. Electrochem. Soc.*, **145**, 2354 (1998).
45. A. López-Cudero, A. Cuesta, and C. Gutiérrez, *J. Electroanal. Chem.*, **579**, 1 (2005).
46. A. Cuesta, A. Couto, A. Rincón, M. C. Pérez, A. López-Cudero, and C. Gutiérrez, *J. Electroanal. Chem.*, **586**, 184 (2006).
47. A. López-Cudero, Á. Cuesta, and C. Gutiérrez, *J. Electroanal. Chem.*, **586**, 204 (2006).
48. D. Strmcnik, D. Tripkovic, D. van der Vliet, V. Stamenkovic, and N. M. Marković, *Electrochem. Commun.*, **10**, 1602 (2008).
49. F. T. Wagner, S. G. Yan, and P. T. Yu, in *Handbook of Fuel Cells*, 1st ed., W. Vielstich, H. Yokokawa, and H. A. Gasteiger, p. 250, John Wiley & Sons Ltd, Chichester (2009).
50. F. Mailard, S. Pronkin, and E. R. Savinova, in *Handbook of Fuel Cells*, 1st ed., W. Vielstich, H. Yokokawa, and H. A. Gasteiger, p. 101, John Wiley & Sons Ltd, Chichester (2009).
51. J. A. Gilbert, N. N. Kariuki, R. Subbaraman, A. J. Kropf, M. C. Smith, E. F. Holby, D. Morgan, and D. J. Myers, *J. Am. Chem. Soc.*, **134**, 14823 (2012).
52. S. Cherevko, A. R. Zeradjanin, A. A. Topalov, N. Kulyk, I. Katsounaros, and K. J. J. Mayrhofer, *ChemCatChem*. **6**, 2219 (2014).
53. H. A. Gasteiger, W. Gu, B. Litteer, R. Makharia, B. Brady, M. Budinski, E. Thompson, F. T. Wagner, S. G. Yan, and P. T. Yu, in *Mini-Micro Fuel Cells*, 1st ed., S. Kakaç, A. Pramuanjaroenkij, and L. Vasiliev, p. 225, Springer Netherlands, Dordrecht (2008).
54. P. D. Beattie, V. I. Basura, and S. Holdcroft, *J. Electroanal. Chem.*, **468**, 180 (1999).
55. S. Shukla, D. Stanier, M. S. Saha, J. Stumper, and M. Secanell, *J. Electrochem. Soc.*, **163**, F677 (2016).
56. H. Liu, H. A. Gasteiger, A. Laconti, and J. Zhang, *ECS Trans*. **1**, 283 (2006).
57. K. Kudo, T. Suzuki, and Y. Morimoto, *ECS Trans*. **33**, 1495 (2010).
58. T. V. Reshetenko and J. St-Pierre, *J. Electrochem. Soc.*, **161**, F1089 (2014).
59. N. P. Subramanian, T. A. Greszler, J. Zhang, W. Gu, and R. Makharia, *J. Electrochem. Soc.*, **159**, B531 (2012).
60. S. S. Kocha, in *Handbook of Fuel Cells*, 1st ed., W. Vielstich, A. Lamm, and H. A. Gasteiger, p. 538, John Wiley & Sons Ltd, Chichester (2009).

61. H. A. Gasteiger, W. Gu, R. Makharia, M. F. Mathias, and B. Sompalli, in *Handbook of Fuel Cells*, 1st ed., W. Vielstich, A. Lamm, and H. A. Gasteiger, p. 593, John Wiley & Sons Ltd, Chichester (2009).
62. S. Zhang, X.-Z. Yuan, J. N. C. Hin, H. Wang, K. A. Friedrich, and M. Schulze, *J. Power Sources*, **194**, 588 (2009).
63. K. Kinoshita, *J. Electrochem. Soc.*, **137**, 845 (1990).
64. K. J. J. Mayrhofer, D. Strmcnik, B. B. Blizanac, V. Stamenkovic, M. Arenz, and N. M. Marković, *Electrochim. Acta.*, **53**, 3181 (2008).
65. C. Simon, D. Kartouzian, D. Müller, F. Wilhelm, and H. A. Gasteiger, *J. Electrochem. Soc.*, **164**, F1697 (2017).
66. D. A. Caulk and D. R. Baker, *J. Electrochem. Soc.*, **157**, B1237 (2010).
67. K. Shinozaki, H. Yamada, and Y. Morimoto, *J. Electrochem. Soc.*, **158**, B467 (2011).

3.2.3. Activity and Stability of Carbon Supported Pt_xY Alloys for the ORR Determined by RDE and Single-Cell PEMFC Measurements

The following section presents the publication "Activity and Stability of Carbon Supported Pt_xY Alloys for the ORR Determined by RDE and Single-Cell PEMFC Measurements",[113] published in the peer-reviewed Journal of The Electrochemical Society in October 2018 as an open access article distributed under the terms of the Creative Commons Attribution 4.0 License, permitting unrestricted reuse of the work in any medium, provided the original work is properly cited. The publication can be downloaded via the permanent web link https://doi.org/10.1149/2.0221815jes. The study was presented at the 234th ECS meeting (AiMES 2018) in Cancún, Mexico (abstract #1478) by Jan N. Schwämmlein.

Short summary.—The manuscript presented here applies the triangular wave voltage cycling AST developed in the previously described study to a novel catalyst. Based on computational considerations, Greeley et al. proposed bimetallic alloys of Pt with rare earth metals (Pt-RE), especially Pt-Y, to be a unique class of highly active ORR catalysts.[153] Nevertheless, only few synthesis methods for bimetallic Pt-Y nanoparticles are present in the literature due to the largely different reduction potential of the noble Pt and the non-noble Y. Recently, Roy et al. presented a method to prepare carbon supported Pt_xY nanoparticles by distributing a halide containing Y precursors on a Pt/C catalyst, followed by heat treatment in reductive atmosphere (H_2).[112]

In this manuscript, we use a similar synthesis route to prepare Pt_xY/C, based on a $20\%_{wt.}$ Pt/C catalyst impregnated with an YCl_3 precursor by freeze drying from acetonitrile and subsequent heat treatment at 1200°C in 5% H_2 in Ar. As a reference, the Pt/C catalyst is heat treated at the same temperature in the absence of YCl_3 (Pt/C-HT). After physical-chemical analysis (XRD, TEM, elemental analysis), the in-house prepared catalyst is thoroughly characterized by RDE measurements (*ECSA*, activation procedure, ORR activity) and finally tested in PEMFC single cells to determine its ORR activity and electrochemical stability.

XRD analysis of the as-prepared catalyst shows that the nanoparticles consist of different Pt-Y phases (mainly Pt_2Y and Pt_3Y) and pure Pt. Furthermore, YOCl and Y_2O_2S are

identified as side-phases of the synthesis, originating from the reaction of YCl_3 with O_2/H_2O before the heat treatment and with Sulphur impurities of the carbon support. YOCl is quantitatively removed in a subsequent catalyst purification step in sulfuric acid, where also the amount of Y_2O_2S is significantly reduced. Analyzing the particle size distribution of the Pt_xY/C catalyst by TEM shows that the heat treatment induces a significant particle growth, resulting in a number-averaged Pt_xY diameter of 12 nm and a surface averaged diameter of 21 nm, comparable to the heat treated Pt/C catalyst. The large particle size of the Pt_xY/C and Pt/C-HT catalysts is also reflected in their low *ECSA* (determined by CO stripping in 0.1 M $HClO_4$) compared to the commercial Pt/C catalyst. Hence, the ORR mass activity of the Pt_xY/C catalyst is lower than that of Pt/C, even though the successful alloying of the two metals causes a significant increase of the surface specific ORR activity. The *ECSA*, as well as the ORR activity of Pt_xY/C is found to increase upon activation by cycling to anodic potentials, originating most likely from a reconstruction of the active surface and the removal of adsorbed species. Considering the change of *ECSA* and ORR activity in RDE experiments, a catalyst activation protocol consisting of voltage cycles between 0.05 and 1.20 V_{RHE} is defined. Subsequently, full cell MEA tests are carried out, utilizing the previously developed activation procedure (slightly modifying the voltage window) and the voltage cycling AST described in the previous section to evaluate the fuel cell performance of cathode catalyst layers based on Pt_xY/C and to determine their stability towards electrochemical degradation. Even though this catalyst initially shows a low ORR mass activity, hence an inferior H_2/air performance compared to Pt/C, the large size of the Pt_xY nanoparticles provides an exceptional stability and finally a superior EOT performance. We can, however, not confirm the hypothesis stated by Greeley et al. that Pt-Y alloys are exceptionally stable versus electrochemical ageing, since we assign the observed high durability of the catalyst, tested in this study, to the large particle size of Pt_xY.

Author contributions.—P.P., G.S.H. and J.N.S. synthesized the catalyst, while A.B., G.S.H. and J.N.S. performed the RDE experiments. PEMFC tests were done by G.S.H. and J.N.S. The data was analyzed by J.N.S. and G.S.H. The manuscript was written by J.N.S. and G.S.H. and was reviewed by all authors.

JES Focus Issue on Electrocatalysis — In Honor of Radoslav Adzic

Activity and Stability of Carbon Supported Pt_xY Alloys for the ORR Determined by RDE and Single-Cell PEMFC Measurements

Jan N. Schwämmlein, [=,*,z] Gregor S. Harzer, [=,*] Philipp Pfändner, Andrea Blankenship,[a] Hany A. El-Sayed, and Hubert A. Gasteiger[**]

Chair of Technical Electrochemistry, Department of Chemistry and Catalysis Research Center, Technical University of Munich, D-85748 Garching, Germany

Bimetallic alloys based on Pt and Y are potential cathode catalysts for proton exchange membrane fuel cells (PEMFCs) due to their high oxygen reduction reaction (ORR) activity. Nevertheless, the synthesis of carbon supported Pt_xY catalysts is challenging due to the low standard reduction potential of yttrium compared to platinum. Hence, extended electrochemical testing in actual PEMFCs remains elusive, especially with respect to catalyst degradation upon voltage-cycling. In this publication, we present the synthesis of a bimetallic Pt_xY/C catalyst via impregnation of commercial Pt/C with an yttrium halide precursor and subsequent heat-treatment in H_2 at 1200°C. This catalyst showed a high specific ORR activity, at a mass activity similar to Pt/C due to its comparably low electrochemical surface area (*ECSA*). On the other hand, the large particle size of the here synthesized Pt_xY/C catalyst (≈10 nm) resulted in a significantly enhanced stability versus degradation in an accelerated stress test (AST) based on voltage-cycling between 0.6 and 1.0 V_{RHE} at 50 mV s^{-1}, showing a superior *ECSA*, ORR activity and H_2/air performance after 30000 cycles compared to a standard Pt/C catalyst.

 [DOI: 10.1149/2.0221815jes]

Manuscript submitted August 2, 2018; revised manuscript received September 12, 2018. Published October 2, 2018. This was Paper 1478 presented at the Cancun, Mexico, Meeting of the Society, September 30–October 4, 2018. *This paper is part of the JES Focus Issue on Electrocatalysis — In Honor of Radoslav Adzic.*

The overall costs of proton exchange membrane fuel cells (PEMFCs) are a major hurdle for their large-scale implementation in fuel cell electric vehicles (FCEVs).[1] Along with other factors, the high costs originate from the use of platinum based electrocatalysts for the hydrogen oxidation reaction (HOR) as well as for the oxygen reduction reaction (ORR). While the anode Pt loadings of state-of-the-art membrane electrode assemblies (MEAs) can be reduced to very low levels (≈0.05 mg_{Pt} cm^{-2} or below) owing to the fast HOR kinetics,[2] the slow ORR kinetics commonly require cathode electrode loadings on the order of 0.1–0.3 mg_{Pt} cm^{-2}.[1] Therefore, one strategy to decrease the noble metal content in the MEA is to develop Pt based cathode catalysts with enhanced ORR activity, whereby it has been shown that the alloying of Pt with other transition metals, e.g., Co or Ni, can enhance the ORR activity per Pt mass by a factor of ≈3–4.[3,4] In addition to those commonly used 3d transition metals, theoretical calculations by Greeley et al. suggested bimetallic alloys based on Pt and Y to be another class of exceptionally active ORR catalysts.[5] Initial measurements on polycrystalline bulk alloys in a rotating disk electrode (RDE) setup confirmed this hypothesis, showing a specific activity for the ORR at 0.9 V vs. the reversible hydrogen electrode (RHE) potential of $i^{spec}_{0.9\,V} \approx 9.4$ mA cm^{-2}_{Pt} for Pt_3Y compared to $i^{spec}_{0.9\,V} \approx 1.5$ mA cm^{-2}_{Pt} for pure Pt (both at 23°C in 0.1 M $HClO_4$, extracted from Figure 4a), suggesting a ≈6.5x higher specific activity of Pt_3Y vs. Pt.[5] Furthermore, the group hypothesized that the combination of those two metals might be beneficial with respect to catalyst durability in acidic electrolytes (i.e., in a PEMFC) due to the large heat of mixing upon alloying. Later on, Hernández-Fernández et al. prepared Pt_xY alloy nanoparticles by a gas-aggregation technique and showed its superior ORR activity compared to pure Pt in RDE measurements.[6]

Despite their promising ORR activity, the synthesis of Pt_xY alloy catalysts and their subsequent implementation into a PEMFC remains challenging due to the low standard reduction potential of yttrium and the associated synthetic difficulties to prepare sufficiently large quantities of Pt_xY nanoparticles supported on carbon, so that MEAs could be prepared for fuel cell testing. Even though ongoing research efforts led to first steps towards a larger scale synthesis of carbon supported Pt_xY alloys (Pt_xY/C),[7,8] many catalysts presented in the literature are either non alloyed, consisting of yttrium (hydr)oxide decorated Pt[9–11] or were prepared by approaches which are not conducive to the preparation of carbon supported Pt_xY nanoparticles (bulk alloys,[5,12] dealloying of bulk alloys,[13] gas-phase deposition methods,[6,14,15] or electrodeposition on glassy carbon substrate).[16] So far, the only Pt_xY catatlyst tested in an actual PEMFC cell were Pt_xY alloys sputter-deposited on a diffusion medium substrate coated with a carbon/ionomer composite layer,[14] but even though its H_2/O_2 performance was shown to be superior to sputter-deposited Pt, no ORR activity or durability data were evaluated, so that a comparison with the state-of-the-art cannot be made.

In this publication, we report a facile synthesis route for carbon supported Pt_xY alloy nanoparticles from a commercial Pt/C precursor by reduction of YCl_3 in H_2 atmosphere at elevated temperature, similar to the approach recently employed by Roy et al.[8] Following a detailed physical-chemical characterization of the Pt_xY/C catalyst by X-ray diffraction (XRD), transmission electron microscopy (TEM), and elemental analysis, its electrochemically active surface area (*ECSA*) and ORR activity was determined by RDE measurements. Subsequently, MEAs with Pt_xY/C as cathode catalyst were prepared and evaluated in a single-cell PEMFC to verify its suitability for fuel cell applications. Following the method outlined in our recent study,[17] voltage-cycling accelerated stress tests (ASTs) were conducted in a single-cell PEMFC (triangular scans between 0.6 and 1.0 V_{RHE} at 50 mV s^{-1} and 80°C) to investigate the Pt_xY/C catalyst stability with regards to its *ECSA*, its ORR activity, and its H_2/air performance over the course of 30,000 voltage cycles.

Experimental

All air- or moisture sensitive chemicals were handled in an Ar-filled glove box (M. Braun Inertgas-Systeme GmbH, Germany) or by using standard Schlenck techniques. All solvents used in the synthesis were of high purity, dried and de-gassed before use. Ultrapure water had a resistance of 18.2 MΩ cm (MilliQ Ingegral, Merck Millipore KGaA, Germany). All gases were supplied by Westfalen AG (Germany) with a 6.0 grade for RDE and 5.0 grade for all other experiments (except

[=] These authors contributed equally to this work.
[*] Electrochemical Society Student Member.
[**] Electrochemical Society Fellow.
[a] Present address: Department of Chemical Engineering, Massachusetts Institute of Technology, Cambridge, Massachusetts 02142, USA.
[z] E-mail: jan.schwaemmlein@tum.de

for CO gas, which had a purity of 4.8). Comprehensive experimental details on RDE,[18,19] and MEA preparation/fuel cell testing[17] were given in previous publications, but the most pertinent information is given below. If not otherwise stated (e.g., E_{cell}), potentials referred to in CVs, polarization curves, and voltage-cycling experiments are referenced to the reversible hydrogen electrode (RHE) potential at a nominal H_2 pressure of 100 kPa_{abs} (V_{RHE}), obtained by correcting the measured potential for the Nernstian shift resulting from H_2 partial pressures different than 100 kPa_{abs}. Furthermore, note that all pressures in fuel cell tests were measured and controlled at the inlet of the fuel cell and are reported as absolute pressures. If not stated otherwise, area-normalized currents refer to the geometric area of the electrode.

Thermogravimetric analysis (TGA).—TGA measurements were performed with a TGA/DSC 1 instrument, equipped with a gas controller (GC 200, Mettler Toledo Corp., Switzerland) set to flows of 40 mL min^{-1} of 5% H_2 in Ar as reactive gas and to 20 mL min^{-1} Ar as cell purge gas. Heating from 25 to 1200°C was performed at a ramp of 20 K min^{-1}. The samples were placed in a 70 µL sapphire crucible with lid (THEPRO GbR, Germany) in an Ar-filled glove box (M. Braun; H_2O and O_2 concentration < 0.1 ppm) and transferred to the TGA furnace with minimum exposure to ambient air. The weight loss of K_2PtCl_4 (99.99%, metal basis, Sigma Aldrich Corp., Germany) was measured to identify the reduction temperature of Pt.

Catalyst preparation.—For the preparation of Pt_xY alloys supported on carbon, the appropriate amount of YCl_3 was mixed in the glove box with a Vulcan carbon supported 20%$_{wt}$ Pt/C catalyst (TEC10V20E, Tanaka Kikinzoku Kogyo K.K., Japan) in an agate mortar at a molar Pt:Y ratio of 1:1. Approximately 1.5 g of the mixture were added to a 25 mL Schlenck tube and dispersed in 6 mL acetonitrile (≥99.9%, Sigma Aldrich Corp., Germany), corresponding to 24 mL $g_{YCl_3}^{-1}$, and then sonicated (Elmasonic S 30 H, Elma Schmidbauer GmbH, Germany) for 3 min. Subsequently, the suspension was cooled by immersion into liquid nitrogen and freeze-dried in vacuum for at least 24 h. The dried catalyst precursor was transferred back into the glove box and homogenized by grinding in a mortar. For the thermal reduction, the desired amount of the precursor (on the order of 0.2 g) was transferred into a 150 µL sapphire crucible with lid. Several crucibles were placed into an aluminum oxide crucible and transferred to an Ar-purged tube furnace (LK 1300-150-600-3, HTM Reetz GmbH, Germany), equipped with an Al_2O_3 tube, while care was taken to minimize the contact of the sample with ambient air. The tube furnace was pre-heated to 1200°C under a constant flow of Ar (500 mL min^{-1}), while the samples remained outside of the heating zone (T < 100°C). Once the temperature of 1200°C was reached, the gas flow was changed to 5% H_2 in Ar (500 mL min^{-1}), and then the crucible was pushed into the heated zone, using an aluminum oxide rod, entering the tube through a polysiloxane sealing. After the desired reaction time (1 h), the heating was turned off, allowing the samples to cool slowly to room temperature (≈5 h) in a pure Ar atmosphere (Ar flow of 200 mL min^{-1}).

After the above described synthesis, the catalyst samples were handled and stored in ambient air. Leaching of the catalysts was carried out by dispersing them (≈0.1 L $g_{catalyst}^{-1}$) in continuously Ar-purged 1 M H_2SO_4 (ACS reagent, Sigma Aldrich Corp., Germany). After 3 h, the sample was recovered by centrifugation (5 min at 11500 rpm), followed by repeated washing with deionized water until a neutral pH was reached (≈5 times). Finally, the catalyst was dried overnight at 60°C in air; the typical amount of catalyst prepared in one synthesis run was ≈1 g.

For comparison, the as-received 20%$_{wt}$ Pt/C catalyst was heat treated at 1200°C in 5% H_2 in Ar according to the same heating protocol as the Pt_xY/C catalyst, while the heating time was increased to 10 h. This catalyst is referred to as Pt/C-HT.

X-ray diffraction.—X-ray powder diffractograms were measured with a Stadi P instrument (Stoe & Cie GmbH, Germany) with Cu $K_{\alpha 1}$ radiation (λ = 1.54059 Å, 50 kV, 30 mA, Ge(111) monochromatized) and a Mythen 1 K areal detector (Dectris Ltd., Switzerland) in transmission mode. The samples were prepared in glass capillaries (0.5 mm outer diameter, Hilgenberg GmbH, Germany). Four diffractograms recorded from 15–100° 2θ with a step size of 0.015° and a hold time of 11 seconds per step were averaged to enhance the signal to noise ratio. Angle correction of the diffractometer was done based on a Si standard, measured prior to every catalyst; manual background correction (especially in the region of the broad reflex from the carbon support) was conducted using the WinXPOW software suite (v. 3.0.2.1). Refinement of diffractograms was performed by structure independent profile fits using the Lebail method and the Topas Software (v. 6). The Thompson-Cox-Hastings pseudo-Voigt function was used for peak profile shape fitting.

RDE measurements.—Glassy carbon (GC) electrodes (5 mm diameter, Pine Research Instrumentation, USA), supported by a PTFE-body (Pine Research Instrumentation, USA) were polished with 0.05 µm Al_2O_3 polishing suspension (Bühler AG, Germany), sonicated various times in ultrapure water and cleaned by subsequent dipping in 5 M KOH (99.99% purity, semiconductor grade, Sigma Aldrich Corp., Germany), 2 M $HClO_4$ (60%, Cica Reagent, Kanto Chemical Co., INC., Japan), and ultrapure water. Inks were prepared by adding ultrapure water to the dry catalyst, followed by high purity 2-propanol (Chromasolv Plus, 99.9%, Sigma Aldrich Corp., Germany). The solvent mixture consisted of 80%$_{vol}$ 2-propanol and 20%$_{vol}$ H_2O. The catalyst content of the ink was adjusted to achieve a thin catalyst layer thickness of ≈1 µm by choosing noble metal loadings of ≈9 μg_{Pt} cm^{-2} (corresponding to ≈36 μg_{Vulcan} cm^{-2} at a packing density of ≈28 µm (mg_{Vulcan} $cm^{-2})^{-1}$).[20] The catalyst suspension was sonicated for 30 min in a sonication bath to achieve a homogeneous suspension. The temperature of the bath was maintained lower than 25°C to avoid evaporation of the solvent. Subsequently, Nafion (5%$_{wt}$ in lower aliphatic alcohols, 15–20% H_2O, Sigma Aldrich Corp., Germany) was added to the suspension to result in an ionomer to carbon (I/C) ratio of 0.1/1 g_I g_C^{-1}. Prior to coating, the ink was sonicated in a low energy sonication bath (USC100T, VWR International GmbH, Germany) for at least 15 min. Finally, 7 µL of ink were dropped on a GC, covered with a small glass vial and left to dry at room temperature.

Electrochemical measurements were performed using an Autolab potentiostat (PGSTAT302N, Metrohm AG, Switzerland) and a rotator (Pine Research Instrumentation, USA) with a polyether ether ketone shaft at room temperature (25°C). Apart from measurements to develop the activation procedure, all experiments to determine the ORR activity followed a catalyst cleaning by cycling the potential 50 times between 0.05 and 1.20 V_{RHE} at 50 mV s^{-1} (room temperature). Afterwards, the electrolyte solution was replaced by fresh 0.1 M $HClO_4$ and saturated with O_2. The resistance was determined by electrochemical impedance spectroscopy (EIS) from 100 kHz to 100 Hz at open circuit potential (OCP) with an amplitude of 10 mV. After fully saturating the electrolyte with O_2, polarization curves were recorded from 1.10 to 0.05 V_{RHE} at 10 mV s^{-1} and 1600 rpm. To determine the *ECSA*, CO stripping was performed by applying a constant potential of 0.06 V_{RHE} and purging CO for 3 min. Subsequently, CO was removed from solution by Ar-purging for 30 min while the potential was kept constant. The adsorbed CO was oxidized in a stripping CV starting with a positive potential scan from the adsorption potential of 0.06 to 1.00 V_{RHE} and then cycling between 0.05 and 1.00 V_{RHE} at a scan rate of 10 mV s^{-1}. The second CV was used as baseline to correct for the capacitance and the roughness factors (*rf*) were calculated from the resulting integral, using a specific charge of 420 µC cm_{Pt}^{-2}. At the end of the measurement, the electrolyte was saturated with pure H_2 to calibrate the reference electrode with the platinum ring (of the ring-disc electrode) via conducting scans into the hydrogen oxidation and hydrogen evolution potential region (−0.05 and 0.1 V_{RHE}) at a scan rate of 50 mV s^{-1} and a rotation rate of 1600 rpm. The potentials at the zero-current intercept of the anodic and cathodic scan were extracted and the average of the two potentials was taken as the RHE

potential. This procedure was used already in earlier publications by our group.[19,21]

Membrane electrode assembly preparation.—All fuel cell tests were conducted with 5 cm^2 MEAs, fabricated by the decal transfer method. Catalyst inks were prepared by mixing the catalyst with a low equivalent weight ionomer in a water-solvent dispersion (700 g $mol^{-1}_{SO_3^-}$, Asahi Kasei Corp., Japan). The ink components were added into a 15 mL capped bottle (HDPE), already containing 16.5 g of 5 mm ZrO_2 beads as grinding medium in the following sequence: catalyst, water, 1-propanol, and finally the ionomer dispersion. The water concentration of the ink was 10%$_{wt}$, while the solid content was 0.04 g mL^{-1}_{ink}, adjusted to an I/C ratio of 0.65/1 $g_I\ g_C^{-1}$. The inks were mixed by placing the bottles onto a roller mill at 60 rpm for 18 h at 25°C. Thereafter, the inks were coated on virgin PTFE decals using the Mayer rod technique with the appropriate bar on a coating machine (K Control Coater, RK PrintCoat Instruments Ltd., England) and dried at ambient temperature followed by drying at 80°C in air. The anode was identical for all experiments, with a loading of 0.1 $mg_{Pt}\ cm^{-2}$ based on a Vulcan carbon supported 20%$_{wt}$ Pt/C catalyst (same as used for the Pt_xY/C catalyst synthesis; see above) and with an I/C ratio of 0.65/1 $g_I\ g_C^{-1}$. The MEAs were assembled by hot pressing a 15 μm membrane (Asahi Kasei Corp., Japan), placed between the anode and cathode decals, at 155°C for 3 min with an applied pressure of 0.11 kN cm^{-2}. The platinum loading of the here prepared Pt_xY/C and Pt/C-HT cathodes was 0.12 $mg_{Pt}\ cm^{-2}$ with a maximum deviation of ±5%, determined by weighing the decals before and after the catalyst layer transfer. As a reference, the performance of MEAs with Pt_xY/C cathodes will be compared with that of MEAs with cathodes based on the same commercial 20%$_{wt}$ Pt/C catalyst that served as precursor for the here synthesized Pt_xY/C catalyst, whereby the cathode loading of the Pt/C MEAs was slightly lower (0.10 $mg_{Pt}\ cm^{-2}$); note that the anode electrodes were the same and that the Pt/C MEA data have been taken from Harzer et al.[17] At least two independent fuel cell measurements were conducted and subsequently averaged with error bars corresponding to the mean absolute deviation.

Fuel cell testing equipment.—Electrochemical measurements were performed on an in-house manufactured, single-cell hardware, using commercial graphite flow fields (0.5 mm lands/channels; manufactured by Poco Graphite, Entegris GmbH, Germany, according to our design).[22] Gas diffusion layers (GDLs) were the same in all experiments (H14C7, Freudenberg KG, Germany) and the GDL compression was adjusted to 20 ± 1% by quasi-incompressible, PTFE-coated fiberglass gaskets (Fiberflon, Fiberflon GmbH & Co. KG, Germany), assembled at a torque of 12 Nm (for details see Simon et al.).[23] Fuel cell tests were performed on automated test stations (G60, Greenlight Innovation Corp., Canada) equipped with a potentiostat (Reference3000, Gamry Instruments, USA) to conduct EIS.

Voltage-cycling AST procedure and PEMFC diagnostics.—All MEAs were conditioned using a voltage-controlled conditioning procedure (H_2/air flows of 1390/3320 nccm at 80°C, 100% relative humidity (*RH*), and 150 kPa_{abs}; nccm is defined at standard conditions of 273 K and 101.3 kPa): 0.6 V for 45 min, 5 min at OCV, and 10 min at 0.85 V; this sequence was repeated 10 times, after which constant performance was reached. MEAs composed of the heat-treated Pt catalyst (Pt/C-HT) and the Pt_xY/C catalyst were activated by 50 potential cycles between 0.07 and 1.20 V_{RHE} at a scan rate of 50 mV s^{-1}, 40°C, ambient pressure, and 200/50 nccm of fully humidified 5% H_2 in N_2/dry N_2, respectively. Before each set of differential flow polarization curves and diagnostic measurements, an MEA recovery step was implemented, consisting of a constant potential hold time at 0.3 V for 2 h in H_2/air (2000 nccm/5000 nccm) at 40°C, 270 kPa_{abs}, and 100% *RH*.

Cyclic voltammetry (CV) of the cathode was recorded at a scan rate of 150 mV s^{-1} between 0.07 and 1.00 V_{RHE}, at 40°C, and ambient pressure. The counter/reference electrode was supplied with 200 nccm fully humidified 5% H_2 in N_2, and the working electrode was initially purged with dry N_2 at 50 nccm, interrupting the gas flow to record the CVs. CO stripping was performed by adsorbing CO (10% CO in N_2, 100 nccm) for 10 min at 40°C and 150 kPa_{abs}, while maintaining the cathode potential at 0.1 V_{RHE}. Subsequently, residual CO was removed from the cell and the gas lines by purging with nitrogen for ≈1.5 h. A CV from the holding potential to 1.1 V_{RHE} at a scan rate of 100 mV s^{-1} was executed to oxidize the adsorbed CO. Two additional sweeps were recorded to verify the full oxidation and removal of CO from the electrode and the gas feed system. The *ECSA* was determined by integrating the area of the first anodic scan with the subsequent sweep as baseline, using a specific charge of 420 μC cm^{-2}_{Pt}.

The proton conduction resistance in the cathode catalyst layer, $R_{H^+,cath}$ (in units of Ω cm^2), was determined from AC impedance spectra, recorded in H_2/N_2 (anode/cathode) at 0.2 V with a peak-to-peak perturbation of 3.5 mV between 500 kHz and 0.2 Hz (20 points per decade), according to a procedure reported in the literature,[24,25] and analyzed based on a transmission line model.[26] In order to ensure reproducibility, the measurement was repeated three times at each condition: 100, 70, 50, and 30% *RH*, while maintaining constant gas partial pressures (i.e., at cell pressures of 270, 255, 246, and 236 kPa_{abs}, respectively) under differential flow conditions (H_2/N_2 at 1000/1000 nccm) at 80°C. The proton resistivity, $\rho_{H^+,cath}$ (in units of Ω cm), was calculated by dividing $R_{H^+,cath}$ by the cathode electrode thickness. The electrode thickness was calculated from the carbon loading of the electrode and its specific packing density in the catalyst layer (22 ± 4 μm $(mg_C\ cm^{-2})^{-1}$).[17]

Differential flow polarization curves were recorded in current-control mode at 80°C, 170 kPa_{abs}, 100% *RH* for both reactants, and constant flows of 2000 nccm of H_2 on the anode and 5000 nccm of O_2 or air on the cathode. Anode and cathode were operated in counter flow mode. At these conditions, the inlet to outlet pressure drop in anode and cathode was approximately 2 and 22 kPa_{abs}, respectively. Prior to recording polarization curves from low to high current densities, the cell voltage was set to 0.75 V for 15 min to reduce Pt oxides. Each current density point was held constant for at least 10 min, averaging the resulting voltage over the final 30 s. The ORR kinetics (mass activity, specific activity, and Tafel slopes) were determined from H_2/O_2 polarization curves after application of two corrections: i) the potential was corrected for the *iR*-drop, using the high frequency resistance (*HFR*) obtained from the x-axis intersect in the Nyquist plot measured by galvanostatic electrochemical impedance spectroscopy (GEIS) in the frequency range from 100 kHz to 10 Hz at each current density (applying a 10% AC amplitude with respect to the current, limited to a minimum/maximum of 0.1/3.0 A); and for the effective proton conduction resistance ($R^{eff}_{H^+,cath}$) ii) the current was corrected for the ohmic short of the membrane, as well as for the H_2 crossover, both determined in H_2/N_2 (600/150 nccm) at 170 kPa_{abs}, 80°C, and 100% *RH* by applying a constant potential of 0.2, 0.3, 0.4, 0.5, 0.6 and 0.7 V for 2 min each.

Aging of the cathode electrodes was performed at 100 kPa_{abs}, 80°C, 100% *RH*, and H_2/N_2 flows of 200 nccm/75 nccm on anode/cathode, respectively. ASTs were composed of triangular wave modulation between 0.6 and 1.0 V_{RHE} at 50 mV s^{-1}. To avoid reductive currents during voltage-cycling, all residual O_2 was removed from the humidifier and gas line system by a N_2 purging procedure, lasting approximately 45 min.

Results and Discussion

Evaluation of YCl_3 reduction via TGA.—The synthesis of Pt_xY/C alloys, presented in this work, is based on the reduction of an yttrium halide precursor to metallic yttrium using H_2 at elevated temperature and simultaneous alloying with platinum in its vicinity. According to the calculations presented by Roy et al., the reduction of YCl_3 by H_2 at elevated temperature is possible when the evolving HCl gas (according to Equation 1) is constantly removed from the system. To verify the reaction according to Equation 1, the mass change of YCl_3 was monitored vs. temperature in H_2 atmosphere. In contrast

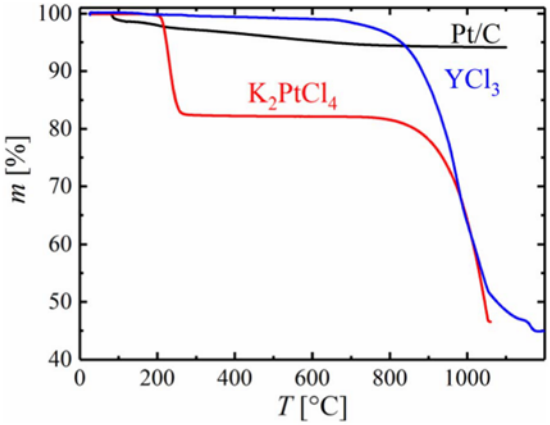

Figure 1. TGA of YCl_3 (blue), K_2PtCl_4 (red) and 20%$_{wt}$ Pt/C (black) showing the mass of the sample, *m*, versus temperature, *T*, at a heating rate of 20 K min^{-1} in 5% H_2 in Ar at a flow rate of 40 mL min^{-1} as reactive gas and 20 mL min^{-1} of Ar as purge gas for the TGA cell.

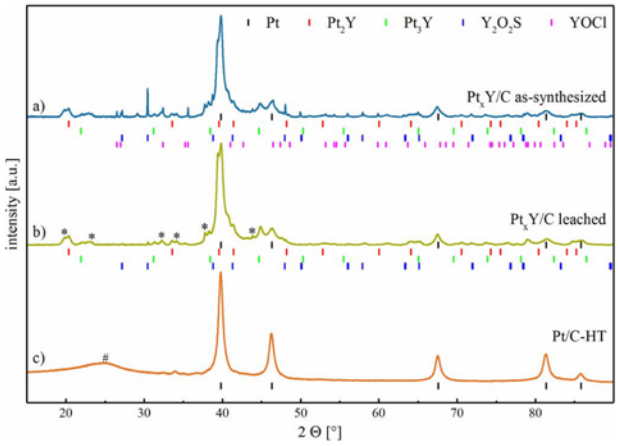

Figure 2. XRD patterns (after background and the angular shift corrections) of the various catalyst powders prepared in this study: a) as-synthesized Pt_xY/C; b) Pt_xY/C after leaching of the as-synthesized material with 1 M H_2SO_4; and, c) heat treated Pt/C catalyst (Pt/C-HT) produced from the same Pt/C material as comparison. The literature *hkl* tick positions are shown for Pt (black),[28] Pt_2Y (red),[29] Pt_3Y (green),[30] Y_2O_2S (blue),[31] and YOCl (magenta).[32] Unidentified reflexes are marked with an asterisk (*), and the hashtag (#) denotes the broad reflex originating from the carbon support (already subtracted for the patterns in a) and in b).

to yttrium halide precursors, the formation of metallic yttrium from many other precursors (e.g., yttrium oxide) occurs at significantly higher temperatures and would not be viable in a similar synthesis procedure.[8]

$$2YCl_3 + 3H_2 \rightarrow 2Y + 6HCl \quad [1]$$

The TGA of YCl_3, provided in Figure 1 (blue line), reveals a total weight loss of 55.0% when the temperature is increased from 25 to 1200°C, which is in excellent agreement with the theoretical loss of 54.5% for the full reduction of YCl_3 to Y (calculated from the stoichiometry of the components and their molar masses, i.e., 195.3, 2.0, 88.9, and 36.5 g mol^{-1} for YCl_3, H_2, Y, and HCl). Even though the mass of the precursor starts to decrease at approximately 800°C, the TGA experiment suggests that the temperature for a complete reduction is >1000°C.

Following this synthesis route for Pt_xY alloys from YCl_3 precursor, Pt_xY/C alloys can either be prepared by co-reduction of YCl_3 and a Pt precursor on carbon or by impregnation of a Pt/C catalyst with YCl_3 and subsequent heat-treatment in a H_2 containing atmosphere. However, in contrast to the high temperature necessary to reduce YCl_3, common platinum precursors are easily reduced to the metal at temperatures on the order of 300°C. As an example, the TGA curve of K_2PtCl_4, provided in Figure 1 (red line), shows a mass loss of 17.8% at ≈270°C, which is in good agreement with the complete reduction to metallic Pt (17.1% mass loss) according to Equation 2 (molar masses of 415.1, 195.1, and 74.6 g mol^{-1} for K_2PtCl_4, Pt, and KCl).

$$K_2PtCl_4 + H_2 \rightarrow Pt + 2KCl + 2HCl \quad [2]$$

We ascribe the additional mass loss in this experiment at temperatures above ≈900°C (red line in Figure 1) to the reduction of KCl to metallic potassium, accompanied by immediate evaporation (the boiling point of potassium is 774°C).

As expected, there is no significant change in the mass of a Pt/C catalyst upon temperature exposure to 1200°C in H_2 (Figure 1, black line), where the small loss (≈6%) can be attributed to the release of water, the removal of minor impurities, and the reduction of surface groups on Pt and carbon in the as-received catalyst. Since the reduction of common Pt precursors is facile and occurs at significantly lower temperatures compared to the formation of metallic Y from YCl_3, the preparation of Pt_xY/C alloys from Pt and YCl_3 precursors does not provide any advantages over the reduction of an yttrium halide salt on a well-known Pt/C catalyst. Therefore, Pt_xY/C catalysts were synthesized based on the reduction of YCl_3 on a commercial 20%$_{wt}$ Pt/C catalyst to simplify the synthesis.

Ex situ catalyst characterization.—Since TGA experiments have shown that the reduction of YCl_3 by H_2 is generally feasible (c.f., Figure 1), Pt_xY/C was prepared by dispersing YCl_3 on a conventional Pt/C catalyst and subsequent heat-treatment in a tube furnace at 1200°C under a flow of 5% H_2 in Ar (500 mL min^{-1}) for 1 h, as described in more detail in the Experimental section. As the melting point of Pt-Y alloys is rather high, ranging between 1000°C (for Y-rich alloys) and 2000°C for Pt-rich alloys,[27] we expected that a comparably high temperature was necessary to ensure sufficient mobility of the metal atoms to form an alloy. According to Greeley et al., Pt_3Y bulk alloys show a high ORR activity,[5] hence a molar ratio of Pt:Y of 3:1 would in principle be desirable for the synthesis. However, quantitative alloying of Y and Pt is unlikely to occur for the here chosen synthesis method, because the YCl_3 precursor was dispersed over the entire Pt/C catalyst, including the carbon support. Therefore, an excess of yttrium compared to the Pt_3Y phase was used in this study (Pt:Y molar ratio of 1:1). The resulting, crystalline Pt-Y alloy phases and side products of the synthesis were analyzed by XRD.

Figure 2a shows the XRD pattern of the as-synthesized Pt_xY/C catalyst (after background and angular shift correction vs. a Si standard), with the respective literature *hkl* tick positions for the identified phases provided below the graph. Phase identification was carried out using the ICDD database. Due to the heterogeneous composition of the sample and the broad, strongly overlapping reflexes in the Pt_xY samples (especially in the range of 40° 2θ), a refinement (*hkl* tick positions or Rietveld refinement) of the diffractogram was not possible. Hence, only the diffractogram of Pt/C-HT was refined for *hkl* tick positions.

As no refinement of *hkl* tick positions for the Pt_xY samples was possible, an exact determination of the phase composition (degree of alloying of Pt with Y in mixed phases) in the as-synthesized and leached Pt_xY/C catalyst was not possible. Nevertheless, it is evident from the XRD patterns provided in Figure 2 that the formation of the desired Pt_2Y and Pt_3Y alloy phases was successful by the reduction of YCl_3 and its simultaneous alloying of Y with Pt at 1200°C. For the heat-treated Pt/C catalyst, lower cell parameters compared to literature (3.921 Å vs. 3.923 Å)[28] were determined by a structure-less refinement using the Lebail method which can be explained by the observation of Solliard et al., who showed that the lattice constant of Pt nanoparticles can be slightly lower compared to bulk materials (Figure 2c).[33] In our

case, the cell parameter of 3.921 Å is in good agreement with literature values for a Pt particle size of approximately 10 nm.[33] This average crystallite size is also in good agreement with the particle size analyzed by TEM, further elaborated upon below (c.f., Figure 3).

Undesired side phases were found in the as-synthesized catalyst, partially identified as Y_2O_2S and YOCl. Especially the formation of Y_2O_2S was unexpected, since no sulfur was intentionally added with the precursors of the synthesis. However, elemental analysis showed that the Vulcan carbon support of the Pt/C catalyst contained approximately $0.5 \pm 0.3\%_{wt}$ sulfur,[34] which was verified to be similar for the platinum containing catalyst ($0.6 \pm 0.2\%_{wt}$ determined by elemental analysis), thereby explaining the occurrence of Y-S phases. The formation of Y_2O_2S at high temperatures (1250°C) in 5% H_2 was also reported by Wang et al., using, amongst others, Y_2O_3 and sulfur as precursors.[35] Interestingly, Y_2O_3 was not found to be the major crystalline side phase at the given reaction conditions, although metallic yttrium is expected to be oxidized upon exposure to ambient air after completion of the synthesis. The formation of YOCl from Y_2O_3 in the presence of Cl_2, was, e.g., reported by Gaviria et al., who studied YOCl formation between 575–975°C.[36] The formation of minor amounts of oxidized yttrium species during the preparation process might originate from the transfer of the sample from the glove box to the tube furnace during which a short air exposure (< 10 s) could not be avoided.

In order to remove the different side phases and leachable non-noble metal cations, the catalyst was washed with sulfuric acid after the synthesis; this is also necessary to avoid a later contamination of the ionomer phase in the MEA with leachable cations, which would negatively affect PEMFC performance. The XRD of the catalyst after leaching in 1 M H_2SO_4 is shown in Figure 2b, including the literature *hkl* tick positions of the identified phases. No change of the reflex positions of Pt and Pt-Y alloy phases was observed after the acid treatment. The YOCl phase was removed quantitatively, while trace amounts of Y_2O_2S remained in the catalyst, indicated mostly by the small reflex at 30.4° 2θ. In addition to the identified phases, minor unknown side phases (marked by an asterisk in Figure 2b) were detected. This unknown phase (or multiple phases) did not match any diffraction pattern of phases containing either Pt, Y, C, O, S, Cl or H found in the ICDD database. While we cannot quantify the weight fractions of the various phases from the XRD data, they nevertheless indicate that the Pt_xY alloy phases and the remaining Pt phase are the majority constituents of the final catalyst. At the same time, elemental analysis of the leached catalyst showed that the total amount of yttrium decreased from $5\%_{wt}$ to $3\%_{wt}$, whereas the platinum quantity remained unchanged at $19\%_{wt}$, which corresponds to an average molar ratio of Pt:Y of ≈3:1, suggesting that at least a major fraction of the leached catalyst contains Pt_3Y and Pt_2Y phases (further on referred to as leached Pt_xY/C catalyst).

Particle size distribution of Pt_xY/C.—The leached Pt_xY/C catalyst prepared by the synthesis method described earlier (1200°C, H_2, 1 h, leached in 1 M H_2SO_4), was imaged by TEM in order to analyze its particle size distribution and dispersion on the carbon support. As comparison, the particle size distribution of a Pt/C catalyst heat treated in the absence of an yttrium precursor was evaluated (Pt/C-HT). The heat-treatment procedure for this reference catalyst was prolonged to 10 h in order to achieve a similar average particle size compared to the Pt_xY/C catalyst. As shown in Figures 3a and 3b, the Pt and Pt_xY particles of these two catalysts span a broad range of particle sizes from ≈4 nm to more than 30 nm, with the majority of particles in both cases having a diameter on the order of 10 nm.

The number-averaged ($\bar{d}_N$) and surface-averaged ($\bar{d}_S$) diameters were calculated according to Equations 3 and 4 for the two catalysts.

$$\bar{d}_N = \frac{\sum_{i=1}^{n} l_i d_i}{\sum_{i=1}^{n} l_i} \quad [3]$$

$$\bar{d}_S = \frac{\sum_{i=1}^{n} l_i d_i^3}{\sum_{i=1}^{n} l_i d_i^2} \quad [4]$$

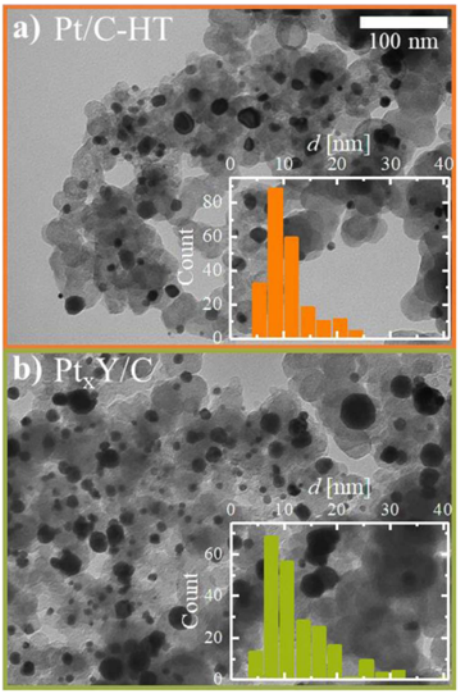

Figure 3. TEM images at a magnification of 52000x and representative particle size distribution (insets) of: a) heat treated $20\%_{wt}$ Pt/C catalyst referred to as Pt/C-HT (prepared at 1200°C in 5% H_2 in Ar for 10 h); b) Pt_xY/C catalyst after leaching (prepared at 1200°C in 5% H_2 in Ar for 1 h and subsequent leaching in 1 M H_2SO_4).

On the one hand, both catalysts had a very similar number-averaged diameter of $\bar{d}_N$ = 11 and 12 nm for Pt/C-HT and Pt_xY/C, respectively. On the other hand, the broader particle size distribution and especially the presence of several very large particles in the Pt_xY/C catalyst (≈30 nm) resulted in a substantially larger surface-averaged particle size of $\bar{d}_S$ = 21 nm compared to that of 14 nm for the Pt/C-HT catalyst. Hence, the particle size of these catalysts is substantially larger than that of the $20\%_{wt}$ Pt/C precursor (TEC10V20E, $\bar{d}_N$ = 2.8 nm[17] and $\bar{d}_S$ = 3.2 nm). The larger surface-averaged particle diameter of the Pt_xY/C catalyst might either originate from the alloying of the platinum nanoparticles with yttrium as opposed to the simple temperature-driven coalescence of platinum nanoparticles in the case of the Pt/C-HT catalyst, but may also be due to the fact that a single large particle can lead to a substantial increase in the calculated value of $\bar{d}_S$, so that its quantification from TEM image analysis is prone to large errors, even when counting several hundred particles. Despite this experimental uncertainty, $\bar{d}_S$ may be used to estimate the *ECSA* based on the surface and volume of a sphere according to Equation 5:

$$ECSA = \frac{6}{\bar{d}_S \cdot \varrho} \quad [5]$$

For the Pt/C-HT catalyst (ϱ = 21.5 g cm^{-3}), this results in an estimated *ECSA* of ≈20 $m^2_{Pt}\ g^{-1}_{Pt}$, compared to ≈85 $m^2_{Pt}\ g^{-1}_{Pt}$ for the commercial $20\%_{wt}$ Pt/C catalyst which was used as precursor. Similarly, we can estimate the *ECSA* of the Pt_xY/C catalyst by assuming an average particle density of ϱ = 15.8 g cm^{-3} (calculated from the crystallographic densities of Pt_2Y (14.9 g cm^{-3}) and Pt_3Y (16.7 g cm^{-3})), predicting a similar *ECSA* of ≈18 $m^2_{Pt}\ g^{-1}_{Pt}$. However, it should be noted, that these numbers present only a rough estimate of the *ECSA*, since Equation 5 assumes perfect spherical particles, a statistically significant particle size distribution (difficult for broad size distributions), and that the contact area between nanoparticles and the support is essentially zero.

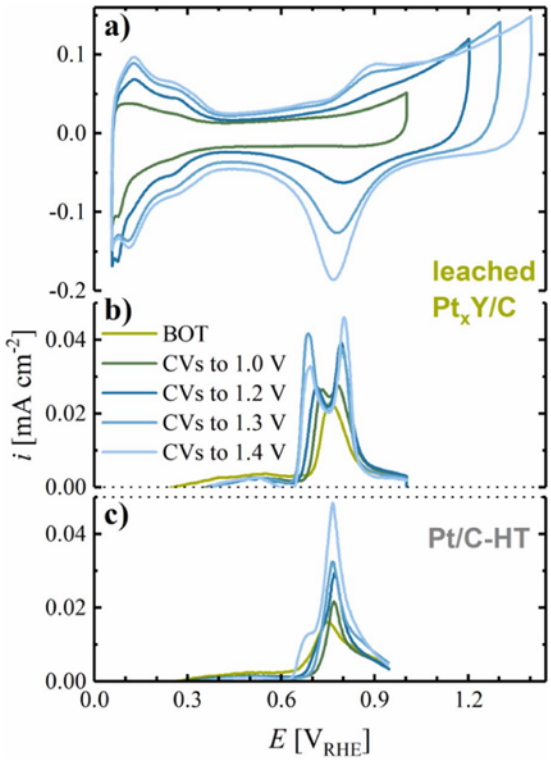

Figure 4. a) Steady-state CVs of the leached Pt_xY/C catalyst in stagnant, deaerated 0.1 M $HClO_4$ at room temperature with a scan rate of 50 mV s^{-1}, a lower potential limit of 0.05 V_{RHE}, and an upper potential limit of 1.0, 1.2, 1.3 or 1.4 V_{RHE}. The measurement consisted of 50 cycles in each potential window, for which only the steady-state CV is shown. b) Baseline-corrected CO stripping voltammograms of the same Pt_xY/C catalyst at a scan rate of 10 mV s^{-1} from 0.06 to 1.00 V_{RHE}. CO stripping was carried out at beginning-of-test (BOT) and after 50 cycles to the respective upper potential limit (shown in the same color). The catalyst was prepared by heat-treatment at 1200°C for 1 h and leached in 1 M H_2SO_4 prior to the measurement. c) Baseline-corrected CO stripping voltammograms of Pt/C-HT prepared by heat-treatment of the 20%$_{wt}$ Pt/C catalyst at 1200°C for 10 h.

Even though the ORR overpotential is expected to increase with decreasing *ECSA*, a higher specific activity of the Pt_xY/C catalyst might yield a comparable or better ORR mass activity as a high surface area Pt/C catalyst, while also providing significantly enhanced stability due to the high thermodynamic stability of large particles. Therefore, the following electrochemical analysis of the prepared catalysts focuses on the evaluation of the *ECSA*, ORR activity, and catalyst stability over the course of a voltage-cycling AST.

ECSA determination via CO stripping.—Electrochemical evaluation of the leached Pt_xY/C catalyst was first performed by cyclic voltammetry in an RDE setup in 0.1 M $HClO_4$, and steady-state CVs for different potential windows are shown in Figure 4a. When initially limiting the upper potential to 1.0 V_{RHE}, the CV of Pt_xY/C shows rather undefined H_{upd} features, with only a broad peak in the potential region from 0.05 to ≈0.30 V_{RHE}, while the formation of surface oxide species above ≈0.8 V_{RHE} is suppressed. Surface oxide formation in the anodic scan is only observed upon opening the upper potential window to 1.2 V_{RHE}, with the corresponding reduction feature at 0.8 V_{RHE}; at the same time, more pronounced H_{upd} features appear in the hydrogen adsorption/desorption regime. The occurrence of H_{upd} peaks may suggest the liberation/formation of Pt sites on the surface of the catalyst, e.g., due to restructuration of the surface, leaching of yttrium from the surface, and/or cleaning of Pt sites from adsorbates. The surface (hydr-)oxide formation charge below 1.2 V_{RHE} and the H_{upd} charge still increase significantly when the upper potential window is increased to 1.3 V_{RHE}, while a further increase of the upper potential limit to 1.4 V_{RHE} is not anymore accompanied by a significant increase in the H_{upd} area.

CO stripping was performed after each cycling step to identify the development of the *ECSA*, as well as to obtain a more elaborate understanding of the surface properties of the Pt_xY/C catalyst. In the CO stripping at beginning-of-test (BOT), i.e., after dipping the electrode into the electrolyte and applying a potential of 0.06 V_{RHE} to adsorb CO, the first anodic scan shows a single oxidative peak at ≈0.76 V_{RHE} (green line in Figure 4b), while the CO oxidation wave separates into two distinct features after 50 cycles with an upper potential limit of 1.0 V_{RHE} (dark green line in Figure 4b). After 50 cycles (each) first to 1.2, then 1.3, and finally to 1.4 V_{RHE}, the CO peaks further separate, reaching constant peak positions at 0.69 and 0.80 V_{RHE} when cycling to ≥1.3 V_{RHE}. Similar to the leached Pt_xY/C catalyst, the Pt/C-HT catalyst, heat treated in 5% H_2 (at 1200°C for 10 h), shows a single CO stripping peak at ≈0.75 V_{RHE} at BOT (green line in Figure 4c). After 50 cycles to 1.0 V_{RHE} this CO stripping peak shifts slightly to 0.77 V_{RHE}, with its position remaining unaltered when cycling to higher upper potential limits. The similarity of the CO stripping voltammograms of Pt/C-HT and the leached Pt_xY/C at BOT and the differences evolving after 50 cycles to higher potentials suggest that cycling to at least 1.2 V_{RHE} is required to clean the catalyst surface from contaminants/adsorbates originating from the synthesis process (this is the reason why 50 cycles to 1.2 V_{RHE} were chosen as activation procedure; see Experimental section). Furthermore, the separation of the CO oxidation features into two peaks on the Pt_xY/C catalyst and the peak position differences compared to Pt/C-HT after cycling to ≥1.2 V_{RHE} provides electrochemical evidence for the incorporation of Y into the Pt structure. The occurrence of two individual CO oxidation waves on Pt_xY/C could be rationalized by several phenomena: i) the presence of different crystal facets on the Pt_xY/C catalyst with different reactivity toward the oxidation of CO; ii) the partial formation of a Pt-enriched shell on the bimetallic alloy core induced by the potential cycling procedure; and/or, iii) the occurrence of several alloy phases of Pt and Y. While we cannot exclude any of the hypotheses, the latter is supported by the XRD diffractograms discussed earlier (c.f., Figure 2b).

Interestingly, none of the CO stripping features of the leached Pt_xY/C coincides with the peak potential for CO oxidation on the heat treated Pt/C-HT catalyst. We therefore conclude that most Pt nanoparticles in the Pt_xY/C catalyst are, at least partially, influenced by the presence of yttrium, e.g., due to partial incorporation of yttrium into the platinum lattice. Thus, the CO oxidation wave at the more positive potential may represent Pt nanoparticles with small amounts of yttrium. This is supported by the decrease in the relative intensity of the CO stripping wave at low potential compared to that at high potential when cycling to 1.4 V_{RHE}, where a loss of yttrium due to dealloying would be expected. Hence, the evolution of the CO stripping waves upon potential cycling indicates both, the presence of different Pt_xY phases in the prepared catalyst and an enrichment of Pt on the surface of the particles due to leaching of Y. Nevertheless, to the best of our knowledge, no CO stripping data on well-defined Pt_xY alloys was reported in the literature, hence no unambiguous assignment of the two CO stripping peaks to specific Pt_xY phases can be carried out.

Since the hydrogen ad- and desorption process on Pt_xY alloys is not well-characterized and might therefore not be a reasonably accurate measure of the catalysts' *ECSA*, the charge originating from CO stripping was utilized to evaluate the surface area of the prepared catalysts. Due to its large average particle size (c.f., Figure 3), the *ECSA* of Pt_xY/C determined by CO stripping is rather small, amounting to 13 ± 2 $m^2_{Pt}\ g^{-1}_{Pt}$ after pre-cycling to 1.0 V_{RHE} and reaching 16 ± 1 $m^2_{Pt}\ g^{-1}_{Pt}$ after pre-cycling to ≥1.3 V_{RHE} (see Figure 6a); the latter is in quite good agreement with the *ECSA* value determined by TEM analysis (≈18 $m^2_{Pt}\ g^{-1}_{Pt}$). These CO stripping derived *ECSA* values are comparable to those obtained for the heat treated Pt/C-HT catalyst (7 ± 1 $m^2_{Pt}\ g^{-1}_{Pt}$ after pre-cycling to 1.0 V_{RHE} and 13 ± 1 $m^2_{Pt}\ g^{-1}_{Pt}$ after

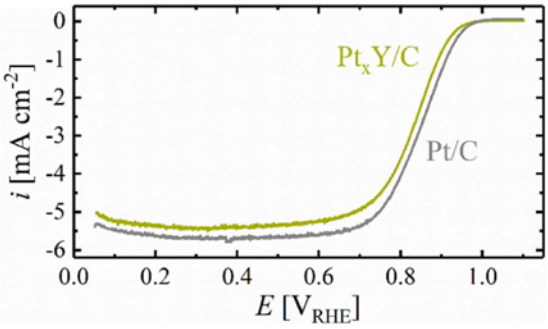

Figure 5. Steady-state anodic voltammetric scan (10 mV s^{-1}) in O_2-saturated 0.1 M $HClO_4$ at room temperature and a rotation rate of 1600 rpm, comparing leached Pt$_x$Y/C (prepared under 5% H_2 at 1200°C for 1 h) with commercial 20%$_{wt}$ Pt/C (i.e., not heat treated) at a loading of 8.7 and 9.3 μg_{Pt} cm^{-2}, respectively. The ohmic resistance measured by EIS was ≈35 Ω, however, the data shown in the figure are not *iR* corrected. Prior to determination of the ORR activity, the electrodes were subjected to 50 potential cycles between 0.05 and 1.20 V$_{RHE}$ at a scan rate of 50 mV s^{-1}.

pre-cycling to 1.4 V$_{RHE}$), but are of course much smaller than those obtained for the commercial 20%$_{wt}$ Pt/C catalyst (74 ± 2 m^2_{Pt} g^{-1}_{Pt}).[34]

ORR activity in RDE.—To identify the suitability of the catalyst for the incorporation into the cathode of a PEMFC, and then to optimize the electrochemical cleaning procedure, the catalyst ORR activity was assessed in O_2-saturated 0.1 M $HClO_4$ in an RDE setup. The anodic scans of the leached Pt$_x$Y/C (green line), as well as of a commercial 20%$_{wt}$ Pt/C catalyst (gray line) are shown in Figure 5 for comparable Pt loadings (8.7 and 9.3 μg_{Pt} cm^{-2}, respectively), with the expected limiting current on the order of 5.5–6.0 mA cm^{-2}.[37] Quite clearly, compared to the commercial Pt/C catalyst, the ORR mass activity of the Pt$_x$Y/C catalyst after preceding cleaning cycles to 1.2 V$_{RHE}$ is significantly lower.

To extract the ORR activity of the catalysts, the potential was corrected for the ohmic drop (measured via EIS at OCV in O_2-saturated electrolyte). Subsequently, the measured current was extracted at 0.9 V$_{RHE}$ and corrected for the capacitive contribution (determined from a CV in Ar-saturated electrolyte at the same potential), as well as for the depletion of the O_2-concentration in the vicinity of the electrode according to Equation 6.

$$i_{kin} = \frac{i \cdot i_{lim}}{i_{lim} - i} \qquad [6]$$

Here, i is the measured current, i_{kin} is the calculated kinetic ORR current, and i_{lim} is the measured limiting current.

Despite the fact that the specific ORR activity of the leached Pt$_x$Y/C before cycling activation (310 ± 40 μA cm^{-2}_{Pt}, Figure 6b) was similar to that of Pt/C (385 ± 40 μA cm^{-2}_{Pt}, gray bar in Figure 7b), its ≈6 times lower *ECSA* (11 ± 2 m^2_{Pt} g^{-1}_{Pt}, Figure 6a) resulted in a low ORR mass activity of only 36 ± 12 A g^{-1}_{Pt} (Figure 6b) compared to the as-received commercial 20%$_{wt}$ Pt/C catalyst (270 ± 5 A g^{-1}_{Pt}, gray bar in Figure 7b). In the course of activation by potential cycling, a clear increase of the specific, as well as of the mass activity of Pt$_x$Y/C was observed. The maximum activity was obtained for an upper cycling limit of 1.2 or 1.3 V$_{RHE}$, where the slight increase in the *ECSA* to 14 ± 2 m^2_{Pt} g^{-1}_{Pt}, along with a significant increase in the specific ORR activity to 740 ± 170 μA cm^{-2}_{Pt} resulted in a mass activity of 106 ± 35 A g^{-1}_{Pt}. It is well known in the literature that bimetallic alloys of Pt and other transition metals (e.g., Co, Ni, Cu) tend to form a Pt-enriched shell on an alloy core when exposed to repeated voltammetric oxidation/reduction cycles.[38] Accordingly, the initial increase of $i^{spec}_{0.9\ V}$ and $i^{mass}_{0.9\ V}$ is likely due to a combination of cleaning of the surface from contaminants originating from the synthesis procedure and of surface restructuration of the

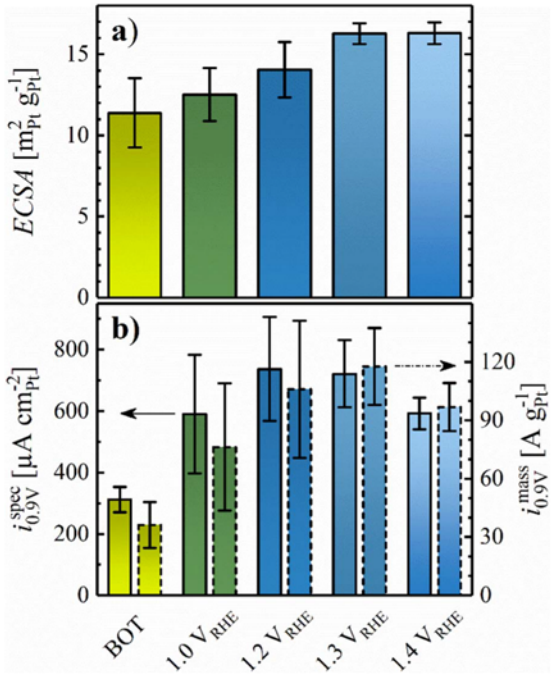

Figure 6. a) *ECSA* as a function of the upper potential limit in preceding cleaning CVs (50 cycles at 50 mV s^{-1} between 0.05 V$_{RHE}$ and the marked upper potential limit at 25°C) for the leached Pt$_x$Y/C catalyst evaluated from CO stripping, using a specific charge of 420 μC cm^{-2}. b) Specific ORR activity (bars with solid lines, left y-axis) and ORR mass activity (bars with dashed lines, right y-axis) at 0.9 V$_{RHE}$ as a function of the upper potential limit in preceding cleaning CVs. Error bars represent the standard deviation of at least 2 measurements.

nanoparticles to form a Pt-enriched overlayer. Even though the *ECSA* remained reasonably constant when cycling to 1.4 V$_{RHE}$, the specific and mass activity of the Pt$_x$Y/C catalyst decreased due to leaching of Y from the catalyst particles, indicated by the above discussed shift in the intensity of the CO oxidation features in Figure 4b. Since the activity after cycling to 1.2 or 1.3 V$_{RHE}$ was comparable, activation of all catalysts described further on in this manuscript was carried out by 50 potential cycles with an upper potential limit of 1.2 V$_{RHE}$ in order to avoid extended exposure of the carbon support to high anodic potentials and yttrium leaching.

Figure 7 shows a comparison of the *ECSA* (Figure 7a) and the ORR activity (Figure 7b) for Pt$_x$Y/C (as-synthesized, blue), Pt$_x$Y/C (leached, green), commercial 20%$_{wt}$ Pt/C (gray), and the heat treated Pt/C-HT (orange). As already indicated, the particle size (c.f., Figure 3) of the Pt$_x$Y/C catalyst is relatively large, resulting from the high synthesis temperature necessary to achieve the complete reduction of YCl_3 and alloying of the two metals. Therefore, both the leached and the as-synthesized catalyst show a significantly smaller *ECSA* compared to Pt/C (70 ± 10 m^2_{Pt} g^{-1}_{Pt}), which is comprised of Pt nanoparticles with an average diameter of ≈3 nm.[17] Similar to the Pt$_x$Y/C catalysts, the *ECSA* of Pt/C-HT was very low (7 ± 1 m^2_{Pt} g^{-1}_{Pt}), reflecting a similarly dramatic particle growth.

While the particle growth upon heat-treatment of Pt/C triggered a moderate increase in the specific ORR activity of this catalyst from 385 ± 40 μA cm^{-2}_{Pt} to 440 ± 30 μA cm^{-2}_{Pt} (gray vs. orange bars in Figure 7b), as one would expect from the literature,[39] the introduction of yttrium leads to a significant enhancement of the specific ORR activity of the as-synthesized Pt$_x$Y/C catalyst (680 ± 40 μA cm^{-2}_{Pt}, blue bars in Figure 7b). As expected, chemical pre-treatment in sulfuric acid did not alter the catalytic properties of Pt$_x$Y/C significantly (740 ± 170 μA cm^{-2}_{Pt}, green bars in Figure 7b), since all catalysts had been subjected to potential cycling in the acid electrolyte for these

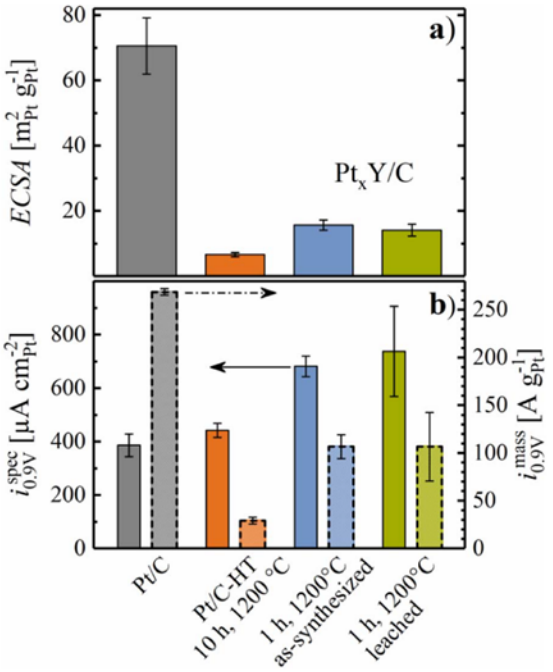

Figure 7. a) *ECSA* of Pt/C, Pt/C-HT, as-synthesized and leached Pt_xY/C after activation by 50 potential cycles between 0.05 and 1.20 V_{RHE} at 50 mV s^{-1} and 25°C, evaluated from CO stripping in RDE, using a specific charge of 420 μC cm^{-2}. b) Specific ORR activity (bars with solid lines, left y-axis) and ORR mass activity (bars with dashed lines, right y-axis) at 0.9 V_{RHE}. Error bars represent the standard deviation of at least 2 independent measurements.

RDE experiments, where leaching of yttrium does not negatively affect performance (in contrast to what one would expect in an MEA, where the proton inventory is limited). In summary, a clear beneficial effect for the introduction of yttrium to Pt/C regarding $i^{spec}_{0.9\ V}$ was identified in this study, but the small *ECSA* of Pt_xY/C resulted in a low $i^{mass}_{0.9\ V}$ (106 ± 35 A g^{-1}_{Pt} for the leached catalyst) compared to the commercial Pt/C catalyst (270 ± 5 A g^{-1}_{Pt}); on the other hand, $i^{mass}_{0.9\ V}$ of the Pt_xY/C catalyst is substantially larger if compared to the Pt/C-HT catalyst with similarly large particles (30 ± 4 A g^{-1}_{Pt}, orange bar in Figure 7b).

The superior specific ORR activity of Pt_xY/C is similar to that reported by Brandiele et al., whereas this group reported additionally an approximately 3x higher ORR mass activity compared to Pt/C due to a smaller average particle size (≈5 nm) resulting from a significantly lower reaction temperature of 600°C compared to our study.[7] The Pt_xY/C catalyst presented by Roy et al. showed a similar improvement of the specific ORR activity over Pt/C, with a slightly improved ORR mass activity.[8] As a comparison, the data from the literature and from this study is summarized in Table I. While the enhancement factor of the specific ORR activity is very similar in all cases, the absolute values deviate significantly. This is partially due to the utilization of different scan rates, since higher scan rates lead to higher current densities at 0.9 V_{RHE}.[37] Furthermore, the referenced data was not corrected for capacitive effects, which becomes increasingly relevant at high scan rates.

Even though the low mass activity of the Pt_xY/C catalyst appears to be disadvantageous, the large particle size is expected to provide a superior stability when exposed to a voltage-cycling AST in a PEMFC.

Voltage-cycling stability and performance of Pt_xY/C in a PEMFC.—The commercially available 20%$_{wt}$ Pt/C catalyst, the heat treated Pt/C-HT catalyst, and the leached Pt_xY/C catalyst were tested in 5 cm^2 MEAs with respect to their stability over 30000 triangular potential scans at 50 mV s^{-1} between 0.6 and 1.0 V_{RHE} under H_2/N_2 flows (200 nccm/75 nccm) at the anode/cathode at 100 kPa_{abs}, 80°C, and 100% *RH*, following a previously published procedure.[17] Note that MEA tests were only carried out with leached catalysts in order to avoid ionic contamination of the ionomer/membrane. The *ECSA* was determined by CO stripping for Pt_xY/C and Pt/C-HT, since this yields a more reliable estimate of the *ECSA* for small electrode *rf* values, and since the correlation between *ECSA* and H_{UPD} charge is not clear for Pt_xY alloys.

Figure 8 shows the *ECSA* evolution over the course of extended voltage-cycling, either in terms of absolute *ECSA* values (Figure 8a) or normalized to the maximum *ECSA* value recorded for each catalyst (Figure 8b). For Pt_xY/C and Pt/C-HT, an activation procedure consisting of 50 potential cycles between 0.07 and 1.20 V_{RHE} (based on the above described experiments in liquid electrolyte; the lower potential limit was increased by 20 mV to limit the hydrogen evolution reaction (HER) current and the temperature was raised to 40°C) was applied after having executed an initial voltage-controlled MEA conditioning procedure (see Experimental section); the commercial Pt/C catalyst was only subjected to the ramp-in procedure. First of all, the large difference in particle size of the catalysts is reflected in their respective *ECSA*. Compared to the as-received Pt/C catalyst (68 ± 1 $m^2_{Pt}\ g^{-1}_{Pt}$, after conditioning, Figure 8a, gray circles), the *ECSA* after heat-treatment at 1200°C in 5% H_2 (Pt/C-HT) was significantly lower at BOT (7 ± 1 $m^2_{Pt}\ g^{-1}_{Pt}$, Figure 8a, orange circles), which agrees well with the values obtained in liquid electrolyte (7 ± 1 $m^2_{Pt}\ g^{-1}_{Pt}$, Figure 7a). Note that both MEA conditioning and activation by 50 cycles between 0.07 and 1.20 V_{RHE} had no influence on the *ECSA* of the Pt/C-HT catalyst. The *ECSA* of the Pt_xY/C catalyst at BOT (12 ± 1 $m^2_{Pt}\ g^{-1}_{Pt}$), as well as its increase to 16 ± 1 $m^2_{Pt}\ g^{-1}_{Pt}$, observed after the MEA conditioning procedure (potential holds between OCV and 0.6 V) match well with the above reported trend of increasing surface area upon catalyst activation in RDE experiments (13 ± 2 $m^2_{Pt}\ g^{-1}_{Pt}$ after cycling between 0.05 and 1.00 V_{RHE}). This initial surface area increase upon MEA conditioning could, in principle, be attributed to the following phenomena: i) a better catalyst layer utilization (e.g., due to water release during ORR); ii) the cleaning of the catalyst surface from adsorbates/impurities; and/or, iii) partial restructuration of the bimetallic surface. However, as no *ECSA* increase was observed for Pt/C-HT, the *ECSA* gain upon MEA conditioning of the Pt_xY/C catalyst is most likely related to the latter two effects. Since the cathode *ECSA* of Pt_xY/C did not further increase after the voltammetric

Table I. Characteristic data for Pt_xY/C catalysts, including heat-treatment temperature (*T*) and time (*t*), number-averaged particle size ($\bar{d}_N$), *ECSA*, $i^{spec}_{0.9\ V}$, $i^{mass}_{0.9\ V}$, and the enhancement factor of the specific ORR activity (f_{spec}) and ORR mass activity (f_{mass}) compared to the Pt/C reference. The data from this study represents the leached Pt_xY/C catalyst, activated by 50 cycles between 0.05 and 1.20 V_{RHE} at 50 mV s^{-1} and measured in O_2-saturated 0.1 M $HClO_4$ at 25°C, 10 mV s^{-1} and 1600 rpm. The data was corrected for the ohmic drop, for capacitive effects and for the depletion of O_2. Brandiele et al. recorded the data at 20 mV s^{-1} and Roy et al. used 50 mV s^{-1}.

Source	*T* °C	*t* h	$\bar{d}_N$ nm	*ECSA* $m^2_{Pt}\ g^{-1}_{Pt}$	$i^{spec}_{0.9\ V}$ μA cm^{-2}_{Pt}	f_{spec} -	$i^{mass}_{0.9\ V}$ A g^{-1}_{Pt}	f_{mass} -
This study	1200	1	12	14 ± 2	740 ± 170	1.9	106 ± 35	0.4
Brandiele et al.[7]	600	5	4	33	1570	1.7	586	2.9
Roy et al.[8]	800	6	12	21	2000	2.0	410	1.5

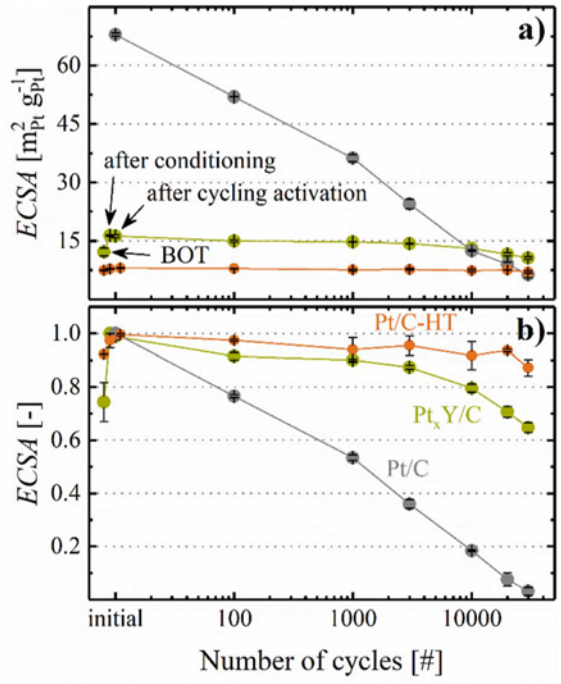

Figure 8. a) Absolute and b) normalized cathode *ECSA* for all tested MEAs over the course of a voltage-cycling AST, determined by CO stripping for leached Pt_xY/C (green circles) and heat treated Pt/C-HT (orange circles); the *ECSA* development for the commercial 20%$_{wt}$ Pt/C (gray circles) was taken from Harzer et al.[17] AST conditions: triangular potential scan between 0.6 and 1.0 V_{RHE} at 50 mV s^{-1}, conducted under H_2/N_2 flows (200 nccm/75 nccm) at the anode/cathode at 100 kPa$_{abs}$, 80°C, and 100% *RH*. The cathode Pt loadings were 0.12 mg$_{Pt}$ cm^{-2} (± 5%) for the Pt_xY/C and Pt/C-HT cathodes and 0.10 mg$_{Pt}$ cm^{-2} (± 5%) for the Pt/C cathodes; error bars represent the mean absolute deviation of two independent measurements. "BOT" refers to the *ECSA* values obtained prior to MEA conditioning, and "after cycling" refers to the *ECSA* values obtained after MEA conditioning (see Experimental section) and after 50 voltage cycles at 50 mV s^{-1} between 0.07 and 1.20 V_{RHE} at 40°C.

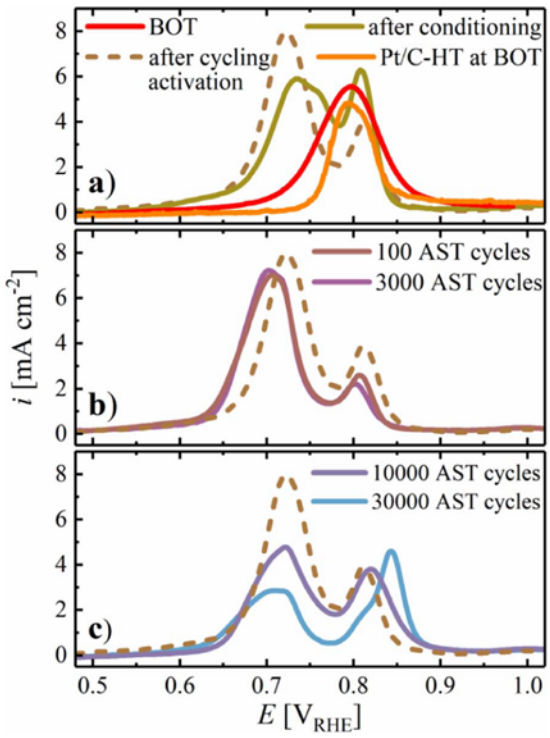

Figure 9. a) Baseline-corrected CO stripping voltammograms of the leached Pt_xY/C catalyst in 5 cm^2 MEAs at BOT, after MEA conditioning by a voltage-controlled ramp-in procedure, and after catalyst cycling activation (50 cycles at 50 mV s^{-1} between 0.07 and 1.20 V_{RHE} at 40°C) compared to Pt/C-HT at BOT. b-c) CO stripping voltammograms of the Pt_xY/C catalyst after different numbers of voltage-cycles throughout the voltage-cycling AST shown in Figure 8, with the CO stripping voltammogram of the cycling activated Pt_xY/C catalyst plotted for reference (brown dashed line). CO stripping was performed at 100 mV s^{-1} with an upper potential limit of 1.1 V_{RHE} at 40°C and 150 kPa$_{abs}$, whereby CO (10% in N_2) was adsorbed for 10 min at a flow rate of 100 nccm while holding the cathode potential at 0.1 V_{RHE}.

cycling activation, we conclude that the MEA conditioning procedure is sufficient to completely activate the Pt_xY/C catalyst. Nevertheless, even though this suggests that no additional catalyst activation by potential cycling to 1.2 V_{RHE} would be necessary for Pt_xY/C, the later discussed CO stripping voltammetry analysis will show that the surface composition of the Pt_xY alloy still changes significantly upon cycling activation.

Over the course of the voltage-cycling AST, the *ECSA* of the commercial 20%$_{wt}$ Pt/C catalyst decreased rapidly due to Ostwald ripening and Pt loss into the ionomer phase,[40] leaving less than 5% of the initial *ECSA* after 30000 cycles (s. Figure 8b). As one would expect based on their large particle size (s. Figure 3), the surface area retention of Pt/C-HT and Pt_xY/C over 30000 voltage cycles is substantially better, owing to the higher stability of large particles towards Pt dissolution.[41] We hypothesize that the relatively stronger *ECSA* loss of the Pt_xY/C catalyst (≈35%) compared to the Pt/C-HT catalyst (≈15%) over 30000 cycles mainly results from the lower initial *ECSA* of Pt/C-HT. Therefore, the *ECSA* loss data in Figure 8b do not provide any evidence for a superior stability of Pt_xY alloys compared to pure Pt, which previously had been proposed by Greeley et al.,[5] whose calculations indicated a high stability of Pt_xY alloys due to their beneficial electronic interaction.

To further investigate the properties of the catalyst surface upon MEA conditioning and cycling activation, CO stripping was performed at BOT and after selected intervals of the voltage-cycling AST for Pt/C-HT and Pt_xY/C. The CO stripping voltammograms are shown in Figure 9, separated into different activation/aging intervals. Figure 9a shows a single CO stripping peak for the Pt_xY/C catalyst at BOT (red line) with a current peak at 0.8 V_{RHE}, which is in good agreement with the CO stripping peak position of the Pt/C-HT catalyst at BOT (orange line). In accordance with the CO stripping measurements performed in liquid electrolyte (Figure 4b), the CO stripping peak of Pt_xY/C separates into two distinct peaks after MEA conditioning (green line in Figure 9a), with maxima at 0.73 and 0.81 V_{RHE} (vs. 0.69 and 0.80 V_{RHE} in Figure 4b; note that these lower CO stripping potentials are likely due to the slower scan rate of 10 mV s^{-1}). The analysis shows that at least a few voltage cycles that are part of the MEA conditioning procedure (see Experimental) are required to clean and restructure the surface of the Pt_xY/C catalyst to approach the steady-state surface properties of the Pt_xY/C alloy. As discussed earlier, the identification of the exact origin of the single CO stripping peak at BOT is not trivial, but we hypothesize that it is caused by residual contaminations from the synthesis. This hypothesis is supported by the fact that the CO stripping peak of the Pt/C-HT catalyst at BOT occurs at the same peak position, but does not separate into two individual peaks after the activation procedure or upon voltage-cycling (data not shown, but analogous to those in Figure 4c).

After cycling activation of the Pt_xY/C catalyst (50 cycles at 50 mV s^{-1} between 0.07 and 1.20 V_{RHE} at 40°C), the overall *ECSA* remained constant (Figure 8), but the ratio of the two peaks changed in favor of the peak at low potentials (dashed brown line in Figure 9a). Similar to the measurements performed in liquid electrolyte (Figure 4b), this trend indicates a restructuration of the catalyst surface. This hypothesis is supported later on by an increase in the Pt_xY/C ORR

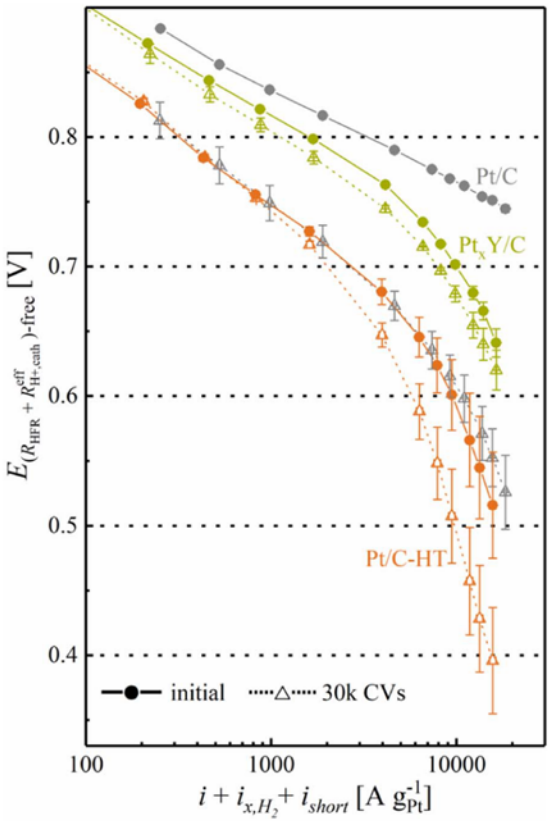

Figure 10. Tafel representation of the H_2/O_2 polarization curves of 5 cm^2 MEAs based on cathodes with the leached Pt_xY/C and the heat treated Pt/C-HT catalysts (at Pt loadings of 0.12 mg_{Pt} cm^{-2}) after MEA conditioning and cycling activation (solid lines and full symbols) and after 30000 AST cycles (dashed lines and open symbols); the data points for the commercial 20%$_{wt}$ Pt/C catalyst (gray color; Pt loading of 0.10 mg_{Pt} cm^{-2}) were taken from Harzer et al.[17] The current was first corrected for hydrogen crossover and electrical shorting currents, and then normalized to the mass of platinum in the cathode catalyst layer. The voltage was corrected for the ohmic resistance (R_{HFR}) and the effective proton conduction resistance ($R^{eff}_{H^+,cath}$). Error bars represent the mean absolute deviation of two independent measurements. AST conditions: triangular potential scan between 0.6 and 1.0 V_{RHE} at 50 mV s^{-1}, conducted under H_2/N_2 flows (200 nccm/75 nccm) at the anode/cathode at 100 kPa_{abs}, 80°C, and 100% *RH*. Polarization curve conditions: H_2/O_2 (2000/5000 nccm), 80°C, 100% *RH*, and 170 kPa_{abs}.

mass activity. The relative ratio of these two CO stripping peaks after cycling activation remains essentially constant over the initial 100 and 3000 AST voltage cycles (Figure 9b), during which also the *ECSA* remains constant (see Figure 8). After 10000 and 30000 AST cycles which are accompanied by a significant loss of *ECSA* compared to 3000 cycles (see Figure 8), the relative intensity of the CO stripping peak at higher potential gradually increases again compared to that at lower potential (Figure 9c). As described earlier for the CO stripping peaks in liquid electrolyte, we hypothesize that these changes originate from leaching of yttrium due to a certain degree of voltage-cycling induced dealloying.

PEMFC performance after a voltage-cycling AST.—The Tafel representation of the differential flow H_2/O_2 polarization curves at 80°C, 100% *RH*, 170 kPa_{abs} before and after 30000 AST cycles are shown in Figure 10, whereby the following corrections to the measured current and voltage were made (for details see Orfanidi et al.):[34] i) correction of the current for the H_2 crossover current (≈5 mA cm^{-2}) and the shorting current (corresponding to a resistance of ≈6 kΩ cm^2), determined at the same conditions with N_2 on the cathode; ii) subsequently, the current was normalized to the mass of platinum in the cathode catalyst layer; iii) correction of the measured voltage for the *HFR* representing the ohmic resistance of the membrane and electric contact resistances; and, iv) voltage correction for the effective proton conduction resistance in the cathode catalyst layer ($R^{eff}_{H^+,cath}$), based on the proton conduction resistances measured by EIS ($R_{H^+,cath}$ values were 31 ± 11 mΩ cm^2 for Pt/C, 34 ± 6 mΩ cm^2 for Pt/C-HT, and 38 ± 4 mΩ cm^2 for Pt_xY/C).

Solid lines/symbols represent the performance after MEA conditioning and cycling activation between 0.07 and 1.20 V_{RHE} for the Pt/C-HT (orange) and the Pt_xY/C (green) based cathodes; cathodes with commercial 20%$_{wt}$ Pt/C catalyst (gray) were solely conditioned. Prior to the AST, the voltage profile of the commercial Pt/C cathodes in Figure 10 follows a straight line with a Tafel slope of 70 ± 1 mV dec^{-1} throughout the entire measurement range. On the other hand, the cathodes with heat treated Pt/C-HT have a substantially lower performance even at low current density, dropping dramatically with increasing current density and not following a straight line of corrected voltage vs. the logarithm of the current density (the apparent Tafel slope being ≈107 ± 9 mV dec^{-1} between 50–200 mA cm^{-2}, corresponding to approximately 500–2000 A g^{-1}_{Pt}), which we attribute to non-Fickian oxygen transport resistance losses due to the low *rf* value of the Pt/C-HT cathodes.[1,17] In comparison, the Pt_xY/C cathodes show significantly lower ORR overpotentials, but they also do not display a straight Tafel line, even though the apparent Tafel slope at low current densities of ≈84 ± 8 mV dec^{-1} (taken between 50–200 mA cm^{-2}) is now much closer to the ideally expected value of ≈70 mV dec^{-1}. We mainly attribute the apparently lower oxygen transport resistance for Pt_xY/C compared to Pt/C-HT to the higher *ECSA* and the faster ORR kinetics of the former.

The Pt/C catalyst based cathodes degraded strongly over the 30000 AST cycles, resulting in an end-of-test (EOT) performance which is similar to that of the Pt/C-HT based cathodes prior to the AST. However, in contrast to the strong degradation of Pt/C based cathodes, cathodes composed of Pt/C-HT retain most of their initial performance at EOT (see Figure 10), consistent with their minor *ECSA* loss over the course of the AST (Figure 8). Similarly, the Pt_xY/C based cathodes show only a slight deterioration at EOT, whereas the higher ORR kinetics of this catalyst results in a significantly higher EOT performance compared to Pt/C-HT. It is especially noteworthy that the EOT performance of Pt_xY/C is significantly superior compared to that of the commercial Pt/C catalyst. This indicates that the most advantageous catalyst would be an alloy catalyst with high specific ORR activity and with an *ECSA* that is high enough to avoid large non-Fickian oxygen transport resistances and low enough to prevent excessive *ECSA* loss over extended voltage-cycling.

The ORR mass and specific activity of the catalysts were determined from an extrapolation of linear regression lines between 50 and 200 mA cm^{-2} (corresponding to 500–2000 A g^{-1}_{Pt}) to 0.9 V_{RHE} from the H_2/O_2 data shown in Figure 10. Artifacts resulting from oxygen transport resistances at high current density can thereby largely be avoided, even though it should be noted that the determination of the ORR activity becomes increasingly more inaccurate for cathode catalyst layers with low *rf* values and/or low ORR activity (e.g., for Pt/C-HT at ≥10000 AST cycles), in which case the linear regression lines have to be extrapolated over almost one order of magnitude of current.

The ORR specific activity of all catalysts displayed in Figure 11b shows a similar trend, namely an approximately 1.5-2x increase from the beginning of the voltage-cycling AST to EOT (e.g., $i^{spec}_{0.9\ V}$ for the Pt_xY/C catalyst increased from 625 ± 45 μA cm^{-2}_{Pt} to 800 ± 170 μA cm^{-2}_{Pt}). While the enhancement of the commercial Pt/C catalyst is mainly due to the growth of the Pt particles, the formation of a Pt-enriched shell upon voltage-cycling is an additional reason for an increase of the specific ORR activity of Pt_xY/C. It shall be noted that the quantification of the ORR mass activity of Pt/C-HT is compromised by the high apparent Tafel slope. On the other hand, the catalysts behave differently with regards to the ORR mass activity (Figure 11a). For the commercial Pt/C based cathodes, it decreases

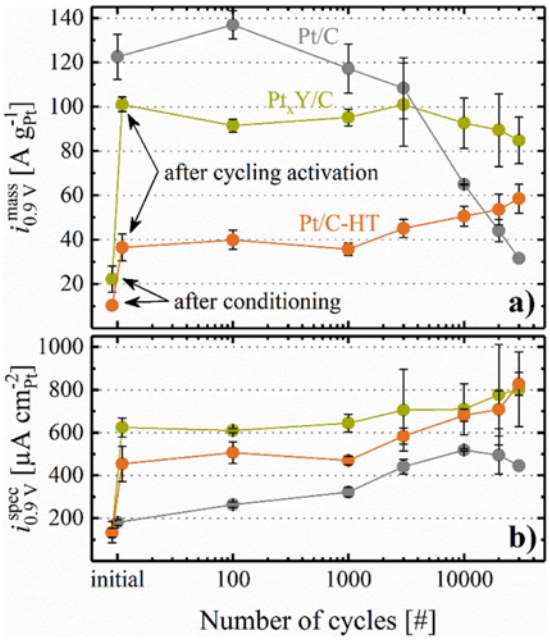

Figure 11. a) ORR mass activity ($i_{0.9\,V}^{mass}$) determined by extrapolation of a linear regression between 50–200 mA cm^{-2} (corresponding to 500–2000 A g_{Pt}^{-1}) to 0.9 V_{RHE} from the H_2/O_2 data. b) Specific ORR activity ($i_{0.9\,V}^{spec}$) obtained from $i_{0.9\,V}^{mass}$ and the *ECSA* shown in Figure 8. Note that the thus determined ORR activities are referenced to an O_2 partial pressure of 123 kPa_{abs} rather than to the frequently used reference value of 100 kPa_{abs} (the latter can be obtained by multiplying the former with 0.78).[34] Error bars represent the mean absolute deviation of two independent measurements. For Pt$_x$Y/C and Pt/C-HT, the first data point was taken after MEA conditioning and the second data point (both indicated by arrows) was recorded after cycling activation (50 cycles between 0.07 and 1.20 V_{RHE} at 50 mV s^{-1} and 40°C). The first data point for the commercial 20%$_{wt}$ catalyst was taken after MEA conditioning and no cycling activation was carried out.

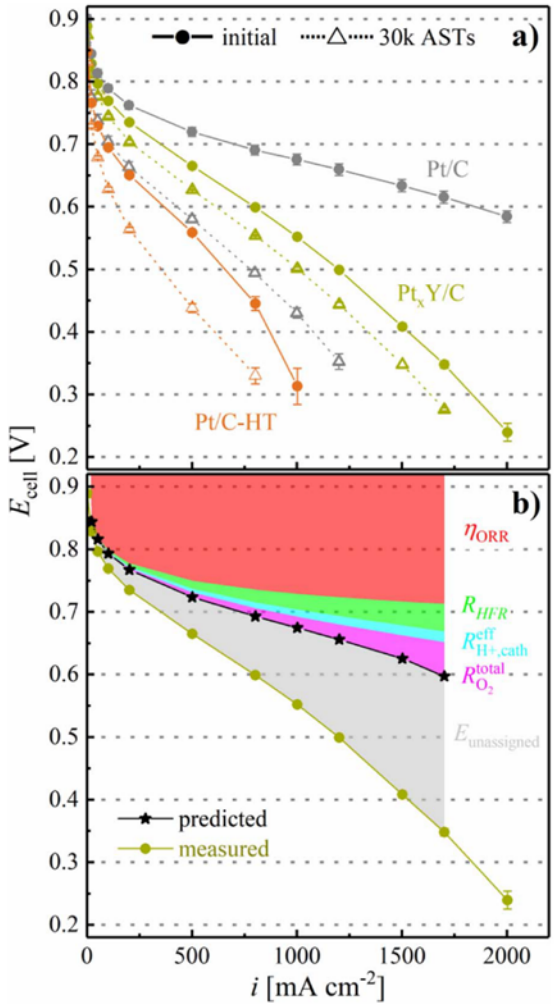

Figure 12. a) Differential flow polarization curves in H_2/air at 80°C, 100% *RH*, and 170 kPa_{abs} before the voltage-cycling AST (solid lines and full symbols) and after 30000 AST cycles (dashed lines and open symbols) for the three catalysts tested in 5 cm^2 MEAs with cathode loadings of 0.12 mg_{Pt} cm^{-2} for Pt$_x$Y/C and Pt/C-HT and of 0.10 mg_{Pt} cm^{-2} for commercial 20%$_{wt}$ Pt/C. The error bars represent the mean absolute deviation of two independent measurements. AST conditions: triangular potential scan between 0.6 and 1.0 V_{RHE} at 50 mV s^{-1}, conducted under H_2/N_2 flows (200 nccm/75 nccm) at the anode/cathode at 100 kPa_{abs}, 80°C, and 100% *RH*. b) Polarization curve for Pt$_x$Y/C (black stars) predicted from the diagnostic measurements (ORR mass activity, *HFR*, proton conduction resistance in the cathode and O_2 mass transport resistance) carried out prior to the voltage-cycling AST. The measured polarization curve for Pt$_x$Y/C from a) is also plotted in b) as a reference. The gray shaded area is the difference between the two curves and resembles the unassigned voltage losses.

significantly in the course of the AST, which can be ascribed to the dramatic loss of *ECSA*, described in more detail in a previous publication.[17] A different trend is observed for the heat treated Pt/C-HT based cathodes, whose ORR mass activity actually increases over the course of 30000 AST cycles. For this catalyst, the ORR mass activity after MEA conditioning (10 ± 2 A g_{Pt}^{-1}, see first orange data point in Figure 11a) increases substantially upon cycling activation (to 36 ± 6 A g_{Pt}^{-1}, see first orange data point in Figure 11a), which we ascribe to a cleaning of the platinum surface, analogous to the albeit much smaller voltage-cycling induced activation seen for the Pt/C catalyst after 100 AST cycles from 0.6 to 1.0 V_{RHE}. Finally, the ORR mass activity of the Pt$_x$Y/C cathodes remains roughly constant over the course of the AST cycles, while they also show a strong mass activity gain upon the initial cycling activation (from 22 ± 6 A g_{Pt}^{-1} after MEA conditioning to 101 ± 3 A g_{Pt}^{-1} after the cycling activation). In this case, the cycling activation process may be understood on the basis of the CO stripping data (Figure 9b), where a significant change in the CO oxidation features is observed between MEA conditioning and cycling activation, which we ascribe to a surface reconstruction in the Pt$_x$Y alloy phases. Important to note is the fact that the ORR mass activity of the Pt$_x$Y/C catalyst is approximately two times higher than that of the conventional Pt/C after 30000 AST cycles. This proves the beneficial effect of incorporating yttrium into the carbon supported platinum catalyst, as its higher specific ORR activity enables the utilization of larger nanoparticles, eventually providing a significantly higher stability for PEMFC cathodes.

Finally, the performance of the three different catalysts in H_2/O_2 was complemented by recording differential flow polarization curves in H_2/air (at 170 kPa_{abs}, 80°C, and 100% *RH*), where O_2 mass transport related properties of the catalyst layer typically become more apparent. Even though the cathode loading of the MEA consisting of commercial Pt/C was solely 0.1 mg_{Pt} cm^{-2}, an excellent performance with a competitive current density of ≈1850 mA cm^{-2} at 0.6 V was observed before the voltage-cycling AST (Figure 12, solid, gray line). As shown by Harzer et al., the excellent performance of these MEAs originates from optimized mass transport properties in the cathode catalyst layer.[17] In contrast, heat-treatment of this catalyst led to a significantly lower initial performance of only ≈360 mA cm^{-2} at 0.6 V (Figure 12, solid, orange line), which at least in part may be ascribed to the very low *rf* value of the Pt/C-HT cathode catalyst layer (10 ± 1 cm^2_{Pt} cm^{-2} compared to 72 ± 4 cm^2_{Pt} cm^{-2} for the commercial

Pt/C) that is reported to cause a large non-Fickian oxygen transport resistance[1] (for Pt/C-HT, this was $R_{O_2}^{total} = 3.31 \pm 0.16$ s cm^{-1}, measured by the limiting current method at 80°C, 170 kPa$_{abs}$, 100% *RH*, according to our previous study;[17] data not shown). However, based on its ≈3-fold lower ORR mass activity compared to Pt/C (see Figure 11a), one would only predict a kinetic ORR voltage loss of ≈33 mV (assuming an intrinsic Tafel slope of 70 mV dec^{-1}), which is ≈3-fold smaller than the voltage difference between the Pt/C and the Pt/C-HT cathodes at 100 mA cm^{-2} (Figure 12), a current density where voltage losses due to non-Fickian oxygen transport resistances should be entirely negligible. Therefore, we suspect that issues related to the ionomer distribution on the catalyst surface or across the cathode electrode must be an additional factor leading to its poor H_2/air performance.

While the average particle size of Pt$_x$Y was comparable to Pt/C-HT, resulting in a similar *rf* value (20 ± 1 cm^2_{Pt} cm^{-2}), its H_2/air performance was far superior, with a current density of 800 mA cm^{-2} at 0.6 V (Figure 12, solid, green line). Compared to the Pt/C benchmark MEA, one would expect identical ORR kinetic losses for the Pt$_x$Y/C based MEA, since the product of ORR mass activity (see Figure 11a) and the platinum loading for the two MEA types predicts the same ORR kinetic current at a given geometric current density. This is reasonably closely observed up to 50 mA cm^{-2}, but already at 100 mA cm^{-2} significant performance differences appear, amounting to ≈100 mV at 1 A cm^{-2}. In part this can be ascribed to the ≈2-fold higher O_2 mass transport resistance of $R_{O_2}^{total} = 1.79 \pm 0.18$ s cm^{-1} for the Pt$_x$Y/C vs. the Pt/C cathodes (0.80 ± 0.02 s cm^{-1}),[17] determined by the limiting current method prior to the voltage-cycling AST (not shown; taken at 80°C, 100% *RH*, and 170 kPa$_{abs}$), which originates largely from the low cathode *rf* value. However, compared to the actually measured H_2/air performance of the Pt$_x$Y/C MEAs (green line in Figure 12), even this high $R_{O_2}^{total}$ value would predict a ≈2-fold higher current density at 0.6 V when using the voltage-loss model described by Harzer et al.[17] The polarization curve predicted by this model is shown in Figure 12b (black stars), including all voltage loss contributions that have been determined prior to the voltage-cycling AST, namely i) the kinetic ORR overpotential (calculated for $i_{0.9\,V}^{mass} =$ 101 A g_{Pt}^{-1} (Figure 11a), *ECSA* = 16 m^2_{Pt} g_{Pt}^{-1} (Figure 8a), a loading of 0.12 mg$_{Pt}$ cm^{-2}, and the theoretical Tafel slope of 70 mV dec^{-1}), ii) the ohmic drop (*HFR*, determined by EIS at each current density, on the order of 25 mΩ cm^2), iii) the effective proton conduction loss in the cathode (using $R_{H^+,cath}^{eff} = 38$ mΩ cm^2), iv) and the estimated O_2 mass-transport loss ($R_{O_2}^{total} = 1.79$ s cm^{-1}). Following this analysis, it is clear that the measured H_2/air polarization curve exhibits significant unassigned voltage losses (e.g., 122 mV at 1 A cm^{-2}), which could not be determined by the currently available diagnostic toolset (gray shaded area in Figure 12b). Even though significant unassigned voltage losses have been observed previously for low cathode *rf* values,[17] we expect that the discrepancy is most likely related to MEA design parameters which affect the homogeneity of the ionomer across the catalyst surface and across the electrode,[34] suggesting that further MEA optimization is required. However, the more reasonable step prior to investing into a time consuming MEA optimization process, is to improve the Pt$_x$Y/C synthesis route with the aim to obtain smaller and more homogeneously alloyed particles, targeting an initial *ECSA* of ≈40 m^2_{Pt} g_{Pt}^{-1}, so that the cathode roughness factor is large enough to still have a minimal non-Fickian oxygen transport resistance at a loading of 0.1 mg$_{Pt}$ cm^{-2} (as explained by Kongkanand and Mathias).[1]

Despite its rather poor H_2/air performance prior to the AST, the performance decay of the Pt$_x$Y/C based cathodes after 30000 voltage-cycles is comparably small (Figure 12, dashed, green line), significantly exceeding the H_2/air performance of the commercial Pt/C catalyst at EOT. In comparison, the H_2/air performance of the Pt/C-HT based MEAs decayed much more compared to Pt$_x$Y/C, which we attribute to the Pt/C-HT catalyst's lower ORR mass activity as well as to its lower *ECSA* and the associated high non-Fickian oxygen transport resistance.

Conclusions

In this study, we showed the successful preparation of a carbon supported bimetallic Pt-Y alloy by impregnation of a commercial Pt/C catalyst with an yttrium halide precursor and subsequent heat-treatment in reductive atmosphere (1200°C for 1 h in 5% H_2 in Ar). Electrochemical measurements in an RDE configuration were used to identify a suitable activation procedure by potential cycling (50 cycles at 50 mV s^{-1} with an upper limit of 1.2 V$_{RHE}$), yielding a high specific ORR activity (740 ± 170 μA cm^{-2}_{Pt}), while the large average particle size (≈10 nm) resulted in a low *ECSA* (14 ± 2 m^2_{Pt} g_{Pt}^{-1}), hence a mass activity (106 ± 35 A g_{Pt}^{-1}) comparable to commercial Pt/C.

Furthermore, measurements in 5 cm^2 single-cells provided consistent results (*ECSA* = 17 ± 1 m^2_{Pt} g_{Pt}^{-1}, $i_{0.9\,V}^{spec}$ = 625 ± 45 μA cm^{-2}_{Pt}, $i_{0.9\,V}^{mass}$ = 101 ± 3 A g_{Pt}^{-1}) with the data collected in RDE. Over the course of 30000 voltage cycles between 0.6 and 1.0 V$_{RHE}$ (50 mV s^{-1}, H_2/N_2 flows of 200 nccm/75 nccm at the anode/cathode, 100 kPa$_{abs}$, 80°C, and 100% *RH*), the mass activity and the *ECSA* of the Pt$_x$Y/C catalyst showed a much better retention compared to the commercial Pt/C catalyst. However, a comparison with a heat treated Pt/C catalyst with similarly large particle size indicates that the high voltage cycling stability of Pt$_x$Y/C is a particle size rather than an alloying effect.

Finally, H_2/air polarization curves of MEAs with the Pt$_x$Y/C catalyst showed an inferior performance to commercial Pt/C, partially originating from the low cathode *rf* value and most likely from MEA design parameters (e.g., ionomer distribution within the cathode). Therefore, the preparation of Pt$_x$Y/C catalysts with higher *ECSA* (i.e., smaller particle size) and improved alloying, as well as MEA optimization are planned for future work.

Acknowledgment

The authors of this work would like to give special thanks to Umicore AG & Co. KG who supported this research financially and scientifically. The efforts by the elemental analysis laboratory at the Technical University of Munich are greatly acknowledged. Furthermore, we would like to direct our thanks to Benjamin Strehle for his expert assistance with the analysis of the XRD data and to Michele Piana for discussion of the XRD data.

ORCID

Jan N. Schwämmlein https://orcid.org/0000-0001-8902-4508
Gregor S. Harzer https://orcid.org/0000-0002-1830-1931

References

1. A. Kongkanand and M. F. Mathias, *J. Phys. Chem. Lett.*, **7**, 1127 (2016).
2. J. Durst, C. Simon, F. Hasché, and H. A. Gasteiger, *J. Electrochem. Soc.*, **162**, F190 (2015).
3. B. Han, C. E. Carlton, A. Kongkanand, R. S. Kukreja, B. R. Theobald, L. Gan, R. O'Malley, P. Strasser, F. T. Wagner, and Y. Shao-Horn, *Energy Environ. Sci.*, **8**, 258 (2015).
4. O. Gröger, H. A. Gasteiger, and J.-P. Suchsland, *J. Electrochem. Soc.*, **162**, A2605 (2015).
5. J. Greeley, I. E. L. Stephens, A. S. Bondarenko, T. P. Johansson, H. A. Hansen, T. F. Jaramillo, J. Rossmeisl, I. Chorkendorff, and J. K. Norskov, *Nat. Chem.*, **1**, 552 (2009).
6. P. Hernández-Fernández, F. Masini, D. N. McCarthy, C. E. Strebel, D. Friebel, D. Deiana, P. Malacrida, A. Nierhoff, A. Bodin, A. M. Wise, J. H. Nielsen, T. W. Hansen, A. Nilsson, I. E. L. Stephens, and I. Chorkendorff, *Nat. Chem.*, **6**, 732 (2014).
7. R. Brandiele, C. Durante, E. Grądzka, G. A. Rizzi, J. Zheng, D. Badocco, P. Centomo, P. Pastore, G. Granozzi, and A. Gennaro, *J. Mater. Chem. A.*, **4**, 12232 (2016).
8. C. Roy, B. P. Knudsen, C. M. Pedersen, A. Velázquez-Palenzuela, L. H. Christensen, C. D. Damsgaard, I. E. L. Stephens, and I. Chorkendorff, *ACS Catal.*, **8**, 2071 (2018).
9. K. G. Nishanth, P. Sridhar, and S. Pitchumani, *Electrochem. commun.*, **13**, 1465 (2011).
10. M. M. Tellez-Cruz, M. A. Padilla-Islas, J. F. Godínez-Salomón, L. Lartundo-Rojas, and O. Solorza-Feria, *Int. J. Hydrogen Energ.*, **41**, 23318 (2016).
11. G. C. d. Silva, N. A. Santos, and J. Perez, *ECS Trans.*, **72**, 23 (2016).
12. I. E. L. Stephens, A. S. Bondarenko, L. Bech, and I. Chorkendorff, *ChemCatChem.*, **4**, 341 (2012).

13. R. Cui, L. Mei, G. Han, J. Chen, G. Zhang, Y. Quan, N. Gu, L. Zhang, Y. Fang, B. Qian, X. Jiang, and Z. Han, *Sci. Rep.* **7**, 41826 (2017).
14. S. J. Yoo, K.-S. Lee, S. J. Hwang, Y.-H. Cho, S.-K. Kim, J. W. Yun, Y.-E. Sung, and T.-H. Lim, *Int. J. Hydrogen Energ.*, **37**, 9758 (2012).
15. P. Malacrida, H. G. S. Casalongue, F. Masini, S. Kaya, P. Hernández-Fernández, D. Deiana, H. Ogasawara, I. E. L. Stephens, A. Nilsson, and I. Chorkendorff, *Phys. Chem. Chem. Phys.*, **17**, 28121 (2015).
16. S.-B. Han, D.-H. Kwak, Y.-W. Lee, S.-J. Kim, J.-Y. Lee, S. Lee, H.-J. Kwon, and K.-W. Park, *Int. J. Electrochem. Sci.*, **11**, 3803 (2016).
17. G. S. Harzer, J. N. Schwämmlein, A. M. Damjanović, S. Ghosh, and H. A. Gasteiger, *J. Electrochem. Soc.*, **165**, F3118 (2018).
18. J. N. Schwämmlein, H. A. El-Sayed, B. M. Stuhmeier, K. F. Wagenbauer, H. Dietz, and H. A. Gasteiger, *ECS Trans.*, **75**, 971 (2016).
19. J. N. Schwämmlein, B. M. Stühmeier, K. Wagenbauer, H. Dietz, V. Tileli, H. A. Gasteiger, and H. A. El-Sayed, *J. Electrochem. Soc.*, **165**, H229 (2018).
20. W. Gu, D. R. Baker, Y. Liu, and H. A. Gasteiger, in *Handbook of Fuel Cells*, 1st ed., W. Vielstich, H. Yokokawa, and H. A. Gasteiger, p. 631, John Wiley & Sons Ltd, Chichester (2009).
21. T. Mittermeier, P. Madkikar, X. Wang, H. A. Gasteiger, and M. Piana, *J. Electrochem. Soc.*, **163**, F1543 (2016).
22. C. Simon, F. Hasché, D. Müller, and H. A. Gasteiger, *ECS Trans.*, **69**, 1293 (2015).
23. C. Simon, F. Hasché, and H. A. Gasteiger, *J. Electrochem. Soc.*, **164**, F591 (2017).
24. R. Makharia, M. F. Mathias, and D. R. Baker, *J. Electrochem. Soc.*, **152**, A970 (2005).
25. Y. Liu, M. W. Murphy, D. R. Baker, W. Gu, C. Ji, J. Jorne, and H. A. Gasteiger, *J. Electrochem. Soc.*, **156**, B970 (2009).
26. M. Eikerling and A. A. Kornyshev, *J. Electroanal. Chem.*, **475**, 107 (1999).
27. W. G. Moffatt, in *The Handbook of binary phase diagrams*, Genium Publishing Corporation, New York (1984).
28. J. W. Arblaster, *Platinum Met. Rev.*, **41**, 12 (1997).
29. N. H. Krikorian, *J. Less-Common Met.*, **23**, 271 (1971).
30. B. Erdmann and C. Keller, *J. Solid State Chem.*, **7**, 40 (1973).
31. M. Mikami and A. Oshiyama, *Phys. Rev. B.*, **57**, 8939 (1998).
32. W. H. Zachariasen, *Acta. Cryst.*, **2**, 388 (1949).
33. C. Solliard and M. Flueli, *Surf. Sci.*, **156**, 487 (1985).
34. A. Orfanidi, P. Madkikar, H. A. El-Sayed, G. S. Harzer, T. Kratky, and H. A. Gasteiger, *J. Electrochem. Soc.*, **164**, F418 (2017).
35. X. Wang, Z. Zhang, Z. Tang, and Y. Lin, *Mater. Chem. Phys.*, **80**, 1 (2003).
36. J. P. Gaviría and A. E. Bohé, *Metall. Mater. Trans. B.*, **40**, 45 (2009).
37. H. A. Gasteiger, S. S. Kocha, B. Sompalli, and F. T. Wagner, *Appl. Catal., B.*, **56**, 9 (2005).
38. P. Strasser, in *Handbook of Fuel Cells*, 1st ed., W. Vielstich, H. Yokokawa, and H. A. Gasteiger, p. 30, John Wiley & Sons Ltd, Chichester (2009).
39. K. J. J. Mayrhofer, D. Strmcnik, B. B. Blizanac, V. Stamenkovic, M. Arenz, and N. M. Marković, *Electrochim. Acta.*, **53**, 3181 (2008).
40. P. J. Ferreira, G. J. la O', Y. Shao-Horn, D. Morgan, R. Makharia, S. Kocha, and H. A. Gasteiger, *J. Electrochem. Soc.*, **152**, A2256 (2005).
41. R. Makharia, S. Kocha, P. Yu, M. A. Sweikart, W. Gu, F. Wagner, and H. A. Gasteiger, *ECS Trans.*, **1**, 3 (2006).

3.3. Fundamental electrochemistry

3.3.1. Direct PtSn Alloy Formation by Pt Electrodeposition on Sn Surface

The following section presents the manuscript “Direct PtSn Alloy Formation by Pt Electrodeposition on Sn Surface”, which was submitted to the peer-reviewed Journal Scientific Reports and is currently under review. Some of the data used in this manuscript was presented at the 227th ECS Meeting (2015) in Chicago, Illinois (abstract #1185) by Jan N. Schwämmlein.

Short summary.—A major degradation mechanism of electrode layers during fuel cell operation is carbon corrosion, e.g., on the cathode during SUSD events[142] or on the anode in the case of a cell reversal.[154] For this, the development of more stable support materials which are similarly conductive and as inexpensive as carbon is desired. Due to their high conductivity, doped oxides, such as ATO, are among the most promising candidates in this field of research.[51,155–157] Another stability issue of current catalyst layers is Ostwald ripening of the Pt catalyst. In contrast to nanoparticles, extended Pt surface films exhibit far superior stability versus potential cycling due to their thermodynamically favorable surface configuration. Hence, thin Pt films might provide superior stability, while maintaining the high ORR mass activity of Pt nanoparticles. The manuscript presented here is based on the idea to combine a novel support material, e.g., based on SnO_2, with a Pt film to enhance fuel cell durability.

The premise of this work is to examine whether the deposition of monolayer-thick Pt films can be accomplished on SnO_2-based substrates by reducing their surface to Sn, followed by the deposition of Pt. The study commences with an evaluation of the electrochemical oxidation and reduction of the Sn surface in borate buffer (pH = 8.4), identifying the redox process as fully reversible between -0.35 and 0.14 V_{RHE}. Subsequently, an experiment is designed to investigate the difference in the electrochemical Pt deposition process on an oxidized versus a metallic Sn surface. This is achieved by introduction of the Pt precursor to the electrolyte at a potential where the surface of the electrode is oxidized, followed by a cathodic potential sweep to slowly transfer the surface into the metallic state while Pt ions are present in the electrolyte. As a comparison, the same experiment is carried out on an electrode, which is free of oxidized species on its sur-

face in the applied potential range or on a Pt electrode. Despite of a large applied overpotential for the deposition of Pt (≈1 V), no electrochemical deposition process is observed on Sn until the surface oxide species are reduced. We conclude that this effect is similar to that, known e.g., from adsorbed hydrogen species[158] and could in principle be used for self-limited Pt deposition in the future. We further hypothesize that the same effect occurs on Pt deposited on the surface of Au, where the deposition process is enhanced at a potential similar to the onset of Pt deposition on pure Pt.

In accordance with those findings, all further deposition experiments are carried out on metallic Sn in the absence of surface oxide species. In order to identify the potential that fully maintains the Sn electrode in a metallic state, another experiment is presented, where the electrode potential is fixed to a certain value, followed by a cathodic scan to reduce oxide species. This experiment provides evidence that a metallic surface is maintained up to an anodic potential of -0.1 V_{RHE}, which is used as the most anodic deposition potential, complemented by deposition at -0.15 and -0.25 V_{RHE}. In general, all three potentials used to deposit Pt on Sn provide a significant cathodic overpotential for the HER. In contrast to the negligible HER kinetics on Sn, Pt provides significant HER currents in the applied potential region and a superposition of HER and Pt deposition occurs at all potentials. Combining the electrochemical data with SEM images of the surface after the deposition process, we conclude that the HER inhibits the deposition of Pt on the Pt deposits, while a higher HER overpotential most likely leads to a lower deposition efficiency (higher relative HER current). Even though, none of the methods is capable to produce a smooth thin film of Pt on the Sn surface, EDX analysis provides an approximation of the deposited thickness (<10 nm). Furthermore, an evaluation of the thickness of the deposits after various deposition times at the same potential provides evidence that the HER is capable to inhibit Pt deposition after a certain film thickness is reached (on the order of 10 nm under the applied conditions). Finally, the formation of a Pt-Sn alloy during the deposition process is confirmed by CO oxidation in liquid electrolyte, where the deposits provide a significantly lower CO oxidation overpotential compared to pure Pt.

Author contributions.—J.N.S. performed all measurements and the data was analyzed by J.N.S. and H.E.S. The manuscript was written by J.N.S. and reviewed by H.E.S.

Direct PtSn Alloy Formation by Pt Electrodeposition on Sn Surface

Jan N. Schwämmlein and Hany A. El-Sayed[z]

Chair of Technical Electrochemistry, Department of Chemistry and Catalysis Research Center, Technical University of Munich, D-85748 Garching, Germany
[z]E-mail: hany.el-sayed@tum.de

Electrochemical deposition is a viable approach to develop novel catalyst structures, such as Pt thin films on conductive support materials. Most studies, reaching out to control electrochemical deposition of Pt to monolayer quantities focus on noble metal substrates (e.g., Au). In contrast, conductive oxides, such as antimony doped tin oxide (ATO), are considered as support material for different applications, e.g., as fuel cell catalysts. Herein, we investigate the deposition process of Pt on Sn, used as a model system for the electrochemical deposition of Pt on non-noble metal oxide supports. Doing so, we shade some light on the differences of a metallic Sn surface and surface oxide species in electrochemical deposition processes. With respect to a borate buffer solution, containing K_2PtCl_4 as Pt precursor, we report for the first time that surface oxides have the capability to fully inhibit the electrochemical deposition of Pt. Furthermore, direct alloying of the deposited Pt with the Sn support during the electrodeposition process yielded a catalyst with a high activity for the oxidation of CO.

Fuel cells are considered as a candidate to replace the currently wide-spread combustion engine and limit the exhaust of CO_2, e.g., caused by automotive traffic. Especially since first car producers, such as Toyota,[1] Hyundai,[2] and Honda,[3] finally brought fuel cell powered vehicles to the market, this technology is in reach of widespread application. Nevertheless, there is a demand for novel electrocatalysts due to the low abundance of Pt and the limited stability of current catalysts under fuel cell operating conditions.[4] In this respect, film-like structures on non-noble metal based supports, such as antimony doped tin oxide (ATO), are of potential interest due to various reasons. First of all, the Pt surface to mass ratio of extended surfaces is similar to that of nanoparticles for sufficiently thin layers. Second, Pt thin film structures may show high specific activity towards the ORR due to a likely exposure of low index facets, providing a superior ORR exchange current density compared to Pt nanoparticles.[5] Third, a contiguous film may protect the underlying support material against corrosion. Finally, conductive oxides were proposed as stable catalysts with respect to high anodic potentials, occurring under certain fuel cell operating conditions, such as start-up or shut-down (SUSD).[6–8]

In contrast to the lack of synthesis methods for Pt thin films on non-noble metal oxides, various methods were already presented to generate low loading platinum deposits on metallic supports. One approach was to utilize the redox replacement of an underpotentially adsorbed Cu layer by Pt from a precursor dissolved in the electrolyte.[9] Another method, developed by Brimaud et al. utilizes the strong adsorption of CO on the deposited Pt to hinder any further deposition after completion of a single Pt monolayer (ML) on a Au(111) single crystal.[10] Though the Pt ML was reported to be stable while CO was adsorbed, the group showed that the structure collapsed to Pt islands as soon as CO was displaced. A similar effect to limit Pt electrodeposition on Au(111) to an amount of Pt equivalent to one ML was presented by Moffat and coworkers.[11] Instead of CO, the potential dependent formation of H_{ads} was used to interrupt the deposition process while the hydrogen evolution reaction (HER) proceeded on the Pt deposit. To avoid the formation of H_2 bubbles, the group used an unbuffered electrolyte with a pH of 4, where the amount of HER was limited due to an evolving pH gradient between the electrode and the bulk of the electrolyte.[12] The scanning tunneling microscopy (STM) images of the resulting deposits showed an island-like morphology of very small Pt deposits on the Au surface. Similar to those studies, most electrochemical deposition techniques, aiming to achieve low loading Pt deposits focus on noble metal substrates, whereas deposition of low platinum quantities on non-noble metals or conductive oxides was only scarcely reported (e.g., on Ni).[13]

In this publication, we present insights into the electrodeposition process of Pt on Sn as a model system for such novel catalysts. Overall, this manuscript aims to deliver a better understanding of the electrodeposition process, eventually leading to a synthesis approach for novel fuel

cell catalysts, comprised of low Pt loaded conductive oxides. At first, the electrochemical behavior of Sn in slightly alkaline solution is investigated to identify the oxidation and reduction processes on its surface. Subsequently, the influence of oxides on the electrochemical deposition process of Pt on the Sn surface is evaluated. Finally, Pt deposition is carried out in the presence of HER, where the resulting Pt film thickness is studied by energy dispersive X-ray (EDX) spectroscopy. The electrochemical oxidation of CO is used as a probe for the structure of the deposits. By this method, we are able to identify the deposits as PtSn alloys, formed directly on the surface of the electrode during the deposition process.

Experimental procedure

Rotating disk electrode (RDE) setup.—Fuel cells are considered as a candidate to replace the currently wide-spread combustion engine and limit the exhaust of CO_2, e.g., caused by automotive traffic. Especially since first car producers, such as Toyota,[1] Hyundai,[2] and Honda,[3] finally brought fuel cell powered vehicles to the market, this technology is in reach of widespread application. Nevertheless, there is a demand for novel electrocatalysts due to the low abundance of Pt and the limited stability of current catalysts under fuel cell operating conditions.[4] In this respect, film-like structures on non-noble metal based supports, such as antimony doped tin oxide (ATO), are of potential interest due to various reasons. First of all, the Pt surface to mass ratio of extended surfaces is similar to that of nanoparticles for sufficiently thin layers. Second, Pt thin film structures may show high specific activity towards the ORR due to a likely exposure of low index facets, providing a superior ORR exchange current density compared to Pt nanoparticles.[5] Third, a contiguous film may protect the underlying support material against corrosion. Finally, conductive oxides were proposed as stable catalysts with respect to high anodic potentials, occurring under certain fuel cell operating conditions, such as start-up or shut-down (SUSD).[6-8]

In contrast to the lack of synthesis methods for Pt thin films on non-noble metal oxides, various methods were already presented to generate low loading platinum deposits on metallic supports. One approach was to utilize the redox replacement of an underpotentially adsorbed Cu layer by Pt from a precursor dissolved in the electrolyte.[9] Another method, developed by Brimaud et al. utilizes the strong adsorption of CO on the deposited Pt to hinder any further deposition after completion of a single Pt monolayer (ML) on a Au(111) single crystal.[10] Though the Pt ML was reported to be stable while CO was adsorbed, the group showed that the structure collapsed to Pt islands as soon as CO was displaced. A similar effect to limit Pt electrodeposition on Au(111) to an amount of Pt equivalent to one ML was presented by Moffat and coworkers.[11] Instead of CO, the potential dependent formation of H_{ads} was used to interrupt the deposition process while the hydrogen evolution reaction (HER) proceeded on the Pt deposit. To avoid the formation of H_2 bubbles, the group used an unbuffered electrolyte with a pH of 4, where the amount of HER was limited due to an evolving pH gradient between the electrode and the bulk of the electrolyte.[12] The scanning tunneling microscopy (STM) images of the resulting deposits showed an island-like morphology of very small Pt deposits on the Au surface. Similar to those studies, most electrochemical deposition techniques, aiming to achieve low loading Pt deposits focus on noble metal substrates, whereas deposition of low platinum quantities on non-noble metals or conductive oxides was only scarcely reported (e.g., on Ni).[13]

In this publication, we present insights into the electrodeposition process of Pt on Sn as a model system for such novel catalysts. Overall, this manuscript aims to deliver a better understanding of the electrodeposition process, eventually leading to a synthesis approach for novel fuel cell catalysts, comprised of low Pt loaded conductive oxides. At first, the electrochemical behavior of Sn in slightly alkaline solution is investigated to identify the oxidation and reduction processes on its surface. Subsequently, the influence of oxides on the electrochemical deposition process of Pt on the Sn surface is evaluated. Finally, Pt deposition is carried out in the presence of HER, where the resulting Pt film thickness is studied by energy dispersive X-ray (EDX) spectroscopy. The electrochemical oxidation of CO is used as a probe for the structure of the deposits. By this method, we are able to identify the deposits as PtSn alloys, formed directly on the surface of the electrode during the deposition process.

Electrode preparation.—Polycrystalline Sn electrodes (99.999%, *MaTecK Material-Technologie & Kristalle GmbH*, Germany) were prepared by polishing in three individual steps using a 9 µm diamond suspension (MetaDi

Supreme) on a VerduTex polishing cloth, a 3 µm diamond suspension (MetaDi Supreme) on a MicroCloth and 1 µm Al_2O_3 (MicroPolish II) on a Microcloth with a polishing machine (MetaServ 250 / vector head), all purchased at *Bühler GmbH* (Germany). Each polishing step was performed for at least 5 minutes and the crystal was sonicated at least five times in ultrapure water before moving on to the next step, mitigating Pt contamination on the Sn crystals.

Electrochemical deposition procedure.— Potential-controlled electrochemical deposition (-0.10, -0.15, -0.25 V_{RHE}) was carried out by introducing K_2PtCl_4 (99.999%, *Sigma Aldrich Corp.*, Germany) to the Ar-saturated electrolyte while the electrode was rotated at 200 rpm. The Pt precursor was dissolved in borate buffer (1 mL) prior to addition and the amount of K_2PtCl_4, added to the cell, was adjusted to yield an overall concentration of 1.5 mM. After the desired time of deposition was reached, the electrode was immediately removed from the solution and rinsed with ultrapure water to remove any remaining Pt ions from the surface of the electrode.

Pt sputtering and scanning electron microscopy (SEM).—Platinum was sputtered on polished Sn samples in Ar atmosphere (0.05 mbar), using a sputtering machine (Sputter Coater SCD 004, *Fluke Corp.*, USA) with a working distance of 5 cm at an applied current of 15, 45, 60, 30 or 60 A for 40, 30, 26, 180 or 52 s to achieve a Pt overlayer thickness of 5, 20, 40, 60 or 80 nm. Images of the deposits were taken with a high resolution scanning electron microscope (JCM-7500F, *Jeol Germany GmbH*, Germany) after washing the samples with ultrapure water and drying them for at least 24 h at room temperature. EDX spectroscopy was carried out on a table top SEM-EDX device (JCM-6000, *Jeol Germany GmbH*, Germany) at 15 kV.

XPS Characterization—The XPS measurements were performed in a Kratos Axis Supra spectrometer with a monochromatic Al Kα X-ray source. The PtSn samples were mounted non-conductive in the sample holder by using a carbon tape and a PTFE sheet to adjust the sample's height. The binding energies for each spectra were corrected using the C 1s peak (284.6 eV) as a reference. The peak areas from the Pt 4f and Sn 3d level were calculated with casaXPS processing software. A Shirley back ground was employed for the background subtraction during the area calculation.

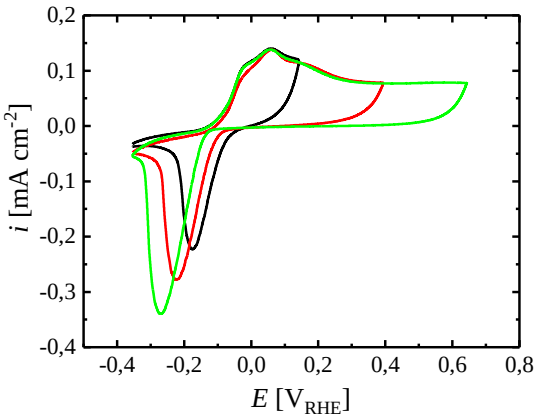

Figure 1. CVs of a Sn electrode in Ar-saturated borate buffer (0.05 M, pH = 8.4) at a scan rate of 20 mV s^{-1} between -0.35 and 0.14 (black), 0.39 (red) or 0.64 V_{RHE} (green) without rotation, measured at room temperature.

Results and Discussion

Electrochemistry of Sn.— As a non-noble metal, Sn readily forms an oxide on its surface if exposed to an oxidizing agent, such as O_2 in air. Furthermore, Sn dissolves to Sn(II) and Sn(IV) species in acidic and alkaline media.[14] In contrast to this, metallic Sn is thermodynamically stable between approximately -0.1 and -1.0 V_{RHE} in solutions with neutral pH.[15] Therefore, Sn can be reversibly oxidized and reduced by potential control in neutral media, e.g., without significant dissolution into the electrolyte.[16] Accordingly, the steady-state CV of a Sn electrode in a borate buffer solution with a pH of 8.4 is presented in Figure 1, showing oxidative features at potentials more anodic than -0.1 V_{RHE}, as well as reductive features at more cathodic potentials. The electrochemical behavior of Sn has been studied in various electrolytes by different groups,[16–19] and the following reaction scheme was proposed for the electrochemical oxidation of metallic Sn in borate buffer by Kapusta et al.[16]

$$Sn + 2\ OH^- \rightarrow Sn(OH)_2 + 2\ e^- \quad [1]$$
$$Sn(OH)_2 + 2\ OH^- \rightarrow Sn(OH)_4 + 2\ e^- \quad [2]$$

In accordance with these reports, the anodic current shown in Figure 1 is assigned to the oxidation of the Sn surface, whereas the cathodic peak is ascribed to the associated reduction to metallic Sn. In the absence of a continuous

reaction (e.g., HER), the extent of reversibility of the redox process can be estimated by dividing the integral of the reductive charge (C_{red}) by the oxidative charge (C_{ox}), passing through the electrode during a single cycle. Considering the CV with an anodic potential limited of 0.14 V_{RHE} (Figure 1, black line), the oxidative and cathodic charges are perfectly balanced ($C_{red}/C_{ox} \approx 1$), hence the process of surface oxide formation on Sn can be considered fully reversible within this potential range. When the anodic vertex of the CV is increased to higher potentials (0.39 and 0.64 V_{RHE}), the oxidative as well as the reductive charge increases and the cathodic peak shifts to more negative potentials (Figure 1, red and green lines). This observation can be explained by the transformation of the anodically formed oxide to a more stable oxide layer on the Sn surface at these higher anodic potentials, leading to an increase in the reduction overpotential in the negative going scan.[16] Furthermore, the charge balance C_{red}/C_{ox} decreases to ≈0.7 and ≈0.6 when the anodic vertex increases to 0.39 and 0.64 V_{RHE}, respectively. The higher oxidative compared to reductive charge indicates an incomplete reduction of the oxide layer within the applied potential region, most likely due to the anodic stabilization of the surface oxide. In alignment with this hypothesis, Kaputsa et al. reported that full removal of certain, anodically grown Sn oxide species requires extended periods at substantially more cathodic potentials, including the formation of H_2 on the electrode.[16]

The role of surface oxides in the electrodeposition of Pt.— In general, the deposition of metals on oxides is associated with a large interfacial energy, often leading to the formation of islands due to a dewetting effect.[20] The effect of Sn oxide on the electrochemical deposition of Pt was studied here using CV in borate buffer solution. Pt deposition on Sn was carried out after potential cycling of the electrode surface in the potential range of the fully reversible oxide formation (i.e., between -0.35 and 0.14 V_{RHE}) until a stable voltammogram was established, whereas high anodic potentials were avoided to abstain from the irreversible oxide formation. When the CV of the Sn electrode reached the anodic vertex of 0.14 V_{RHE}, an already dissolved Pt(II) precursor (K_2PtCl_4) was added to the electrolyte and the potential was scanned in cathodic direction. Hence, an oxide is present on the surface of the electrode when the precursor is introduced to the system. Figure 2a) shows the CV prior to addition of the Pt precursor (black line) and the subsequent cathodic scan in the presence of Pt ions (red line). With respect to thermodynamics, facile Pt deposition on the electrode surface is expected in the entire applied potential region, due to the large cathodic overpotential of more than 1 V with respect to the standard reduction potential of $PtCl_4^{2-}$ (0.755 V_{SHE}) according to the following reaction scheme.[21]

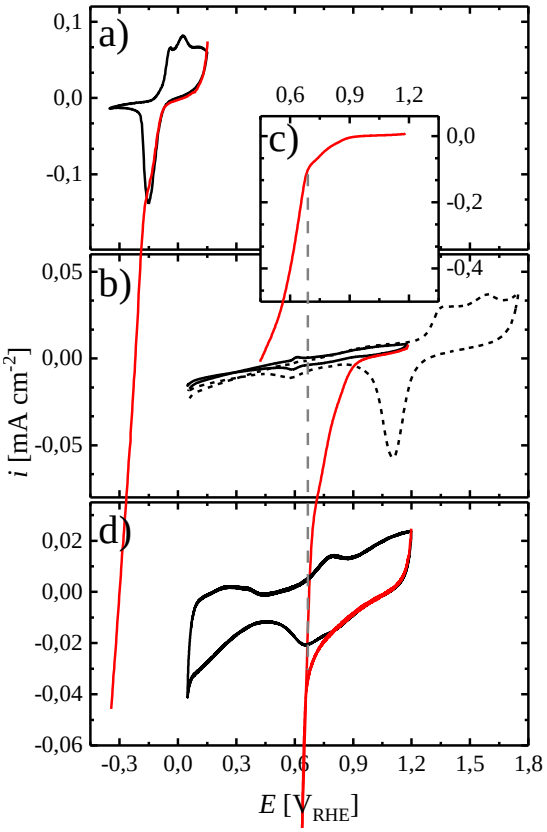

Figure 2. The solid, black lines show CVs of a) Sn (-0.35 – 0.14 V_{RHE}), b) Au (0.05 – 1.18 V_{RHE}) with a zoomed inset in c) and d) Pt (0.05 – 1.20 V_{RHE}) in Ar-saturated borate buffer (0.05 M, pH = 8.4) at a scan rate of 10 mV s^{-1}, applying a rotation rate of 400 rpm, measured at room temperature. At the anodic vertex of the CV, a solution containing K_2PtCl_4 (1.5 mM) was added to the electrolyte, with the red lines showing the cathodic scan directly after addition of the Pt precursor. The dotted, black line in b) shows a CV of a Au electrode at more anodic potentials (0.05 – 1.75 V_{RHE}), as a comparison. The dashed, grey line is solely a guide for the eye to indicate the change of slope in the deposition transient.

$$PtCl_4^{2-} + 2e^- \rightarrow Pt + 4Cl^- \quad [3]$$

Nevertheless, as shown (red line) in Figure 2a), the current in the cathodic sweep after the addition of the Pt precursor initially follows the previous cycle, where no $PtCl_4^{2-}$ ions were present in the electrolyte. The absence of a cathodic current in addition to that originating from the redox process on the Sn electrode indicates that Pt deposition from a borate buffer solution does not occur on the Sn electrode between 0.14 and ≈-0.12 V_{RHE}. Nevertheless, the current increases significantly when the potential is scanned further cathodic into the range corresponding to the reduction of Sn oxide species, indicating the onset of Pt deposition. Sweeping the potential further cathodic leads to a linear increase of the current, accounting for ongoing reduction of Pt ions from solution and HER on the resulting deposits. According to these findings, we hypothesize that Pt deposition on Sn is not possible under the applied conditions as long as the metallic surface is covered with oxide species. It can be excluded that the observed phenomenon is due to a time transient effect, where the Pt precursor would not be present at the surface of the electrode until the increase of the current is observed, since the electrode was rotated (400 rpm) during the experiment, ensuring a quick transport of the already dissolved precursor to the electrode surface. Furthermore, similar experiments were performed at different potentials (shown at a later point of the study, Figure 4) where the insertion of the precursor led to an instant rise of the cathodic current. In order to verify that surface oxides hinder the electrochemical deposition process on Sn, a similar experiment was carried out on a Au electrode. Compared to Sn, the electrochemical oxidation of Au in borate buffer takes place at substantially more anodic potentials >1.2 V_{RHE} (dashed, black line, Figure 2b). Limiting the anodic vertex of the CV to a potential before the oxidation of Au ensures the metallic state of the electrode, hence no reductive peaks appear in the cathodic scan of the CV (solid, black line, Figure 2b). By adding the Pt precursor at 1.2 V_{RHE} and scanning the potential cathodic, the onset of Pt deposition on Au was found at ≈0.9 V_{RHE} (red line, Figure 2b). Owing to the fact that this potential lies more than 1 V anodic of that found on Sn, we conclude that Pt deposition on Sn is indeed fully prevented in the presence of an oxide layer on the surface. Continuing the cathodic sweep reveals a change of slope with respect to the increase in the deposition current at a potential of approximately 0.66 V_{RHE}, best visible in Figure 2c). The charge that passed the electrode in the cathodic scan before reaching 0.66 V_{RHE}, is approximately 720 µC cm^{-2}. Considering a $2e^-$ process for the reduction of $PtCl_4^{2-}$ according to Equation [3], and assuming 100% efficiency, this charge corresponds approximately to the deposition of one Pt monolayer on Au (assuming a hypothetical roughness factor of ≈1.5 cm^2_{Pt} cm^{-2} for the Au disk). Hence, the majority of the Au surface is already covered with Pt when the potential of 0.66 V_{RHE} is reached. Repeating the deposition experiment on a Pt electrode (Figure 2d) gives further insight into the Pt deposition process. Similar to Sn, deposition of Pt on Pt starts after the removal of surface oxides on the metal (red line, Figure 2d). The onset of Pt deposition on the Pt disk was ≈0.66 V_{RHE}, coinciding well with the potential where a change of slope was observed when Pt is deposited on the Au disk (red line, Figure 2b). Hence, we hypothesize that Pt deposited on Au at potentials more anodic than 0.66 V_{RHE} is oxidized quickly, forming a layer of oxide species. This layer may hinder the continuation of the deposition process, similar to that on a Pt (or Sn) electrode and might eventually stop the process entirely in a certain potential region. By sweeping the potential further cathodic, metallic Pt is exposed and Pt deposition can continue unabated, leading to an increase in the deposition current, thus a change of slope in the cathodic scan of Figure 2b) is observed. According to the results presented here, we propose that oxide species on the surface of Pt and Sn electrodes are capable of fully inhibiting Pt deposition under the conditions applied here, even though high cathodic overpotentials are applied to the system. As mentioned earlier, similar self-limiting mechanisms with respect to the deposition of Pt were observed by other researchers who utilized this effect to prepare Pt-ML structures on Au. Brimaud et al. deposited Pt electrochemically on Au in the presence of CO in the electrolyte. They reported that the rapid adsorption of carbon monoxide on the Pt surface fully blocks further electrodeposition.[10] Liu et al. employed a similar method to obtain a Pt-ML on Au, where they used the underpotential deposition of hydrogen (H_{upd}) to stop the Pt deposition after the formation of the first layer.[11] If developed further, the mechanism reported in this publication could potentially be utilized in a similar way to obtain a Pt-ML or thin film on a non-noble metal support.

Since Pt deposits only on metallic Sn, an experiment was designed to identify the potential at which Sn oxide formation takes place on the surface of the electrode. First of all, a CV, ter-

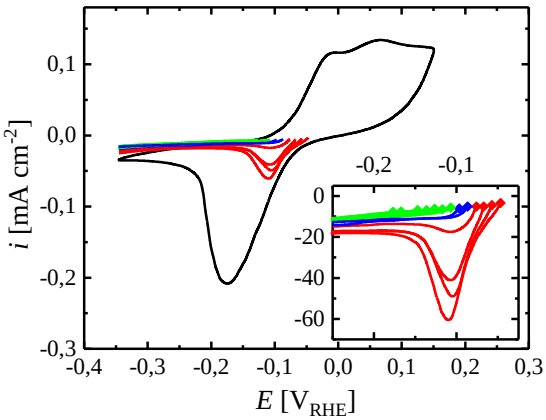

Figure 3. Steady state CV (black line) of a Sn electrode in Ar-saturated borate buffer (0.05 M, pH = 8.4) at a scan rate of 20 mV s^{-1} between -0.35 and 0.14 V_{RHE}, measured at room temperature. Red, blue and green lines show linear potential scans in cathodic direction at 20 mV s^{-1} after a constant potential was applied for 120 s. The applied potential is indicated by a diamond. The inset shows a zoom of the same graph.

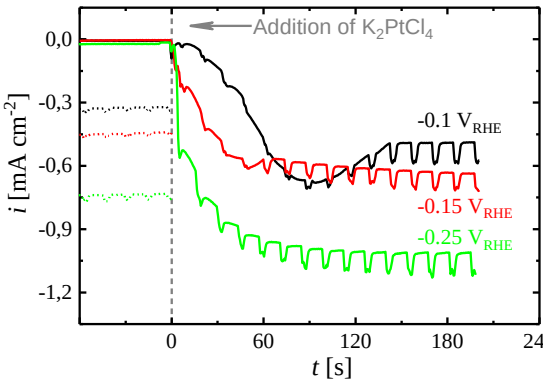

Figure 4. Current transient of potentiostatic measurements on Sn electrodes at -0.1 (black), -0.15 (red) and -0.25 V_{RHE} (green) in deaerated borate buffer (0.05 M, pH = 8.4) at a rotation rate of 200 rpm, interrupted by a 3 s rotational pulse of 3000 rpm every 15 s, measured at room temperature. A solution, containing K_2PtCl_4, was added to the electrolyte (time of addition depicted by a grey arrow), resulting in an overall concentration of 1.5 mM.

minating at a potential of -0.35 V_{RHE}, was carried out to reduce the surface oxide of the Sn electrode. Thereafter, the potential of interest was applied for 2 minutes (chronoamperometric period) to either stabilize the surface in the metallic state or to form surface oxide species. Subsequently, the potential was scanned cathodic to probe for the appearance of a peak, corresponding to the reduction of the surface oxide to metallic Sn. When potentials more negative than -0.1 V_{RHE} are applied during the chronoamperometric period, no peak appears in the cathodic scan (green lines, Figure 3), thus no oxidation of the metallic surface has taken place and the probed potential is considered suitable for the electrodeposition of Pt. In contrast to that, clear reduction features are observed after applying potentials more positive than -0.09 V_{RHE} (red lines, Figure 3) due to (partial) oxidation of the Sn surface. In the transition region between those two potential regions, no clear peak is found but slight reoxidation of the surface cannot be fully excluded (blue lines, Figure 3).

The nature of electrodeposited Pt on Sn.— In order to obtain an insight into the deposition process, as well as into the morphology of the resulting Pt deposits, potentiostatic electrodeposition was carried out at different potentials and the deposits were imaged by SEM. Furthermore, the change in the electrochemical properties of the Pt deposits, as well as the increase in the film thickness throughout the deposition process with respect to the deposition time are addressed in this section.

To ensure the metallic state of Sn prior to the electrodeposition process, potentiostatic Pt deposition was solely carried out at sufficiently cathodic potentials, ensuring the absence of oxide species on Sn according to Figure 4, viz., -0.1, -0.15 and -0.25 V_{RHE}. Prior to deposition, the Sn oxide on the electrode surface was reduced by scanning the potential cathodic to -0.35 V_{RHE}, followed by a stabilization period at the respective deposition potential for 120 s (in the absence of Pt ions in the solution). Thereafter, K_2PtCl_4 pre-dissolved in borate buffer was added to the solution to initiate Pt deposition on Sn. During the electrochemical deposition process, a rotation rate of 200 rpm was applied, interrupted every 15 s by a rotational pulse of 3000 rpm for 3 s to remove hydrogen bubbles from the surface of the electrode.

As shown in Figure 4 (solid lines), the current at each potential remains constant before the addition of the Pt precursor, indicating steady conditions and the absence of additional reductive processes, e.g., due to the removal of residual surface oxides. As soon as K_2PtCl_4 is introduced to the electrolyte, the current increases in all experiments, eventually sloping out to a plateau

for the remainder of the potentiostatic period. Therefore, the current increase can clearly be ascribed to the reduction of Pt ions at the surface of the electrode, superimposed with a co-current from HER on the Pt deposits. In contrast to Sn,[22] Pt is highly active for HOR/HER in a wide range of pH values.[23–27] Therefore, a significant increase of the current is expected for a Sn electrode once it is at least partially covered with Pt due to the large applied HER overpotential. Consistently, the cathodic current after the addition of the Pt precursor originates from Pt deposition, as well as from HER on the Pt deposits. The application of a larger HER overpotential (more cathodic potential) therefore causes a higher current during the plateau phase. Moreover, the time needed to reach the plateau is clearly dependent on the applied potential, with more cathodic potentials enhancing the rate of the deposition process. As a result, the Sn surface is more quickly covered with Pt at more cathodic potentials and the plateau, corresponding to the maximum rate of HER, is reached more quickly. Consistently, the current measured at -0.1 V_{RHE} (Figure 4, black line) requires significantly more time to reach steady state and reproducibly shows a current peak before the final plateau. We account this to an overlap of Pt deposition on uncovered Sn sites with the current originating from HER on Pt, since covering the electrode with Pt requires more time compared to -0.15 (Figure 4, red line) and -0.25 V_{RHE} (Figure 4, green line). However, according to Strmcnik et al., the surface of Pt is fully covered with H_{ads} in the relevant potential region (≤-0.1 V_{RHE}).[28] Liu et al. utilized the rapid formation of Pt-H_{ads} on the surface of the deposited Pt to prepare a Pt-ML on a single crystalline gold surface, where Pt electrodeposition was fully prevented by the adsorbed hydrogen.[11] Since the potential range utilized for deposition experiments in this study is similar to that of Liu et al. (-0.33 V_{RHE}), one might expect a comparable inhibition of the deposition process on Sn. However, the electrolyte used by Liu et al. was an unbuffered NaCl solution (0.5 M), where the pH at the surface of the electrode shifts due to the consumption of H^+ during HER on Pt.[12] The advantage of this approach is the possibility to adjust the rate of H_2 evolution to a moderate level by choosing the solution pH accordingly. Hence, using an electrolyte with a pH of 4 (according to Liu et al.) results in an HER limiting current of ≈100 µA cm^{-2} at a rotation rate of 400 rpm.[11] In this case, the associated molar flux of H_2 produced at the surface of the electrode is as low as ≈0.5 nmol s^{-1} cm^{-2} (calculated via Faraday's law at a current density of 100 µA cm^{-2} in a 2 e^- transfer reaction). In contrast to this rather low H_2 production rate, the maximum flux transported away from the electrode through diffusion under the applied conditions is on the order of 15 nmol s^{-1} cm^{-2} (calculated via Fick's first law, assuming a diffusion boundary layer thickness of 40 µm at 400 rpm, a maximum H_2 concentration of 1.3 mM at 25°C,[25] a diffusion coefficient of $4.5 \cdot 10^{-9}$ m^2 s^{-1} and the absence of H_2 in the bulk of the solution),[29] allowing the produced H_2 to be easily transported away from the electrode into the bulk of solution without forming bubbles on the electrode surface. In accordance with this, a solution pH of 8.4, i.e., as used in all Pt deposition experiments in this article, results in a theoretical limiting current of 12 nA cm^{-2} (calculated via the Levich equation using a diffusion coefficient of $7 \cdot 10^{-9}$ m^2 s^{-1} and a rotation rate of 400 rpm)[30] due to the comparably low proton concentration. However, in unbuffered electrolytes, the concentration of protons at the surface of the electrode depletes when HER proceeds, resulting in a shift of the surface pH. Hence, due to the limited stability window of Sn with respect to pH (Sn dissolves in acidic and alkaline media),[15] a buffered electrolyte was used in all experiments described here. Since protons can be readily replenished in buffers, a change of the solution pH is avoided and the H^+ concentration in the vicinity of the electrode does not deplete analogously to an unbuffered electrolyte. Therefore, the current observed on a polycrystalline Pt disk (Figure 4, dotted lines) in the same electrolyte, at the potentials used for electrochemical deposition, i.e., -0.10, -0.15 and -0.25 V_{RHE}, ranges between 0.34 – 0.76 mA cm^{-2} at a rotation rate of 400 rpm. Hence, the rate of H_2 evolution at the surface of the electrode is approximately one order of magnitude larger compared to Liu et al. Accordingly, H_2 bubbles can form on the surface of the electrode, eventually being released into the electrolyte. The surface sites liberated in this process may serve as template for further Pt deposition, hence the deposition process is not expected to be fully inhibited under the conditions applied here. Nevertheless, it is expected that the rate of Pt deposition is significantly decreased due to blockage of Pt sites by adsorbed hydrogen. In principle, a rough estimation of the efficiency of the deposition process during the plateau phase can be made by subtraction of the charge originating from HER on pure Pt from the charge obtained during the electrodeposition experiments. Dividing this

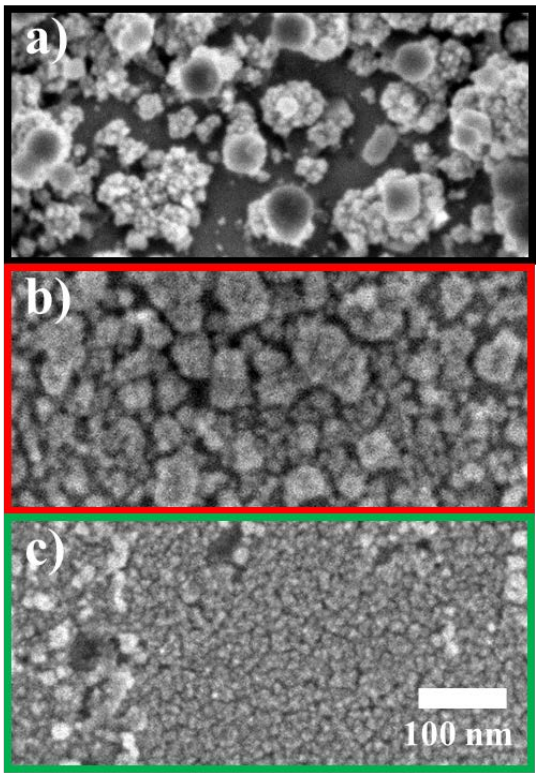

Figure 5. SEM images of Pt deposits on Sn, prepared by electrodeposition in borate buffer (pH = 8.4, 0.05 M) at a) -0.10, b) -0.15 and c) -0.25 V_{RHE} for 204 s, applying a rotation rate of 200 rpm, interrupted by a 3 s rotational pulse of 3000 rpm every 15 s.

"HER-corrected" charge by the total charge delivered during the same period of time yields a maximum deposition efficiency of 30, 23 and 24% at -0.10, -0.15 and -0.25 V_{RHE}. Even though an extraction of the amount of deposited Pt by this method is rather delicate due to differences in the nature of the electrode (Pt deposits on Sn versus pure Pt), the electrode morphology, and the additional salt in the electrolyte, the low calculated efficiency indicates that the deposition of Pt on the electrodes is strongly limited.

This is then also reflected in the morphology of the resulting deposits, which is shown in the SEM images of the electrodes after the electrodeposition experiment (Figure 5a-c). In general, the electrodes are composed of a variety of small, well-connected Pt deposits with an island-like morphology. The lateral size of the deposits varies with respect to the applied deposition potential in the order -0.1 > -0.15 > -0.25 V_{RHE}. The average island diameter at the most cathodic deposition potential of -0.25 V_{RHE} (Figure 5c) is on the order of 10 nm, while de-

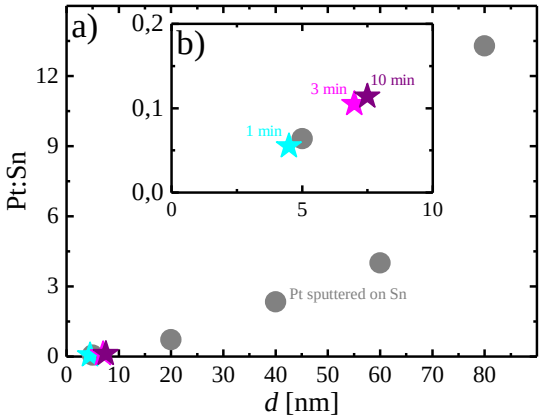

Figure 6. Ratio of the Pt:Sn counts vs. the thickness, *d*, of the Pt deposit on Sn. The counts were obtained by measuring an EDX at 15 kV. The Pt layer was either prepared by sputter deposition (grey circles) or by electrochemical deposition for 1 (black star), 3 (red star) or 10 min (green star). While the full range of prepared samples is shown in a), the inset b) represents a zoom below 10 nm.

posits produced at -0.15 and -0.1 V_{RHE} have slightly larger dimensions. We conclude that the higher overpotential with respect to the HER on Pt at more cathodic potentials, causes the evolution of large amounts of H_2 on the surface of the Pt deposits. This ongoing reaction shields the Pt deposits from successive reduction of ions on their surface, while pure Sn sites are more exposed to the solution. Hence, Pt deposition on Sn is favored over the deposition on the Pt islands and smaller deposits are formed. This, however, implies that the average film thickness would not grow significantly during longer potential application, since most of the charge in the plateau phase would correspond to HER as soon as a high coverage on the electrode is achieved. It shall be mentioned at this point, that the effect of the high H_2 concentration in the vicinity of the electrode on the chemical stability of the $PtCl_4^{2-}$-complex was not studied here and a certain amount of chemical deposition due to reduction of Pt ions by H_2 cannot be fully excluded.

To further investigate the Pt deposition efficiency during the plateau phase, electrochemical deposition using the same procedure employed earlier was carried out at a constant potential of -0.25 V_{RHE}, varying the time from 68, 190 to 626 s (termed 1, 3 and 10 min hereafter). While the shortest deposition time is still in the region where the current increases, the other two deposition times were chosen such that the current plateau was reached, remaining at these condi-

tions for a different amount of time. The equivalent thickness of the resulting deposits was analyzed by EDX, where the electron beam penetrates through the Pt surface layer into the Sn metal. Therefore, the ratio of the X-rays emitted by Pt and Sn contains intrinsic information about the thickness of the Pt overlayer. The Pt layer thickness was estimated by comparing the Pt:Sn count ratio to those obtained from samples of defined Pt layer thickness on Sn, obtained by sputter deposition. The thickness of the sputter-deposited Pt films was controlled using a quartz crystal microbalance (QCMB) in the deposition chamber. As expected, the Pt:Sn ratio of the sputter-deposited samples increases with nominal Pt layer thickness, as shown in Figure 6 (grey circles). While the increase is nearly linear for thin Pt layers, a strong increase is observed for thicker layers (e.g., Pt:Sn ≈ 13 for 80 nm), which we hypothesize to originate from the lower beam penetration through the Pt layer as the thickness increases. Nevertheless, the general correlation of the Pt:Sn count ratio and the Pt overlayer thickness can be used to estimate the thickness of the Pt deposits on Sn, which have a comparably small Pt:Sn ratio of 0.055, 0.105 and 0.114 for 1, 3 and 10 min of electrodeposition, shown in the inset of Figure 6 (turquoise, magenta and purple stars). The obtained values correspond approximately to a thickness of 4 nm after 1 min and 7-8 nm after 3 and 10 min. We therefore conclude that the efficiency of Pt deposition is highest in the initial phase, where most of the Sn surface sites are available. On the other hand, the deposition process slows down significantly in the plateau phase, where a large fraction of the current originates from HER on the Pt deposits, shielding the electrode surface.

Electrochemical analysis of Pt deposits on Sn.—Since the preceding EDX analysis showed that the approximate thickness of the deposits does not increase significantly during the current plateau phase, the analysis of this effect was complemented by measuring CVs of the electrodeposits in borate buffer solution, provided in Figure 7a). First, it has to be noted that the general shape of the CV for all prepared deposits is similar, whereas the oxidative, as well as the reductive charge of the sample prepared at 1 min is significantly lower compared to 3 and 10 min. Furthermore, the charge of the CV of the electrodeposit after 3 min compares well with that after 10 min deposition time, indicating a similar exposed surface area. Since the main deposition time for both samples (3

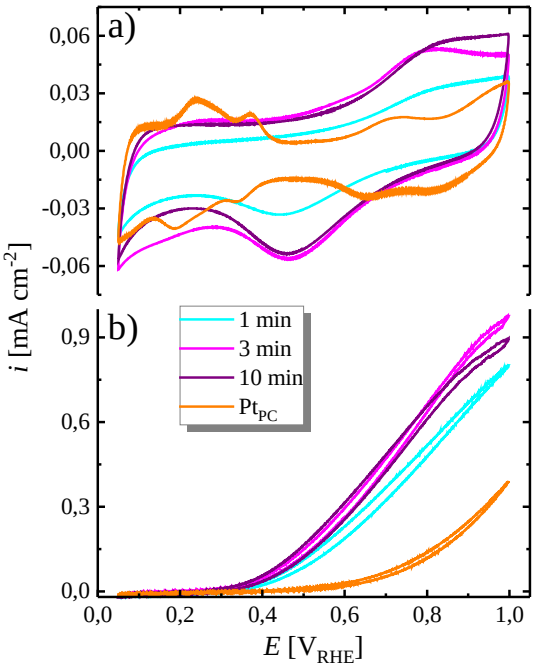

Figure 7. a) CVs of electrochemically deposited Pt on Sn after a deposition for 1 (turquoise line), 3 (magenta line) and 10 min (purple line) at -0.25 V_{RHE} in Ar-saturated borate buffer (0.05 M, pH = 8.4) at a scan rate of 20 mV s^{-1} between 0.05 and 1.00 V_{RHE}, measured in stagnant electrolyte at room temperature. The CV of a polycrystalline Pt disk is shown as comparison (orange line). b) CVs of the same deposits after saturating the electrolyte with CO and scanning at 10 mV s^{-1} and a rotation rate of 400 rpm.

and 10 min) was passed during the plateau phase, the previously stated hypothesis that the deposition during this phase is strongly limited, while the major fraction of the charge originates from HER, is hereby confirmed. Moreover, the charge of the CVs in the oxide formation / removal region ($E > 0.4$ V_{RHE}) after Pt electrodeposition on Sn is higher compared to a bare Pt_{PC} disk. This is indicative of a high roughness factor (*rf*) of the Pt deposit on Sn, stemming from the highly structured surface compared to the flat, polished Pt electrode ($rf \approx 1.3$, extracted from the averaged H_{upd} charge in the anodic and cathodic scan). Furthermore, the electrochemical features on the Pt electrodeposits are very different from pure Pt_{PC} (orange line), especially at low potentials, where no distinct adsorption features for the H_{upd} are present on the electrodeposits. Additionally, the oxidation and reduction potential of the Pt electrodeposit is further separated compared to pure Pt, indicating a larger required overpotential for this process.

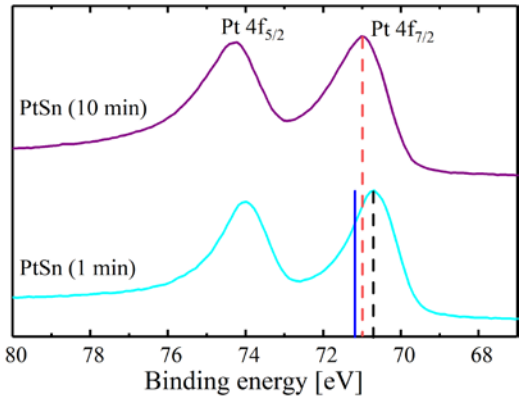

Figure 8. XPS spectra of the Pt 4f region of PtSn samples after 1 min (turquoise line) and after 10 min (purple line) of electrochemical deposition. The blue solid line represents the Pt $4f_{7/2}$ binding energy for a pure Pt sample reported in the literature.[35–37]

The differences of the CVs compared to pure Pt can be understood by considering the presence of Sn in the vicinity of Pt. In fact, Pt-Sn alloys are known to exhibit distinct electrochemical features compared to Pt, visible e.g., in acidic electrolyte.[31,32] This can also be observed in the CVs shown in Figure 7a, where the oxidative and reductive features of the PtSn catalysts extend over a wider potential range compared to pure Pt (orange line) and the features in the potential window of the Hupd are not clearly resolved. Since such alloys are furthermore well-known to be excellent catalysts for the oxidation of carbon monoxide,[33,34] the electrolyte was saturated with CO, reporting steady-state CVs in Figure 7b) in order to probe the deposits for a possible alloy formation. Compared to Pt_{PC} (≈0.6 V_{RHE}), the onset potential of the oxidation of CO on the Pt deposits on Sn is shifted approximately 200 mV cathodic, which is comparable to the results presented in the literature for PtSn alloys.[34] Additionally, depositing Pt for 1 min results in a slightly lower activity towards the CO oxidation, which might be mainly related to the incomplete coverage of Pt on the Sn surface, hence a lower *rf* value, as indicated by the CV in Figure 7a). Therefore, the formation of a Pt-Sn alloy upon electrochemical deposition from borate buffer solution was confirmed by the CVs and CO oxidation experiments.

To further confirm the formation of the PtSn surface alloy, XPS was used to analyze the Sn samples that were exposed to 1 min and 10 min of Pt deposition. Figure 8 shows the spectra of the Pt 4f level for the two PtSn samples obtained at different deposition times (1 min and 10 min). The photoelectron peaks of the PtSn samples show a shift towards lower biding energies when compared to a pure Pt reference obtained from literature.35–37 Moreover, the Sn ample on which Pt was deposited for 1 min shows the largest shift compared to the Pt reference, with a deviation of 0.5 eV. The nature of this shift can be explained by the formation of an alloy between the deposited Pt and Sn on the surface of the electrode.35,36 On the other hand, the sample on which Pt was deposited for 10 min shows a smaller shift from the pure Pt reference, suggesting that the alloying between Pt and Sn is most likely diluted by pure Pt that couldn't reach the Sn surface.

Conclusions

Herein, we report insights into the electrochemical deposition process of Pt on Sn from a pH neutral borate buffer solution. Under the tested conditions, Pt electrodeposition was fully prevented when the Sn surface was covered with an oxide layer, even though high cathodic overpotentials were applied. In addition, the same general principle of self-limitation was found to be valid for Pt deposition on a Pt electrode and for a Pt covered Au surface. We conclude from these findings that the concept of surface oxide blocking, introduced here for the first time, has potential to be further developed into a controllable self-limiting deposition process. Such a process could, e.g., be based on the deposition of a Pt-ML on a metallic surface, thereafter oxidizing the surface of the Pt deposit and stopping further deposition.

Furthermore, a method was developed to deposit Pt on Sn in the absence of surface oxide, while HER proceeded on the Pt deposits. In this study, the effect of the applied deposition potential and -time on the resulting morphology were investigated. After an initiation period of a constant potential deposition, where the largest fraction of the Sn surface was covered with Pt, the deposition process was found to be self-limiting due to ongoing HER on Pt. Hence, increasing the deposition time resulted essentially in the same deposited layer thickness (<10 nm) and similar electrochemical behavior of the electrodes. Deposited Pt was found to alloy immediately with the Sn substrate, providing a high activity towards the oxidation of CO. In conclusion, the deposition procedure presented here can be used to reliably obtain Pt over-

layers in the nanometer range, alloyed with the substrate in a single step.

Acknowledgement

Special thanks are directed to Thomas Mittermeier for consulting the authors during the time frame of this work. Financial support in the frame of the European Community's Seventh Framework Program (FP7/2013-2016) for the Fuel Cell and Hydrogen Joint Technology Initiative under grant agreement CATAPULT n°.325268 is gratefully acknowledged. Furthermore, the authors would like to thank Katia Rodewald for supplying SEM images.

Contributions

H.E. and H.G proposed the idea and outline of the research. J.N.S. designed and performed the experiments and P.L.T. carried out the XPS experiments and data analysis. J.N.S. wrote the manuscript under the supervision of H.E.

References

1 Toyota Motor Co. (accessed 01/04/2019), http://newsroom.toyota.co.jp/en/detail/4198334/.
2 Hyundai Motor Co. (accessed 05/18/2017), http://globalpr.hyundai.com/prCenter/news/newsView.do?dID=1581.
3 Honda Motor Co., Ltd. (accessed 01/04/2019), http://hondanews.com/honda-automobiles/channels/clarity-fuel-cell-press-releases/releases/southern-california-customers-take-delivery-of-new-2017-honda-clarity-fuel-cell-sedan.
4 U.S. Department of Energy (accessed 01/04/2019), http://energy.gov/sites/prod/files/2014/02/f8/fctt_roadmap_june2013.pdf.
5 K. Kinoshita, J. Electrochem. Soc. 137, 845 (1990).
6 C. A. Reiser, L. Bregoli, T. W. Patterson, J. S. Yi, J. D. Yang, M. L. Perry and T. D. Jarvi, Electrochem. Solid-State Lett. 8, A273 (2005).
7 Y. Yu, H. Li, H. Wang, X.-Z. Yuan, G. Wang and M. Pan, J. Power Sources. 205, 10 (2012).
8 T. Mittermeier, A. Weiß, F. Hasché, G. Hübner and H. A. Gasteiger, J. Electrochem. Soc. 164, F127 (2017).
9 S. R. Brankovic, J. X. Wang and R. R. Adžić, Surf. Sci. 474, L173-L179 (2001).
10 S. Brimaud and R. J. Behm, J. Am. Chem. Soc. 135, 11716 (2013).
11 Y. Liu, D. Gokcen, U. Bertocci and T. P. Moffat, Science. 338, 1327 (2012).
12 I. Katsounaros, J. C. Meier, S. O. Klemm, A. A. Topalov, P. U. Biedermann, M. Auinger and K. J.J. Mayrhofer, Electrochem. Commun. 13, 634 (2011).
13 Y. Liu, C. M. Hangarter, D. Garcia and T. P. Moffat, Surf. Sci. 631, 141 (2015).
14 A. F. Holleman, E. Wiberg and N. Wiberg, Lehrbuch der anorganischen Chemie, de Gruyter, Berlin, New York (2007).
15 M. Pourbaix, Atlas of electrochemical equilibria in aqueous solutions, National Association of Corrosion Engineers, Houston, Texas (1974).
16 S. D. Kapusta and N. Hackerman, Electrochim. Acta. 25, 1625 (1980).
17 El Wakkad, S. E. S., El Din, A. M. Shams and El Sayed, Jeannette A., J. Chem. Soc., 3103 (1954).
18 S. N. Shah and D.E. Davies, Electrochim. Acta. 8, 663 (1963).
19 A. Palacios-Padrós, F. Caballero-Briones, I. Díez-Pérez and F. Sanz, Electrochim. Acta. 111, 837 (2013).
20 C. T. Campbell, Faraday Trans. 92, 1435 (1996).
21 D. C. Harris, Quantitative chemical analysis, W. H. Freeman; Palgrave distributor, New York, Basingstoke (2007).
22 O. Azizi, M. Jafarian, F. Gobal, H. Heli and M. G. Mahjani, Int. J. Hydrogen Energ. 32, 1755 (2007).
23 K. C. Neyerlin, W. Gu, J. Jorne and H. A. Gasteiger, J. Electrochem. Soc. 154, B631 (2007).
24 W. Sheng, H. A. Gasteiger and Y. Shao-Horn, J. Electrochem. Soc. 157, B1529 (2010).
25 P. J. Rheinländer, J. Herranz, J. Durst and H. A. Gasteiger, J. Electrochem. Soc. 161, F1448 (2014).
26 J. Durst, A. Siebel, C. Simon, F. Hasché, J. Herranz and H. A. Gasteiger, Energy Environ. Sci. 7, 2255 (2014).
27 W. Sheng, Z. Zhuang, M. Gao, J. Zheng, J. G. Chen and Y. Yan, Nat. Commun. 6, 5848 (2015).
28 D. Strmcnik, D. Tripkovic, D. van der Vliet, V. Stamenkovic and N. M. Marković, Electrochem. Commun. 10, 1602 (2008).
29 R. T. Ferrell and D. M. Himmelblau, AIChE J. 13, 702 (1967).
30 S. H. Lee and J. C. Rasaiah, J. Chem. Phys. 135, 124505 (2011).
31 M. C. Santos and L.O.S. Bulhões, Electrochim. Acta. 48, 2607 (2003).
32 F. Colmati, E. Antolini and E. R. Gonzalez, Electrochim. Acta. 50, 5496 (2005).
33 H. A. Gasteiger, N. M. Marković and P. N. Ross, J. Phys. Chem. 99, 8945 (1995).
34 H. A. Gasteiger, N. M. Marković and P. N. Ross, Catal. Lett. 36, 1 (1996).
35 J. M. Ramallo-López, G. F. Santori, L. Giovanetti, M. L. Casella, O. A. Ferretti and F. G. Requejo, J. Phys. Chem. B. 107, 11441 (2003).
36 G. J. Siri, J. M. Ramallo-López, M. L. Casella, J. L.G. Fierro, F. G. Requejo and O. A. Ferretti, Appl. Catal., A. 278, 239 (2005).
37 J. F. Moulder and J. Chastain, Handbook of X-ray Photoelectron Spectroscopy, Update, Perkin-Elmer Corporation, Eden Prairie, Minn. (1992).

4. Conclusions

The goal of the thesis was to understand basic principles of HOR and ORR electrocatalysis in acid and base and to provide guidelines for the development of novel catalysts. Another aim was to develop an understanding of the degradation phenomena in the anode and cathode catalyst layer of PEMFCs, as well as of H_2 and O_2 mass-transport processes within these electrodes. A further question to be answered was whether current state-of-the-art anion exchange membranes are suitable for the use in AEMFCs for automotive applications particularly with regards to low-temperature operation.

First of all, the significantly slower kinetics of the HOR in alkaline compared to acidic environment were addressed at the example of the Pt-Ru system. The preparation of Ru@Pt core-shell nanoparticles with different shell thickness and, most importantly, partially as well as fully Pt covered Ru cores enabled a distinction between the so-called bifunctional mechanism and the electronic effect. Clear evidence was found that fully Pt encapsulated Ru particles provide a much higher HOR/HER exchange current density compared to partially covered particles, demonstrating that Ru does not actively participate in the HOR mechanism by supplying hydroxide species on the surface of the particle.

Transitioning from electrocatalysis in alkaline media to AEMFCs, the conductivity of a state-of-the-art anion exchange membrane was investigated. In this frame, a method to establish a defined water content in the membrane while cooling the system below the freezing point of water was developed to measure the *HFR* at different temperatures. Additionally, an ex-situ experiment helped to identify the contribution of the contact resistance to the *HFR* in order to obtain the membrane conductivity. The analysis of the conductivity in hydroxide and, more drastically, in carbonate form at low temperature showed that AEMs are currently not applicable in the automotive field, since they would likely not allow for a successful freeze start-up.

Further studies focused on the more advanced PEMFCs, where we were able to describe the degradation of the anode catalyst layer during SUSD for the first time in low temperature fuel cells. The anode *ECSA*-loss was quantified along with the cathode,

showing that Ostwald ripening is the dominant SUSD ageing mechanism on the anode. Furthermore, an AST based on voltage cycling of the anode was designed to simulate anode degradation during SUSD without deteriorating the cathode catalyst layer. This AST enabled the determination of the HOR overpotential as a function of the *ECSA*-loss by the H_2 pump method. Furthermore, diluting the H_2 feed gas in the H_2 pump measurement revealed significant H_2 mass-transport losses after ageing. Finally, the analysis of the HOR overpotential as a function of the anode *rf* showed that future anodes with very low Pt loadings on the order of 25 $\mu g_{Pt}\,cm^{-2}$ are not capable to sustain low HOR overpotentials when exposed to similar ageing conditions.

Keeping the focus on degradation phenomena in the MEA, square wave and triangular wave voltage cycling profiles were applied to cathode catalyst layers while measuring various key performance indicators, such as *ECSA*, ORR activity, proton sheet resistance and O_2 mass-transport resistance. The introduction of a triangular wave with a hold at the vertex potentials provided evidence that the scan rate has little influence on cathode degradation, since this AST resulted in the same losses as the square wave voltage cycling AST (per cycle). Furthermore, exposing cathode catalyst layers with high and low Pt loadings to voltage cycling showed two different contributions to the O_2 mass-transport resistance. First of all, a non-linear dependency of the *rf* and the pressure independent O_2 mass-transport resistance was identified. Second, electrode degradation due to voltage cycling resulted in an additional O_2 mass-transport overpotential. Through our analysis, carbon corrosion could be excluded as a main contributor to degradation in the ASTs (up to 1 V_{RHE}). Furthermore, a voltage loss analysis of differential-flow H_2/air polarization curves showed high unassigned losses in cathodes with low *rf*, clarifying the necessity to improve the current in-situ diagnostic toolset for single cell tests. Finally, lowering the upper potential limit during the AST to 0.85 V_{RHE} resulted in a full conservation of the initial performance and therefore is a viable approach to extend PEMFC lifetime.

The above developed voltage cycling AST combined with a full voltage loss analysis was subsequently applied to a novel Pt_xY/C catalyst for the ORR. The synthesis of this catalyst was achieved by dispersing YCl_3 on a commercial Pt/C catalyst by freeze drying and subsequent heat treatment in H_2 atmosphere. While the high synthesis tempera-

ture yielded large particles with a comparably small *ECSA*, this method was able to yield a sufficient quantity of Pt_xY/C for PEMFC testing. After physical-chemical characterization and RDE testing of the electrocatalyst, single cell tests showed that the catalyst is more durable compared to the commercial Pt/C catalyst, but a comparison with Pt particles of a similar size as the Pt_xY/C catalyst showed that the high stability originates simply from a particle size effect. Furthermore, the low *ECSA* of the Pt_xY/C catalyst resulted in high unassigned voltage losses due to the low *rf*. Nevertheless, the stability of the catalyst preserved a large fraction of the ORR activity and therefore caused a superior H_2/air performance of Pt_xY/C compared to Pt/C after the voltage cycling AST.

In the last manuscript of this thesis, we studied the electrochemical deposition process of Pt on Sn as a model system for the development of novel catalysts consisting of extended monolayer-thick Pt films supported on conductive oxides. It was possible to show that the deposition of Pt on Sn in borate buffer solution is completely suppressed by Sn oxide species on the surface, even at large applied overpotentials. Furthermore, the CO oxidation behavior of the deposits in RDE experiments provided evidence that the final product of the deposition is an alloy of Pt and Sn. The EDX analysis of the deposits on the metallic Sn electrode furthermore suggested that the deposition process is limited to approximately 10 nm at the applied conditions due to the blocking effect of the HER on the bimetallic Pt-Sn surface.

To conclude, this thesis contributed to the field of electrocatalysis and to the understanding of performance limitations and degradation mechanisms of ion exchange membrane fuel cells. The study on the HOR catalysis of Ru@Pt core-shell nanoparticles provided fundamental insights into the mechanism of the HOR in alkaline media, hence provides a guideline for the development of novel catalyst. Similarly, the conductivity measurement of an anion exchange membrane below the freezing point of water sheds light on the current limitations of AEMFCs and sketches a pathway to improve future membranes with respect to low temperature conductivity and CO_2 tolerance. Moreover, the presented studies on PEMFC ageing aid to understand the degradation phenomena on the anode and cathode during SUSD and voltage cycling. The quantification of H_2 as well as O_2 mass-transport losses helps to point out where future improvements regard-

ing MEA design and stability have to be achieved. For applications of fuel cell technology, reducing mass-transport resistances and enhancing lifetime are among the most crucial challenges. Finally, the development of novel ORR catalysts, such as Pt_xY/C or extended Pt films on conductive oxides helps to direct future research efforts to new pathways in order to reduce the overall Pt loading in the MEA, hence reduce the cost of automotive fuel cell systems.

5. Bibliography

1 United Nations Framework Convention on Climate Change (accessed 01/04/2019), https://unfccc.int/sites/default/files/english_paris_agreement.pdf.

2 United States Environmental Protection Agency (accessed 01/04/2019), https://www.epa.gov/ghgemissions/global-greenhouse-gas-emissions-data.

3 European Federation for Transport and Environment (accessed 01/04/2019), https://www.vcd.org/fileadmin/user_upload/Redaktion/Themen/Auto_Umwelt/CO2-Grenzwert/2018_04_CO2_emissions_cars_The_facts_report_final.pdf.

4 BMW AG (accessed 01/04/2019), https://www.press.bmwgroup.com/global/article/detail/T0285608EN/technical-specifications-of-the-bmw-i3-120-ah-and-the-bmw-i3s-120-ah-valid-from-11/2018?language=en.

5 BMW AG (accessed 01/04/2019), https://www.press.bmwgroup.com/global/article/detail/T0260191EN/specifications-bmw-1-series-5-door-hatch-120i-125i-m140i-m140i-xdrive-07/2016?language=en.

6 K. G. Gallagher, S. Goebel, T. Greszler, M. Mathias, W. Oelerich, D. Eroglu and V. Srinivasan, *Energy Environ. Sci.* **7,** 1555 (2014).

7 O. Gröger, H. A. Gasteiger and J.-P. Suchsland, *J. Electrochem. Soc.* **162,** A2605 (2015).

8 Toyota Motor Co. (accessed 01/04/2019), https://www.toyota.com/content/ebrochure/2018/mirai_FuelCellTech.pdf.

9 Strategic Analysis Inc. (accessed 01/04/2019), https://www.osti.gov/servlets/purl/1343975.

10 Strategic Analysis Inc. (accessed 01/04/2019), https://www.researchgate.net/profile/Brian_James5/publication/323176008_Mass_Production_Cost_Estimation_of_Direct_H2_PEM_Fuel_Cell_Systems_for_Transportation_Applications_2017_Update/links/5a8463cfa6fdcc201b9eeb48/Mass-Production-Cost-Estimation-of-Direct-H2-PEM-Fuel-Cell-Systems-for-Transportation-Applications-2017-Update.pdf.

11 Landeshauptstadt München (accessed 01/04/2019), https://www.muenchen.de/rathaus/dam/jcr:8be559ce-8285-4212-b78c-51637334b79c/jt180703.pdf.

12 Stadtwerke München GmbH (accessed 01/04/2019), https://www.muenchen.de/leben/strom-erdgas-fernwaerme-wasser/strom.html.

13 New West Technologies, LLC (accessed 01/04/2019), https://afdc.energy.gov/files/u/publication/evse_cost_report_2015.pdf.

14 ARK Invest (accessed 01/04/2019), https://ark-invest.com/research/supercharger-cost-comparison#fn-6240-2.

15 Tesla, Inc. (accessed 12/05/2018), https://www.tesla.com/de_DE/supercharger.

16 National Renewable Energy Laboratory (accessed 07/17/2018), https://www.nrel.gov/docs/fy13osti/56412.pdf.

17 I. A. Richardson, J. T. Fisher, P. E. Frome, B. O. Smith, S. Guo, S. Chanda, M. S. McFeely, A. M. Miller and J. W. Leachman, *Int. J. Hydrogen Energ.* **40,** 8122 (2015).

18 manager magazin Verlagsgesellschaft mbH (accessed 01/04/2019), http://www.manager-magazin.de/unternehmen/autoindustrie/volkswagen-wie-teuer-wird-der-abgasskandal-a-1100826.html.

19 Joint Research Center (accessed 01/04/2019), https://iet.jrc.ec.europa.eu/about-jec/downloads.

20 AG Energiebilanzen e.V. (accessed 01/04/2019), https://ag-energiebilan-zen.de/index.php?article_id=29&fileName=20181019_brd_stromerzeugung1990-2017.pdf.

21 Umwelt Bundesamt (accessed 01/04/2019), https://www.umweltbundesamt.de/sites/default/files/medien/1410/publikationen/2018-05-04_climate-change_11-2018_strommix-2018_0.pdf.

22 01/04/2019), https://www.iea.org/publications/freepublications/publication/TechnologyRoadmapHydrogenandFuelCells.pdf.

23 K. Bareiß, C. de La Rua, M. Möckl and T. Hamacher, *Appl. Energy*. **237,** 862 (2019).

24 Toyota Motor Co. (accessed 01/04/2019), https://media.toyota.co.uk/wp-content/files_mf/1444919532151015MToyotaMiraiTechSpecFinal.pdf.

25 International Energy Agency (accessed 01/04/2019), http://ieahydrogen.org/Activities/Task-28/Task-28-report_final_v2_ECN_12_2_v3.aspx.

26 Greentech Media (accessed 01/04/2019), https://www.greentechmedia.com/articles/read/desertec-update-funding#gs.DXrdOMI.

27 W. Kempton and J. Tomić, *J. Power Sources.* **144,** 280 (2005).

28 International Electrotechnical Commission (accessed 01/04/2019), https://www.iec.ch/whitepaper/pdf/iecWP-energystorage-LR-en.pdf.

29 J. Neubauer and A. Pesaran, *J. Power Sources.* **196,** 10351 (2011).

30 International Energy Agency (accessed 01/04/2019), https://webstore.iea.org/global-ev-outlook-2018.

31 Hyundai Motor Co. (accessed 01/04/2019), https://www.hyundai.com/worldwide/en/eco/ix35-fuelcell/highlights.

32 Toyota Motor Co. (accessed 01/04/2019), http://newsroom.toyota.co.jp/en/detail/4198334/.

33 Honda Motor Co., Ltd. (accessed 01/04/2019), http://hondanews.com/honda-automobiles/channels/clarity-fuel-cell-press-releases/releases/southern-california-customers-take-delivery-of-new-2017-honda-clarity-fuel-cell-sedan.

34 Mercedes-Benz Sales Germany (accessed 01/04/2019), https://media.daimler.com/marsMediaSite/en/instance/ko/Mercedes-Benz-GLC-F-CELL-Market-launch-of-the-worlds-first-electric-vehicle-featuring-fuel-cell-and-plug-in-hybrid-technology.xhtml?oid=41813012.

35 Audi AG (accessed 01/04/2019), https://www.audi-mediacenter.com/de/pressemitteilungen/audi-ag-jahrespressekonferenz-2018-o-ton-paket-vorstandsreden-stadler-seitz-9928.

36 BMW AG (accessed 01/04/2019), https://www.press.bmwgroup.com/deutschland/article/detail/T0268845DE/rede-und-praesentation-von-harald-krueger-vorsitzender-des-vorstands-der-bmw-ag-bilanzpressekonferenz-2017.

37 General Motors: and Honda Clarity Fuel Cell, *Fuel Cells Bulletin.* **2017,** 8 (2017).

38 Tesla, Inc. (accessed 01/04/2019), https://www.tesla.com/semi.

39 Nikola Motor Co. (accessed 01/04/2019), https://nikolamotor.com/press_releases/nikola-launches-stunning-truck-for-european-market-53.

40 Hyundai Motor Co. (accessed 01/04/2019), https://www.hyundai.news/eu/technology/hyundai-motor-presents-first-look-at-new-truck-with-a-fuel-cell-powertrain-ahead-of-iaa-commercial-vehicles-2018-announcement/.

41 Toyota Motor Co. (accessed 01/04/2019), https://newsroom.toyota.co.jp/en/corporate/23722307.html.

42 01/04/2019), https://www.alstom.com/press-releases-news/2018/9/world-premiere-alstoms-hydrogen-trains-enter-passenger-service-lower.

43 ABB Ltd. (accessed 01/04/2019), https://new.abb.com/news/detail/5360/abb-and-ballard-power-systems-to-jointly-develop-zero-emission-fuel-cell-power-plant-for-shipping-industry.

44 TÜV Süd AG (accessed 01/04/2019), https://www.tuev-sued.de/company/press/press-archive/germany-had-the-highest-increase-of-hydrogen-refuelling-stations-worldwide-in-2017.

45 Statista GmbH (accessed 01/04/2019), https://www.statista.com/statistics/525544/number-of-petrol-fuel-filling-stations-in-germany/.

46 Strategy Advisory Committee of the Technology Roadmap for Energy Saving and New Energy Vehicles and the Society of Automotive Engineers of China (accessed 01/04/2019), http://www.ihfca.org.cn/file/FCV%20Tech%20Roadmap.pdf.

47 Ministry of Economy, Trade and Industry (accessed 01/04/2019), http://www.meti.go.jp/english/press/2017/pdf/1226_003a.pdf.

48 M. Doyle and G. Rajendran, *Handbook of Fuel Cells,* 1st ed., W. Vielstich, A. Lamm and H. A. Gasteiger, p. 351, John Wiley & Sons Ltd., Chichester (2009).

49 K. D. Kreuer, *Handbook of Fuel Cells,* 1st ed., W. Vielstich, A. Lamm and H. A. Gasteiger, p. 420, John Wiley & Sons Ltd., Chichester (2009).

50 A. Orfanidi, P. Madkikar, H. A. El-Sayed, G. S. Harzer, T. Kratky and H. A. Gasteiger, *J. Electrochem. Soc.* **164,** F418 (2017).

51 M. Dou, M. Hou, F. Wang, D. Liang, Q. Zhao, Z. Shao and B. Yi, *J. Electrochem. Soc.* **161,** F1231 (2014).

52 C. Simon, F. Hasché and H. A. Gasteiger, *J. Electrochem. Soc.* **164,** F591 (2017).

53 C. Simon, D. Kartouzian, D. Müller, F. Wilhelm and H. A. Gasteiger, *J. Electrochem. Soc.* **164,** F1697 (2017).

54 J. S. Allen, S. Y. Son and S. H. Collicott, *Handbook of Fuel Cells,* 1st ed., W. Vielstich, H. Yokokawa and H. A. Gasteiger, p. 687, John Wiley & Sons Ltd., Chichester (2009).

55 A. B. LaConti, M. Hamdan and R. C. McDonald, *Handbook of Fuel Cells,* 1st ed., W. Vielstich, A. Lamm and H. A. Gasteiger, p. 647, John Wiley & Sons Ltd., Chichester (2009).

56 N. Konno, S. Mizuno, H. Nakaji and Y. Ishikawa, *SAE Int. J. Alt. Power.* **4,** 123 (2015).

57 J. Durst, C. Simon, F. Hasché and H. A. Gasteiger, *J. Electrochem. Soc.* **162,** F190 (2015).

58 G. S. Harzer, J. N. Schwämmlein, A. M. Damjanović, S. Ghosh and H. A. Gasteiger, *J. Electrochem. Soc.* **165,** F3118 (2018).

59 B. Han, C. E. Carlton, A. Kongkanand, R. S. Kukreja, B. R. Theobald, L. Gan, R. O'Malley, P. Strasser, F. T. Wagner and Y. Shao-Horn, *Energy Environ. Sci.* **8,** 258 (2015).

60 T. A. Greszler, D. Caulk and P. Sinha, *J. Electrochem. Soc.* **159,** F831 (2012).

61 J. P. Owejan, J. E. Owejan and W. Gu, *J. Electrochem. Soc.* **160,** F824 (2013).

62 A. Kongkanand and M. F. Mathias, *J. Phys. Chem. Lett.* **7,** 1127 (2016).

63 G. S. Harzer, A. Orfanidi, H. El-Sayed, P. Madkikar and H. A. Gasteiger, *J. Electrochem. Soc.* **165,** F770 (2018).

64 T. R. Garrick, T. E. Moylan, V. Yarlagadda and A. Kongkanand, *J. Electrochem. Soc.* **164,** F60 (2017).

65 S. Jomori, K. Komatsubara, N. Nonoyama, M. Kato and T. Yoshida, *J. Electrochem. Soc.* **160,** F1067 (2013).

66 V. Yarlagadda, M. K. Carpenter, T. E. Moylan, R. S. Kukreja, R. Koestner, W. Gu, L. Thompson and A. Kongkanand, *ACS Energy Lett.* **3,** 618 (2018).

67 U.S. Department of Energy (accessed 01/04/2019), http://energy.gov/sites/prod/files/2014/02/f8/fctt_roadmap_june2013.pdf.

68 J. N. Schwämmlein, P. J. Rheinländer, Y. Chen, K. T. Freyer and H. A. Gasteiger, *ECS Trans.* **80,** 927 (2017).

69 H. A. Gasteiger, J. E. Panels and S. G. Yan, *J. Power Sources.* **127,** 162 (2004).

70 R. Mukundan, G. James, J. Davey, D. Langlois, D. Torraco, W. Yoon, A. Z. Weber and R. Borup, *ECS Trans.* **41,** 613 (2011).

71 P. J. Ferreira, G. J. la O', Y. Shao-Horn, D. Morgan, R. Makharia, S. Kocha and H. A. Gasteiger, *J. Electrochem. Soc.* **152,** A2256 (2005).

72 Y. Shao-Horn, P. Ferreira, G. J. La O', D. Morgan, H. A. Gasteiger and R. Makharia, *ECS Trans.* **1,** 185 (2006).

73 Y. Shao-Horn, W. C. Sheng, S. Chen, P. J. Ferreira, E. F. Holby and D. Morgan, *Top. Catal.* **46,** 285 (2007).

74 J. Zhang, B. A. Litteer, W. Gu, H. Liu and H. A. Gasteiger, *J. Electrochem. Soc.* **154,** B1006 (2007).

75 S. G. Bratsch, *J. Phys. Chem. Ref. Data.* **18,** 1 (1989).

76 J. P. Meyers and R. M. Darling, *J. Electrochem. Soc.* **153,** A1432 (2006).

77 A. P. Young, J. Stumper and E. Gyenge, *J. Electrochem. Soc.* **156,** B913 (2009).

78 R. L. Borup, D. D. Papadias, R. Mukundan, D. Spernjak, D. A. Langlois, R. Ahluwalia, K. L. More and S. Grot, *ECS Trans.* **69,** 1029 (2015).

79 T. Mittermeier, A. Weiß, F. Hasché, G. Hübner and H. A. Gasteiger, *J. Electrochem. Soc.* **164,** F127 (2017).

80 A. Damjanovic, A. Dey and J. O.'M. Bockris, *J. Electrochem. Soc.* **113,** 739 (1966).

81 S. Cherevko, S. Geiger, O. Kasian, A. Mingers and K. J.J. Mayrhofer, *J. Electroanal. Chem.* **773,** 69 (2016).

82 S. Cherevko, S. Geiger, O. Kasian, A. Mingers and K. J.J. Mayrhofer, *J. Electroanal. Chem.* **774,** 102 (2016).

83 H. A. Gasteiger, W. Gu, B. Litteer, R. Makharia, B. Brady, M. Budinski, E. Thompson, F. T. Wagner, S. G. Yan and P. T. Yu, *Mini-Micro Fuel Cells,* 1st ed., S. Kakaç, A. Pramuanjaroenkij and L. Vasiliev, p. 225, Springer Netherlands, Dordrecht (2008).

84 T. Engl, L. Gubler and T. J. Schmidt, *Energy Technol.* **4,** 65 (2016).

85 Y. Y. Jo, E. Cho, J. H. Kim, T.-H. Lim, I.-H. Oh, S.-K. Kim, H.-J. Kim and J. H. Jang, *J. Power Sources.* **196,** 9906 (2011).

86 W. Gu, R. N. Carter, P. T. Yu and H. A. Gasteiger, *ECS Trans.* **11,** 963 (2007).

87 J. H. Kim, E. A. Cho, J. H. Jang, H. J. Kim, T. H. Lim, I. H. Oh, J. J. Ko and S. C. Oh, *J. Electrochem. Soc.* **157,** B104 (2010).

88 J. H. Kim, Y. Yeon Jo, E. A. Cho, J. H. Jang, H. J. Kim, T.-H. Lim, I.-H. Oh, J. J. Ko and I. J. Son, *J. Electrochem. Soc.* **157,** B633 (2010).

89 F. T. Wagner, S. G. Yan and P. T. Yu, *Handbook of Fuel Cells,* 1st ed., W. Vielstich, H. Yokokawa and H. A. Gasteiger, p. 250, John Wiley & Sons Ltd., Chichester (2009).

90 T. W. Patterson and R. M. Darling, *Electrochem. Solid-State Lett.* **9,** A183 (2006).

91 Y. H. Lai and D. A. Dillard, *Handbook of Fuel Cells,* 1st ed., W. Vielstich, H. Yokokawa and H. A. Gasteiger, p. 403, John Wiley & Sons Ltd., Chichester (2009).

92 E. Endoh, *Handbook of Fuel Cells,* 1st ed., W. Vielstich, H. Yokokawa and H. A. Gasteiger, p. 361, John Wiley & Sons Ltd., Chichester (2009).

93 M. Pourbaix, *Atlas of electrochemical equilibria in aqueous solutions,* National Association of Corrosion Engineers, Houston, Texas (1974).

94 K. C. Neyerlin, W. Gu, J. Jorne and H. A. Gasteiger, *J. Electrochem. Soc.* **154,** B631 (2007).

95 U. A. Paulus, T. J. Schmidt, H. A. Gasteiger and R. J. Behm, *J. Electroanal. Chem.* **495,** 134 (2001).

96 H. A. Gasteiger, S. S. Kocha, B. Sompalli and F. T. Wagner, *Appl. Catal., B.* **56,** 9 (2005).

97 M. Warshay and P. R. Prokopius, *J. Power Sources.* **29,** 193 (1990).

98 B. B. Blizanac, P. N. Ross and N. M. Marković, *Electrochim. Acta.* **52,** 2264 (2007).

99 S. Lu, J. Pan, A. Huang, L. Zhuang and J. Lu, *Proc. Natl. Acad. Sci. U.S.A.* **105,** 20611 (2008).

100 Z. Chen, J.-P. Dodelet and J. Zhang Dodelet, *Non-Noble Metal Fuel Cell Catalysts*, Wiley-VCH Verlag GmbH & Co. KGaA, Weinheim, Germany (2014).

101 W. Sheng, H. A. Gasteiger and Y. Shao-Horn, *J. Electrochem. Soc.* **157,** B1529 (2010).

102 P. J. Rheinländer, J. Herranz, J. Durst and H. A. Gasteiger, *J. Electrochem. Soc.* **161,** F1448 (2014).

103 D. Strmcnik, M. Uchimura, C. Wang, R. Subbaraman, N. Danilovic, van der Vliet, Dennis, A. P. Paulikas, V. R. Stamenkovic and N. M. Marković, *Nat. Chem.* **5,** 300 (2013).

104 I. Ledezma-Yanez, W. D. Z. Wallace, P. Sebastián-Pascual, V. Climent, J. M. Feliu and Koper, Marc T. M., *Nat. Energy.* **2,** 17031 (2017).

105 W. Sheng, Z. Zhuang, M. Gao, J. Zheng, J. G. Chen and Y. Yan, *Nat. Commun.* **6,** 5848 (2015).

106 J. R. Varcoe, P. Atanassov, D. R. Dekel, A. M. Herring, M. A. Hickner, P. A. Kohl, A. R. Kucernak, W. E. Mustain, K. Nijmeijer, K. Scott, T. Xu and L. Zhuang, *Energy Environ. Sci.* **7,** 3135 (2014).

107 L. Geniès, R. Faure and R. Durand, *Electrochim. Acta.* **44,** 1317 (1998).

108 C. K. Mittelsteadt and H. Liu, *Handbook of Fuel Cells,* 1st ed., W. Vielstich, H. Yokokawa and H. A. Gasteiger, p. 345, John Wiley & Sons Ltd., Chichester (2009).

109 H. Yanagi and K. Fukuta, *ECS Trans.* **16,** 257 (2008).

110 K. N. Grew, X. Ren and D. Chu, *Electrochem. Solid-State Lett.* **14,** B127 (2011).

111 J. N. Schwämmlein, B. M. Stühmeier, K. Wagenbauer, H. Dietz, V. Tileli, H. A. Gasteiger and H. A. El-Sayed, *J. Electrochem. Soc.* **165,** H229-H239 (2018).

112 C. Roy, B. P. Knudsen, C. M. Pedersen, A. Velázquez-Palenzuela, L. H. Christensen, C. D. Damsgaard, I. E. L. Stephens and I. Chorkendorff, *ACS Catal.* **8,** 2071 (2018).

113 J. N. Schwämmlein, G. S. Harzer, P. Pfändner, A. Blankenship, H. A. El-Sayed and H. A. Gasteiger, *J. Electrochem. Soc.* **165,** J3173 (2018).

114 U. A. Paulus, T. J. Schmidt and H. A. Gasteiger, *Handbook of Fuel Cells*, 1st ed., W. Vielstich, A. Lamm and H. A. Gasteiger, p. 555, John Wiley & Sons Ltd., Chichester (2009).

115 K. Shinozaki, Y. Morimoto, B. S. Pivovar and S. S. Kocha, *J. Power Sources.* **325,** 745 (2016).

116 Y. Garsany, I. L. Singer and K. E. Swider-Lyons, *Journal of Electroanalytical Chemistry*. **662,** 396 (2011).

117 R. D. Deegan, O. Bakajin, T. F. Dupont, G. Huber, S. R. Nagel and T. A. Witten, *Nature*. **389,** 827 (1997).

118 P. J. Rheinländer, S. Henning, J. Herranz and H. A. Gasteiger, *ECS Trans.* **50,** 2163 (2013).

119 J. Zheng, Y. Yan and B. Xu, *J. Electrochem. Soc.* **162,** F1470-F1481 (2015).

120 G. S. Harzer, *Boosting High Current Density Performance of Durable, Low Pt-Loaded PEM Fuel Cells*, PhD Thesis, Technical University of Munich, Munich, Germany (2018).

121 K. C. Neyerlin, W. Gu, J. Jorne, A. Clark and H. A. Gasteiger, *J. Electrochem. Soc.* **154,** B279 (2007).

122 R. Makharia, M. F. Mathias and D. R. Baker, *J. Electrochem. Soc.* **152,** A970 (2005).

123 D. R. Baker, D. A. Caulk, K. C. Neyerlin and M. W. Murphy, *J. Electrochem. Soc.* **156,** B991 (2009).

124 P. Zihrul, I. Hartung, S. Kirsch, G. Huebner, F. Hasché and H. A. Gasteiger, *J. Electrochem. Soc.* **163,** F492 (2016).

125 K. C. Neyerlin, W. Gu, J. Jorne and H. A. Gasteiger, *J. Electrochem. Soc.* **153,** A1955 (2006).

126 J. Durst, A. Siebel, C. Simon, F. Hasché, J. Herranz and H. A. Gasteiger, *Energy Environ. Sci.* **7,** 2255 (2014).

127 J. Durst, C. Simon, A. Siebel, P. J. Rheinländer, T. Schuler, M. Hanzlik, J. Herranz, F. Hasché and H. A. Gasteiger, *ECS Trans.* **64,** 1069 (2014).

128 J. N. Schwämmlein, P. J. Rheinländer, Y. Chen, K. F. Freyer and H. A. Gasteiger, *J. Electrochem. Soc.* **165,** F1312 (2018).

129 J. N. Schwämmlein, H. A. El-Sayed, B. M. Stuhmeier, K. F. Wagenbauer, H. Dietz and H. A. Gasteiger, *ECS Trans.* **75,** 971 (2016).

130 S. St. John, R. W. Atkinson, R. R. Unocic, T. A. Zawodzinski and A. B. Papandrew, *J. Phys. Chem. C.* **119,** 13481 (2015).

131 Y. Wang, G. Wang, G. Li, B. Huang, J. Pan, Q. Liu, J. Han, L. Xiao, J. Lu and L. Zhuang, *Energy Environ. Sci.* **8,** 177 (2015).

132 S. St. John, R. W. Atkinson, K. A. Unocic, R. R. Unocic, T. A. Zawodzinski and A. B. Papandrew, *ACS Catal.* **5,** 7015 (2015).

133 K. Elbert, J. Hu, Z. Ma, Y. Zhang, G. Chen, W. An, P. Liu, H. S. Isaacs, R. R. Adzic and J. X. Wang, *ACS Catal.* **5,** 6764 (2015).

134 M. E. Scofield, Y. Zhou, S. Yue, L. Wang, D. Su, X. Tong, M. B. Vukmirovic, R. R. Adzic and S. S. Wong, *ACS Catal.* **6,** 3895 (2016).

135 S. St. John, R. W. Atkinson, A. Roy, R. R. Unocic, A. B. Papandrew and T. A. Zawodzinski, *J. Electrochem. Soc.* **163,** F291 (2016).

136 N. M. Marković, T. J. Schmidt, B. N. Grgur, H. A. Gasteiger, R. J. Behm and P. N. Ross, *J. Phys. Chem. C.* **103,** 8568 (1999).

137 N. Furuya and S. Koide, *Surf. Sci.* **220,** 18 (1989).

138 A. Ruban, B. Hammer, P. Stoltze, H.L. Skriver and J.K. Nørskov, *J. Mol. Catal. A: Chem.* **115,** 421 (1997).

139 J. Rossmeisl, K. Chan, E. Skúlason, M. E. Björketun and V. Tripkovic, *Catal. Today.* **262,** 36 (2016).

140 El Sawy, Ehab N., H. A. El-Sayed and V. I. Birss, *Chem. Commun.* **50,** 11558 (2014).

141 K. Fukuta, H. Inoue, S. Watanabe and H. Yanagi, *ECS Trans.* **19,** 23 (2009).

142 C. A. Reiser, L. Bregoli, T. W. Patterson, J. S. Yi, J. D. Yang, M. L. Perry and T. D. Jarvi, *Electrochem. Solid-State Lett.* **8,** A273 (2005).

143 D.A.J. Rand and R. Woods, *J. Electroanal. Chem. Interfacial Electrochem.* **35,** 209 (1972).

144 K. Kinoshita, J. T. Lundquist and P. Stonehart, *J. Electroanal. Chem. Interfacial Electrochem.* **48,** 157 (1973).

145 S. Kawahara, S. Mitsushima, K. Ota and N. Kamiya, *ECS Trans.* **3,** 625 (2006).

146 Y. Sugawara, A. P. Yadav, A. Nishikata and T. Tsuru, *J. Electroanal. Chem.* **662,** 379 (2011).

147 M. Uchimura, S. Sugawara, Y. Suzuki, J. Zhang and S. S. Kocha, *ECS Trans.* **16,** 225 (2008).

148 K. Yu, D. J. Groom, X. Wang, Z. Yang, M. Gummalla, S. C. Ball, D. J. Myers and P. J. Ferreira, *Chem. Mater.* **26,** 5540 (2014).

149 M. Uchimura and S. S. Kocha, *ECS Trans.* **11,** 1215 (2007).

150 S. Arisetty, X. Wang, R. K. Ahluwalia, R. Mukundan, R. Borup, J. Davey, D. Langlois, F. Gambini, O. Polevaya and S. Blanchet, *J. Electrochem. Soc.* **159,** B455 (2012).

151 A. Ohma, T. Mashio, K. Sato, H. Iden, Y. Ono, K. Sakai, K. Akizuki, S. Takaichi and K. Shinohara, *Electrochim. Acta.* **56,** 10832 (2011).

152 S. Shukla, D. Stanier, M. S. Saha, J. Stumper and M. Secanell, *J. Electrochem. Soc.* **163,** F677 (2016).

153 J. Greeley, I. E. L. Stephens, A. S. Bondarenko, T. P. Johansson, H. A. Hansen, T. F. Jaramillo, J. Rossmeisl, I. Chorkendorff and J. K. Norskov, *Nat. Chem.* **1,** 552 (2009).

154 R. Borup, J. Meyers, B. Pivovar, Y. S. Kim, R. Mukundan, N. Garland, D. Myers, M. Wilson, F. Garzon, D. Wood, P. Zelenay, K. More, K. Stroh, T. Zawodzinski, J. Boncella, J. E. McGrath, M. Inaba, K. Miyatake, M. Hori, K. Ota, Z. Ogumi, S. Miyata, A. Nishikata, Z. Siroma, Y. Uchimoto, K. Yasuda, K.-i. Kimijima and N. Iwashita, *Chem. Rev.* **107,** 3904 (2007).

155 H.-J. Jeon, M.-K. Jeon, M. Kang, S.-G. Lee, Y.-L. Lee, Y.-K. Hong and B.-H. Choi, *Mater. Lett.* **59,** 1801 (2005).

156 K. Kakinuma, Y. Chino, Y. Senoo, M. Uchida, T. Kamino, H. Uchida, S. Deki and M. Watanabe, *Electrochim. Acta.* **110,** 316 (2013).

157 M. Yin, J. Xu, Q. Li, J. O. Jensen, Y. Huang, L. N. Cleemann, N. J. Bjerrum and W. Xing, *Appl. Catal., B.* **144,** 112 (2014).

158 Y. Liu, D. Gokcen, U. Bertocci and T. P. Moffat, *Science.* **338,** 1327 (2012).

6. Acknowledgements

It is of no doubt that my biggest acknowledgement is directed to **Prof. Dr. Hubert A. Gasteiger** who I had the extraordinary chance to get to work with for the past 6 years. Already since my time as a Bachelor's student, I had the pleasure to work with him and be fascinated for electrochemistry. The fact that one could always go to him and find an open ear for every scientific and personal matter makes him not only an outstanding researcher, but also a great mentor. Furthermore, I would like to thank him for numerous meetings until late at night where we would only stop to discuss fuel cell research when the last subway was about to leave. Also, his willingness to support me with any scientific idea that was reasonable and interesting has significantly shaped this thesis.

Another big acknowledgement is clearly directed to all of my fellow researchers that allowed me to guide them during their studies for a Bachelor's Thesis, a Master's Thesis, as a student researcher, or as a technician in our laboratories. Not only did many of them work with extraordinary motivation to acquire the incredible amounts of data and contribute significantly to the outcome of this thesis, but they often became great friends that I am happy to meet in research or in private: **Björn Marcel Stühmeier**, **Ana Marija Damjanovic**, **Nhat Long Tran Pham**, **Katharina Tabitah Freyer**, **Andrea Blankenship**, **Duc Hien Nguyen**, **Yongsheng Chen**, **Philipp Pfändner**, **Carmen Ruiz Fernandez**, **David Fischermeier**, **Masamitsu Egawa**, **Michael Sorg**, **Shang Gao**, **Susana Suttor**, **Thomas Pehl** and **Thomas Braun**.

I am also very grateful for the researchers who guided me as a student at the Chair of Technical electrochemistry. First of all, I would like to thank **Dr. Michele Piana** for the great and gentle introduction to battery research during my Bachelor's Thesis where we often discussed the results of my work until the late evening. Furthermore, I thank **Dr. Stefano Meini** for showing me how much fun research is during my research internship and in the time as a student researcher. During my Master's Thesis, I had the extraordinary luck to be a student of **Dr. Hany El-Sayed** who is an exceptional guide for students and has the capability to fascinate his researchers. I am happy to remember many discussions about every little detail of our research, where we often came up with

new ideas and with even more work. He also became a close friend and I was always happy to work with him in various projects ever since.

During the beginning of my Ph.D. I was fortunate to work with **Dr. Thomas Mittermeier** who introduced me to fuel cell research and made me think of so many little details of fuel cell experiments. I would like to thank him for discussing my thoughts about many projects without actually being involved in them, especially when I simply appeared in his office for lengthy scientific considerations.

I would also like to thank my fellow colleagues who it was a great pleasure to work with. The friendly working atmosphere and the solid scientific knowledge of them was the key to several joint publications. It was also a great pleasure to work with them in a team and supervise students together. Great thanks are directed to **Dr. Gregor Simon Harzer**, **Philipp Jan Rheinländer**, and **Dr. Thomas Mittermeier**.

Furthermore, I would like to that **Dr. Kenneth Charles Neyerlin** who hosted me as a visiting scholar at the National Renewable Energy Laboratory in Denver. Especially the warm and welcoming atmosphere of this research group together with their extraordinary scientific knowledge was a great experience for me.

Additionally, I would like to acknowledge the help of **Teilo Heinz Schaller** and **Dr. Gregor Simon Harzer** for their great efforts of proof-reading this thesis.

Not only in the frame of this thesis, but in my whole life, my parents, **Marianne and Gerd Schwämmlein** supported me in every concern and they always stood up for me, no matter how challenging the times were. There is no doubt that I would have never gotten so far without their care, their education and all of their support.

I also owe a great thanks to my brothers, **André and Marc Schwämmlein**, who I could always rely on in any situation that my life has provided me with or which it will still hold for me. The great childhood that we spent together and the great relationship that we have nowadays gives me new strength whenever I think about it.

Finally, I thank my wife **Sarah Susanne Edith Schwämmlein**, who has become the most important person of my life since the day that I met her. No words could express my gratefulness for our joint time. Whenever a scientific or personal cloud would dark-

en the light, she is the one to remove it and back me up. The strength of this relationship gave me so much support in life and recently, also our son, **Luis Maximilian Schwämmlein** contributed to this wellbeing.